Title
Microfluidic technologies for quantitative single cell analysis

Author
Novak, Richard

Publication Date
2013

Peer reviewed|Thesis/dissertation

Microfluidic Technologies for Quantitative Single Cell Analysis

by

Richard Novak

A dissertation submitted in partial satisfaction of the

requirements for the degree of

Joint Doctor of Philosophy
with University of California, San Francisco

in

Bioengineering

in the

Graduate Division

of the

University of California, Berkeley

Committee in charge:

Professor Richard A. Mathies, Chair
Professor Martyn T. Smith
Professor Joseph L. DeRisi

Fall 2013

Microfluidic Technologies for Quantitative Single Cell Analysis

by

Richard Novak

Abstract

Microfluidic Technologies for Quantitative Single Cell Analysis

by

Richard Novak

Joint Doctor of Philosophy in Bioengineering
University of California, Berkeley
and
University of California, San Francisco

Professor Richard A. Mathies, Chair

Multicellular organisms, from roundworms to humans, are composed of interacting individual cells that give rise to an ensemble behavior. Most current technologies enable observation of only the population-level average and often ignore the vast degree of cell heterogeneity present even in clonal populations. Single cell resolution assays of DNA, RNA, proteins, and other biomolecules can yield insights into the complex interactions present in tissues, organs, and whole organisms. Microfluidic systems facilitate single cell analyses by leveraging the micron-scale geometry for improving sensitivity, decreasing reaction time, decreasing reagents consumption, and improving parallelization and automation for high throughput. Microfluidically-generated droplets, in particular, offer extremely high scalability of reactions and straightforward single cell manipulation. This thesis presents the development of microfluidic droplet generator designs and their application for single cell analysis.

Developments in microfabricated chip design presented here have resulted in versatile droplet generation tools for a wide range of applications, while novel microfabrication techniques dramatically reduced fabrication time in commercially-viable materials. A radial micropump design increased throughput per device up to $3x10^6$ droplets per hour, allowing us to detect via digital PCR a single pathogenic *E. coli* O175 in a background of 10^5 nonpathogenic bacteria. Developing a rapid nickel mold fabrication method has facilitated prototyping and testing of microfluidic designs in thermoplastic materials in as little as 1-3 hours. These microfabrication innovations have accelerated the pace of device development to meet the needs of single cell analysis and other applications.

Microfluidic technologies are opening up research paths that so far have been difficult to pursue using conventional methods. High-throughput droplet generation is used to screen purified DNA from healthy subjects exposed to carcinogens for the lymphoma-related t(14;18) chromosomal translocation with a limit of quantitation of less than 1 mutation in 10^7 genomes and a dynamic range of 10^5. We also identify unique breakpoint sites and demonstrate the ability to quantify the relative and absolute mutation frequencies *within* individuals for subjects with multiple mutation events. For analysis of single cell genomes, we present a novel approach for robust DNA purification and analysis using microfluidic agarose droplet encapsulation of single cells. Agarose provides a rigid yet porous shell around cells that enables purification of whole

genomes for thousands of cells in parallel without the loss of single cell fidelity. We apply this method to detecting cells containing the t(14;18) translocation and sequencing two DNA targets per cell. This is extended to 9-plex forensic profiling of single cells, thus enabling analysis of complex crime scene samples with multiple contributors or samples with excessive DNA contamination.

Finally, droplets are applied to investigating multiple biological parameters per cell, including growth rate, gene expression, and alternative splicing. We perform cell culture in nanoliter droplets for fast generation and monitoring of colonies originating from single cells. Colonies are subsequently assayed for telomerase hTR RNA and hTERT mRNA expression levels and hTERT splice variants. We observe a large degree of expression level bimodality for several splice variants and significant reductions in bimodality coupled with increases in alpha splicing following exposure to sub-lethal concentrations of the anti-cancer compound curcumin. Prospects for microfluidic droplets are discussed in the context of multiparameter single cell analysis as well as applications of single cell analysis to microfluidic organs-on-a-chip. Understanding basic molecular biology mechanisms from the perspective of single cells will yield insights into behavior of multicellular populations with far-reaching scientific and clinical impacts.

~ In loving memory of my grandparents ~

Table of Contents

List of Figures

List of Tables

Acknowledgements

They say it takes a village to raise a child, and the trek toward a PhD is no different. I am grateful to many people who provided support and motivation and just plain good advice along the way. First among them are my parents, Jan and Lea, who raised me with the idea that life should be fun and filled with exploration. Some of my earliest memories are collecting mushrooms and fossils and looking at puddle scum under a microscope in Prague. Then in Alabama, I am grateful for what must have been (for you) excruciating times of intense bug collecting, snake catching, and similar forays into nature. I am particularly glad for the first chances to experience real science: pathology in the form of dissecting roadkill and then stuffing it in semi-lifelike poses, and molecular biology and genetics in the form of trapping turtles and sampling DNA to find out how related they are and whether they migrate or not. Without your dedication and tireless pursuit of a good life in this country, I'm sure I would have turned out differently.

I am also in awe of my sister, Marketa, who against all odds of growing up in a science household somehow managed to get out into the real world. But thank you for helping me catch my lizards and bugs nevertheless. You constantly show me how important the non-science aspects of life are, and you are a first-rate example of how to be happy, be an amazing kind-hearted friend, and through that, bring joy to those around you.

Aside from my family, three fantastic people helped steer me toward graduate school. Bob Pollard, my biology teacher, mentor, and good friend from Indian Springs School, gave me the chance to flourish in high school and pushed me to really do what interests me but do it well. I also owe him my constant urge to travel around the world, which I put to good use in starting Future Scientist with Bob assisting with the first trip. At Emory I was fortunate to have two incredible advisors. Arri Eisen helped me start doing research my first month in college, and I am immensely grateful for personally taking me under his wing and teaching me not only basic techniques but importantly, how to do good science and think scientifically. Chris Beck suffered through two years of advising my honors research where I kept building and breaking things. It was work in your lab that made me realize that bioengineering, more than pure biology, is what I most enjoy and am good at. Both of you also urged me to apply to grad school, saying "just interview and see if you like it." It was a trick, I know, since here I am.

At UC Berkeley, Rich Mathies gave me a home in his group in response to my notification that I would be gone for several weeks at the end of my rotation, by saying that I can go as long as I begin working on my thesis project when I returned. From then on I knew to expect the unexpected with Rich. I am grateful for the chance to have worked with you. From the inquisition-like first group meeting, I learned to think critically, present clearly, and realize that one only has a case if one has data. I appreciate the results-focused approach, which gave me the freedom to pursue interests outside of my thesis research. I should also highlight here the immense role that Mary Hammond and Dennie Ho played in shielding me from Rich's wrath and

providing immense assistance and empathy. Without you, getting a PhD would have been quite an arduous and stressful slog.

Of course the professor is only part of the lab. I joined the lab because of the many incredible scientists and just plain good people. I am particularly grateful to Yong Zeng for working with me for several years and discussing many wild ideas. Sam Cronier, Numrin Thaitrong, and Nav Ranu were wonderful labmates and amazing friends outside of grad school. I am also grateful for the talented undergraduate researchers who somehow ended up with me: Kristina Hart, Roy Tangsombatvisit, and Chih-Han Lee. I am also honored to have worked with and learned from the other Mathies lab members, including Tao Geng, Amy Twite, and the many others on DNA side as well as Raman side. I also would like to acknowledge the members of the Smith lab, including Joe Shuga, Sarah Daniels, Fenna Sille, Luoping Zhang, and Martyn Smith. You provided me with an astounding amount of your time and expertise and a chance to just chat. Joe, I look forward to many more dinners where we can discuss science over some good drinks. My graduate experience wouldn't have been complete without the three months spent in Peter Ertl's lab in Vienna. Thank you Peter, Jakub Dostalek, Verena Charwat, Simone Hageneder, and the rest of the Ertl and Dostalek labs as well as Gunther Lepperdinger for welcoming me and teaching me a thing or two about Austrian wine. Let's try to put together another "high altitude biotechnology conference" in the Alps.

Lastly, my friends have been the bedrock of my sanity, providing support when times were bad and helping celebrate the good. Rick Henrikson, my roommate of 4 years, taught me how to throw a party and how to enjoy life. Gautham Venugopalan, my soulmate of food and wine selection, taught me to appreciate a good (and bad) pun. I am also indebted to your effort in turning Future Scientist from a random student organization into a real nonprofit. Jesse Arp and Monica Gan helped me get away from it all by being very dependable climbing partners since my first week in Berkeley. And life in the Bay Area would certainly not have been as much fun without the efforts of Karen Ring, Steve Ervin, Cleya Ormiston, Mark Levrette, Laura Nahm, and countless others. Finally, I am immensely grateful to Francesca Gazzaniga, my lovely fiancée and partner in adventure and science. I am truly lucky to have found you and look forward to our lives of science, wine, and the outdoors.

Chapter 1: The complex world of single cells

Single cell analysis is the next frontier of biology. What is going on in the most basic of all units of life: the cell? Yes, it is an approach that, at least to the casual observer, may seem like "missing the forest for the trees" and too deconstructionist an approach. However, it is anything but. Single cell analysis is the addition of information for each cell and synthesizing it to understand the population as a whole. It is an acknowledgement that biological processes occur fundamentally at the level of a cell. The genes, proteins, and countless many other molecules held inside that tiny phospholipid sack are the key interacting components of biological pathways, with one cell possessing the capability to be quite distinct from its neighbors. In fact, we have most likely been missing and misunderstanding many phenomena by viewing the population as representative of the cells it is composed of. This misses the outliers in the populations, which may be the cells responsible for disease or improving health. Being able to observe the workings in each cell, for each cell in a tissue, organ, or organism, will provide deep scientific insights into how cells work and how they interact, which will bring about transformational diagnostic and therapeutic applications.

1.1 Motivation for single cell analysis

There are two main reasons for pursuing single cell analysis: 1) detection and analysis of extremely rare cells for diagnostic and monitoring purposes, 2) understanding the fundamental biology of cellular processes, from relationships between the environment and gene expression to the relevance of biological noise on evolution.

Sensing very infrequent, or "rare," cells in a vast population of background cells is a key step toward detecting early disease that is possibly easier to cure. In addition, the ability to parse out the few cells of interest and actually have the assay sensitivity for meaningful analysis is opening up avenues of research previously not conceived with older technologies. For example, circulating cancer or stem cells can now not only be detected and counted, but they can be shuttled into downstream assays that provide a glimpse of their pathogenicity.[1–3] However, an incredible technological advance is the capability to accurately quantify the number of rare cells of interest despite a background population of cells that is many orders of magnitude greater.

The real strength of rare cell detection lies in early cancer detection and treatment monitoring as well as investigation of stem cell biology. Cancer generally becomes deadly following metastasis, where cells from the initial tumor spread through the circulatory or lymphatic systems to other tissues in the body. Yet the level of these metastasizing cells is exceedingly low, precluding the use of traditional "bulk" analytical tools. A number of methods have been developed to concentrate and isolate circulating cells for quantification and downstream analysis.[1,4,5] Many of the developed tools rely on microfluidic technologies that can leverage the small scale of the channels in order to efficiently screen passing cells for cancer biomarkers, such as cell adhesion molecules that should not appear in healthy circulating cells. This high-resolution approach has yielded dramatic results in terms of correlating the frequency of circulating cells with patient survival and therapy response.[4–6] However, the ability to detect exceedingly rare cells has only opened up additional questions that need to be answered before the detection of circulating tumor cells can become clinically viable. In particular, the captured cells, presumably originating from a single or possibly a small number of tumors, have been highly variable in phenotype and

genotype.[4,7] Understanding this cellular heterogeneity is crucial toward a more accurate view of biological processes related to cancer development and therapy response.

Clonal cells under identical environmental conditions can be very different in terms of biological response to stimuli. This is largely due to the stochastic and discrete nature of cellular biology and the dominant role of packaging into small volumes. In a cell, the machinery that transcribes DNA into mRNA, that shuttles the mRNA out of the cell, that translates mRNA into protein, not to mention all other processes, relies on discrete molecules subject to thermodynamics and molecular motion. With discrete, moving, and closely packed molecules encased in a flexible membrane while undergoing more deterministic processes, a cell is really a microscopic bag of marbles that is being randomly shaken about. One would not expect two such bags, even if they start out with identical "marble" positions, to remain identical even moments later. Cells are far more complex than bags of marbles, with slight variations in the copy number of molecules possible immediately after cell division, which can then affect all downstream functions. Analyzing cells in a bulk sample can give pleasing uniform results, but such an analysis will hide the tremendous variation, or noise, that is inherent in biological mechanisms. As an example, consider the scenario presented in Figure 1.1. Bulk analysis confirms the presence of 6 "red" and 6 "blue" proteins in a sample. However, these proteins could have originated from a truly random distribution (top) or possibly from a perfectly bimodal distribution (bottom). While the random distribution cannot be discounted, only single cell measurements can distinguish between the two options and a range of intermediate scenarios. It is interesting to observe even in this simplistic example the role of packaging by cell membranes in cell-cell heterogeneity. With small protein numbers per cell, any cellular noise can quickly change an initially homogeneous population into one with greater diversity of states, including significant extremes.

Michael Elowitz was one of the first to extensively investigate the origins and relevance of biological noise.[8,9] Using a synthetic genetic "repressilator" circuit in *E. coli*, consisting of an oscillating circuit of three mutually-inhibitory genes and a fluorescent reporter, his group showed that gene expression noise consists of intrinsic and extrinsic factors. Intrinsic factors are the fluctuating biochemical components of gene expression, from transcription to translation, due to diffusion, reaction rates, and other stochastic and mostly biophysical phenomena. Extrinsic noise, on the other hand, consists of variable numbers of polymerases, regulatory proteins, and translational machinery. Extrinsic noise is driven by intrinsic noise, since noisy production of a single protein, such as an RNA polymerase, will then result in greater extrinsic noise that affects genes globally within a cell. Both sources of noise combine to give the final heterogeneity that affects cellular behavior. Studies in *E. coli* and yeast using high-throughput fluorescent reporter methods have greatly contributed to our understanding of cell heterogeneity due to noisy cellular mechanisms.[9–11]

The ability to perform single cell analysis has led to insights into biological regulatory mechanisms and evolutionary processes. While extrinsic noise is the primary driver of heterogeneity,[9,12] intrinsic noise dominates for genes with low levels of transcription and translation.[11] At copy numbers of approximately 1-2 per cell, the presence or absence of a single additional copy of mRNA makes as much as a 100% difference in concentration and it is impossible to produce only half of an mRNA or protein. As a result, low-expression genes tend to exhibit more bursting patterns of expression, which is primarily affected by intrinsic noise. Genes with large copy numbers, such as metabolic genes, are more susceptible to extrinsic noise, where

the abundance of metabolites or other components has a greater impact than the dynamics of transcription and translation.[11]

There have been a number of hypotheses for the role of cell heterogeneity and biological noise. First, the noisiness of one gene can help regulate a number of downstream genes, since the bursting pattern, rather than the copy number, of a low-copy gene will dictate the expression of genes the resulting protein regulates. This leads to more robust frequency-based control of protein production in the downstream genes, rather than relatively unstable amplitude control. Second, noise in biological networks helps a population of identical cells probe various states, which can allow at least a fraction of the population to succeed under a broad range of environmental conditions and stressors. A similar process is thought to occur among stem cells, where differentiation occurs probabilistically due to noisy signaling pathways, driving the development of embryo tissue as well as maintaining stem cell populations in adults while sustainably allowing differentiation to maintain tissues.[13–15] Finally, noise-induced cell heterogeneity can lead to evolution in long-term scenarios, where a subpopulation of cells is selected for by the environmental conditions, leading to a shift toward that specific phenotype, which can then become stabilized in the population through acquisition of genetic mutations.[16,17]

Single cell genomics will bring about a dramatic change in our understanding of biological processes. Bulk analyses have hidden the diversity of responses and phenotypes of single cells. And it is particularly this diversity that has hindered progress in cancer treatment.[18] Patients with heterogeneous tumors were found to have cancer that progressed more rapidly and was less susceptible to treatment than patients with low tumor heterogeneity.[19–22] These results support the role of gene expression noise in enhancing environmental stress survival and population evolution and extend this idea to tumors living in the patient "environment." Much more work remains before cell heterogeneity can be factored into targeted therapies as part of personalized medicine. For example, not only the tumor heterogeneity matters; the heterogeneity of healthy cells could also have a significant impact in patients. Using single cell transcriptome sequencing, the Regev group has found that immune cells respond in different degrees and with different gene expression profiles to the same antigen stimulus.[23] This suggests that even with homogeneous and identical diseases, patients will respond differently to treatment even based on their baseline cell heterogeneity.

Significant headway is being made in understanding the diversity present within seemingly homogeneous tissue. Although most of the studies to date have focused on synthetic circuits or tumors due to the relative ease with which they can be manipulated and the diversity that they offer, recent work has shown cellular heterogeneity to extend to normal cells. In addition to the immune cell work discussed above, which reflects primarily heterogeneity of gene expression, McConnell et al. have shown neurons in mice and humans to exhibit dramatic gene copy number variation.[24] This suggests that many studies are forthcoming that will help elucidate what is really going on in our bodies in the healthy state.

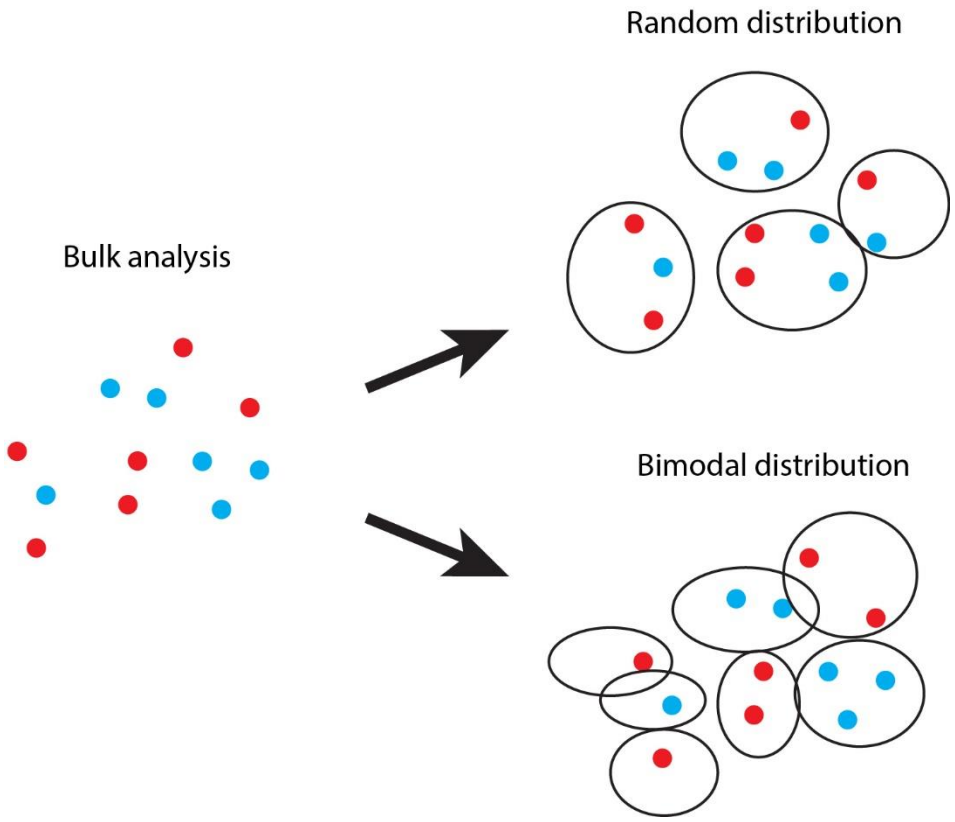

Figure 1.1. Motivation for single cell analysis. Analysis of a sample consisting of 6 red and 6 blue "proteins" by bulk methods (left) provides that information. However, this belies the importance of compartmentalization at the cell level. Two extreme possibilities, random and bimodal distributions, are shown here. Both situations contain equal ratios of red and blue "proteins" and would result in identical bulk measurements. The lower, bimodal, scenario highlights the non-random assortment of proteins in cells, which would presumably have significant biological effects and would be entirely missed by bulk analysis. Also note the importance of small volume compartmentalization in both scenarios, where single cells can have very different protein levels due to stochastic fluctuations.

Many initially contradictory findings are being explained by the use of single cell-level analysis tools that overcome the technological limits of earlier studies. As a result, there has been a push toward the development of assays, hardware, and software with the sensitivity and throughput required for single cell analysis. Microfluidic systems have been applied extensively due to the ability to manipulate cells and reagent volumes at approximately the scale of a single cell, provide large signal-to-noise ratio data for even single molecule detection, consume small volumes of reagents per assay, and enable extreme parallelization and automation required for the processing of thousands or millions of single cells in order to understand how individual variation adds up to the behavior of an entire population. Technology developments will further drive our understanding of single cell-level biology through more information and more parameters analyzed per cell.

1.2 Established technologies for single cell analysis

Technology development in the context of single cells has spanned from the invention of the microscope in the 17th century through the present microfluidic approaches. The ability to visually discern single cells marked the beginning of single cell analysis, and the amount of information gleaned from each cell has been continually increasing. The technologies that will be discussed here have generally relied on microscopy and related optical detection methods as the primary technological innovation, unlike sequencing-based methods and microfluidic platforms that present improved cell manipulation and produce higher resolution molecular information. This section focuses on recent developments in the more traditional fields of technology in the context of multi-parameter single cell analysis.

1.2.1 Microscopy-based methods

Microscopy has enabled single cell analysis by allowing researchers to detect morphological differences or changes at the single cell or sub-cellular levels. Earliest developments involved the use of staining to provide biologically-relevant contrast agents, and chemical stains, such as hematoxilin-eosin or periodic acid-Schiff stains, have been used for the last century and are still widely applied in pathology. The underlying premise consists of differential binding of the dyes to various cellular components. Different cell types and diseased cells exhibit distinct staining patterns that can be analyzed, offering greater information content than what can be achieved with brightfield microscopy. In the latter half of the 20th century, the discovery of monoclonal antibodies and fluorescent labeling led to the adoption of immunofluorescent assays that offer drastically higher sensitivity and specificity compared to chemical stains. This led to the natural multiplexing of assays, which can now provide spatial and abundance information of proteins of possibly hundreds of targets.[25] The discovery of green fluorescent protein (GFP) in the jellyfish *Aequoria victoria* by Shimomura et al. in the 1960s revolutionized single cell analysis by providing an "internalized" single cell assay that could be monitored in real time and did not require external reagents.[26] Applied as a reporter of gene expression by Chalfie et al., GFP enabled the study of gene expression patterns, including most of the cellular noise work described earlier, while conjugating GFP to proteins resulted in an upheaval in how protein localization studies are performed.[27,28] It resulted in a dramatic surge in single cell studies for the cases where prior genetic

manipulation of cells did not impact the application, particularly opening up subcellular localization and dynamics of gene expression to analysis through microscopy and other optical means. Raman microscopy, where the output is a Raman spectrum per image pixel, has allowed label-free imaging of tissue and cells and is promising in terms of its ability to discern healthy from diseased cells.[29,30] It is particularly sensitive to lipids, which has allowed researchers to circumvent the lack of specific lipid labels.

The development of robust karyotyping in the 1950's provided a level of genetic information not available prior.[31] By being able to see chromosomes from single cells, it was possible to obtain information on large genetic changes, which led to the discovery of the Philadelphia chromosome and subsequent investigations of the role of genetic mutations in cancer development.[32] Recently, the basic karyotype has evolved into an information-rich tool as a result of fluorescence *in-situ* hybridization (FISH), where synthetic fluorescently-labeled DNA is used to hybridize to DNA or RNA targets of interest.[33,34] This method has been expanded to the whole genome using SKY (Spectral Karyotyping) by marking regions of chromosomes with specific colors, thus providing sequence-level data for high-throughput chromosome modification studies.[35,36] Although improvements in fluorescence detection and labeling have allowed for the detection of single RNA molecules, *in-situ* PCR amplification offers greater sensitivity by amplifying the single target of interest for subsequent labeling.[37] Though the method initially suffered from high background signal, it is now gaining traction with the advent of non-PCR nucleic acid amplification methods that can offer greater control over nonspecific amplification. In particular, Larsson et al. have been able to detect single mRNA molecules with spatial information inside single cells for a wide range of targets with excellent specificity.[38] This allows the spatial context of single cells in the tissue to be preserved and incorporated into analysis.

Imaging single cells, primarily based on innovations and adaptations of microscopy, have been the workhorse of single cell analysis at many levels of biology. The amount and type of information obtained from single samples has growth tremendously, and commercial systems called High Content Analysis (or Information) systems are leveraging the data acquisition primarily for drug screening applications.[39] This trend will only grow as additional imaging modalities are integrated. While microscopy offers excellent resolution and sensitivity, throughput remains relatively low, which is especially problematic for low-abundance targets. For areas of research requiring analysis of many thousands of cells per sample, such as immunology, flow cytometry has been the primary tool of choice.

1.2.2 Flow cytometry

Flow cytometry at its most fundamental involves taking an average fluorescence measurement for the whole cell as it passes through a modified fluorescence microscope. In doing so, the readout of information is controlled by the physical translocation of the sample, which can take place on the order of 10 kHz. As a result, it is feasible to analyze very large and possibly diverse cell populations. Due to the extensive development of antibody-based immunofluorescence staining for microscopy and the relative ease of access, the primary targets of flow cytometry were cell surface proteins. This led to the discovery of immune cell subpopulations that have revolutionized our understanding of the immune system and its diseases. Flow cytometry also provided the first strong evidence for heterogeneity of cells otherwise considered to be identical, since the method

enables dynamic cell response assays that showcase cellular heterogeneity. Finally, flow cytometry was coupled with sorting to provide a way to not only analyze single cells based on their surface markers, but it allows for the collection of the analyzed and living cells for subculture or deposition into individual genetic analysis reactions.

As with microscopy, the hardware is not limited to a particular type of bioanalysis. Aside from extensive surface protein assays, flow cytometry has been used to determine the phosphorylation status of intracellular proteins, DNA content of cells, telomere length, and gene expression using fluorescent protein reporters and FISH staining of mRNAs.[40–45] Nevertheless, the biggest drawback has been the relatively low level of multiplexing possible, since a readout has to take place in less than a millisecond, and, unlike microscopy, there is no possibility for repeat measurements of the same cell.

The spectral limit of flow cytometry has been improved by the addition of various tandem dyes, dyes with narrow excitation and emission wavelengths, and the expansion of the available spectral range via the development of far-red and far-violet dyes.[46,47] This approach has led to the ability to screen up to 36 proteins at a rate of approximately 1 kHz.[46] As an alternative, the Nolan group developed a tandem flow cytometer coupled with time-of-flight mass spectroscopy detection of lanthanide-labeled antibodies called CyTOF.[46–48] The key advantage of this approach lies in the lack of lanthanide elements in biological systems, thereby offering extremely low background signals. Furthermore, the exquisite resolution of the mass spectrometer avoids any spectral overlap that is inherent in fluorescence-based assays. In the first demonstration of the method, the researchers investigated pathway regulation in single cells, since they were able to monitor the levels of 18 protein phosphorylation states simultaneously.[48] This method will provide extremely detailed single cell information and likely will become more widespread once the system can be made cheaper and more robust.

1.2.3 Cell sorting

The strength of flow cytometry lies in its ability to process hundreds of thousands of cells with single cell resolution. While multiplexing capabilities have improved, especially in the last five years, access to genetic information has been quite limited. Although RNA-FISH has been adapted to flow cytometry, it does not facilitate the discovery of novel genetic targets as it requires *a priori* knowledge of the target sequence. GFP-transfected cells can provide greater versatility for discovery-based assays in cell lines, but the transfection process itself can in some cases confound the results and does not lend itself to clinical samples. For discovery-focused studies, cell sorting has been coupled with downstream assays in order to provide single cell genetic information coupled with flow cytometric measurements of surface protein levels or selection of rare cell populations.

The sorting approach has been applied especially well to immunology. As with the development of flow cytometry and the pursuit of cell heterogeneity, the real driver of the technology has been the inherent DNA-level heterogeneity in antibody-producing immune cells. Since B and T cells undergo a recombination event that removes part of their genome and shuffles the loci that generate antibodies, the importance of cellular heterogeneity had been well-appreciated. As a result, research focused on the development of single cell assays from the very

start. Indeed, the single cell sequences of the heavy and light chains of immunoglobulins have been of particular importance, since both the heavy and light chain determine antigen specificity. Cell sorting has been used to manipulate cells of a specific lineage, labeled with specific fluorescent antibodies, and place single cells in 96 well PCR plates for reverse transcription and cDNA library generation.[49,50] Similarly, flow sorting has been applied to a number of single cell RNA-seq and whole genome amplification studies, resulting in large scale genomic sequence data for single cells.[23,51,52] Additionally, cell sorting with subsequent genetic analysis has been used to investigate immune cell response diversity at both the mRNA and protein level by correlating flow cytometry measurements with the mRNA data via indexing of the cell protein data with the downstream well location.[53,54]

1.2.4 Summary

The optics-based methods discussed here have relied on a history of technology development. The methods, while utilizing traditional hardware approaches for the most part, have provided a wealth of single cell data that is difficult to obtain any other way. The preservation of tissue context is the hallmark of microscopy, which is for now unique to this method. Flow cytometry, on the other hand, has throughput that meets the requirements of single cell analysis in highly heterogeneous populations (e.g., immune system), and that throughput has not been met by other established technologies. Further combinations of parameters with high degrees of multiplexing for each will further advance our understanding of biological pathways and cellular diversity. However, there are many opportunities for improving cell handling, especially with small numbers of cells, reducing reagent consumption, and offering dynamic experimental conditions not possible with traditional technologies.

1.3 Microfluidic approaches for single cell analysis

Microfluidic systems consist of devices that have channel geometries on the scale of a few to several hundred micrometers in cross section, or approximately that of single cells or small tissues. Reducing the scale of the fluidic channels provides a number of advantages for single cell analysis that are impossible to achieve in macro scale systems.

- **Reduced reagent consumption.** By virtue of the small channel dimensions, the volume of reagents required drops by many orders of magnitude. This is of great importance for expensive or rare molecules such as antibodies or purified antigens, enzymes, and cytokines. Furthermore, microfluidic devices allow for metering and transport of picoliters and nanoliters of reagents, enabling extremely accurate dosing of cells at even these small volumes.
- **Increased throughput.** Packing individual reactions into smaller volumes allows for a greater reaction density. In the space of a 96 well PCR plate, it is possible to analyze hundreds of thousands of cells using several microfluidic approaches. Using smaller volumes can also result in a more rapid manipulation of samples, which, at the human scale, is limited by pipetting.
- **Ease of efficient automation.** Microfluidic devices can be operated much like computer chips and, in fact, share many similar functional features. As a result of integration of these

components in a single device, microfluidic devices can perform complex programmable fluid handling operations with minimal sample loss and high precision.

- **Decreased assay times.** Reducing size scales also reduces the time for molecular diffusion throughout a reactor. Diffusion time, t, in three dimensions follows the equation:

$$t = \frac{x^2}{6D} \qquad \text{(Eq. 1)}$$

D is the diffusion coefficient, and x is the diffusion displacement. One can therefore see that reducing the displacement requirements by a factor of 100 (a reduction corresponding roughly to going from a standard PCR tube to a single microdroplet) reduces the time for complete diffusion by a factor of 10^4. In addition, single molecules become effectively concentrated if located in smaller volumes. This then increases reaction kinetics as well, since reactions occur at a rate proportional to the concentration of each reagent.

- **Increased temporal and spatial control.** In microscale systems, transport of analytes is not complicated by chaotic turbulence. Not only does this provide greater accuracy for simulations, it enables the design of systems for dynamic and selective spatial control of reagents, microenvironments, etc… The Reynold's number, Re, which expresses the ratio of inertial forces to viscous forces, can be calculated from:

$$Re = \frac{QD_H}{\nu A} \qquad \text{(Eq. 2)}$$

Where Q is the volumetric flow rate, D_H is the hydraulic diameter, ν is the kinematic viscosity, and A is the cross sectional area of the channel. For most microfluidic systems under typical conditions, the Reynold's number tends to lie between 10^{-6} and 10, which is well below the transition from turbulent flow to laminar flow at approximately Re = 2,000.[55] As a result, mixing in channels occurs almost entirely due to diffusion, allowing for devices to leverage this property for generation of drug gradients, well-defined pulses of stimuli, and capture of cells using hydrodynamic flows.

1.4 Microfabrication methods

The field of microfluidics began as an offshoot from the semiconductor industry, where microscale features could readily be made using photolithography. The transition proceeded via the development of several key analytical chemistry tools, such as HPLC, gas chromatography, and capillary electrophoresis that all rely on microscale capillaries.[56] For active fluid control, the field borrowed from the invention of microelectromechanical systems (MEMS). While MEMS resulted in the creation of various mechanical features that are being used extensively today (e.g., accelerometers in cell phones and cars), MEMS concepts were applied to integrated valving and the idea of high density integration of diverse functional components. As a result of this history, the earliest devices were fabricated from silicon, a material with extensive and optimized fabrication protocols thanks to the semiconductor industry, and later from glass as a result of the analytical chemistry origins. Over the last 10-15 years, however, microfluidic devices have been fabricated more commonly from poly (dimethyl siloxane) or PDMS, a clear elastic polymer.

The fabrication process, as shown in Figure 1.2, begins with a silicon wafer, which is coated with a UV-curable epoxy photoresist (A). The process involves spin-coating the photoresist to the desired thickness, followed by baking to solidify the polymer. Next, the photoresist-coated wafer is exposed to UV light through a lithography mask (B), which in the case of the most commonly used photoresist, SU-8, blocks light from the areas between fluidic channels. The UV exposure results in a crosslinking of the polymer's epoxide moieties and hardening of the exposed polymer regions (C), which remain in place during development in a solvent, while the unexposed polymer is washed off. This silicon wafer with hardened polymer features is used as a master mold and is sometimes coated with a fluorinated silane to aid demolding (D). PDMS, typically mixed at a 10:1 ratio of monomer:curing agent, is poured over the mold to the desired height and allowed to polymerize at 60-70 ^{o}C for several hours (E). The molded PDMS is then removed (F), via holes are punched out, and the device is completed by bonding the PDMS features to a glass slide using a brief oxygen plasma treatment of both glass and PDMS (G).

The advantage of this method, and one of the principal reasons it is so widely adopted, is the relative ease with which micron-resolution PDMS devices can be made. The entire process is highly optimized and uses standard microfabrication equipment commonly found at most research universities. Compared to initial glass and silicon devices, PDMS fabrication is much faster: at the fast end for each method, it takes approximately 3-5 h for PDMS versus several days for glass. PDMS also exhibits a number of attractive material properties for certain applications. Its elasticity and softness enable fabrication of dynamic features, such as valves, fluidic capacitors, and various actuators. The polymer can also be readily functionalized by well-established chemical reactions, and its optical clarity with minimal autofluorescence combined with a high degree of gas permeability make it well-suited for cell assays.

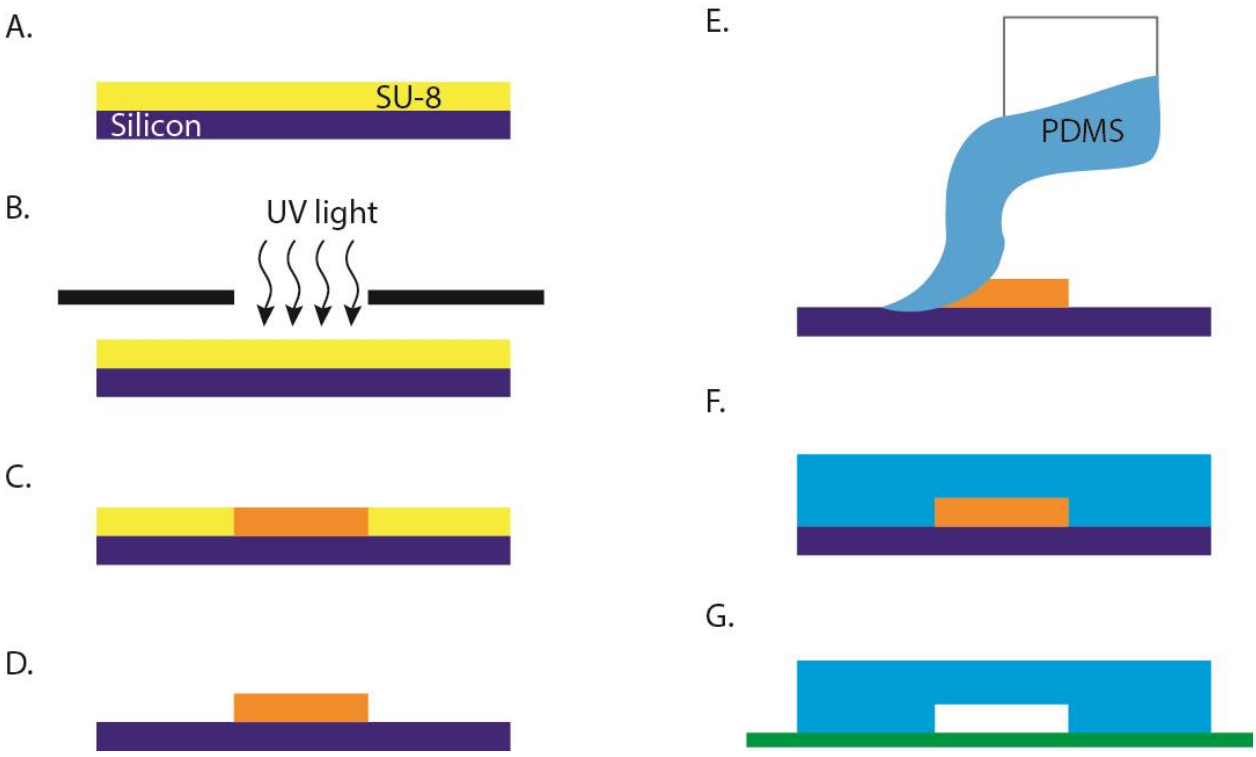

Figure 1.2. Diagram of a standard PDMS fabrication workflow using photolithography. (A) A silicon wafer is spin-coated with liquid SU-8 photoresist that is then baked to harden it. (B) The photoresist is polymerized in the desired pattern by exposing it to UV light through a mask. The polymerized features (C) are developed to leave only the network on raised channels or other features (D). (E) PDMS, composed of a mixture of base polymer and curing agent mixed together and degassed, is poured on the SU-8 mold and allowed to polymerize (F). The molded PDMS is peeled off and bonded to a glass slide by oxygen plasma surface treatment.

Nevertheless, PDMS is also too often used without giving thought to the negative aspects of the polymer for cell analysis.[57] PDMS, by virtue of being a hydrophobic and porous polymer, is notorious for absorbing and adsorbing various small molecules. Fluorescent compounds can produce a large background signal on the channels walls while small molecule drug candidates can dissolve into the chip matrix and end up being screened at unpredictable concentrations. The PDMS surface can cause significant absorption and denaturation of proteins, which can affect protein level readout or inhibit cell culture reliant on very low concentrations of cytokines and other medium supplements. The gas permeability of PDMS is also a hindrance when controlled gas level and composition is required or when the devices are used at high temperatures (e.g., PCR), resulting in evaporative loss of the contents. As a consequence, there is an increased push toward the development of practical alternative microfabrication methods, not only to counteract the problems described here but also to facilitate commercial production of successful designs.

Thermoplastics, polymers that can be molded or re-molded by heating to a softening point, are especially desirable materials for commercial applications. These materials can be incorporated into existing high-speed production processes, specifically injection molding and hot embossing, to produce large quantities of inexpensive devices. In addition, thermoplastics offer a wide range of mechanical, optical, chemical, and biocompatibility properties that enable the selection of the most suitable properties to fit a given application while still being manufacturable. The limiting factor, however, has been the lack of a microfabrication process for making molds that is comparable in speed and tool requirements to that of PDMS devices. Thermoplastic production, especially for commercial applications where thousands of devices are produced per run, require more durable molds that have been difficult to fabricate quickly and without specialized machines. This is in contrast with PDMS fabrication in research settings where molds typically do not need to last more than tens of molding cycles. However, the lack of suitable fabrication methods has not proven insurmountable and several alternatives exist, including those discussed in Section 1. Future device development will almost certainly take place in commercially-viable thermoplastic materials from the beginning as molding methods gain wider adoption by the research community.

1.5 Fluid actuation

Once a microfluidic device is made, actuating liquid, such as cells and other analytes as well as reagents, becomes the main problem. The entire motivation to moving to the microscale or even smaller is to be able to manipulate small particles, such as cells or proteins, in small volumes. Yet standard macroscale actuators are too crude for directly handling single cells or nanoliter volumes. As a result, fluid actuation at these small scales has relied either on bulk fluid flow combined with physical micro- and nanoscale phenomena or microfabricated actuation.

Experiments involving externally-driven flows typically use syringe pumps to push liquid through channels more or less in a continuous manner. This is particularly useful for assays or processes that can be operated without a need for switching reagents or extensive stopping and routing of liquid. In addition, reliance on physical phenomena, such as droplet generation using fluid flow instabilities that will be discussed later in this chapter, has the possibility for extremely high actuation rates. In the case of droplet generation, frequencies in excess of 1 MHz have been documented using both fluid instability and ultrasonic actuation of a microfluidic nozzle while

flowing with typical macroscale actuators.[58,59] The resulting droplets are on the order of femtoliters to picoliters, which would be difficult to achieve using macroscale actuation.

Despite the relatively simple device fabrication and high throughput, continuous flow approaches have numerous limitations that may be undesirable for certain applications. Placing reagents and cells in syringes means that a separate syringe and actuator is required for each input, larger volumes are required, and switching between reagents is difficult to automate and requires a transition period for fluid flow to reach equilibrium. Furthermore, cells tend to fall out of suspension in syringes and can get sheared in the needle at high flow rates. Reliance on physical properties for applications such as droplet generation means that any changes in reagent composition require re-optimization of experimental conditions and sometimes even microfluidic geometry redesign.

To combat these pitfalls, microfluidic valves were developed, which enable routing and actuation within a fully integrated device. The first valves were designed by the Quake[60] and Mathies[61] groups, and both consist of a thin, elastic PDMS membrane overlaying a fluidic channel. The biggest difference lies in the mode of operation, as highlighted in Figure 1.3A and B. The Quake design is a "push to close" design where the PDMS membrane is pushed down with air or liquid pressure over a continuous fluidic channel to close it. The Mathies design, in contrast, is a "pull to open" design where vacuum is applied to the membrane, lifting it up and connecting a discontinuous fluidic channel. As a result, Quake valves are normally open while Mathies valves are normally closed. The Mathies design also offers greater backpressure handling capability and generally more robust sealing due to the fluidic channel discontinuity, whereas the Quake design is more prone to leaks without significant optimization of the microfabrication process. While alternative valve types have been developed since then, often based on gel swelling and other physical behavior of solids, the Mathies and Quake designs have been by far the most widely adopted in academia and industry. They enable large scale integration of fluidic components analogous to the way computer chips integrate millions of transistors for seamless operation.[62] Valving arrays have been applied to partitioning thousands of individual compartments for digital PCR assays[63] and for versatile, assay-agnostic fluid handling using a microfluidic automaton.[64,64] Control of individual valves is managed through the actuation of pneumatic solenoid valves, which facilitate the transduction of pressure or vacuum to microscale valves. Numerous approaches have been developed that allow multiplexing and demultiplexing of actuation, including the use of standard Boolean operations, thereby alleviating the problem of having one macroscale actuator per input.[65,66] Recently, microvalves have been designed in the Mathies lab for integration with a wide range of substrates, including pre-functionalized glass for immunoassays.[67] These "lifting-gate" valves enable the entire fluidic actuation and routing geometry, including an open fluidic channel network, to be fabricated separately from the substrate, allowing widespread use in applications where surface functionalization and patterning can be difficult to perform within standard, bonded microchannels. This was not possible previously, as the traditional Mathies and Quake valves require microfabricated channels rather than flat substrates, while Quake valve operation without adequate device bonding can result in delamination of the surface from the microfabricated structure.

While valves can be used for on-off operations to switch reagents or stop flow, serially arraying 3 valves results in a peristaltic pump, as shown in Figure 1.3C.[60,61] The flow of liquid is now controlled entirely by integrated microscale valves. Aside from eliminating the requirement

for syringe pumps and other bulky hardware, micropumps offer extremely high accuracy of timing and metering, since a single pump stroke results in a geometrically-defined bolus of fluid to be pushed forward. The number of pump strokes can therefore determine fluid volumes with picoliter accuracy and at flow rates practical for single cell analysis. Furthermore, integrated pumps along with valves allow full automation of a microfluidic device, with rapid, seamless switching between reagents with minimal dead volume and cross-contamination. Finally, the elimination of syringe pumps facilitates interconnections between devices and other components and avoids the need to pre-load reagents and cells.

The development of microscale valves and pumps spurred innovation in many areas of bioanalysis.[68] At its most fundamental, the concept of microvalves solves the problem of interfacing the microfluidic chip with the macroscale world. Valves have been instrumental in automated immunoassays,[69] digital PCR,[63,70] single cell analysis in droplets,[71] and organ-on-chip culture.[72] Large scale integration is becoming more common in commercial devices (e.g., Fluidigm, Inc.) and will become even more prevalent as commercial-scale fabrication processes become adapted to precision alignment and other steps needed for microvalves.

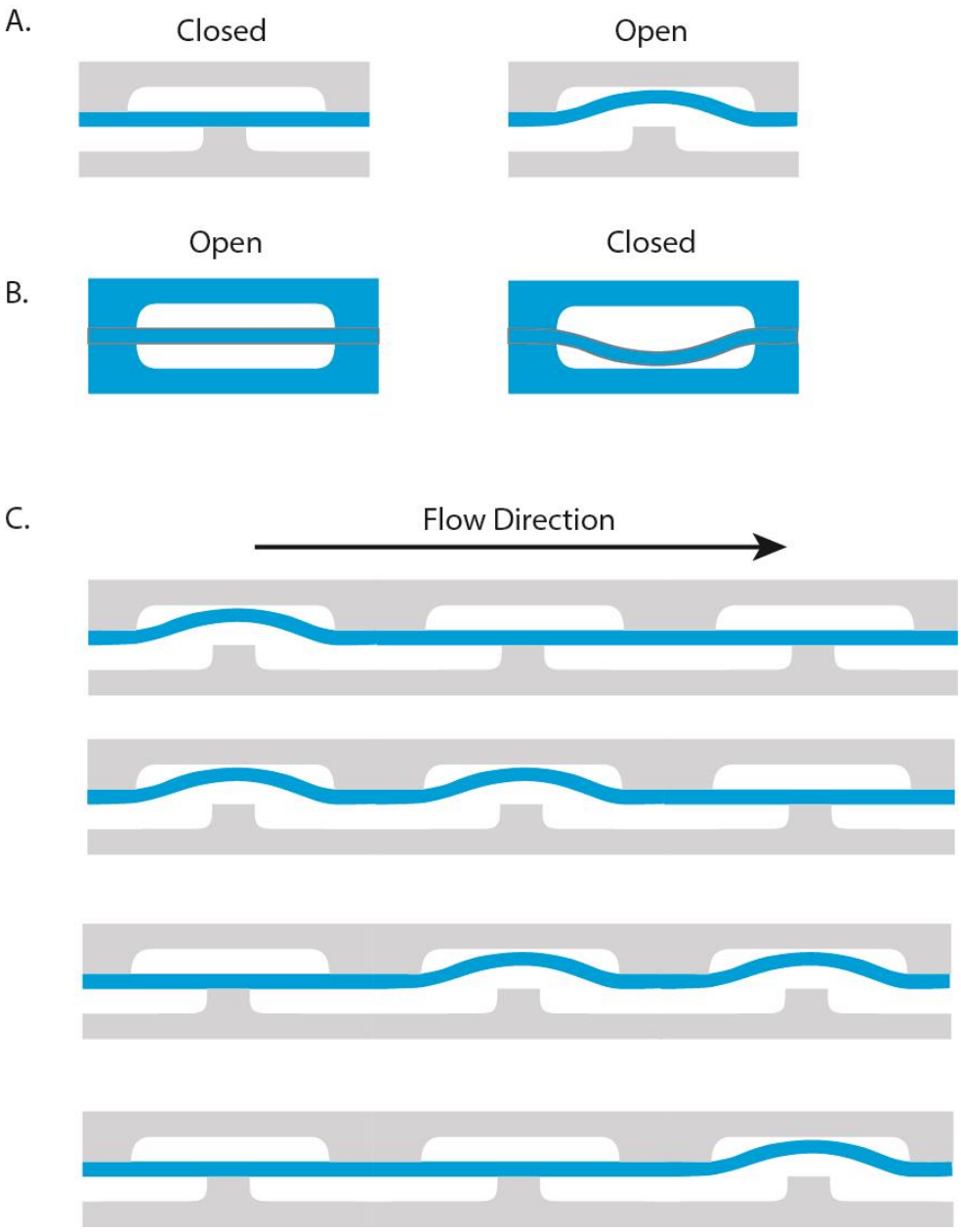

Figure 1.3. Cross-sectional illustration of valve and pump operating principles. (A) In the default state (left), Mathies valve design consists of a PDMS membrane closing off two discontinuous channel beneath it. Upon actuation with vacuum (right) in the top pneumatic control channel, the membrane is lifted up, connecting the two fluidic channels. (B) The Quake valve design, shown here in a channel cross section with fluid flow going into or out of the page, also implements a PDMS membrane spanning the fluidic channel, but the default state is an open fluidic channel (left). Actuation with pressure (right) pushes the membrane down into the fluidic channel, thereby closing it off. (C) Three valves connected in series can be actuated sequentially to form a peristaltic pump. The net fluid flow rate is determined by the frequency of actuation, vacuum and pressure used to drive the valves, and volume of the central valve.

1.6 Microfluidic devices for single cell analysis

Due to the small scale of microfluidic channel, automation capability, and ease of parallelization, microfluidics have been applied to various aspects of single cell analysis. Aside from droplet generation, which will be discussed separately, microfluidic systems have been designed to capture or otherwise isolate single cells for further analysis. The main approaches consist of cell traps, where single cells can be arrayed into easily-imaged patterns, and compartments, which randomly or deterministically segregate individual cells and avoid cross talk during assay reactions.

Cell trapping has been demonstrated using both passive sedimentation of single cells into microwells as well as active, hydrodynamic trapping. In passive trapping, microwells of the dimensions of single cells act merely as physical restraints against cell motion due to device or cell movement and allow researchers to rapidly image large fields of single cells without imaging artifacts (e.g., overlapping cells). This approach has been used in various forms to analyze cell signaling, as well as for improving image-based cell cytometry.[73–75] Similar arraying of individual cells was also demonstrated using traps that offer greater capture efficiency of single cells. Microposts, with gaps either horizontally between the post and the device ceiling, or vertically between several posts, provide a physical trap for cells. The flow of liquid through the gaps results in a single cell becoming trapped at each site, thereby obstructing flow and preventing double occupancy.[76,77] Using this active trapping approach, it is possible to achieve high-density single cell capture using arbitrary concentrations of cells, unlike passive microwells that can capture multiple cells at high loading densities. Similar approaches use gaps between parallel channels to trap cells,[78,79] with one design demonstrating highly efficient co-culture of two different cell types.[80] The arrays are open to a shared medium or assay reagent and are thus limited to live-cell imaging of non-motile cells.

Isolating cells in distinct compartments offers the possibility of implementing assays that involve cell lysis or detection of secreted molecules. Microwells form the basis of most single cell analysis approaches due to their relatively simple fabrication and operation. Cells are captured randomly by sedimentation, perfused with reagents, and sealed off to allow the reaction to proceed without crosstalk between wells. Despite the design simplicity, microwells have been used for single cell lysis and mRNA capture to provide heavy and light chain immunoglobulin information from single cells,[81] measurement of antibody secretion through "microengraving,"[82,83] and combined antibody secretion and mRNA analysis for single cells.[84]

The addition of microvalves to the microfabrication repertoire offers the possibility for dynamic formation of capture and reaction chambers. The Hansen group has shown numerous devices based on this approach, with thousands of individually addressable chambers per device for investigating single cell signaling, proliferation, and gene expression.[85–87] They recently combined this type of device with droplets to minimize cross-contamination during sample retrieval.[88] Fluidigm recently released a commercial microfluidic cartridge based on the valved reactor array design, the C1 Single Cell Autoprep chip, and supporting hardware that hydrodynamically captures single cells, performs single cells lysis, mRNA extraction, and on-chip SMARTer amplification of mRNA molecules for direct next-generation sequencing using the Illumina platform.

The advantage of any reactor-based system is the ability to use assays that can otherwise diffuse and cause cross-talk between samples. The dynamic, valve-based systems offer the added capacity to address single reaction chambers, modify reaction conditions cell by cell, and retrieve samples without losing single cell-level information for downstream assays. These capabilities are possible only due to a tradeoff in design, fabrication, and operation complexity, as well as a finite number of reaction chambers per chip. The decision to use valve-based designs will be determined primarily by the experimental questions.

1.7 Microemulsions for ultra-sensitive, high-throughput bioanalysis

Microemulsions, emulsions where the dispersed phase is typically less than 200 μm in diameter, hold great possibilities for applications in bioanalysis. Their main advantage is the speed of production, and, unlike chamber-based devices, are scalable to meet the throughput needs of virtually any experimental design. Although originally developed for various industrial and food preparation applications in the mid-20th century, only recently have emulsions been applied for assays and other biological applications, and even more recently have microfluidically-generated emulsions been engineered for creating highly monodispersed microreactors.

The earliest microemulsions created using microfluidics consisted of T-channel[89] and co-flow[90] geometries and demonstrated the ability to produce highly uniform droplets with a range of volumes by controlling the relative flow rates of oil and aqueous phases, as well as modifying the nozzle diameter and viscosity and surface tension of the liquids. This initial development led to significant innovations in both droplet engineering as well as applications. Generation of a wide range of droplet types, using numerous geometries and physical phenomena were demonstrated by several groups, including creation of Janus[91] and nonsperical[92] particles as well as multi-layered vesicles.[93] Despite these technical advances, only within the last decade have droplets been applied to significant biological problems.

1.8 Droplet generation

Droplet generation, whether microfluidic or not, relies on the immiscibility of two phases, typically an oil and an aqueous liquid. For most biological applications, the dispersed phase, i.e., the phase that composes the interior of the droplets, is water-based, while the continuous phase that surrounds droplets can be composed of any number of oils. Surfactants are used to stabilize the droplets and prevent merging of multiple droplets during experiments and provide biocompatibility.[94] In addition, surfactants reduce the interfacial tension between the two liquids, allowing the generation of smaller droplets. A wide range of microemulsion generation methods have been described, from stirring two solutions together to microfabricated nozzles and boundary channels to ultrasonic droplet generation.[59,95–101] Given the scope of this thesis, only droplet generation using microfabricated nozzles will be described in detail.

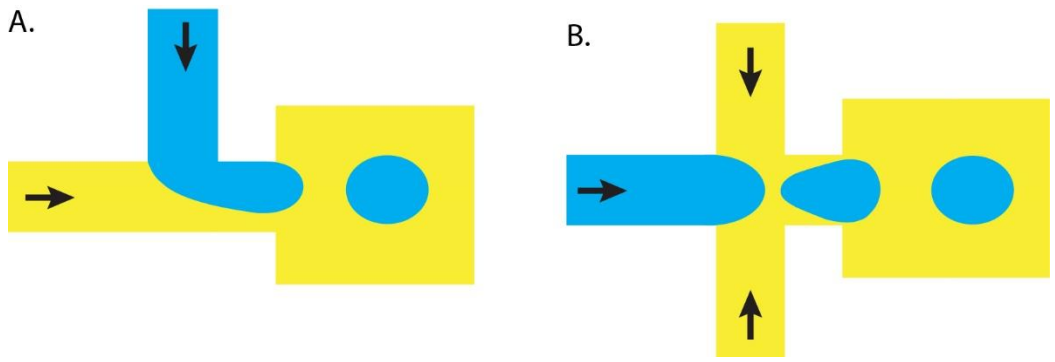

Figure 1.4. Illustration of two dominant microfluidic droplet generation approaches. In both designs, the aqueous phase (blue) produces water-in-oil droplets when combined with the immiscible oil phase (yellow). (A) The T-channel nozzle relies on a high shear rate of the oil stream to pinch off droplets. (B) The cross-channel geometry nozzle involves varying degrees of flow focusing of the aqueous stream by the oil phase prior to entering the nozzle. Multiple regimes of droplet generation exist for this design due to a number of physical phenomena, such as fluid viscosity, surface tension, relative flow rate, involved with varying dominance depending on experimental conditions.

Microfluidic droplet generation typically uses one of two main nozzle designs: the T-channel nozzle (Figure 1.4A) and the cross-channel flow focusing nozzle (Figure 1.4B). In both scenarios, the aqueous phase (blue) and oil phase (yellow) are flowed through the channels using syringe pumps or micropumps and combine at the nozzle, resulting in instability and the generation of droplets. The T-channel design primarily generates droplets by a high shear rate and resulting extension of the aqueous stream, causing a droplet to pinch off. The size of the droplets has been approximated with the following equation:

$$D = \frac{2\sigma}{\mu_C \varepsilon} \qquad \text{(Eq. 3)}$$

The droplet diameter, D, is the ratio of interfacial surface tension, σ, to viscosity of the continuous phase, μ_C, and the shear rate, ε. Intuitively, a low surface tension, such as from the addition of surfactant, coupled with a viscous oil will result in small droplet size for a given flow rate. Increasing the oil flow rate increases the shear rate, also giving smaller droplets. However, the shear rate generally needs to be determined experimentally for a particular nozzle geometry, since the diameter of both channels combined with flow rates of each liquid are critical parameters. T-channel nozzles provide a space-saving design for droplet generation, which is critical for highly parallelized droplet generation schemes for high throughput.[102]

Cross channel nozzles that take advantage of flow focusing of the aqueous phase prior to droplet generation are typically more versatile and more broadly adopted at the expense of greater complexity in the design due to additional physical phenomena involved. Figure 1.4B shows an example of flow focusing for droplet generation. The aqueous phase is squeezed by the oil phase prior to entering the nozzle, hence the term "flow focusing," where droplets are produced. Figure 1.5 illustrates four possible regimes of droplet generation. In Figure 1.5A, the flow rate of oil to aqueous phases is relatively low (~1:1), the nozzle walls restrict the size of the aqueous phase, resulting in it blocking the continuous phase, and causing droplet generation to occur primarily due to pressure buildup due to oil flow, and rapid elongation and droplet formation.[98,103] This geometric constraint provides relatively robust droplet generation conditions, albeit at somewhat slower rates (up to a few kHz) than what can be achieved using other approaches. However, the main advantage is the ability to create relatively large droplets, on the order of a few nanoliters, which is critical for single cell culture. This is the primary regime used in this thesis. While syringes can be used for actuation, several projects described later in this thesis involve pneumatic pumping for actuating the droplet phase. The mode of droplet generation is still geometrically constrained, but the pulsatile pumping of the fluid results in a transient reverse flow, causing droplet pinch off to proceed "on demand" with each pump stroke. This method, while limited in speed due to mechanical motion of pneumatic valves, provides extremely high robustness for droplet generation with a very wide range of liquids, from low-viscosity PCR mix to high-viscosity agarose, with minimal process optimization. As the pump stroke volume determines droplet size, droplet volume can be programmed arbitrarily based on experimental design requirements, thus avoiding lengthy device characterization and optimization.

In other droplet generation regimes, as the flow ratio of oil to aqueous phases increases, the droplet generation regime shifts toward thread formation (Figure 1.5B) where an aqueous thread extends past the nozzle.[104,105] Droplets much smaller than the nozzle pinch off from the thread. This is a relatively rare regime with a narrow range of suitable conditions and for only

some types of surfactants. It is generally not used in single cell analysis. In Figure 1.5C, the dripping regime consists of a high-shear region that forms the aqueous phase into a stable triangle, with droplets budding off from the tip, within one half of the distance of the nozzle diameter. This regime provides extremely high monodispersity (<2%).[103,104] Droplet size is a function of the shear rate, nozzle dimensions, interfacial surface tension, viscosity, and flow rates but droplets are typically around the size of the nozzle or smaller. As the ratio of viscosity to interfacial surface tension increases (proportional to the Capillary number, Ca), viscous forces dominate and droplet generation occurs farther downstream from the nozzle in what is called the jetting regime (Figure 1.5D).[104] This is the result of the aqueous phase being able to extend into a column-like structure due to the greater influence of viscosity. Droplet formation occurs primarily due to the Raleigh-Plateau instability, where interfacial surface tension overcomes viscosity and the jet of liquid breaks into round droplets. Jetting provides an extremely fast way to generate droplets with good uniformity.

As mentioned above, surfactants are required to maintain droplet stability after generation. Typically, surfactants are dissolved in the continuous phase. This provides ample surfactant for droplet maturation over time (milliseconds to seconds) but also avoids negative effects to cells. This has the advantage of being implemented for cell lysis upon cell encapsulation but not prior, since the partitioning of surfactant from the oil into the aqueous phase can be used to initiate lysis. Typical surfactants include Tween, Triton, and Span for silicone and mineral oils and Krytox, Pluronic F68, and various synthesized fluorinated polymers with PEG moieties for fluorinated oils.[94,106–109] Presently, a number of commercial sources exist for oils premixed with surfactants at optimal concentrations for digital PCR applications. Most are also biocompatible for cell culture in droplets. Addition of large polymers, such as Pluronic or PEG, or proteins, such as BSA or collagen, can help further stabilize droplets, particularly during thermal cycling for PCR amplification, pipetting, and other high-stress manipulations. Surface treatment of the channels is also critical in robust droplet generation. PDMS and glass devices can be functionalized with hydrocarbon or fluorocarbon groups via silanization and devices can withstand relatively long-term operation (~hours to days of continuous operation). Proteins in the aqueous phase can, however, adsorb to strongly hydrophobic surfaces, rendering them hydrophilic and affecting droplet generation characteristics over time.

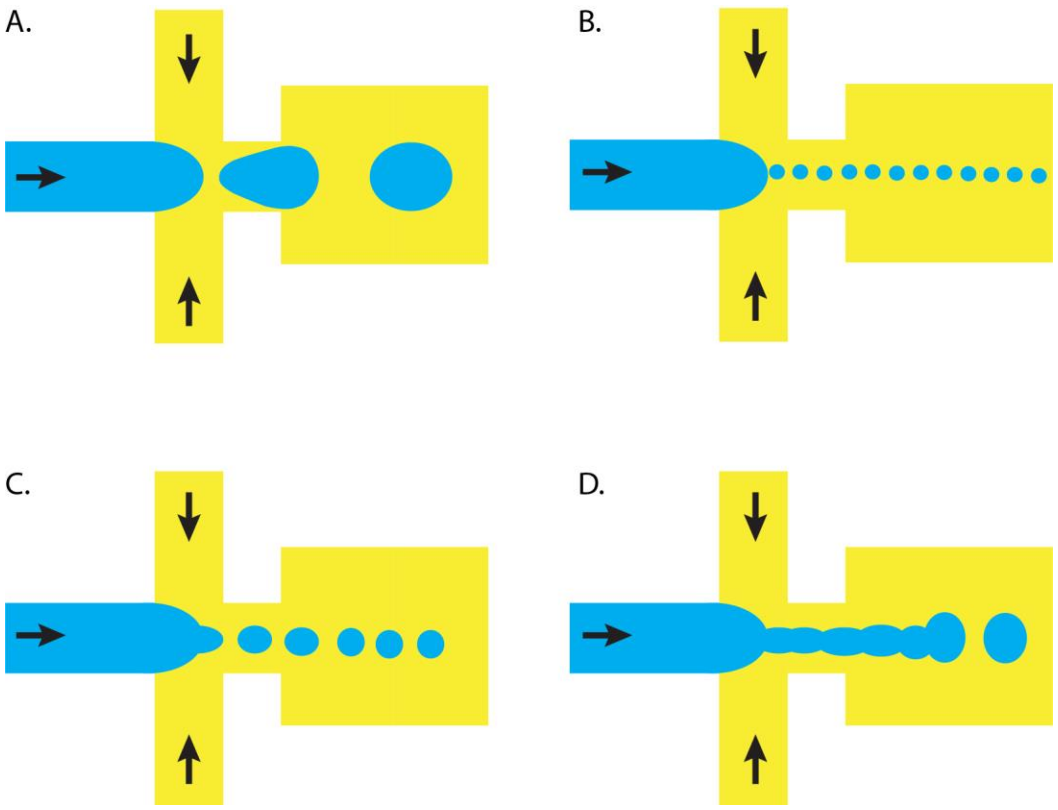

Figure 1.5. Illustration of four droplet generation regimes in flow focusing devices. (A) Geometrically constrained regime. (B) Thread formation regime. (C) Dripping regime. (D) Jetting regime. While the regimes are arranged approximately in order of increasing Capillary number, some regimes, such as the tread formation regime in particular, are entirely absent from specific experimental conditions. Key parameters involve relative flow rates, nozzle dimensions, viscosity of both liquids, and interfacial surface tension, and experimental characterization of prototype designs provides the best way to develop droplet generating devices.

While many studies have attempted to characterize droplet generation, the reality of the situation is that there are simply far too many parameters that can be changed to generalize detailed scaling laws. The results published by researchers demonstrate the influence of specific physical phenomena or material properties for given droplet generation regimes, but it is difficult to predict droplet size and generation rate with sufficient accuracy for digital PCR and other assays that rely greatly on a pre-defined droplet size. The main parameters are typically nozzle geometry, specifically the diameter of the nozzle constriction, viscosity of both phases, interfacial surface tension, and relative flow rates. The approach taken by most groups has been to prototype droplet generator designs and characterize them under the desired experimental conditions. In general, rapid prototyping is a broadly applicable approach that yields accurate results.

1.9 Poisson distribution

The Poisson distribution plays a significant role in droplet engineering, digital PCR readout, and single cell analysis. The mathematics behind the distribution came about as a result of simplification of the binomial distribution for discrete events and was published by Siméon Denis Poisson in 1837.[110] The distribution became widely known only after the work of Ladislaus Bortkiewitcz at the end of the 19th century, where he analyzed frequency of lethal horse kicks in the Prussian army and found their occurrence to follow the Poisson distribution due to their fortunate rarity.[111] Despite the tumultuous beginnings, the Poisson distribution is vital for understanding and analyzing rare events.

The Poisson distribution expresses the probability of one or more events occurring during a defined period of time or space, and relates the average probability with the probability of 0, 1, 2, etc… discrete events per unit of time or space.

$$p(X = k) = \frac{\lambda^k e^{-\lambda}}{k!} \qquad \text{(Eq. 4)}$$

Here λ is the average frequency for an event over the entire time or space, and *k* is the number of discrete events in a particular unit of time or space. As an example, one can use this equation to find the probability of seeing two cells in a single droplet given that the average frequency of cells is 0.1 cells per droplet (p = 0.0045). This is particularly useful when designing a single molecule or single cell experiment in that the researcher can predetermine the level of error that is acceptable for meaningful results. For example, in the above case of two cells co-occurring, 4.5% of the positive droplets will actually contain 2 cells. If the experiment is trying to analyze colonies resulting from single cells, a 4.5% error rate, where those colonies were initiated by 2 cells, might pose a significant limit to the experiment's ability to detect rare events. Using this equation, it is possible to adjust the experimental conditions to match the desired outcome limits. However, a more useful derivation of this equation enables the calculation of frequency of any nonzero event (e.g., a "positive" droplet). We let k = 0:

$$p(X = 0) = \frac{\lambda^0 e^{-\lambda}}{0!} = e^{-\lambda} \qquad \text{(Eq. 5)}$$

This gives us the probability of observing "negative" events, such as empty droplets. Although this results in a loss of information (k events), in digital PCR and other applications, it can be hard or even impossible to determine whether a particular positive droplet or other unit of time or space came from 1, 2, 3, or more events. As a result, transforming the equation to only have a dependence on the average frequency of events is useful from a practical standpoint. Subtracting from 1 gives us the inverse probability, namely the probability of seeing a positive unit of time or space with any number of events (k>0):

$$p(X > 0) = 1 - e^{-\lambda} \qquad \text{(Eq. 6)}$$

Solving the equation for λ gives:

$$\lambda = -\ln(1 - p) \qquad \text{(Eq. 7)}$$

This equation allows the fitting of a distribution of positive and negative events, such as those resulting from digital PCR, and obtaining an average frequency or target concentration in the entire sample. Performing serial dilutions, where λ changes by a fixed amount, such as a factor of 10, provides confirmation of single molecule analysis. Since λ is changing by a known amount, the Poisson distribution can be used to predict the outcome frequencies at each λ value and compared to the experimental frequency data. If an assay is in fact detecting single molecules, the frequency of positive events at each dilution will give the same λ value when λ is adjusted by the correct dilution factor. Assays that require more than one molecule for a positive event, on the other hand, will result in a sudden drop in observed positive event frequency once the number of molecules per unit space or time drops below the threshold and will no longer agree with the Poisson distribution. By fitting experimental data using Equation 6, it is therefore possible to both estimate the average target frequency, λ, and validate single molecule detection.

1.10 Digital detection

Digital detection is the concept of counting single molecules or cells rather than measuring an average, analog, level. This approach provides inherent error insensitivity not present in analog assays. In a digital assay, the output is a string of "yes" and "no" or "1" and "0," which are then tallied and the positive count is divided by the negative count to give a final frequency. In this case, an assay only has to determine whether a cell is positive or negative for the target or whether an assayed DNA or RNA molecule is the target or not. This can reduce the assay quality requirements while still providing extremely accurate results.

For example, a sample might contain 10 cells of interest (10 "yes" or "1") and 10 million other cells (the "no" or "0"). The whole sample is analyzed cell by cell, and each cell is determined to be positive or negative. Dividing 10 positive cells by 10 million total cells gives a frequency of 1/1,000,000, or 1/10,000%. Analog assays, the other hand, measure the net frequency of a target in the sample as a whole. They output a number from some type of sensor that can range between a maximum and a minimum and is related to the real frequency by a standard curve made with known concentration standards. These types of assays are extremely common and work quite well

for relatively high frequencies, such as gas tank gauges, pool chlorine tests, and many biological assays like qPCR for high frequency targets. The problem becomes apparent at low concentrations: as the number of target molecules decreases, the sensor output decreases until it can be hard to distinguish the true value from background fluctuations and noise in the sensor. While a low frequency capability in a gas tank gauge is of least concern for a driver (at that point, any low levels of gas are all bad), the ability to detect low concentrations of RNA using qPCR can mean the difference between classifying a patient sample as negative while it really does contain low-level biomarkers. In the example above, being able to distinguish 10 positive cells from 0 in a background of 10,000,000 cells by analog sensing is very difficult and, while possible, relies on highly optimized assays or hardware. By minimizing bias due to sensor limitations, digital assays provide accurate results at low analyte concentrations.

Digital assays not only buffer against errors, as in digital electronics systems, but they also provide a high degree of precision in the measurement. In a reasonably well-performing assay, the resolution limit is a single target molecule. The assay is just counting the targets, and assay precision is determined by the total number of molecules or cells examined. For example, the standard deviation in measurements that follow the Poisson distribution, which is generally the case for low frequency counting, is the square root of positive "yes" or "1" values. Therefore, sampling 90 cells with 9 positive gives a 10% frequency with a standard deviation of 3, or 3.3%. Increasing sample size to 9000 with the same frequency of target cells still results in a measurement of 10% frequency, but this time with a standard deviation of only 0.33% of the sample size. Therefore, the precision of the measurement in digital assays is directly linked to the output frequency and can be adjusted to meet experimental requirements.

Finally, accuracy is greatly improved in single cell analysis compared to bulk analyses. Since measurements are being taken cell by cell or images are analyzed with single cell resolution and all cells are assayed, there is an internal control built into the measurement. Independently of the number of cells in a particular tube or container, single cell analysis outputs a self-normalized frequency and does not require a standard curve to transform analog sensor readouts (which are often times in Volts or other units that do not by themselves correspond to biological targets) into meaningful values. Digital analysis therefore provides greater accuracy and precision to enable extremely sensitive detection of rare analytes of interest.

1.11 Digital PCR

Digital PCR is the application of digital detection to DNA and RNA. In all approaches, the reagent, containing dilute template DNA or RNA, is divided into separate reaction compartments. As discussed earlier, this is presently accomplished using microvalves and other microfabricated structures or via droplet generation. PCR amplification using target-specific primers results in each compartment either containing many thousands to millions of DNA copies or no additional DNA. This can be read out using several methods, from intercalating dyes such as SYBR Green to hydrolysable fluorescent probes to using capture beads and fluorescent primers for detection of bound targets. The result is a count of positive reactions and negative reactions, enabling the calculation of target concentrations using Poisson statistics.

The earliest digital PCR did not utilize microfluidics at all and was termed "limiting dilution PCR." Rather, it consisted of manual or robotic pipetting of very dilute template into hundreds of separate bulk PCR reaction wells and treating each plate or set of plates as a single compartmentalized assay.[112] This did prove quite useful and allowed significant headway in single cell analysis that helped pave the way for microfluidic techniques.[113] In between the large volume reactions and microfluidic systems, the groups of Katsura, Vogelstein, Griffiths, and other researchers developed emulsion PCR by mechanically agitating PCR reagents with oil containing stabilizing surfactant to form polydisperse emulsions.[95,114,115] The ease of droplet generation provided a simple manner of scaling up the previous tediously-produced compartments. Technological improvements, such as BEAMing, where amplicons are bound to microbeads for labeling and counting using flow cytometry, helped propel digital PCR into the forefront of nucleic acid detection.[95,116] However, the biggest drawback of polydisperse emulsions is the lack of reaction rate control due to a broad range of droplet volumes. Although the reactions are allowed to run to completion, the differential volumes can lead to inaccurate quantitation since kinetics can be affected to render amplification reactions ineffective and the quantitation of targets using Poisson statistics relies on having uniform and discrete reaction volumes.

Current digital PCR involves microfabricated devices to generate highly uniform reactor volumes. Initial approaches focused on the use of valved reactor chambers to isolate compartments, most likely due to the initial difficulty of developing suitable oil-surfactant combinations that maintain droplet stability and biocompatibility during PCR. The process for all devices consists of filling the chip with the reagent and template mixture, closing valves or otherwise sealing chambers from one another, and thermally cycling while detecting fluorescence either in real time or at the endpoint.[63,117–121] These devices, while limited in the number of reactors by the device design, have been scaled to over 1 million compartments.[63] Due to the earlier development, fabricated microreactor arrays have been commercially available for some time in the form of Fluidigm's Digital Array.

To reduce fabrication and operation complexity, a hybrid microwell-droplet array approach was developed, and a commercial version exists in Life Technologies' QuantStudio machine. In this approach, microwells or hydrophilic patterns as well as the entire chamber are filled with the reagents containing template. To segregate the individual compartments, oil is introduced into the chamber, thereby sealing off the microwells or hydrophilic patterns through droplet formation.[117,122–124] Further development of microfluidic devices aimed at solving the droplet stability problem, consists of droplet capture chambers that provide physical separation of droplets to avoid droplet merging and other instabilities.[97] One particularly unique design, the SlipChip, generates droplets inside glass chambers by the rotation of the device following filling with reagents.[123,125,126] Although limited to a finite number of reactors, the Ismagilov group dramatically increased the device's dynamic range by fabricating chambers with increasing size and using Poisson statistics to back-calculate the target concentration over approximately a 6 order of magnitude concentration range.[127]

Droplets have recently become the dominant approach for digital PCR due to the lack of moving parts, simple fabrication and operation, and especially the scalability of droplet generation that is not constrained to a finite number of wells or other physical features. Innovation in the area of surfactant stabilization of emulsions has particularly supported this growth.[94] A number of groups developed variations on microfluidic droplet generation for digital PCR applications, all of

which rely on a droplet generation nozzle, droplet thermal cycling, followed by fluorescence analysis of droplets for products.[96,108,128–130] The key driving advantage of droplet reactions is throughput. Droplet generation, possible at up to 1 MHz in some cases, provides a limitless number of reactors for extremely high-throughput applications. For example, we have used droplet-based digital PCR to detect concentrations of the chromosomal translocation t(14;18) at levels below 1 target in 10^7 normal genomes in healthy subjects.[70] Recent innovation has been aimed at increasing the information content per droplet, allowing greater assay multiplexing to be performed.[128,131] The difficulty of handling droplets, particularly for reagent exchange, has been addressed by the incorporation of agarose in the dispersed phase. Gelling of the droplets results in rigid but porous reactors that can be manipulated in bulk without losing the initial compartmentalization.[71,132,133] Alternatively, complex fluid handling operations have been incorporated into fully integrated devices where droplets are diluted, merged with additional reagents, and routed as needed for multi-step assays.[134] Digital PCR is quickly maturing into a technology that is becoming widely accepted outside of microfluidics labs. Proof of that trend is the commercialization of droplet technologies by Bio-Rad and RainDance and their widespread adoption by molecular biology groups. As complex fluid handling on-chip becomes more robust, droplet-based approaches will see even wider applications in biology and other fields.

A.

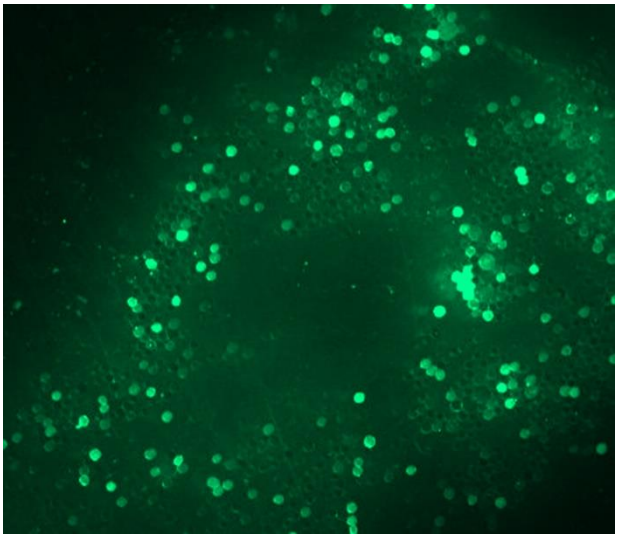

B.

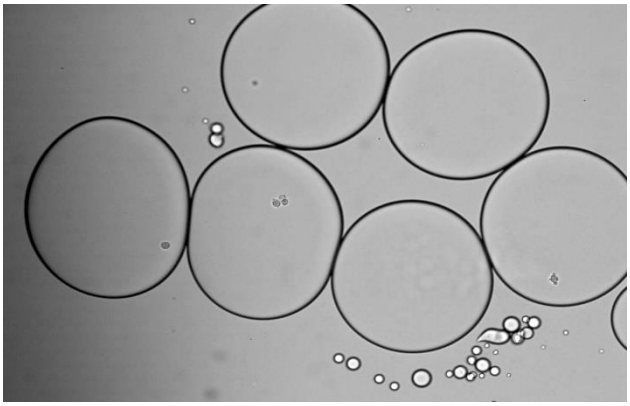

Figure 1.6. Photographs of microfluidically generated emulsions applied to single cell analysis. (A) Fluorescence image of a field of droplets following RT-PCR on dilute Sci-1 cells with the housekeeping gene GAPDH used as a target. Bright droplets contain amplicons stained with the intercalating dye EvaGreen and therefore indicate GAPDH amplification and cell presence. (B) Photograph of droplet-based single cell culture of K562 cells 24 h post-encapsulation demonstrating variability in cell division rates when viewed at the single cell level.

1.12 Droplet applications for single cell analysis

Digital PCR has enabled the analysis of single DNA and RNA molecules in lysates or purified template, but the method does not provide information about co-occurrence of mutations or gene expression within single cells. Furthermore, investigations of non-nucleic acid analytes require altogether different and more versatile platforms for single cell analysis. To that extent, the scalability of droplet assays is being applied to whole cells. Nucleic acid detection based on digital PCR or RT-PCR has been demonstrated on single cells using several droplet generation systems.[102,134,135] Figure 1.6A presents an example of GAPDH mRNA detection in single cells via emulsion RT-PCR. EvaGreen is used to fluorescently label droplets containing target amplicons. Agarose droplets offer added ease of manipulation of droplets for downstream assays, and a demonstration of this concept for RNA detection in single cells was recently published, though the authors did not fully leverage the capabilities of gelled emulsions.[133] I demonstrated a sample pre-treatment application of agarose droplets as part of this thesis, where encapsulated single cells were lysed and protease-digested to purify the genomes in bulk solutions while maintaining single cell compartmentalization.[71] The purified genomes were subjected to in-droplet PCR for detecting mutant cells and for multiplex sequencing of DNA targets in single cells. The agarose-based DNA purification approach has been applied to single cell forensic analysis, where 9-plex emulsion PCR is used to obtain short tandem repeat signatures of mixtures of cells, enabling identification of victims and criminals from contaminated crime scenes with multiple individuals' tissues present.[136]

Droplets have been applied to non-genomic analysis of mammalian cells as well. Since fluorinated oils provide exceptionally high rates of oxygen permeability, single cells can be cultured in droplets, as shown in Figure 1.6B. Although only short-term (< 3 day) culture is possible without exchanging culture medium in droplets, the scale of cell encapsulation provides vast numbers of single cells for high-throughput screens.[107] This has been applied to measuring protein expression,[137,138] enzymatic activity,[139,140] drug screening of phosphatase inhibitors,[141] and antibody production in hybridomas.[142] In addition, in-droplet screening of whole blood for *Plasmodium* parasites highlights the scalability and versatility of droplets for single cell detection and analysis applications with possible diagnostic capabilities.[140] As the line between engineering and biology becomes less distinct, many more applications of droplets for single cell analysis, particularly mammalian cells, will appear both in research and commercial settings.

1.13 Summary

Single cell analysis, stemming from the idea that tissues and even cell lines are far from homogeneous populations of cells, will have lasting impacts on cell biology and medicine. As we begin to comprehend the sheer diversity and heterogeneity present within our bodies, analyzing biomolecular pathways will shift toward single cell and ultimately sub-cellular measurements. The noise inherent in signaling pathways and gene expression gives rise to complex interplays between biology and the environment that can only be understood at the level of individual cells rather than the population, or ensemble, average. The measurements have been driven to a large degree by advances in technology, from early microscopy and cytometry methods to current state-of-the art microfluidic devices. The ability to create thousands or millions of highly uniform reaction compartments with orders of magnitude lower reagent consumption has spurred innovation of

novel bioassays and applications for examining large populations of single cells. Droplets in particular offer a versatile platform for single cell analysis that will only grow in capability and applications as multidisciplinary research groups take on the challenge of peering into the workings of single cells.

1.14 Scope of the thesis

The goals of the work presented in this thesis are: 1) the development of microfabrication methods and microfluidic designs that facilitate single cell analysis in droplets, 2) the application of droplets for detecting single DNA molecules in purified DNA samples and single cells, 3) the extension of droplet-based technologies to multiparameter analysis of single cells beyond the genomic components, and 4) the application of single cell analysis concepts to synthetic tissues and organs through the development of highly sensitive analytical technologies.

The first section of my thesis focuses on microfabrication methods for designing and building microfluidic droplet generators from a variety of materials:

Chapter 2 describes the development and scaling up of micropump-actuated droplet generation in glass-PDMS devices. It highlights specific design features, such as the concentric micropump, for robust and highly parallel droplet generation, and characterizes the toolbox of droplet generators, from 4-channel to 96-channel Microfluidic Emulsion Generator Arrays (MEGA). Using the MEGA devices, pathogenic *E. coli* O157 bacteria are detected using PCR in varying backgrounds of the non-pathogenic *E. coli* K12 strain with a limit of detection of approximately 1 pathogenic bacterium in 10^5 non-pathogenic bacteria, demonstrating highly sensitive single cell detection in droplets.

Chapter 3 highlights the development of a rapid fabrication method for efficient prototyping of microfluidic devices in thermoplastic polymers. Using a computer controlled cutter to cut out non-conductive masks out of adhesive polymer sheets, it is possible to quickly electroplate nickel molds for hot embossing of most available thermoplastic materials in as little as 1-3 hours directly from a CAD design.

Chapter 4 presents an optimized and detailed protocol for thermoplastic device fabrication using nickel electroplating combined with photolithography.

The second section of my theis highlights several applications of microdroplets for single molecule detection and single cell DNA analysis:

Chapter 5 presents a digital PCR approach to detecting the t(14;18) chromosomal translocation in healthy human subjects. Droplet PCR enabled assay sensitivity to be increased to quantitatively detecting less than 1 target in a background of over 10^7 genomes and limited only by the amount of input DNA. Using this extremely sensitive detection method accurate measurements were made of t(14;18) levels in 94 subjects. Coupling of single molecule sequencing facilitated the determination of genomic breakpoint sites for each subject, as well as the first demonstration of

relative intra-subject mutation variation and frequency measurement for subjects with multiple mutation events.

Chapter 6 describes a novel application of agarose droplets for single cell DNA purification and massively parallel analysis. Single cells are encapsulated in agarose droplets and gelled, permitting bulk DNA extraction methods to be used while maintaining single cell information of the genomes. Detection and sequencing of t(14;18) and β-actin is demonstrated in a cell line model system.

Chapter 7 extends agarose droplet-based genome purification to 9-plex PCR for forensic profiling. Single cell short tandem repeat (STR) profiles are determined for mixtures of two DNA standard cell lines, demonstrating the ability to resolve individuals from complex tissue mixtures. Furthermore, the method is shown to drastically reduce the impact of contaminating DNA, enabling the direct recovery of forensic profiles with as much as 2 contaminating copies per cell.

The third section of my thesis focuses on multiparameter analysis of single cells using droplets:

Chapter 8 presents an optimized protocol for single non-adherent cell culture in microfluidic droplets.

Chapter 9 characterizes single cell culture of lymphoid cancer cell lines in droplets for determination of growth rate for individual cells. In addition, the single cells or colonies are assayed using highly optimized RT-PCR and fragment analysis via capillary electrophoresis of fluorescently labeled amplicons to determine the expression level of hTR and hTERT telomerase genes and alternative splice variants of hTERT mRNA. A bimodal distribution of expression is observed for several hTERT alternative splice variants, and sub-lethal curcumin treatment results in decreased bimodality and increased alpha splicing patterns. This work demonstrates the multiparameter assays of single cells for studying low-expression genes with applications in drug screening.

Lastly, Chapter 10 describes tissue- and organ-on-chip devices for studying small numbers of cells in native-like conditions and presents future directions for single cell analysis, particularly droplet-based technologies, in studying interactions of single cells. These technologies are particularly aimed at developing suitable model systems with parallel monitoring and analysis technologies for rapid and efficient drug screens and discovery of novel regulatory mechanisms. The goal of multiparameter single cell analysis of whole tissues and organs is a holistic investigation of biological phenomena, where biological interactions are recognized to be collective phenotypes originating from the heterogeneous behavior of single cell components. A single cell perspective to molecular biology will have a tremendous impact on understanding fundamental biological processes and developing targeted therapies for a spectrum of diseases.

Section 1: Microfluidic device development and fabrication

Section overview

Microfabrication of microfluidic devices underlies any application. Droplet generators in particular rely on highly reproducible and high resolution fabrication of channels and nozzles. The chapters in this section describe several methods for building microfluidic droplet generators as well as a wide variety of other devices. Chapter 2 presents early work published in *Analytical Chemistry* on developing glass-PDMS droplet generation devices, which incorporate both classic microfluidic channels and features in glass and PDMS membrane valves for fluid actuation. A particularly noteworthy development is the invention of circular diaphragm pumps for high density integration of pumping for parallel droplet generation, which permitted droplet generation rates to attain in excess of 2×10^6 droplets per hour. The chapter also details optimization of droplet PCR for detecting single pathogenic O157 *E. coli* in a vast background of nonpathogenic *E. coli*. This demonstration of robust and fast droplet generation applied to DNA detection is the foundation of subsequent single molecule and single cell work presented in Sections 2 and 3.

Although the early devices are very robust and useful for a broad range of fluids for encapsulation, glass fabrication is a lengthy and relatively low-yield production process. In research environments, there exists a need to rapidly prototype versions of initial designs to identify and characterize variables for optimization. Prototyping using all-PDMS devices, on the other hand, can lead to problems for final device implementation due to surface property differences between PDMS and the final production materials. To meet this need, Chapter 3 describes an extremely rapid approach to device microfabrication in thermoplastic polymers that was published in *Lab on a Chip*. It focuses on facile nickel mold fabrication, which until now had been a big barrier to widespread adoption in the research community. By quickly prototyping devices in the final production materials using a highly scalable process, it is now possible to test many device designs per day and develop design modifications in direct response to the experimental outcomes. This dynamic design approach is further expanded in Chapter 4, which presents an optimized protocol using photolithography for making hot embossing-capable nickel molds with higher resolution than possible with the protocol described in Chapter 3. The new protocol is based on substantial optimization and process modifications I developed following the initial publication. The chapter provides a versatile microfabrication process that has potential for wide adoption in the research and commercial environments. The fabrication methods described in this section are practical processes for building nearly all microfluidic devices.

Chapter 2: High-performance single cell genetic analysis using microfluidic emulsion generator arrays

2.1 Abstract

High-throughput genetic and phenotypic analysis at the single cell level is critical to advance our understanding of the molecular mechanisms underlying cellular function and dysfunction. Here we describe a high-performance single cell genetic analysis (SCGA) technique that combines high-throughput microfluidic emulsion generation with single cell multiplex PCR. Microfabricated emulsion generator array (MEGA) devices containing 4, 32 and 96 channels are developed to confer a flexible capability of generating up to 3.4×10^6 nanoliter-volume droplets per hour. Hybrid glass−polydimethylsiloxane diaphragm micropumps integrated into the MEGA chips afford uniform droplet formation, controlled generation frequency, and effective transportation and encapsulation of primer functionalized microbeads and cells. A multiplex single cell PCR method is developed to detect and quantify both wild type and mutant/pathogenic cells. In this method, microbeads functionalized with multiple forward primers targeting specific genes from different cell types are used for solid-phase PCR in droplets. Following PCR, the droplets are lysed, the beads are pooled and rapidly analyzed by multi-color flow cytometry. Using *E. coli* bacterial cells as a model, we show that this technique enables digital detection of pathogenic *E. coli* O157 cells in a high background of normal K12 cells, with a detection limit on the order of $1{:}10^5$. This result demonstrates that multiplex SCGA is a promising tool for high-throughput quantitative digital analysis of genetic variation in complex populations.

2.2 Introduction

Traditional biological analyses probe large ensembles on the order of 10^3–10^6 cells, thereby revealing only the average genotypic and/or phenotypic characterization of the population. The advent of single cell analysis has revealed marked cellular heterogeneity in gene and protein expression,[8,143–145] genetic/genomic alterations,[146–148] and responsiveness to environmental and chemotherapeutic stimuli.[149,150] A better understanding of cellular heterogeneity and the quantitative detection of rare mutants, such as circulating tumor cells present at an estimated frequency of 1 per 10^6–10^7 nucleated blood cells,[151] demands high throughput single cell analysis techniques to both detect these very infrequent members of the population and to provide good statistical information regarding these stochastic events.

Microfluidics offers unprecedented capabilities for precisely manipulating small volumes and for enhancing reaction speed and efficiency by increasing relative analyte concentration, reducing diffusion time, and facilitating large-scale integration and automation. These capabilities suggest that microfluidic systems will be very valuable for ultrahigh throughput single cell analysis.[56,75,118,152] Emulsion polymerase chain reaction (ePCR) provides another powerful tool for high-throughput genetic analysis because one can perform massively parallel single copy PCR reactions by partitioning statistically diluted targets (DNA or RNA) into small droplets dispersed in an oil phase.[115,153] Conventional ePCR has found many applications, including next-generation sequencing,[154] detection of rare mutations,[155–157] and quantification of DNA methylation.[158] However, ePCR also suffers from inherent limitations due to the use of mechanical agitation for emulsion generation, which produces high shear force and polydisperse droplet sizes. The transition to droplet microfluidics overcomes these limitations and has substantially improved the performance of emulsion-based bioassays.[135,137,159–162]

Microfluidic droplet generation technology enables the production of monodisperse droplets with precise control over the droplet size, while maintaining high-throughput. This capability not only enables uniform efficiency of enzymatic reactions or affinity binding,[160] but also permits digital quantification of the absolute number of targets present in the initial sample.[130,162] In addition, microfluidic encapsulation significantly reduces the damage to cells caused by vigorous mechanical agitation. Microfluidic operation is normally performed with a shear stress lower than 10 dynes/cm^2, while vigorous mechanical agitation can potentially generate much higher shear stress that can disrupt cells.[163] Our previous work indicated greater than 90% cell viability following microfluidic emulsification versus less than 80% for other encapsulation methods.[135,164] Integrated microfluidic circuits also allow programmable *in situ* manipulation of droplets, such as droplet steering, trapping,[138] and fusion,[165] leading to a much broader spectrum of applications, including real time PCR,[160] protein expression studies,[137] and drug screening.[166]

Our previous work established a high-throughput single copy genetic amplification (SCGA) technique based on the use of a hybrid glass-PDMS-glass microdroplet generator (μDG) integrated with a three-valve diaphragm micropump for effective transport and encapsulation of large microbeads and cells into uniform nanoliter-volume droplets.[135] To enable detection of extremely low frequency events in a vast population, herein we scale up the single-channel μDG to 4, 32, and 96-channel microfluidic emulsion generator array (MEGA) systems, further increasing the generation throughput up to 3.4×10^6 droplets per hour. In these MEGA systems, on-chip micropumps provide sufficient power to drive multiple droplet generators in parallel while the symmetrically designed microfluidic networks ensure even fluidic transport which is crucial for uniform droplet encapsulation. A new compact micropump composed of three coaxial ring-shaped valves is designed to enable the implementation of a 96-channel MEGA on a 4" wafer. This improvement simplifies device fabrication and operation and substantially reduces the dead volume.

The integration of multiplex PCR with high-throughput emulsion generation is valuable for the analysis of genomic deletion, forensic genotyping, mutation and polymorphism analysis, and identification of pathogens.[167] To detect and quantify both normal and mutant/pathogenic cells, herein we describe a multiplex single cell PCR approach, as illustrated in Figure 2.1, which allows efficient high-throughput PCR amplification of multiple target genes specific to different cell types. In this process, primer-linked beads and cells are diluted in the PCR mix such that isolated individual beads or cells are encapsulated into individual uniform reaction droplets dispersed in the carrier oil. Statistically, a small fraction of droplets will contain both one bead and one or more cells. Every bead is functionalized with forward primers for all targets, and the PCR mix contains reverse primers each labeled with a unique fluorescent dye. Thousands of such droplets, generated by MEGA chips within minutes, are collected in standard PCR tubes and thermally cycled in parallel. Each bead in a droplet containing only a single cell will carry one type of dye-labeled double-stranded amplicons after PCR, while a bead compartmentalized with different types of target cells will be labeled with multiple dyes. Post-PCR beads are recovered from the emulsion and rapidly analyzed by flow cytometry for multi-color fluorescent digital counting of each single cell detection event.

To demonstrate the utility of the multiplex SCGA technique for high-throughput single cell analysis of complex sample mixtures, we perform the detection and quantification of a major

foodborne bacterial pathogen, *E. coli* O157:H7, which alone causes an estimated 73,000 infections and 61 deaths annually in the United States.[168,169] High-throughput digital multiplex SCGA allows us to detect and quantify pathogenic *E. coli* O157:H7 cells in a background of normal *E. coli* K12 cells with a detection limit on the order of $1:10^5$ within a 30 min microdroplet generation time. Such sensitivity is critical for many applications, such as food safety, where microbial pathogen detection needs to meet a zero tolerance policy for many foods.[170] The results presented here also suggest that our technique has the potential for high-throughput single cell genotyping and quantitative detection of rare mutations in circulating fluids.

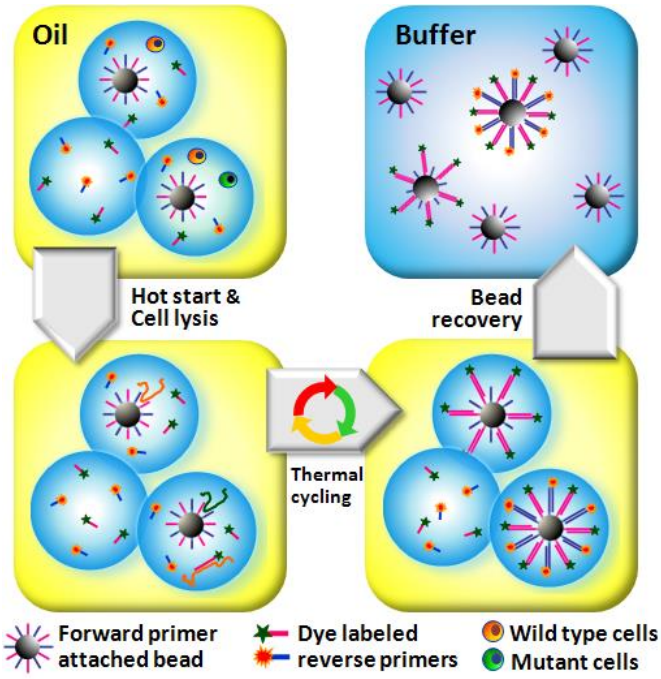

Figure 2.1. Multiplex Single Cell/Copy Genetic Analysis (SCGA). Statistically dilute beads and templates are encapsulated into uniform nanoliter volume PCR-mix-in-oil droplets, which are then thermally cycled for PCR amplification. Each bead is functionalized with forward primers for all targets. PCR mix contains reverse primers each labeled with a unique fluorescent dye. Each bead in a droplet containing only a single target will carry one type of fluorescent amplicon after PCR, while a bead compartmentalized with two different templates or cells will be linked with multiple dye-labeled products. Following emulsion PCR, the droplets are broken and the beads are recovered and analyzed by flow cytometry for multi-color detection of the bound amplicons.

2.3 Materials and Methods

MEGA Fabrication and Preparation. The four-layer MEGA chip shown schematically in Figure 2.2 is constructed from three 100-mm-diameter glass wafers and a thin PDMS membrane following a process similar to that described by Grover *et al.*[61] The glass channels were coated with octadecyltrichlorosilane (OTS, Sigma-Aldrich) to render the surface hydrophobic. The devices were assembled with a custom plexiglass manifold (Figure 2.2D) which provides fluidic connections for oil infusion and emulsion collection.

Cell Preparation. All cell culture and preparation were performed in a Class II biosafety cabinet (Labconco, Kansas City, MO) to avoid contamination. Two types of cells, *E. coli* K12 (ATCC #700926) and nontoxigenic *E. coli* O157 (ATCC 700728), were grown separately in Tryptic Soy Broth medium (TSB, Hardy Diagnostics K131, CA) overnight at 37 °C. *E. coli* K12 cells were transformed with a 3.9-kb pCR 2.1-TOPO vector (Invitrogen, Carlsbad, CA) to confer ampicillin resistance and grown with 1 mg/mL ampicillin added to the media. *E. coli* O157 was untreated and frequently tested for contamination by PCR. Cells were washed three times in 1× PBS and the final cell density was determined by using a hemacytometer.

Bead and PCR Preparation. All samples were handled in a UV-treated laminar flow hood (UVP, Upland, CA). Primers specific to the KI#128 island on the K12 genome and the OI#43 island on the O157 genome were designed to prevent cross-amplification between strains.[171] Reverse primers were labeled with 6-FAM or Cy5 dye on the 5-prime end. 5' amine modified forward primers were linked to agarose beads (34 μm mean diameter, Amersham Biosciences, NJ) via amine-NHS conjugation chemistry.[135] The coupling reaction was performed at a ratio of ~1.5 μmol oligos per gram beads for pUC18 target. For *E. coli* cells, equimolar forward primers were used at a concentration of ~0.3 μmol oligo per gram beads. PCR mixes contain forward primer functionalized beads (40 beads/μL) and varied amounts of freshly prepared template DNA or cells.

Device Operation and PCR Quantification. A homemade pneumatic system controlled by Labview was used to operate the on-chip micropump. The microchip was prerun with a coating solution to minimize non-specific adsorption on glass, PDMS and tubing surfaces. PCR-mix-in-oil droplets were then generated at 5–8 Hz and collected into individual PCR tubes containing 40 μL microfine solution[154] for subsequent thermal cycling. After emulsion PCR, beads were recovered from the droplets and analyzed using a multicolor flow cytometer (FC-500, Beckman Coulter). (See Appendix A for detailed methods)

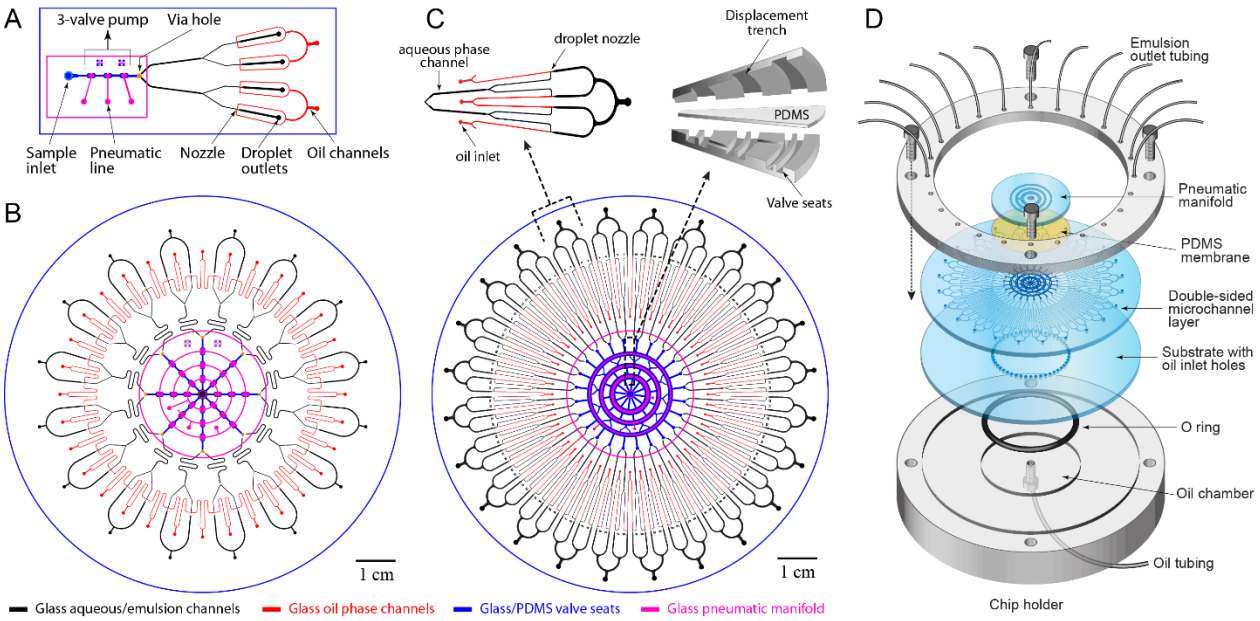

Figure 2.2. Microfluidic Emulsion Generator Array (MEGA) devices. (A) Layout of a glass/PDMS/glass hybrid 4-channel MEGA device with a pneumatically-controlled three-valve micropump integrated to drive four nozzles for droplet generation. (B) Design of a 32-channel MEGA device using an array of eight identical micropumps to operate 32 nozzles simultaneously. Two adjacent emulsion channels are combined to increase device density. (C) Layout of 96-channel MEGA on a 4" wafer composed of a single ring pump and 96 droplet generators. Inset: close-ups of a single repeating unit composed of four T-shaped nozzles (left) and the pump structure schematically showing three pairs of coaxial ring-shaped valves and displacement trenches (right). (D) Exploded view of the complete 4-layer 96-channel MEGA device and the plexiglass assembly module used to infuse oil and to collect the generated emulsion.

2.4 Results

MEGA Design. The 4-channel MEGA illustrated in Figure 2.2A is a multilayer device consisting of a bonded glass-glass microfluidic chip, a PDMS membrane, and a microfabricated manifold wafer. The glass-glass fluidic chip contains a microfabricated pattern of valve seats exposed on the top surface (blue), which is connected through a 'via' hole to an all-glass microfluidic network enclosed between two thermally bonded wafers. The assembly is then completed by contact bonding a manifold wafer (magenta) onto the fluidic chip with a PDMS membrane to form the micropump structure. The microfluidic network consists of the symmetrically bifurcated channels for the aqueous phase (black) and oil phase (red), which form four parallel crosses or droplet nozzles at the junctions. The 4-channel array defines a basic unit that is used to build up multiplexed MEGAs, such as the 32-channel MEGA with eight such arrays integrated onto a 4" wafer (Figure 2.2B). Further multiplexing of the MEGA on a 4" wafer is restricted by the number of individual pumps that can be symmetrically arranged in a circle. To achieve a higher density, we designed a new ring micropump composed of three pairs of coaxial ring-shaped valve seats connected by offset channels, as well as corresponding circular displacement trenches (Figure 2.2C, top right). This compact micropump, along with the T-shaped nozzle design (Figure 2.2C, top left) enables the implementation of a 96-channel MEGA on a 4" wafer (Figure 2.2C, bottom). In 32- and 96-channel MEGAs, oil channels are connected to the oil inlet holes drilled on the bottom substrate of the device.

A manifold module is employed to support MEGA devices, as sketched in Figure 2.2D, providing oil infusion and routing generated droplets into PCR tubes for thermal cycling. The bottom part of the manifold is designed to form a circular oil reservoir when sealed against the MEGA chip. The oil pressure in the circular reservoir is uniformly distributed across the area on the bottom side of the chip, evenly infusing oil into channels via the symmetric inlet holes. This design minimizes the number of syringe pumps and tubing connections required for oil infusion.

Droplet PCR Performance of MEGAs. The symmetric design of the MEGA assures uniform fluidic transport across the array, leading to the generation of monodisperse droplets from all channels. A microphotograph in Figure 2.3A (left) demonstrates the generation of uniform 4 nL droplets by flow focusing at the cross-injectors of a 32-channel MEGA device. The droplets were collected from eight nozzles for the size measurement revealing a mean diameter of 198 μm with a size deviation of only 2.5% (Figure 2.3A, middle). Because of the pulsatile nature of the on-chip diaphragm pump, the droplet formation rate corresponds precisely with the pumping frequency of 5.6 Hz. At this speed, the 32-channel device offers a total throughput of 6.4×10^5 droplets per hour (dph).

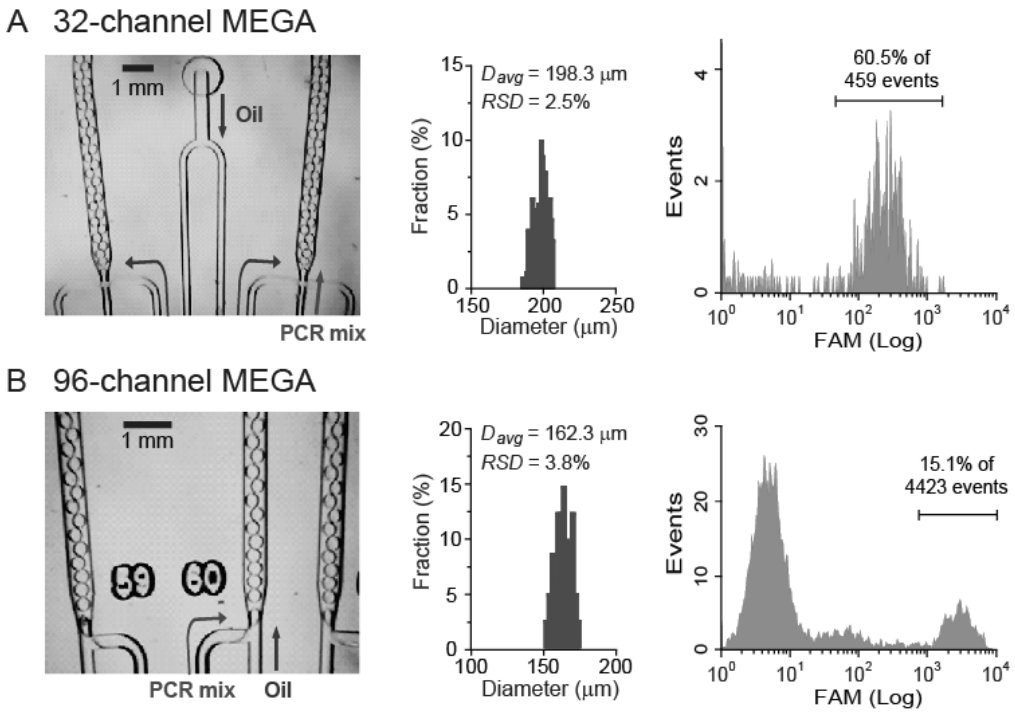

Figure 2.3. Characterization of droplet generation and PCR amplification using MEGAs. (A) 32-channel MEGA chip. Left: photo of the cross-shaped nozzles each generating ~4 nL droplets at 5.6 Hz (6.4×10^5 droplets per hour). Middle: size distribution of uniform droplets collected from eight nozzles in a device. RSD: relative standard deviation. Right: a representative flow cytometric analysis of 624 bp amplicons on beads amplified from pUC18 template (1 copy/droplet) in ~3 nL droplets generated from four nozzles in a device. (B) 96-channel MEGA. Left: image of droplet production at the T-shaped nozzles with a total throughput of 2.4×10^6 droplets per hour. Middle: size distribution of uniform ~2 nL droplets collected from sixteen nozzles in a device. Right: a representative flow cytometric histogram of beads carrying the FAM labeled PCR product from *E. coli* K12 at 0.2 cells per droplet (cpd) in 2.5 nL droplets. For all tests of droplet generation, the mock PCR mix containing ~100 beads per μL was used.

To characterize the performance of bead-based droplet PCR using the 32-channel MEGA, pUC18 DNA molecules were compartmentalized into ~3 nL droplets at 1 copy/droplet as the templates, from which a 624 bp product was amplified. The post-PCR beads recovered from each PCR tube were randomly mixed prior to flow cytometric analysis. The result obtained from 4 droplet generators is presented in Figure 2.3A (right), showing that 60.5% of the bead population (459 events) gains FAM signal due to the bead-bound amplicons, in line with the value expected from Poisson statistics (63.2%). The fluorescence intensity of the positive beads indicates an averaged PCR yield of ~150 attomoles of DNA product per bead, consistent with the yield obtained from our previous single-channel device.[25] The results from other channels confirm that the 32-channel MEGA offers constant digital emulsion PCR performance as a result of the uniformity of droplet compartmentalization.

Incorporation of a compact ring-shaped micropump in the 96-channel MEGA maintains the generation performance while increasing throughput. Uniform droplets can be formed from a mock PCR mix containing agarose beads by flow shearing at the T-shaped injectors (Figure 2.3B, left). The mean diameter of the droplets collected from 16 nozzles via 4 randomly chosen outlets was determined to be 162 μm (2.2 nL) with a deviation of only 3.8% (Figure 2.3B, middle). Furthermore, such size uniformity is preserved across a range of droplet volumes (1-5 nL; RSD < 5%). When the on-chip pump is operated at 7 Hz, the device produces up to 2.4×10^6 dph. To assess the encapsulation performance of the 96-channel MEGA, single cell emulsion PCR was performed targeting the KI#128 island on the K12 genome. Bacterial *E. coli* K12 cells and the forward primer linked beads were introduced at a statistical dilution of 0.2 cells and 0.1 beads per 2.5 nL droplet, respectively. After PCR and isolation, flow cytometric analysis (Figure 2.3B, right) shows that 15.1% of the total bead population (4423 beads) is strongly fluorescent, corresponding well to a theoretical value of 18.1% predicted by the Poisson distribution. This good agreement in yield indicates that successful single copy genetic amplification resulted from uniformly distributed cells and beads.

Pathogen Detection Using Multiplex SCGA. Multiplex single cell genetic analysis (SCGA) is demonstrated here by detecting pathogenic *E. coli* O157 cells in a background of normal *E. coli* K12 cells. Unique genes on the K12 genome (KI#128 island) and on the O157 genome (OI#43 island) are targeted by primers labeled with different fluorophores so that these two strains can be identified. For all pathogen detection, ~2.5 nL droplets were used and beads were introduced at ~0.1 beads per droplet (bpd). A 4-channel MEGA device was operated for ~18 min. to obtain ~3000 beads for flow cytometric analysis. A mixed *E. coli* bacterial sample containing 50% O157 cells was first analyzed at an average cell concentration (C_{avg}) of 0.2 cells per droplet (cpd) using a 4-channel MEGA device. As seen in Figure 2.4A, the flow cytometry profile shows four distinct bead populations: 212 FAM positive beads due to the amplicons from K12 (7.93%, green), 198 Cy5 positive beads for O157 (7.40%, red), 45 double positive beads due to coexistence of both cell types in a single droplet (1.68%, orange), and 2220 negative beads (82.99%, blue). The O157 cell ratio (O157 positive beads/total positive beads) is then determined to be 0.48, in good accord with the input O157 cell fraction of 0.5. Figure 2.4B presents the detection of a lower input O157 ratio of 1/10 at C_{avg} = 0.07 cpd: 5.20% of the beads are positive for K12, 0.66% are positive for O157, 0% are double positive beads. The experimental O157/K12 ratio of 1.1/10 is consistent with that expected.

4-channel MEGA

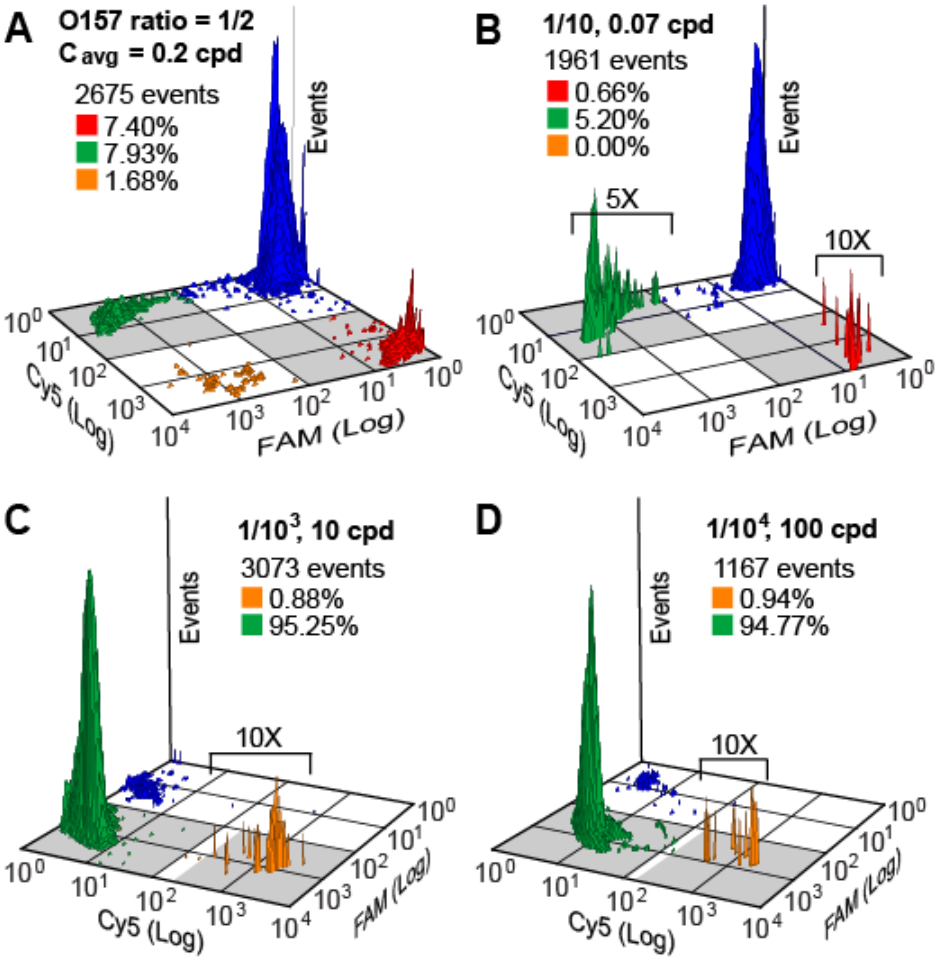

96-channel MEGA

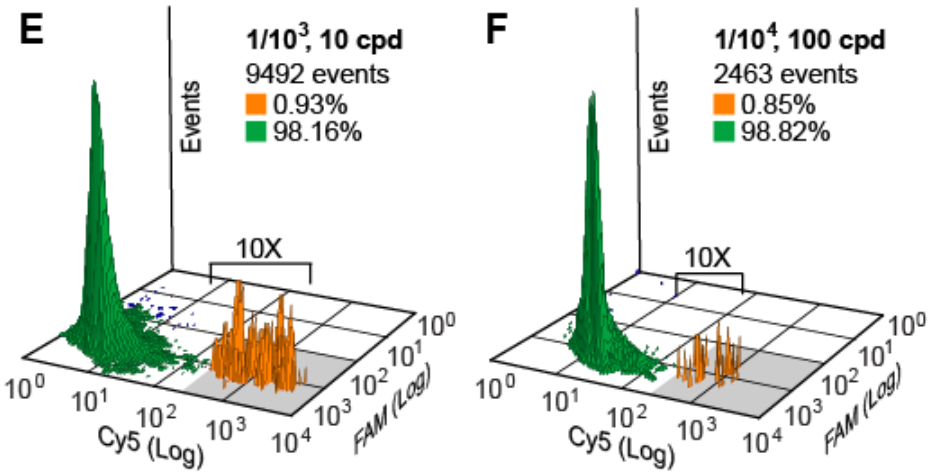

Figure 2.4. High-throughput digital multiplex detection of E. coli O157 in a background of E. coli K12 with various input ratios and average cell concentrations (C_{avg}) using MEGAs. (A, B) With $C_{avg} \leq 0.2$ cpd, flow cytometry profiles of beads show four distinct populations: negative (blue), FAM positive beads specific for K12 (green), Cy5 positive beads specific for O157 (red), and double positive beads for both cells (orange). Small populations are expanded along the event axis for better visualization, as indicated. The gray regions mark the population gating. The measured O157 ratios (O157 positive beads/total positive beads) are (A) 0.48 (expected: 0.5) and (B) 0.11 (expected: 0.1). (C, D) When $C_{avg} \geq 10$ cpd while keeping O157 cells at 0.01 cpd, double positive beads quantify O157 since a single O157 cell is co-compartmentalized into a droplet with multiple K12 cells. In this case the ratios of double positive beads divided by C_{avg} give the measured O157 ratios: (C) $0.92/10^3$ (expected: $1/10^3$) and (D) $0.98/10^4$ (expected: $1/10^4$). Up to 3000 beads can be analyzed using a 4-channel device for ~25 min. run time. Increasing C_{avg} to 100 cpd reduces the number of beads required, improving the detection sensitivity to $1/10^4$ without excessively extending run time. (E, F) O157 detection using a 96-channel MEGA shows the measured O157 ratios consistent with the inputs: (E) $0.94/10^3$ vs $1/10^3$ and (F) $0.85/10^4$ vs $1/10^4$. Up to 10^4 events were processed within 5 min. run time. The capability offered by 96-channel MEGA (up to 3.4×10^6 droplets per hour) greatly increased analysis throughput and decreased processing time necessary for detecting a statistically significant population of a low-frequency sample. Bead concentration was 0.1 bpd for all cases.

Improving Throughput and Sensitivity. The multiplex SCGA process discussed above uses droplets/beads inefficiently because cells are highly dilute so that most droplets are empty. The detection of low frequency genetic variations requires high analysis throughput in order to obtain the statistically significant population for the target. One way to increase the process efficiency is to perform multiplex SCGA at elevated cell density, while still keeping the cells of interest statistically dilute. This is realistic because the target pathogen or mutant cells are typically present at very low relative concentrations compared to normal cells. Figure 2.4C demonstrates the use of a 4-channel MEGA device to detect *E. coli* O157 cells at a frequency of $1/10^3$. By increasing C_{avg} from 0.2 cpd (Figure 2.4A) to 10 cpd, the effective density of O157 cells is raised from 0.0005 to 0.01 cpd, reducing the number of droplets/beads that must be processed by 50-fold. In this case, all beads should be FAM fluorescent due to co-encapsulated K12 cells and the presence of O157 cells in the droplets will modify only a fraction of beads with the Cy5 dye. As expected, a vast majority of beads (1846 out of 1961 events, 96.13%) are FAM positive and a small fraction of double positive beads (102 events, 0.88%) are observed. The measured O157 ratio is determined to be $0.92/10^3$ (the ratio of double positive beads over all positive beads divided by C_{avg}), close to the input, $1/10^3$. Multiplex SCGA preserves the quantitative performance for pathogen detection even when the average concentration is up to 100 *E. coli* cells per 2.5 nL droplet. As seen in Figure 2.4D, an experiment carried out at C_{avg} = 100 cpd records 11 O157 positive events in a total of 1167 events, giving an output of $0.98/10^4$ in response to the input O157 ratio of $1/10^4$.

When C_{avg} is higher than 100 cells per 2.5 nL droplet, non-specific amplification was found to be significant in the multiplex PCR assay, causing false positive scores for O157. To further improve the detection sensitivity, therefore, it is necessary to use highly multiplexed MEGA devices for high throughput droplet generation. A 96-channel MEGA device was evaluated for multiplex PCR detection of *E. coli* O157 cells, where the device was operated at ~7 Hz, allowing us to encapsulate up to 10^4 cells within a 5 min. microdroplet generation time. As shown in Figure 2.4E and F, the experiments at input ratios of $1/10^3$ (10 cpd) and $1/10^4$ (100 cpd) detect 88 and 21 O157 positive events, giving an output fraction of $0.94/10^3$ and $0.85/10^4$, respectively. A small number of negative events were observed in Figure 2.4C–F, which may be due to cell debris aggregates or unlysed cells. We have optimized the bead cleaning protocol for the 96-channel trials to remove cell debris and other interfering species. The high percentage of positive events (> 99%) in Figure 2.4E and F results from the combination of high efficiency droplet PCR and improved bead clean-up.

To verify that the observed performance is the result of digital quantification of each strain, we compare the percentage of positive beads obtained with various input ratios and average cell concentrations to that predicted by the Poisson distribution (Figure 2.5). The multiplex detection is seen to follow Poisson statistics even when individual O157 cells were detected within a high background of 100 cells per droplet. The good correspondence indicates successful single cell emulsion PCR, which allows digital quantification of the absolute cell concentration. For instance, with C_{avg} = 100 cpd and O157 cells diluted to $1/10^4$ in a K12 background, the O157 cell density is 0.01 cpd and the detection resulted in 0.91% ± 0.04% double positive beads, consistent with the predicted ratio of 0.995%. Because of the presence of negative events, the average percentage of O157 positive beads is corrected to be 0.93% ± 0.05% (double positive beads divided by total positive beads), from which the O157 cell concentration is determined to be 3.7 ± 0.2 cells/μL (input 4 cells/μL).

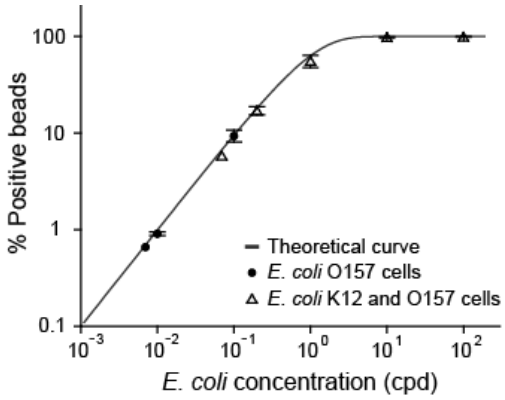

Figure 2.5. Comparison of the percentage of positive beads over total beads versus starting cell concentration. The red curve represents the value expected from Poisson statistics. The experimental data were obtained by detecting *E. coli* O157 cells in a background of *E. coli* K12 with overall cell concentrations of 0.07–100 cpd. By maintaining cells of interest (O157) at a statistically dilute concentration (0.007, 0.01 and 0.1 cpd), the multiplex detection follows Poisson statistics even in a background of high normal cell density, which enables performing single cell genetic analysis with highly improved throughput and efficiency. Error bars represent standard deviation ($n \geq 3$).

Limit of Detection and Dynamic Range. To determine the limit of detection (LOD) of multiplex SCGA for *E. coli* O157 detection, the assay was carried out at lower pathogenic ratios and C_{avg} = 100 cpd using a 96-channel MEGA. Figure 2.6A presents a representative analysis at an input ratio of $1/10^6$ where the experimental output ratio ($1.4/10^5$) is one order of magnitude higher than that expected. In this case, to define a statistically significant population at the extremely low cell density (0.0001 cpd for O157 cells), a large volume of PCR mix (1500 μL) was used to produce ~8×10^5 droplets within 20 min., which leads to 45419 total events analyzed and 65 Cy5 positive events detected. The experimental readout at the input of $1/10^6$ ($1.8/10^5 \pm 0.66/10^5$, $n = 4$) is significantly above the expected value ($p = 0.01$), indicating that there is significant background signal. It is seen in Figure 2.6A that the peak for K12 cells (FAM positive only) tails off into the Cy5 positive region, suggesting that the background could be attributed to misamplification caused by the non-specific binding of O157 primers to the K12 templates. It is also possible that the false positive events stem from the buildup of trace environmental contamination in the lab during the analysis development process.

Figure 2.6B shows a representative result obtained with an input ratio of $1/10^5$ which detects 33 Cy5 positive beads. At this pathogenic ratio, the experimental readouts ($2.4/10^5 \pm 0.91/10^5$, $n = 4$) are in the same order as the expected value and significantly different from that obtained at $1/10^6$ at $p = 0.05$ using the two-sample student's *t*-test. By subtracting the background, the corrected value at the input ratio of $1/10^5$ is determined to be $0.69/10^5 \pm 0.34/10^5$ ($n = 4$). Figure 2.6C summarizes the background corrected calibration of *E. coli* O157 detection as a function of the input O157 fraction, which shows a linear dynamic range for O157 fraction higher than $1/10^5$ ($y = 1.043x - 0.033$). From this plot, the concentration detection limit is determined to be $3/10^5$ with a 99% confidence.

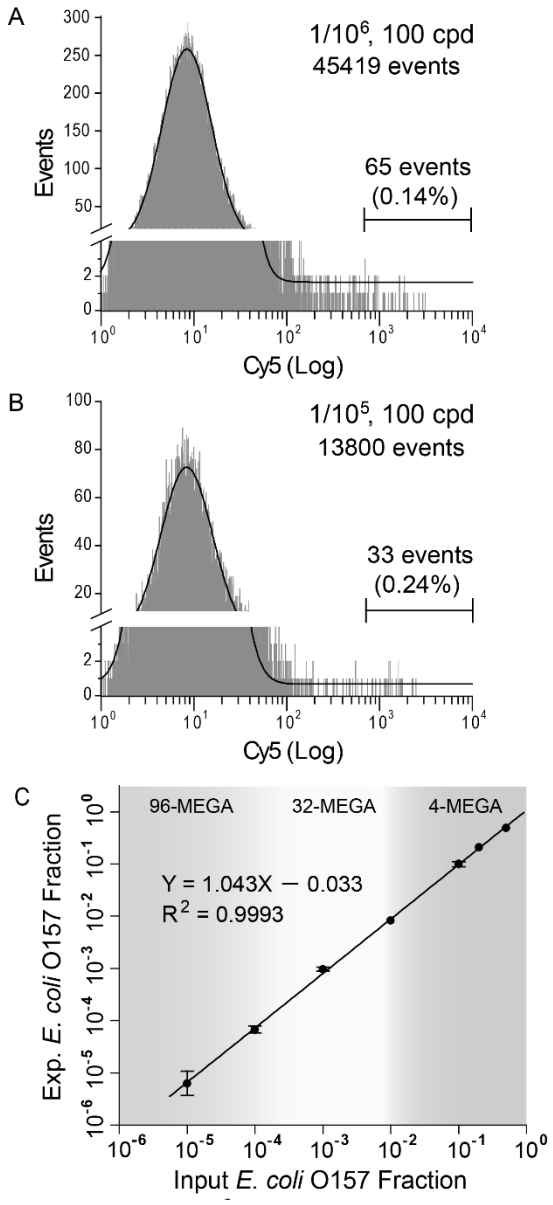

Figure 2.6. Detection limit and dynamic range of multiplex SCGA for *E. coli* O157 detection at C_{avg} = 100 cpd. (A, B) Representative cytometric histograms (events vs. Cy 5 signal) obtained with input O157 ratios of $1/10^6$ and $1/10^5$, respectively, using a 96-channel MEGA. The measured O157 ratios (ratios of double positive beads divided by C_{avg}) are: (A) $2.4/10^5$ (expected: $1/10^5$) and (B) $1.4/10^5$ (expected: $1/10^6$), suggesting that the limit of detection of current assay is on the order of $1/10^5$ due to non-specific amplification and/or environmental contamination. The solid lines represent the Gaussian fittings for the Cy5 negative populations. (C) Plot of experimental readout vs input O157 fraction showing a linear dynamic range for O157 fraction higher than $1/10^5$. The color regions roughly mark the detection windows that meet the throughput offered by different MEGA devices within experimentally accessible run time. Error bars represent standard deviation ($n \geq 3$).

2.5 Discussion

High-Throughput MEGA Devices. Continuous-flow microfluidic droplet techniques rely on external mechanical agitation, such as magnetic stirring, to maintain the uniform dispersion of objects with a higher density than the carrier fluid (e.g. cells, beads, etc.) during droplet encapsulation.[106] We found that the pulsatile nature of the integrated diaphragm pump effectively overcomes this problem of sedimentation. This observation was further confirmed by the reproducible results obtained for both single-copy DNA amplification and single-cell detection which agreed well with Poisson statistical analysis. However the generation rate from a single channel, determined by the frequency of pneumatically controlled pumping, is limited to ~ 10 Hz for nanoliter-volume droplets because of the response time of the PDMS membrane in the valve structure (tens of milliseconds).[65]

One of the advantages of the on-chip pump is that the microvalve structure can be precisely engineered to adjust pumping capacity, thereby conferring great flexibility in the multiplexing of droplet generators to increase throughput. Our results show that by increasing the valve dimensions for the single-channel device by 20%, the pump is able to drive four droplet generators in parallel without changing the pump actuation pressure/vacuum. This 4-channel design serves as a basic unit that is readily scalable to construct symmetric generator arrays for balanced fluidic transport, and thus uniform droplet formation. We demonstrate a 32-channel MEGA device containing an array of 8 such pumps. A maximum of 12 on-chip pumps and 48 droplet generators can be arranged on a 4" wafer to produce a device that generates up to 1.7×10^6 dph.

To further increase the throughput, we successfully implemented a new compact micropump composed of three coaxial ring-shaped valves, pushing the multiplexing limit on the 4" wafer to 96-channels. Utilizing the original pump array design would mandate a 6" device that would lead to increased dead volume and difficulty in fabrication and operation. Moreover, the operation of this integrated ring pump was found to be more robust than that of the array of individual pumps. In the pump array, bubbles trapped inside the valves of one or few pumps can cause unbalanced fluidic pressure applied to the individual generators, resulting in the production of polydisperse droplets. In contrast, the 96-channel MEGA system integrated with the ring pump shows greater tolerance to bubbles, because the larger volume of the ring-shaped valves reduces the impact of bubbles on pumping and the entire droplet generator array is driven by a single pump. The successful implementation of 96-channel MEGA offers a throughput of 3.4×10^6 dph, which greatly lowers the detection limit and decreased processing time necessary for detection of low-frequency events.

Multiplex SCGA. Multiplex single cell PCR is the cornerstone of the high-throughput SCGA technique, which maximizes the genetic information extracted from each single cell detection event. In this process, it is critical to compartmentalize single cells and beads into monodisperse nanoliter-volume droplets. Our results clearly demonstrate that the droplet uniformity enables strict Poisson statistical analysis to calibrate the performance of digital single cell PCR which is determined collectively by the statistical encapsulation of beads and cells, cell lysis, and PCR reaction. Such analysis permits digital quantification of the absolute number of targets in the initial sample. Other digital PCR techniques using agitation-based emulsification fundamentally lack this capability because of the extremely polydisperse droplets produced.[155] In addition, the uniform droplets contain the same amount of reactants enabling a quantitative comparison of the PCR

products. Thus one should be able to perform large-scale gene expression profiling at the single cell level, by transforming reverse transcription-PCR (RT-PCR) assays to the SCGA format.[172]

The multiplex SCGA displays great tolerance to PCR inhibition as the cell lysate and debris are significantly diluted in the large nanoliter droplets generated by MEGA and each reaction is independent. Efficient and specific multiplex PCR amplification can be achieved even when each droplet is loaded with up to 100 *E. coli* cells on average, which greatly increases the analysis throughput and hence the detection sensitivity, without excessively extending the droplet production time. This result indicates the feasibility of SCGA for the large-scale genetic analysis of larger and more complex mammalian cells. For instance, the analysis of cancer development and progression, circulating tumor cells, and stem cell differentiation, where single cell resolution may facilitate a deeper understanding of the biological mechanisms involved, can be envisioned.

Pathogen Detection. Most PCR-based microdevices reported the detection of only one bacterial strain by PCR, with detection limits ranging from a few to 10^4 bacterial cells.[173–175] Recent work in our group showed that PCR reactions in a 250 nL microreactor can detect *E. coli* O157:H7 in a mixture with the K12 strain down to a ratio of 1:500,[176] and that the detection limit of the microscale PCR can be as low as 1:1000 by using on-chip affinity cell preconcentration.[171] Our quantitative digital format remarkably outperforms previous low-throughput microsystems with its capability to identify and quantify both *E. coli* O157 and K12 cells down to a pathogen-to-background ratio in the order of $1:10^5$ (Figure 2.6). Such sensitivity makes the technique a promising candidate to achieve the level of detection and speed required for zero-pathogen-tolerance policy. Droplet generation using the 96-channel MEGA requires less than 30 min run time to achieve a limit of detection of $1:10^5$. The entire procedure, including PCR thermal cycling, post-PCR cleanup, and flow cytometry takes approximately 4 hours and compares favorably to standard PCR-based detection assays while providing better sensitivity. In contrast, most commonly used methods today require at least two days to achieve this level of sensitivity since they rely on pathogen culturing.[170] The SCGA technique can be further extended to detect multiple pathogenic microorganisms in one sample. Compared to the small beads used in the "BEAMing" technique, the large surface area of the microsphere used here allows multiple different primers to be conjugated with a density that supports efficient on-bead PCR reaction for each target. Thus our detection multiplicity is limited primarily by the number of fluorescent dyes that a flow cytometer can detect (commonly 5 colors) since that is a relatively standard degree of PCR multiplicity.

We believe that the detection limit of our multiplex SCGA can be further improved to beyond one in a million. Some nonspecific amplification was observed when the 2.5 nL droplets were loaded with 100 *E. coli* cells. Although the multiplex PCR conditions have been optimized to minimize non-specific amplification, it still can contribute to the false positive scores which limit the low-abundance detection to the level of $1:10^5$ in this proof of concept work. In practical applications, we can perform droplet generation for longer periods of time at lower cell concentrations to minimize the effect of non-specific PCR amplification, and thus lower the detection limit. On the other hand, trace exogenous contamination from microorganisms and/or DNA present in air, reagents and instruments may cause considerable interference at these extremely low level detection limits. We did see false positive events occasionally in negative control experiments performed at a cell concentration lower than 1 cell/droplet. Sample

preparation and experimental operation with more stringent environmental controls should prevent contaminations and lower the detection limit to $1{:}10^6$ or lower.

2.6 Conclusions

The past few years have witnessed remarkable progress in the understanding and use of micro-emulsions for high throughput, sensitive biological analysis and next-generation sequencing. The results presented here show that the use of ultrahigh-throughput microfluidic platforms will enable large-scale quantitative genotypic studies of complex biological systems at the single molecule and single cell level. The multiplex SCGA technique enables the multi-parameter acquisition of digital genetic information to elucidate the importance of stochastic variations in biological populations and should lead to the detection and numeration of rare mutants for clinical diagnosis of diseases, such as chromosomal translocations in blood cells for the early detection of leukemia and lymphoma and the measurement of minimal residual disease and relapse.

2.7 Acknowledgements

We thank James Yang and Palani Kumaresan for their early contributions to this work. Microfabrication was carried out at the Microfabrication Laboratory at the University of California, Berkeley. This work was supported through the trans-NIH Genes, Environment and Health Initiative, grant U54ES016115. R. N. is supported by an NSF Graduate Research Fellowship, and J. S. is supported by the Canary Foundation and ACS Early Detection Postdoctoral Fellowship.

Chapter 3: Rapid fabrication of nickel molds for prototyping embossed plastic microfluidic devices

Reprinted from Novak, R., Ranu, N., and Mathies, R.A. Rapid fabrication of nickel molds for prototyping embossed plastic microfluidic devices. *Lab on a Chip*, 2013, 13, 1468 with permission from The Royal Society of Chemistry.

3.1 Abstract

The production of hot embossed plastic microfluidic devices is demonstrated in 1-2 h by exploiting vinyl adhesive stickers as masks for electroplating nickel molds. The sticker masks are cut directly from a CAD design using a cutting plotter and transferred to steel wafers for nickel electroplating. The resulting nickel molds are used to hot emboss a variety of plastic substrates, including cyclo-olefin copolymer and THV fluorinated thermoplastic elastomer. Completed devices are formed by bonding a blank sheet to the embossed layer using a solvent-assisted lamination method. For example, a microfluidic valve array or automaton and a droplet generator were fabricated with less than 100 μm x-y plane feature resolution, to within 9% of the target height, and with 90±11% height uniformity over 5 cm. This approach for mold fabrication, embossing, and bonding reduces fabrication time and cost for research applications by avoiding photoresists, lithography masks, and the cleanroom.

3.2 Introduction

Microfluidic devices have been fabricated from silicon, glass, and poly(dimethyl siloxane) (PDMS), but there is now a move toward thermoset and thermoplastic materials, especially for commercial applications.[177–179] The wide variety of polymers offers a choice of material properties for microfluidics-based sensors and analyzers, including hydrophobicity, flexibility, elasticity, adsorption, and light transmission.[57,177–180] Furthermore, plastic chips can be integrated with electrodes[181] and surface functionalized[182] like those made from glass and PDMS.

Despite the practical and commercial advantages of plastic microfluidics, plastic materials are not commonly used in research applications. One possible explanation for this disconnect is the lack of simple, inexpensive, and rapid plastic prototyping methods. Hot embossing and injection molding machines for high throughput applications are expensive and not part of most microfabrication facilities. In addition, the fabrication of metal molds used in both systems is time consuming and does not lend itself to rapid prototyping. As a result, significant effort has gone into the development of alternative plastic microfluidics prototyping methods.[183] Milled steel, aluminum, and brass,[178,180,184] cast PDMS,[185,186] epoxy,[187,188] and photoresist[189,190] have all been used as hot embossing molds for low throughput and prototyping applications. However, many of these methods still suffer from relatively long fabrication times and cannot withstand more than several dozen embossing cycles. Milled metal molds take significant time to fabricate, require high-precision milling machines, and can be relatively limited in resolution. Other plastic fabrication approaches, such as laser engraving,[191] xurography,[192,193] and thermoset polymer casting of SU-8 molds[194,195] offer low production rates and limited materials.

As an alternative, we describe here a "sticker mask" fabrication method that offers rapid and inexpensive prototyping of nickel molds for hot embossing of microfluidic devices within 1-2 h starting from a CAD design. The sticker mask approach is based on cutting vinyl adhesive films with a plotter to generate an insulating mask on a steel wafer. The exposed designs are electroplated to form raised features, which are hot embossed using a hydraulic press with a simple heated platen insert followed by bonding to a featureless plastic sheet. Sticker mask microfabrication offers researchers access to a versatile and simple fabrication process for plastic microfluidic devices.

3.3 Experimental

Detailed experimental procedures are available in Appendix B. Briefly, positive electroplating masks were produced by cutting designs into insulating adhesive films with a Graphtec Craft Robo Pro CE5000-40 Cutting Plotter (Graphtec America, Inc.) directly from a CAD file. The "sticker masks" were transferred to stainless steel wafers pretreated with a nickel strike. The exposed features were then electroplated in a nickel sulfamate solution to fabricate nickel molds of desired height. After removing the sticker masks, the molds were used to produce cyclo-olefin copolymer (COC) and THV 500 fluorinated elastomer microfluidic devices in a hot embossing press built in-house. Functional devices were bonded to unfeatured plastic wafers using a solvent-assisted lamination protocol in a Peach 3500 Photo Pouch Laminator (PEACH 3500, Oregon Laminations, Inc.). Valves were fabricated by sandwiching a 250 μm PDMS membrane between two embossed layers and bonded using UV/O_3 oxidation.

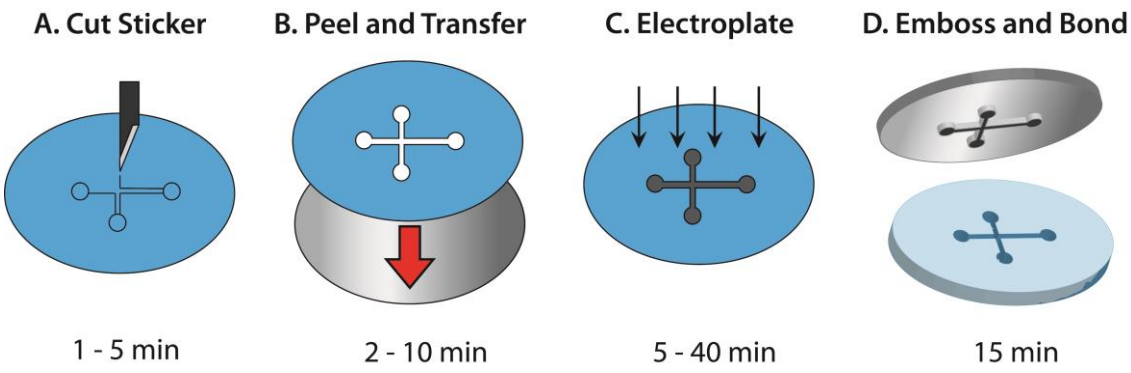

Figure 3.1. Workflow for fabricating hot embossed plastic microfluidic devices. (A) The CAD design is cut into a vinyl sticker using a plotter, (B) transferred to a stainless steel wafer, and (C) electroplated to form the nickel mold. After sticker removal, (D) the nickel mold is hot embossed into the desired plastic. The entire process can take less than 1 h, depending on the complexity of the microfluidic design.

3.4 Results and discussion

Nickel hot embossing molds for prototyping plastic microfluidic devices were fabricated using vinyl sticker patterns as shown in the workflow in Figure 3.1. In Fig. 3.1A, a cutting plotter translates the CAD design into a sheet of vinyl adhesive, and the cut features are removed. Fig. 1B shows the plotted sticker used as an insulating mask for electroplating a steel wafer. Electroplating the exposed features in a nickel sulfamate bath (Fig. 3.1C) forms raised structures. Fig. 1D shows hot embossing of the mold into plastic sheets to produce microfluidic devices using a hydraulic press with heated platen inserts as shown in Fig. B1. The embossed features are closed by bonding a sheet of featureless polymer using a solvent-assisted bonding method. The overall time required for producing functional microfluidic devices from digital CAD designs was as low as 1 h. Even the most complex and tall designs tested did not require more than 3 h. A single mold costs approximately $2 in materials: $1.50 per steel wafer (not including machining labor), $0.25 for each of the two vinyl adhesive sheets, and negligible cost for the electroplating chemicals per wafer. This is in contrast to recent polymer device fabrication methods that are either slow and expensive[196] or relatively fast (<2 h starting with a prepared UV mask) but produce relatively weak and deformable molds that are limited to hot embossing only low T_g materials.[189] The sticker mask approach resulted in durable nickel and steel molds that could be used to emboss devices into a wide range of polymers.

The plotting accuracy, electroplating rates, and feature quality for the sticker mask approach were characterized. Fig. 3.2A shows the relationship between theoretical feature dimensions in the CAD design and experimental feature dimensions of electroplated nickel molds. The slope of the regression line (1.006) and value of the correlation coefficient (0.999) indicate a high degree of plotting precision and accuracy over the range tested. We observed a real resolution limit of approximately 100 μm as shown by the inability to plot features below 100 μm. This could be due to slight lateral movement of the vinyl sheet during cutting as well as momentum of the blade assembly. The addition of small (~5-10 μm) rectangular features before and after any large steps or changes in direction improves the final design resolution when cutting features smaller than 200 μm by reducing blade momentum and minimizing travel distance between reference points. Multi-layer sticker masks only slightly decreased the resolution limit. Since many microfluidic devices consist of relatively wide channels, the 100 μm lateral resolution is not a significant drawback in such devices, and the tight control of feature height in a relatively rigid polymer is attractive for applications such as imaging-based cell assays[197] or for control of flow-induced shear.[198] For higher resolution features, nickel production molds can be fabricated using SU-8 photolithography with only minimal modifications to the workflow.

Fig. 3.2B explores the dependence of electroplating rate as a function of current densities. The plating rate is expected to be proportional to the current density based on the following equation:

$$rate = \frac{600{,}000 \cdot \varepsilon \cdot I \cdot A}{Q \cdot F \cdot \rho \cdot S} \qquad \text{(Eq. 8)}$$

The rate is a function of the efficiency (ε), current (I, Amperes), molecular mass (A, g-mol^{-1}), charge of the nickel ions (Q), Faraday's constant (F, Coulomb-mol^{-1}), nickel density (ρ, g-cm^{-3}),

and exposed surface area of the cathode (S, cm^2). The 60,000 multiplier is used to convert the electroplating rate to μm-min^{-1}. The slope of the data indicates an efficiency of 53% relative to the maximum theoretical plating rate across a wide range of feature sizes and currents tested. It is important to include the exposed wafer edges in the total surface area calculation (2.2 cm^2 for the wafers used here), particularly in the case of small features, to accurately predict the plating rate. We were able to predict the final feature height to within 9% of the actual height and the observed height uniformity was 90±11% across 5 cm.

Reducing the lipping of plated features is important to achieve uniform feature heights. Lipping occurs due to greater electric field density at the edges of a conductive surface where electric field lines concentrate. To minimize this undesirable effect, boundary features were added at constant distances from all perimeter features in the design to improve the current density distribution of exposed cathode surfaces. The addition of boundaries was not necessary for high-density features and did not impede the fabrication of complex designs. Fig. B2 presents the degree of lipping as a function of the current density and distance of the boundary features. The plot shows that decreasing current density decreases lipping for all boundary distances, but features with boundary-feature gaps of 250 μm and 500 μm exhibit a 15% lipping at all current densities tested. SEM images showing improved electroplating quality are presented in Fig. B3. This finding indicates that adding boundary features produces reproducible feature heights and maintains mold quality while enabling fast plating rates. The optimal plating rate was found to be 1.5-3 μm/min. Nickel molds can also be subjected to chemical mechanical polishing to eliminate lipping.

Fig. 3.3 presents examples of nickel molding and embossed features fabricated using sticker masks. Fig. 3A shows a droplet generator design with boundaries to produce uniform flow rates. Fig. 3B shows a clean flat channel embossed into COC from the mold in Fig. 3.3A. The nickel mold and embossed design enabled analysis of dimensional stability after hot embossing. For Zeonor 1060R, we observed dimensional fidelity of 101±1% in the x-y plane and 99±1% in the z-axis with respect to the nickel mold. Fig. 3C shows the cross section of a channel and nearby boundary formed by solvent-assisted lamination of an unfeatured 1420R COC wafer to the embossed design. Note the rectangular geometry of the left channel that indicates minimal channel collapse as a result of bonding. The ability of this method to bond extremely low aspect ratio features (< 1:100) in approximately 50 μm deep devices without channel collapse or distortion is demonstrated by the uniform fluorescence of the bonded design in Fig. B4A. A slight increase in fluorescence can be seen around the channel edges due to lipping as a result of not incorporating boundaries during electroplating.

A.

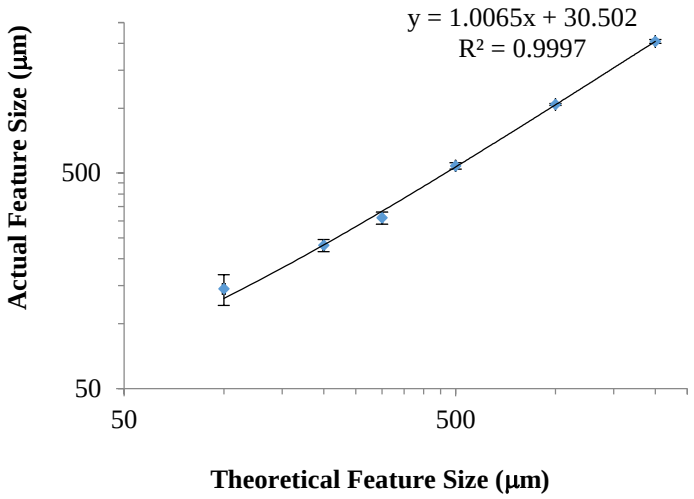

B.

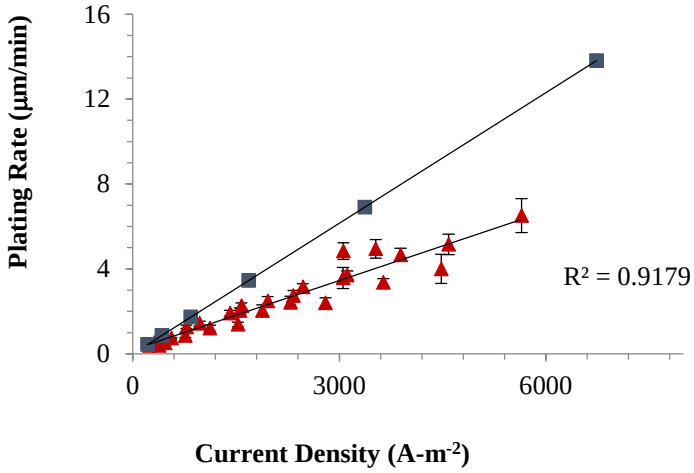

Figure 3.2. (A) Plot showing a linear correspondence between final nickel feature resolution and the CAD design above 100 µm; below 100 µm the plotter fails to produce distinct features (gray hatching). The resolution is limited by the 10 µm resolution of the plotter and the stability of the vinyl sticker during cutting. (B) Plot of electroplating rate as a function of current density for a wide range of feature shapes and areas (triangles). The experimental plating efficiency is 53% relative to the theoretical limit (squares). All error bars show standard deviation of the mean.

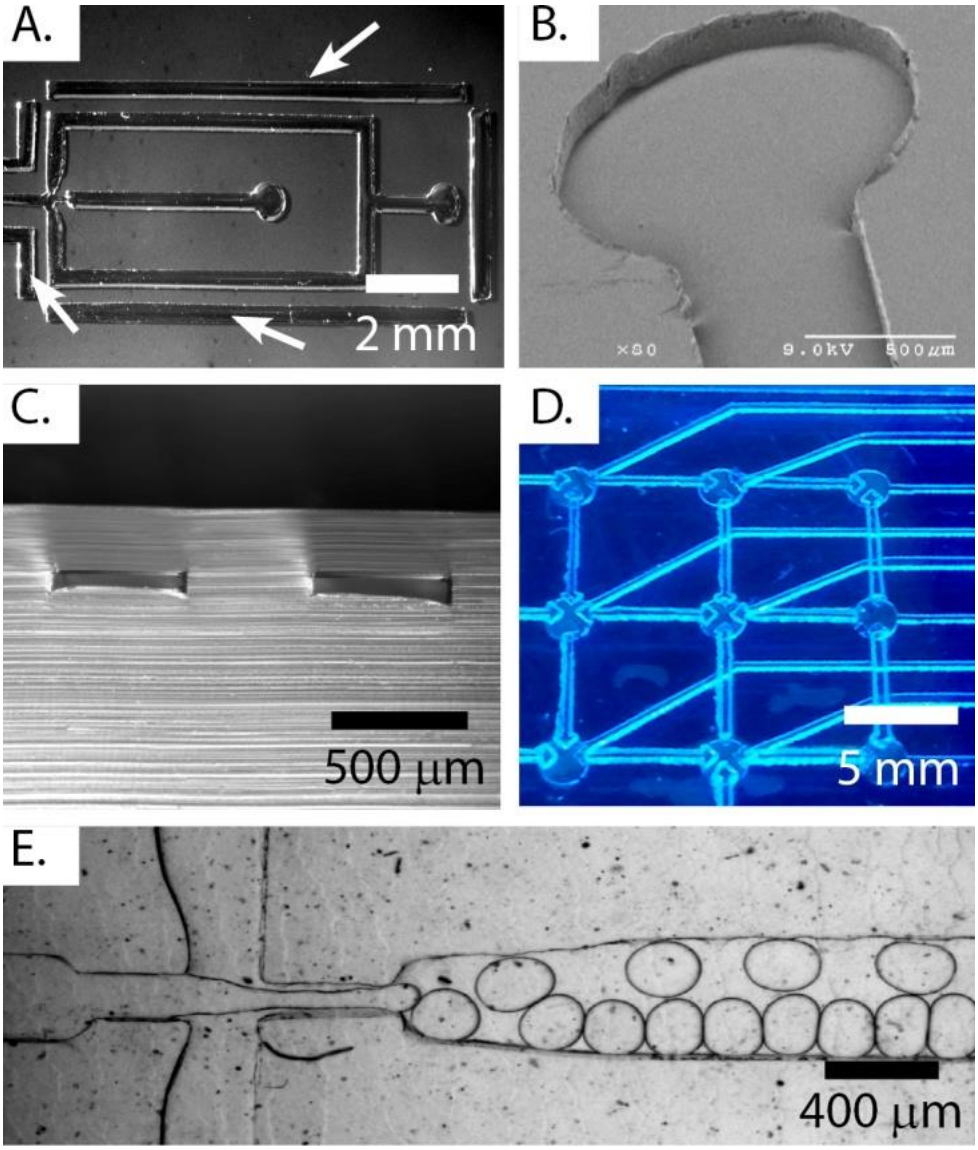

Figure 3.3. (A) Photograph of nickel mold incorporating electroplating boundaries, indicated by arrows. (B) SEM image of an embossed channel in COC. (C) Xylene-assisted lamination produces low aspect ratio channels in cyclo-olefin copolymer with minimal distortion as seen in this cross section. Note the slight asymmetry of the boundary (right feature) that is used to block stray electrical current to the fluidic channel during electroplating (left). The rapid prototyping method can be used to produce functional components, such as an automaton (D), consisting of an array of pneumatic valves, as well as a droplet generator nozzle (E) made from THV500 fluorinated elastomer.

The sticker mold fabrication method was used to create examples of microfluidic features for fluid handling. Pneumatically actuated valves play a critical role in fluid routing operations, including dilutions, combinations, volume splitting, and pumping.[61,64] The plastic microfluidic automaton in Fig. 3D demonstrates the ability of the sticker fabrication method to produce pneumatic valves in COC. Fig. B4B presents a detailed view of a single four-way valve. Valves remained functional for several weeks of operation in pumping applications. Fig. 3.3E shows the production of 2 nL droplets of PCR mix in fluorinated oil at a rate of approximately 250 Hz in a droplet generator fabricated from the fluorinated elastomer THV500. Droplet generators are becoming widely adopted for digital PCR and single cell analysis[71,102,135]; easily fabricated disposable polymer droplet generators can be used to avoid cross contamination of samples and obviate the need for surface coating that degrades with use and can disrupt PCR reactions. Sticker masks result in durable nickel and steel molds that others have shown to last over 1,000 molding cycles[196,199] and allow prototyping with the desired materials.

3.5 Conclusions

We have demonstrated and characterized a versatile approach for fabricating nickel molds for plastic device embossing. The sticker-based method can be used to produce microfluidic devices with 100 μm resolution and tight control of feature height. Boundaries incorporated around features improve the quality of electroplated designs and permit production of functional microfluidic components such as valves and droplet generator nozzles. The simplicity and speed of the sticker mold fabrication method make it well suited for rapid prototyping and the production of disposable plastic microdevices.

3.6 Acknowledgments

The authors would like to thank Paul Lum and Verena Charwat for helpful discussions. RN was supported by an NSF Graduate Research Fellowship, and NR was supported by a Haas Scholars Program grant. Fabrication was performed at the Biomolecular Nanotechnology Center at UC Berkeley. Work was supported by the trans-NIH Genes, Environment and Health Initiative, Biological Response Indicators of Environmental Systems Center Grant U54 ES016115-01 and by the Mathies Royalty Fund.

Chapter 4: Optimized protocol for hot embossing microfluidic devices in thermoplastic materials

4.1 Introduction

Since the publishing of the initial rapid prototyping method presented in the previous chapter, a number of improvements have resulted in a more robust and higher-resolution method with broader scalability. In particular, my main modification is the substitution of photolithographic patterning of a dry film photoresist electroplating mask instead of the one previously cut from adhesive sheets. Dry film resist offers excellent adhesion to steel and generally easy removal, unlike SU-8 photoresist, although S-1818 resist shows adequate adhesion to steel and has been used by a collaborator to replicate the protocols presented below. The method presented here is environmentally friendly as it uses basic salt solutions at low concentrations for both developing and stripping. Using this method as described, resolution is limited to 1:1 aspect ratios, giving a final resolution limit of approximately 75 μm. Furthermore, substituting different types of dry film photoresists can improve feature resolution to the several micron range and can be integrated with existing microfabrication setups. Using photoresists results in smooth side walls for easy demolding during hot embossing and clean device channels that are less prone to bubble nucleation. Lastly, a protocol variation is described for embedding metal electrodes in plastic devices via hot embossing as shown in Figure 4.1. This chapter presents detailed protocols for fabricating the nickel mold and nickel electrodes, with the hot embossing and device bonding steps remaining unchanged from the previous chapter.

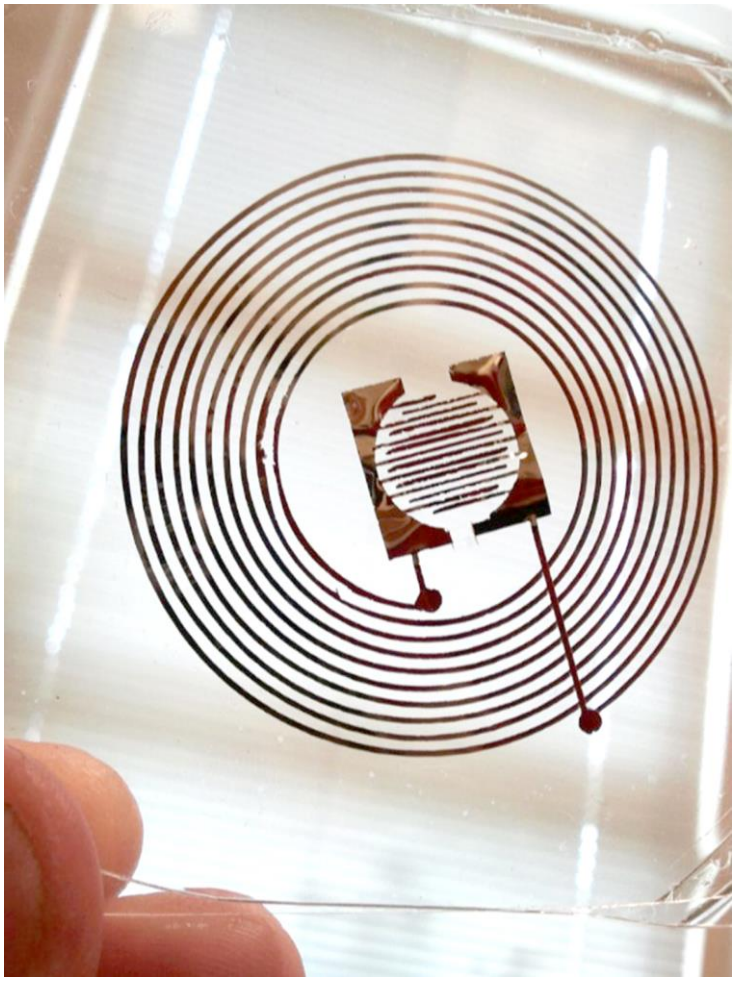

Figure 4.1. Photograph of two electroplated nickel electrodes embedded in polycarbonate sheets after thermal bonding. The spiral consists of a single nickel electrode distinct from the interdigitated central electrodes, which are in a separate polycarbonate sheet. This design was used to demonstrate proof of concept for nickel electrode fabrication via hot embossing for producing a basic mockup RFID device.

4.2 Materials and equipment

- DuPont Riston Goldmaster GM100 series dry film photoresist
- Steel wafers with "mirror-like" finish; any desired diameter and typically 0.75 mm thick for optimal handling without excess weight. The wafers can be sheared out of a large sheet of metal and then turned on a lathe to produce circular wafers with minimal stress. Be sure to keep the protective films on the wafers.
- Developer solution: 1% w/v K_2CO_3; approximately 200 mL in glass dish and another 500 mL in squeeze bottle
- Stripper solution: 3% w/v NaOH or KOH; approximately 200 mL in glass dish
- Wafer tongs
- Hot laminator set to 115 ^oC, with speed set to lowest setpoint
- Hot plate set to 100-120 ^oC
- Photolithography mask with desired features. CAD/Art is an excellent resource for inexpensive mylar masks with down to 10 μm feature size. Masks can also be cut from Rubylith film using a Graphtec computer controlled cutter or similar machine for fast prototyping where feature resolution is not the primary concern. For the protocols described here, the background should be clear to polymerize the background of the wafer and leave exposed only the channels and other features for electroplating.
- UV lamp on stand, commercial photolithography UV exposure system, or similar
- Nickel electroplating reagents, including nickel strike bath and commercial bright nickel plating bath as described in the previous chapter.
- Hot embossing machine or home-built setup as described in Chapter 3 and Appendix B.

4.3 Nickel mold microfabrication protocol

1. Prepare a steel wafer by removing protective films, washing with isopropyl alcohol and water, and drying with air or nitrogen. Preheat to on a hot plate to dry wafer and improve photoresist annealing. Immediately before next step, remove wafer from the hot plate.
2. Peel off the thicker, translucent protective film from Riston Goldmaster photoresist, and place photoresist on steel wafer, taking care to avoid trapping bubbles. A squeegee, such as the plastic one used to seal PCR plates, can be helpful.
3. Cut off any large pieces of excess resist. The photoresist is only slightly adhered to the wafer, so care is required.
4. Pass wafer with photoresist through the laminator. For high-density features, it is advisable to repeat lamination a total of 2-3x to improve adhesion.
5. Allow to cool and cut off all excess photoresist.
6. Expose photoresist to UV through mask to polymerize the exposed features. If using a commercial system, follow instructions for the specific machine. If using a UV lamp, best reproducibility is obtained by clamping the light source a fixed distance above a table and preheating the lamp. A UV lamp can allow a research group to quickly build up photolithography capability without any costly hardware, though there is a slight tradeoff in resolution. In all cases, it is necessary to optimize exposure empirically for the given UV system in use and the particular grade of Goldmaster film used. After exposure, the features should be slightly visible.

7. Remove thin, clear protective layer from exposed photoresist. Slightly better resolution can be obtained by removing the film prior to exposure, though the resist is quite tacky and can be problematic with mask removal.
8. Develop wafer in developer solution. For batch processing in dishes, it is best to place the wafer in the dish while agitating the solution. As the features are nearly fully developed (they begin to look silvery as the photoresist washes away), hold the wafer with wafer tongs and spray developer on the wafer to dislodge any remaining unexposed photoresist. A fully developed wafer should have clean, sharp features with the slight steel texture clearly visible.
9. Expose entire wafer to UV illumination for 2-5 min to fully polymerize photoresist. This step can be omitted for low resolution and low density features, but it dramatically improves photoresist adhesion during nickel plating particularly for high density features.
10. Perform a nickel strike in the Wood's strike bath described in Chapter 3 with optimal strike deposition being obtained at very low electroplating rates and longer times (3-5 min). The exposed features should now look a semi-matte gray with no shiny spots visible. The spots are indicative of bubble formation during the nickel strike that precludes strike deposition and eventually results in uneven nickel plating.
11. Wash wafer with distilled water and transfer to bright nickel electroplating bath for plating to the desired height.
    a. Alternatively, it is possible to overplate all features and then polish the wafer with increasing grades of sandpaper to the height of the photoresist. While this approach limits the user to a limited range of feature heights, the resulting features are highly uniform in height across the wafer while using only a DC power supply for electroplating. A pulsed power supply can improve electroplating uniformity and avoid the need for polishing.
    b. If polishing, a final bright nickel layer can be deposited following resist removal by performing a quick nickel strike followed by 1-2 min of bright nickel plating. This results in significantly improved optical properties of the features.
12. Following plating of features to the desired height, remove the photoresist by submerging wafer in the stripper solution for several minutes until the photoresist begins to warp and flake off. Agitation and scrubbing can aid in resist removal. The mold is now ready for hot embossing of microfluidic devices.

4.4 Nickel electrode fabrication via hot embossing

Fabrication of nickel electrodes enables rapid prototyping of electrical features in microdevices with the same speed and low equipment requirements of the previous protocol. The protocol modifications presented here are based on a photolithography approach, though the "sticker mask" approach presented in Chapter 3 works very well, albeit with the stated resolution limitations.

1. Prepare a steel wafer with dry film photoresist and perform UV exposure through a photolithography mask as described in section 4.3 steps 1-9.
2. Omit the nickel strike in step 10 and proceed directly to nickel plating in step 11. Electroplate the desired electrode thickness. Thin electrodes exhibit poor adhesion to plastic and must be coated with a thin polymer layer to prevent delamination, thus limiting their use to higher frequency measurements and other situations where the thin insulating layer can be bypassed. However, a protective polymer layer can make the nickel electrodes

biocompatible. Thicker electrodes, particularly those that have been overplated resulting in a mushrooming of the features, embed permanently in plastic devices and are well-suited for direct metal-fluid contact in microchannels. Thickness can be tailored to meet mechanical needs, as the nickel features could be used to produce springs and other mechanical components.

3. Remove the photoresist, taking care to avoid dislodging the nickel features.
4. Hot emboss the wafer in the desired thermoplastic polymer. The nickel features will delaminate from the steel wafer and embed in the plastic, flush with the surface. Higher heat and pressure improve nickel embedding.
5. The embedded electrodes can be bonded to a hot embossed microfluidic device using solvent-assisted bonding described in Chapter 3 or using any other protocol. As mentioned above, thin nickel electrodes should be spin-coated with thermoplastic prior to bonding. Dissolving the thermoplastic in a suitable solvent and spin coating to a final thickness of ~0.5-1 μm, determined empirically for the particular polymer-solvent solution, will prevent electrode delamination and provide environmental insulation.

Section conclusion

This section is the result of work arising from my desire to improve methods for building microfluidic devices for droplet generation and to rapidly prototype a range of designs without requiring access to uncommon equipment. Initial experience with droplet generation led to the increase of throughput with radial droplet generator arrays. In addition, the ability to select droplet generators to meet experimental throughput needs enabled efficient data collection without wasting reagents and time. The work also highlights robust digital PCR in stable emulsions, which is the foundation of the work presented in the following section.

The fabrication of microfluidic devices was modified to reflect the need to build and test numerous variations before settling on a particular design. The method initially published in *Lab on a Chip* and reprinted in Chapter 3 met the primary needs and allowed production of devices in as little as 1-3 h directly from a CAD design. Chapter 4 builds on that work by adapting the method to photolithographic approaches compatible with steel wafers, thereby improving the feature resolution and overall device quality for producing plastic microfluidics with commercially-relevant materials and processes. My discovery that metal electrodes could be fabricated using only a slightly modified protocol extends the acceleration of device development to electronic components in microfluidic devices.

The work presented in this section addresses several key issues faced in developing novel microfluidic droplet generators and other devices. Applications using many of the fabrication and assay innovations are described in the remainder of this thesis.

Section 2: Applications of microdroplets for single molecule detection and single cell DNA analysis

Section overview

DNA offers an attractive target for analysis at the single molecule and single cell level. It is relatively stable in solution, there are robust established amplification methods for single molecule detection without complex hardware, and, unlike RNA, DNA occurs at predictable frequencies in single cells (i.e., 1 or 2 gene copies per cell for all but a few genes and highly mutated cell types), facilitating straightforward assay characterization and optimization. DNA is also at the root of the Central Dogma and small modifications to DNA can result in vast changes across the transcriptome and proteome, more so than similarly subtle changes in a single protein's expression level. Examining the frequency of rare mutations as single molecules or the frequency of mutation co-occurrence in single cells opens the possibility for detailed investigations of cancer initiation, progression, and metastasis, while the capability to detect and analyze single cells is extremely useful for forensic identification of complex mixtures or miniscule amounts of tissue.

This section explores several applications of the microfluidic droplet generators and droplet PCR described in Section 1, particularly Chapter 2. Chapter 5 presents a study of the t(14;18) chromosomal translocation in healthy subjects, reprinted from work published in *Nucleic Acids Research*. This mutation is an early mutation involved in lymphoma, though detectable levels occur in healthy people and frequency is positively correlated with age. The work presents a method for accurately quantifying t(14;18) frequency in extracted Buffy coat DNA with a limit of detection below 10^{-7} mutations per genome. It is a demonstration of the extreme levels of sensitivity, precision, and accuracy possible with digital PCR detection. The method is extended to the analysis of mutations by sequencing the amplicons stemming from single mutant DNA molecules. The resulting sequence data are used to assemble a map of genome breakpoint sites and frequencies at chromosomes 14 and 18. Finally, the ability to "count" single molecules and subsequently sequence them enables the accurate determination of mutation variants within single subjects, which previously had not been possible.

Chapter 6 applies single molecule analysis to detecting two targets in whole cells, as published in *Angewandte Chemie, International Edition*. The primary innovation here lies in the incorporation of agarose as the dispersed phase, allowing single cells to be encapsulated in a rigid, yet porous, scaffold. This single cell DNA purification protocol enables thousands or millions of single cells to be transformed in parallel into single genomes with high quality and pure DNA without the unpredictable inhibition due to DNA-binding proteins and other intracellular molecules. The method also minimized the need for microfluidics; the purified genomes are incubated in PCR reagents, and droplets are reformed by shaking the agarose droplets in emulsion oil. A second microfluidic droplet generation step is not required, increasing throughput. The result of this work is the ability to screen millions of single cell genomes for co-occurrence of multiple genomic mutations.

Chapter 7 extends single cell DNA purification work to detecting 9 different targets in a highly multiplexed single cell PCR for forensic analysis, as described in our publication in *Analytical Chemistry*. Short tandem repeat (STR) profiles are obtained from single cells with very high yields and few PCR loci dropouts. In addition to being able to discern the forensic profiles of two contributing individuals at various ratios, the single cell analysis approach reduces the impact of contaminating DNA. Traditional bulk STR typing can be impacted by contaminating DNA, since the contaminant's profile will overlap with that of the real targets. Single cell analysis dramatically improves the resolvability of profiles by relying on a random distribution of

contaminating DNA, whereas the single cell profile remains constant. It is therefore possible to subtract peaks that do not occur regularly, leaving only the profile of interest even at relatively high contamination levels.

The applications described in this section provide an overview of the power of droplet-based techniques in DNA analysis. The tools developed in these works expand the capability of researchers to investigate cancer-related mutations in single cells, including deep analysis of circulating tumor cells, while single cell forensics will reduce the impact of crime scene contaminants and facilitate discrimination of profiles from highly complex tissue mixtures at crime scenes. DNA analysis using droplets is maturing into a robust platform technology with multiple commercial players. The applications demonstrated in this section are examples of what will become widely available in the future.

Chapter 5: Single molecule quantitation and sequencing of rare translocations using microfluidic nested digital PCR

Shuga, J., Zeng, Y., Novak, R., Lan, Q., Tang, X.,Rothman, N., Vermeulen, R., Li, L., Hubbard, A., Zhang, L., Mathies, R.A., Smith, M.T. Single Molecule Quantitation and Sequencing of Rare Mutations Using Microfluidic Nested Digital PCR. *Nucleic Acids Research*, 2013, 41(16):e159 by permission of Oxford University Press.

5.1 Abstract

Cancers are heterogeneous and genetically unstable. New methods are needed that provide the sensitivity and specificity to query single cells at the genetic loci that drive cancer progression, thereby enabling researchers to study the progression of individual tumors. Here we report the development and application of a bead-based, hemi-nested microfluidic droplet digital PCR (dPCR) technology to achieve *quantitative* measurement and single molecule sequencing of somatically acquired carcinogenic translocations at extremely low levels ($<10^{-6}$) in healthy subjects. We use this technique in our healthy study population to determine the overall concentration of the t(14;18) translocation, which is strongly associated with follicular lymphoma. The nested dPCR approach improves the detection limit to $1x10^{-7}$ or lower, which is one order of magnitude lower than that of the existing droplet-based dPCR methods, while maintaining the analysis efficiency and specificity. Further, the bead-based dPCR enabled us to isolate and quantify the relative amounts of the various clonal forms of t(14;18) translocation in these subjects, and the single molecule sensitivity and resolution of dPCR led to the discovery of new clonal forms of t(14;18) that were otherwise masked by the conventional qPCR measurements. In this manner we created a quantitative map for this carcinogenic mutation in this healthy population and identified the positions on chromosomes 14 and 18 where the vast majority of these t(14;18) events occur.

5.2 Introduction

Tumor-specific somatic mutations can provide highly useful molecular biomarkers and therapeutic targets for cancer diagnosis, prognosis, and treatment. Central to the use of these genetic biomarkers in clinical oncology is sensitive and quantitative measurement of rare mutations in a vast excess of wild-type alleles. For instance, discovering driver mutations that lead to carcinogenesis in a rare subset of cells is one key approach to the risk assessment, early detection and treatment of cancer.[200,201] Investigation of genetic variants in rare circulating tumor cells (CTCs) in metastatic cancer patients would help understand the biology of metastasis and development of drug resistance in chemotherapy.[6] Moreover, quantification of low-level mutated sequences in cancer patients during and after treatments can provide informative data for evaluating therapy efficacy, monitoring minimal residual diseases (MRD), and detecting disease relapse.[202]

In recent years, technical advances have enormously improved the capacity to analyze genetic variants, yielding novel methods for the detection of rare mutations.[203] For instance, quantitative polymerase chain reaction (qPCR), a widely used approach in genetic analysis, measures the analog fluorescence signal of targets and thus is limited in the detection sensitivity and/or quantification accuracy due to instrumental and experimental variation. An attractive alternative to this analog technique is digital PCR (dPCR) which providing a superior sensitivity to conventional qPCR by allowing absolute quantification of target molecules.[153,157,204,205] Here we report the development and application of a bead-based, hemi-nested microfluidic digital droplet PCR (simplified as nested dPCR hereafter) approach to achieve *quantitative* measurement of somatically acquired carcinogenic translocations at extremely low levels ($<10^{-6}$) in healthy subjects. This sensitive nested dPCR approach has an overall clinical sensitivity that is mainly limited by the amount of DNA that is available for screening.[206] In contrast to other dPCR methods using emulsion droplets,[204,205] our bead-based dPCR approach provides not only superior

quantification performance at extremely low levels, but also the capacity to sequence and quantify each mutated clone in a subject after millions of discrete single molecule reactions are conducted in parallel. Therefore this novel dPCR method can be used to measure the amounts of various clones within a subject or population over time and thus monitor for clonal expansion prior to clinical disease progression.

The model translocation that we chose for technology validation, the *BCL-2/IgH* translocation t(14;18), is highly prevalent in many blood cancers, including ~80% of follicular lymphoma (FL) cases and ~25% of large-cell B-cell lymphoma cases.[207,208] The translocation brings the *BCL2* (B Cell Lymphoma-2) gene from 18q21 under the control of the strong enhancers of the *IgH* locus, ultimately disrupting *BCL2*'s normal pattern of expression in B cells.[209,210] *BCL2* is an anti-apoptotic protein and its overexpression can be intimately involved in the pathogenesis of B cell neoplasms.[211] t(14;18) is found in a relatively small fraction of the peripheral blood mononuclear cells (PBMCs) of healthy individuals and may be a biomarker of early lymphoma.[212–214] The mutation concentration in healthy individuals is ~1000-fold lower than for individuals with stage III/IV FL[206] and it is believed that clonal expansion of atypical B cells is required for lymphoma progression.[212,214–216] t(14;18) prevalence at any level in healthy populations has been reported in the range of 8% to 88%, which reflects the differences both in the populations studied and in the techniques used to assay t(14;18).[213,217,218] Thus *highly sensitive and quantitative* detection of t(14;18) is essential for fully investigating the clinical value of t(14;18) for risk assessment and early diagnosis of lymphoma. Furthermore, clinical studies have observed clonal evolution of t(14;18) associated with disease progression in individual patients.[219] A high-throughput technique that can sequence and quantify multiple $t(14;18)^+$ clones could provide insight into the molecular pathology and clinical importance of t(14;18).[220,221]

Using the nested microfluidic dPCR method, we were able to quantitatively detect and sequence a single t(14;18) copy in 9 μg (~ $3x10^6$ copies) of clot gDNA from individuals in a healthy study population. We also applied nested dPCR to develop a quantitative genomic map of t(14;18) by sequencing and quantifying the unique t(14;18) clones found in individual subjects within this study population. The genomic map that we produced represents a baseline for this healthy population, and further sampling of this population can be used to monitor for expansion of particular clonal forms as part of disease progression.

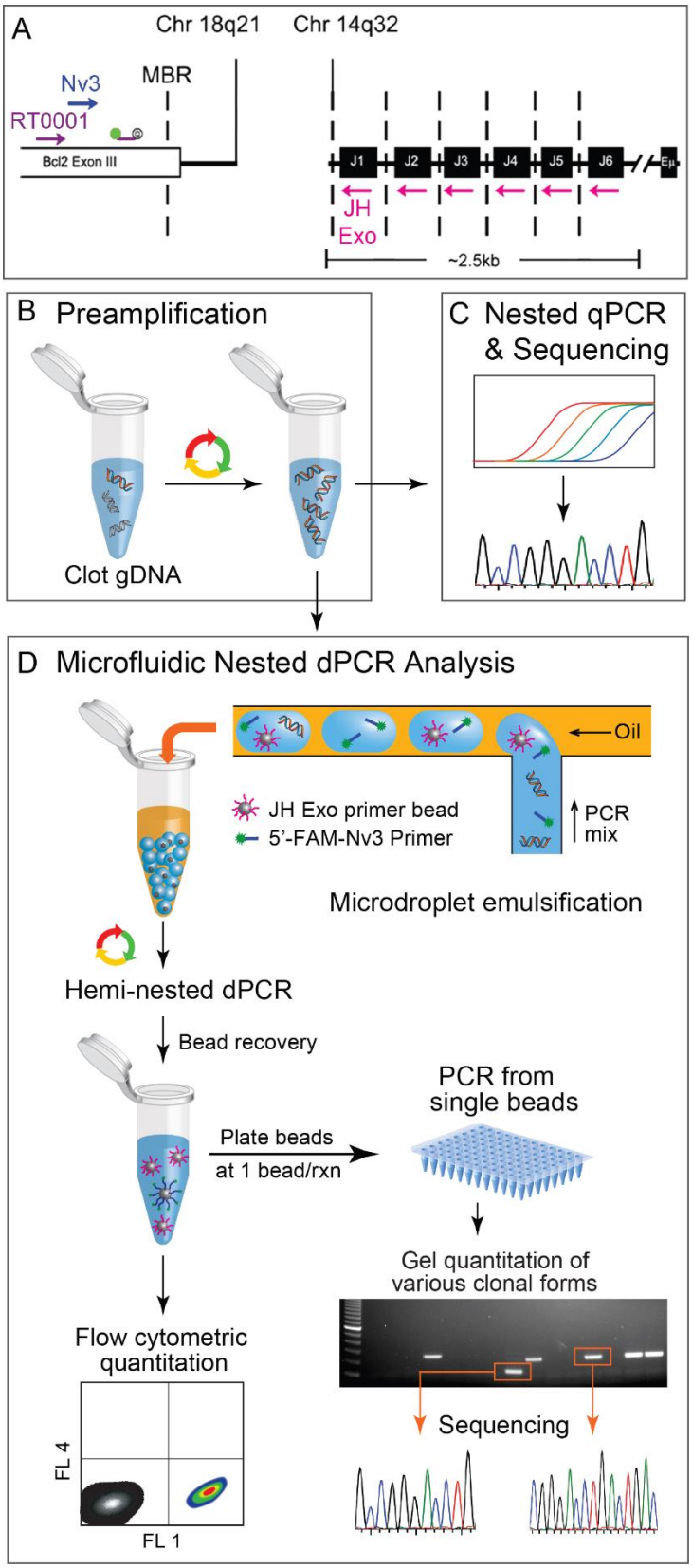
A
Chr 18q21
Chr 14q32
Nv3
MBR
RT0001
Bcl2 Exon III
J1
J2
J3
J4
J5
J6
JH
Exo
~2.5kb
B Preamplification
Clot gDNA
C Nested qPCR
& Sequencing
D Microfluidic Nested dPCR Analysis
Oil
JH Exo primer bead
5'-FAM-Nv3 Primer
PCR
mix
Microdroplet emulsification
Hemi-nested dPCR
Bead recovery
Plate beads
at 1 bead/rxn
PCR from
single beads
Gel quantitation of
various clonal forms
Sequencing
Flow cytometric
quantitation
FL 4
FL 1

Figure 5.1. Workflow and methodology for digital detection of t(14;18) in the clot gDNA of healthy subjects. (A) The PCR strategy for t(14;18) detection is illustrated by mapping the primers and probes used to their genomic targets. The first round of PCR were primed with the outer primer pair [consisting of an *IgHJ* consensus primer (JH Exo) and a *BCL*2-specific primer (RT0001)]. The hemi-nested secondary rounds of PCR were primed with a nested BCL2 primer (Nv3) while retaining the use of the IgHJ consensus primer (JH Exo). (B) A preamplification PCR (20 cycles) produced t(14;18) amplicon from 3 µg of clot gDNA. The product of this first amplification step was then used as template in secondary rounds of hemi-nested PCR. Two different types of quantitative PCR were conducted: (C) standard qPCR using a BCL2-specific fluorescent probe (see Appendix Fig. C2); and (D) microfluidic emulsion single molecule PCR using JH Exo-functionalized beads and 5'-FAM-labeled Nv3 for t(14;18) detection. A microfluidic emulsion generator array was used for high throughput ($>10^6$/hr) production of monodisperse reaction volumes. Following emulsion generation, the nL-scale reaction droplets were cycled to achieve single copy genetic analysis of the template. If a copy of t(14;18) and a bead were both present in a reaction droplet then the bead was labeled with fluorescent amplicon during PCR, otherwise beads remained unlabeled. Beads were then recovered and analyzed by flow cytometry to determine t(14;18) concentration within a sample. In addition, some of the beads were distributed at ~1 bead/well in 96-well plates in order to confirm that FAM+ concentration among beads corresponds with t(14;18)+ concentration as determined using a *BCL2*-specific probe. This tertiary round of amplification also produced sufficient template to conduct standard sequencing reactions that were derived from single molecule reactions.

5.3 Results

Digital Quantitation and Single Molecule Sequencing of t(14;18): Method Design and Performance. We found that our standard qPCR method was not sensitive enough to quantify and sequence t(14;18) from the clot gDNA of healthy subjects (Appendix Fig. C1), so we developed a nested PCR approach (Fig. 5.1A,C) for digital analysis of t(14;18). This approach starts with a preamplification (preamp) reaction (Fig. 1B) and the resultant target copies are then quantified and sequenced using both a conventional nested qPCR method and the microfluidic nested dPCR for direct comparison of their performance. The nested qPCR detection was conducted in 50 µL reaction volumes with a *BCL2*-specific cleavable probe sequence (Fig. 5.1C,D) to determine the threshold cycle (C_t) values (Fig. 5.1C and Appendix Fig. C2). The dPCR methodology uses our custom-built MEGA devices and a bead-based emulsion PCR assay[102] to achieve high-throughput digital quantitation and single molecule sequencing of t(14;18) (Fig. 5.1D). In this methodology 2.5-nL droplets serve as digital reaction volumes and droplets containing both single copies of t(14;18) and an IgH primer-functionalized bead yield clonal DNA beads labeled by FAM-labeled BCL2 primer after thermal cycling. A portion of the post-PCR beads are then analyzed by flow cytometry to quantify the target copies. Remaining beads are used as templates for further PCR amplification for single-molecule counting and sequencing of the genetic variants of the mutation (Fig. 5.1D).

Fig. 5.2 directly compares the detection performance of both nested assays using the standards of $t(14;18)^+$ gDNA spiked into wild-type human gDNA. The qPCR methodology had an efficiency of 93.8% and a linear dynamic range that spanned five $\log_{10}$ t(14;18) concentrations (Fig. 5.2A). Each 50 µL reaction had a quantitative limit of ~3.3×10^{-6} copies of t(14;18) per genome (one copy per µg of gDNA) with an ultimate limit of detection of ~10^{-6} copies of t(14;18) per genome (one copy in three µg of gDNA) (Fig. 5.2A). The microfluidic nested dPCR technique offered quantitative detection down to a concentration of ~10^{-6} copies t(14;18) per genome (one copy in three µg of gDNA) and the theoretical detection limit was determined to be 10^{-7} copies per genome as the experimental signal is well above the background noise (Fig. 5.2B). Further dilutions of the lowest concentration preamp standard were used to demonstrate quantitative detection down to equivalent concentrations near ~2×10^{-8} (Fig. 5.2B, inset), indicating the detection and quantitation limits of the microfluidic nested dPCR detection is constrained by the amount of DNA input (maximum of 3 µg) that can be used in the 50 µL preamp reactions.

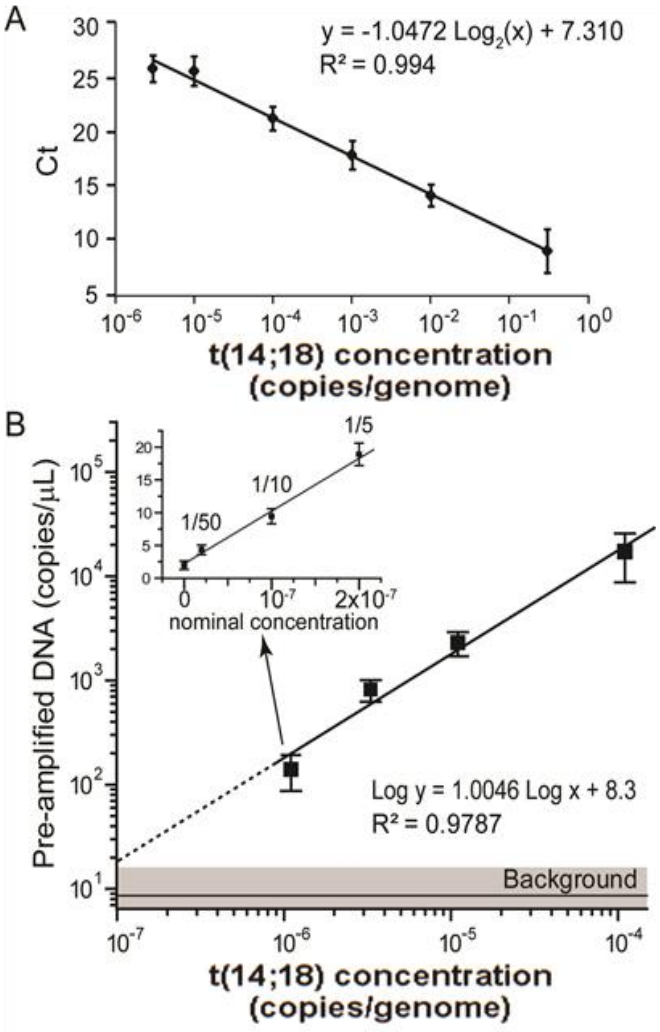

Figure 5.2. Characterization of hemi-nested real time PCR (qPCR) and microfluidic digital PCR (dPCR) assays for quantitation of the t(14;18) translocation. (A) The hemi-nested qPCR analysis of t(14;18) copies spiked in negative human genomic DNA shows a linear standard curve of the threshold cycle (Ct) as a function of the t(14;18) concentration (copies of t(14;18)/total genomic copies) with a dynamic range spanning 5 orders of magnitude and a limit of detection (LOD) near 10^{-6} copies t(14;18)/genome. The error bars represent standard deviation (n = 3). (B) The hemi-nested microfluidic dPCR assay quantitatively measures t(14;18) concentration with an LOD on the order of 10^{-7}. The error bars represent standard deviation ($n \geq 3$). The inset demonstrates quantitative measurements of further dilutions (down to 1/50) of the pre-amplified product from the lowest concentration standard (~10^{-6} copies t(14;18)/genome). The error bars indicate standard error.

Digital Detection and Quantification of t(14;18) in Occupationally Exposed Subjects. To validate the microfluidic dPCR method for digital analysis of rare t(14;18) mutations, we examined the clot gDNA samples of 93 healthy Chinese subjects, 42 of whom had been occupationally exposed to formaldehyde. All the samples were first characterized using the bulk nested qPCR method (Fig. 5.1B,C). Three aliquots of 3 µg gDNA from each subject were pre-amplified and assayed (Fig. 5.3A, circles under each subject indicate number of assays). Two samples from Subjects Q and X are included for internal quality control, giving six reactions for each of these subjects. We found that there were detectable levels of t(14;18) in 41 out of 93 (~44%) study subjects, as summarized in Fig. 5.3A. 32 of these $t(14;18)^+$ subjects show one or more negative reactions (indicated by the open circles in Fig. 5.3A), presumably due to the stochastic distribution of rare targets in the 3 µg gDNA aliquots. The overall concentration in these $t(14;18)^+$ subjects ranged from $\sim 7.7 \times 10^{-5}$ (~23 copies per µg) in Subject A down to $\sim 4 \times 10^{-7}$ (a single copy in a total of 9 µg gDNA assayed) in Subject OO. The median level of t(14;18) in the 41 positive study subjects was 2.23 copies per µg and the mean level of t(14;18) among the positive study subjects was 3.83 copies per µg (genomic concentrations of 7.4×10^{-6} and 1.3×10^{-5}, respectively). Furthermore, we used sequencing and sequence analysis to definitively confirm and fully define at least one clonal form in all 41 $t(14;18)^+$ study subjects, and to confirm that the forms of t(14;18) found in these subjects were unique and different from that found in the positive control CRL 2261 positive control cell line. In several subjects more than one unique clonal form was identified, and for these subjects the total number of t(14;18) clones identified is displayed above the bars for each subjects (Fig. 5.3A).

To assess the microfluidic nested dPCR technology for rare translocation detection and molecular profiling, we focused our studies on the subjects with extremely low concentration of t(14;18) and/or multiple clonal forms. We analyzed a total of 69 preamp reactions which consisted of 50 positive reactions and 10 negative reactions from 28 $t(14;18)^+$ subjects (circles marked with "e" in Fig. 5.3A) and 9 reactions randomly chosen from $t(14;18)^-$ subjects. The t(14;18) concentration results obtained by the nested microfluidic dPCR analysis agreed with those obtained by the standard qPCR. This parallel comparison also demonstrated the robust nature of both ultrasensitive assay variants. There was not a single instance of disagreement between the two methods for determination of positive/negative preamp reactions. We assayed 10 negative preamp reactions from 7 positive subjects at the low end of t(14;18) concentration as determined by qPCR. All the nested dPCR assays yielded consistently negative results, a finding that strongly suggests true negatives given the sensitivity of the methods used. Only one of the three preamp reactions from many of the subjects contained t(14;18), and the single positive qPCR trial for some subjects (e.g. subject OO with a C_t value of 28.8), corresponded to ~1 copy in 3 µg gDNA, which suggests digital t(14;18) detection in the single positive assay reaction for these subjects. These observations demonstrate the ability of these nested methodologies to detect a single copy of t(14;18) in 9 µg of gDNA (relative genomic concentration of $\sim 4 \times 10^{-7}$). Thus, the overall clinical sensitivity of this method, like other ultrasensitive techniques that achieve mutation detection at the single copy level, is limited mainly by the amount of gDNA available for screening.[113,206]

The scatter plot of the nested dPCR measurements of the preamp reactions (Fig. 5.3B) shows that the positive population is distinctly separated from the negatives which represent an extremely low background (below genomic concentration of 10^{-7}). Such detection performance and background level are consistent with those obtained using the gDNA standards. The measured concentration of some positive reactions were lower than the lowest concentration possible in our assays using 3 µg gDNA (1×10^{-6}), which we found is largely attributed to the degradation of

DNA caused by the freeze-thaw of the preamp samples. Regression of the parallel measurements from the $t(14;18)^+$ preamp reactions showed good correlation between the microfluidic nested dPCR and the standard nested qPCR ($R^2 \sim 0.75$, Fig. 5.3C). Overall, these observations confirm that our nested dPCR methodology is ultrasensitive and capable of quantifying rare mutations at concentrations of 10^{-6} and lower.

In addition, the same clonal form(s) of t(14;18) were identified using both nested techniques for all positive preamp reactions, except that an additional form of t(14;18) was discovered by microfluidic nested dPCR for two subjects (J and Q, note asterisks in Fig. 5.3A). This discovery demonstrates a key advantage of dPCR: single molecule analysis allows each clonal form to be amplified, detected, and quantified without competition from other clonal forms; whereas a high concentration clonal form can mask the presence of a less concentrated clone in bulk analysis. Beyond the discovery of novel, low-frequency clones, the dPCR technique can also be used to discretely amplify similarly sized clones that are contained within a single sample, and thus allow these distinct clonal forms to be resolved (see discussion of subjects H and HH in the next Results section). The results from single molecule quantification and sequencing are detailed below.

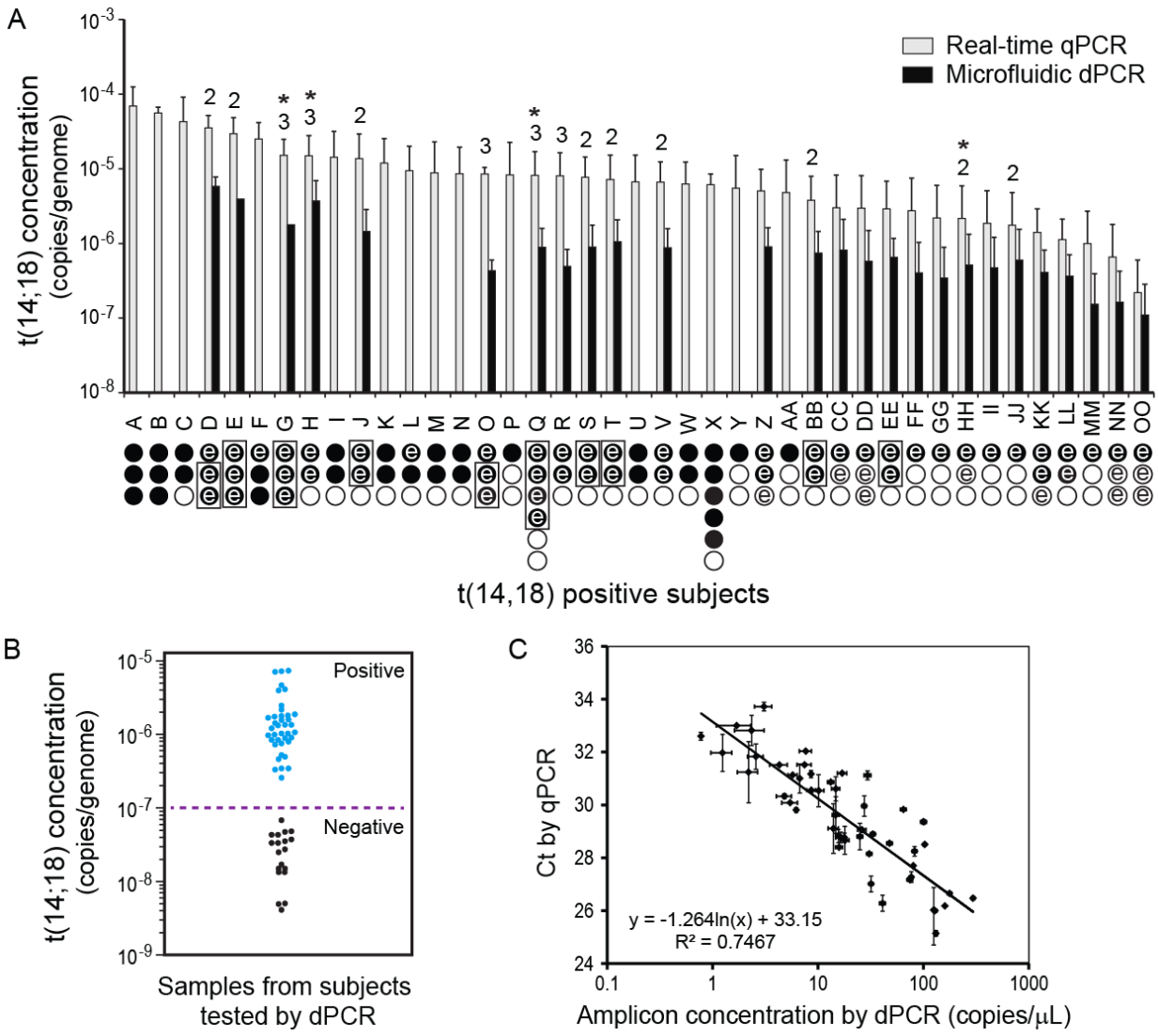

Figure 5.3. Concentration of t(14;18) in positive study subjects. We detected t(14;18) in the clot gDNA of 41/93 healthy test subjects (~44% prevalence). (A) Subject IDs are given on the abscissa and the bar-height indicates the average concentration of t(14;18) in a given subject as determined by the hemi-nested PCR techniques. The error bars indicate the standard deviation in the measurement. Below the subject ID on the abscissa, the number of 3 µg preamplification (preamp) reactions conducted on the subject's gDNA is indicated by the total number of circles. Filled circles indicate that a preamp reaction was positive by standard qPCR, while open circles indicate that the preamp reaction was found negative by standard qPCR. If an assay circle is marked with the letter "e," that preamp reaction was also tested using microfluidic PCR and in these cases the quantitative result from dPCR is also given. A box grouping preamp reactions indicates that these reactions were pooled before dPCR analysis. The data from these parallel measurements (when positive) contributed data to part C of this figure. For all positive subjects, at least one clonal form of t(14;18) was confirmed by sequence analysis; and in some subjects, multiple clonal forms of t(14;18) were defined. If multiple clonal forms were found in a subject, the total number of defined clones is

indicated above the error bars. An asterisk indicates that one clonal form for that subject went undetected in qPCR and was then discovered and/or defined in dPCR. (B) The dot scattered plot of the nested dPCR measurements of the preamp reactions showing the distinct populations for the t(14;18) positive and negative subjects. The dashed line indicates the detection limit of 10^{-7} determined in Fig. 2. (C) The two methods represented in Fig. 1c and Fig. 1d correlate well for quantitating t(14;18) both in cell line-derived DNA standards and in clot DNA samples from chemically-exposed workers. The horizontal error bars are standard error and the vertical error bars are standard deviation (n = 2).

Single Molecule Sequencing to Define and Quantify t(14;18) Clones. To fully define the various t(14;18) clones and to definitively confirm positive assay reactions, we purified various clonal forms of t(14;18) by size using agarose gel electrophoresis and then extracted the amplicons for sequencing reactions. When multiple clones are present in the same preamp reaction, the standard "bulk" nested qPCR technique yields multiple bands in the same lane and it is impossible to estimate the relative ratio of clonal forms. However, when the same preamp reaction is analyzed using the microfluidic nested dPCR technique each positive reaction droplet amplifies a single molecule of t(14;18) amplicon (Fig. 5.4 and Appendix Fig. C3). The gel and sequencing data from single molecule derived sequencing reactions can then be used to estimate the relative concentration of each clonal form in a preamp reaction. Following the nested dPCR from one particular preamp reaction conducted on subject D, flow cytometry revealed that the resulting primer beads were 27.8% positive for t(14;18) (Appendix Fig. C3A). A representative section (19/96 wells) from a plate of single molecule sequencing reactions (~1 bead/reaction on average) is displayed in Fig. 4 and reveals close agreement in the concentration of beads that are $t(14;18)^+$ (6/19 [~31.6%] vs. 27.8%). Further, this section of the plate estimates the relative ratio of clone 1: clone 2 as 1:5 (Figure 5.4). More single-bead reactions from two 96-well plates were considered and provided a better quantitative agreement with cytometry (53/192 [~27.6%] vs. 838/3017 [27.8%]) and a more accurate estimate of the ratio of clone 1: clone 2 as 18:37 (Appendix Fig. C3B). The overall C_t from qPCR for this preamp reaction was 22.15, corresponding to ~18 copies per µg or a genomic concentration of $\sim 6 \times 10^{-5}$ copies per genome. When the data from both methods are considered we can estimate that clone 1 is present at a concentration of $\sim 2 \times 10^{-5}$ copies per genome and that clone 2 is present at a concentration of $\sim 4 \times 10^{-5}$ copies per genome. This analysis demonstrates the key strength of single molecule analysis via dPCR: each clonal form can be uniquely quantified and tracked. We used this approach to develop a quantitative map of the t(14;18) landscape in our healthy Chinese study population (see next Results section).

Another advantage of dPCR is that the technique can be used to resolve similarly sized clones carried by a subject. Subjects H and HH carried similarly sized clones, and the conventional bulk qPCR approach was unable to resolve the clonal forms present in preamp reactions. In these cases, the various clones of t(14;18) that were concurrent in preamp reactions were similar in size and were not adequately separated on gel prior to purification for sequencing reactions. Subsequent sequencing reactions yielded reads with consensus near the Nv3 sequencing primer but with mixed traces as the clonal forms diverged (Appendix Figures C4A and C5A for Subjects H and HH, respectively). Therefore, we used the microfluidic nested dPCR method to discretely package the various clonal forms of t(14;18) prior to nested amplification and we then used a tertiary round of PCR to produce sufficient amplicon for sequencing. In both cases, dPCR and single molecule derived sequencing allowed us to purify and define the similarly sized clones of t(14;18) that were present in a particular preamp reaction (Appendix Figures C4B,C and C5B,C).

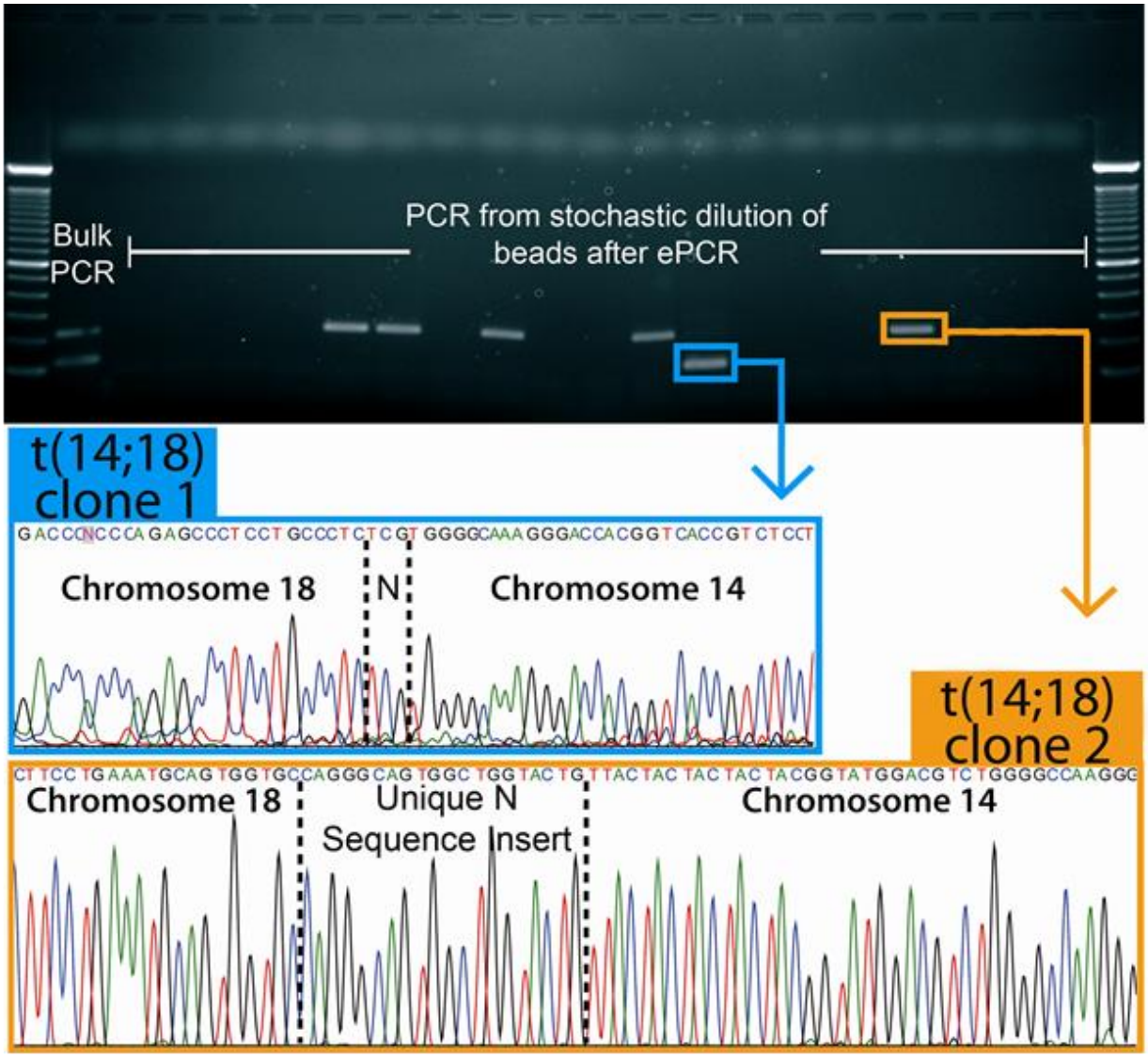

Figure 5.4. Definition and quantitation of clonal forms within subject samples. Representative results for the gel and sequence analysis of a single subject ("D") who was found to be positive for two unique clonal forms of t(14;18). The gel bands were excised for sequencing reactions and sequence analysis defined the clonal forms of t(14;18) present in the sample. In bulk assays, both clonal forms amplify together, and it is not possible to estimate their relative concentration. However, in digital microfluidic dPCR the different clonal forms are discretely encapsulated in nL-scale reaction droplets along with primer-functionalized beads. The resulting digital reactions load individual beads with amplicon that represents only a single form of the translocation. By simply counting the number of "large" and "small" bands or sequence reads, the relative ratio of clonal forms within a sample can be estimated. In this gel section, the ratio of clone 1:clone 2 is 1:5, but gel analysis of more reactions from this subject estimates the ratio as approximately 18:37 (see Appendix Fig. C3B).

Quantitative Genomic Mapping of t(14;18) Breakpoints. We defined all of the clonal forms present in positive assay reactions and found that most positive subjects carried a single unique t(14;18) clone, although nine subjects carried two unique clonal forms and five subjects carried three unique clonal forms. We used the dPCR method to resolve each t(14;18) clone in subjects carrying multiple clonal forms, and thus were able to quantify the relative amount of each clonal form. These relative ratios were then scaled by the results from conventional qPCR, which can only measure the total amounts of t(14;18) within a subject, to quantify all 60 clonal forms that were defined in this study. A quantitative genomic map of the chromosome 14 and chromosome 18 breakpoints for the 60 t(14;18) clones identified in this healthy Chinese population shows typical breakpoint clustering along both chromosomes for this translocation (Figure 5.5).

The chromosome 14 breakpoints were always found on the heptamer side of V(D)J recombination signal sequences (RSSs), with most chromosome 14 breakpoints occurring near the J4, J5 or J6 RSS (Fig. 5.5, Appendix Fig. C6, Appendix Table C1). This clustering on chromosome 14 is consistent with the theory that errors in V(D)J recombination are responsible for t(14;18) formation.[219,222] We found that t(14;18) breakpoints in the BCL-2 major breakpoint region (MBR) on chromosome 18 cluster around positions 3520, 3571, and 3629 on NM_000633.2, consistent with prior reports on FL cases and healthy individuals.[213,223] This quantitative genomic map of t(14;18) breakpoints represents a baseline mutational landscape in these study subjects, and a time-course of such measurements could reveal clonal expansion on the path to lymphoma. For complete details for all t(14;18) clones, including the *de novo* "N sequence" inserts, please see Appendix Table C1.

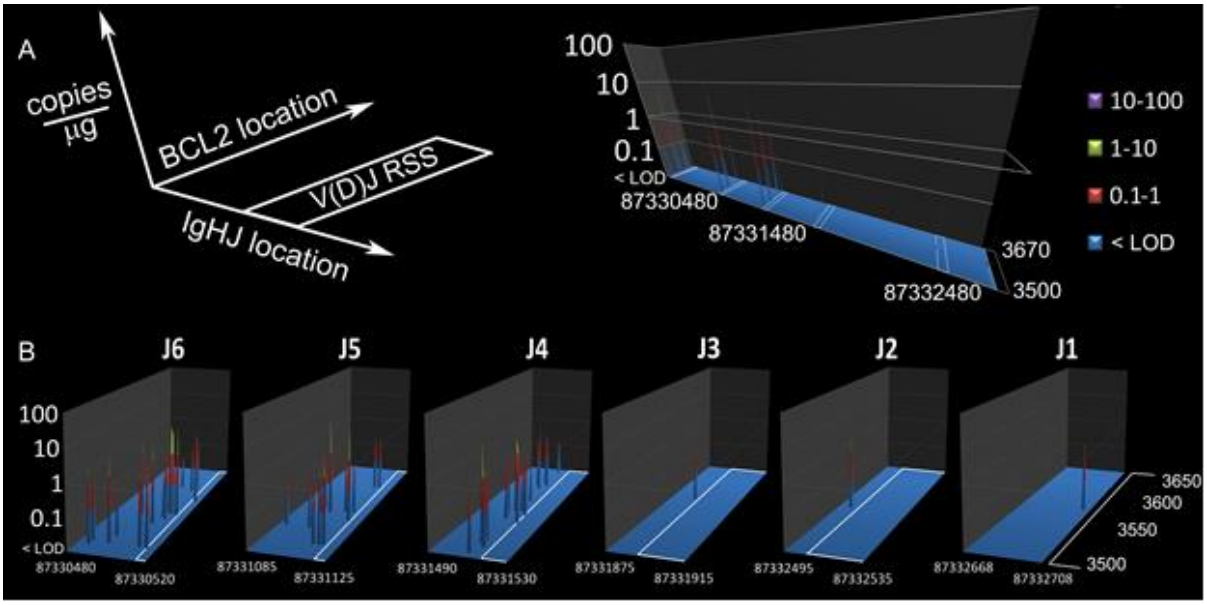

Figure 5.5. Quantitative genetic profile of t(14;18) breakpoints in positive study subjects. The clonal form of t(14;18) defined in this study are quantitatively mapped to their breakpoint coordinates on Chromosomes 14 (position on NT_026437.11) and Chromosomes 18 (position on NM_000633.2). Most positive subjects (27/41) were positive for a single, unique form of t(14;18); however, 9/41 positive subjects were confirmed to be positive for 2 unique clonal forms, and 5/41 were confirmed to be positive for 3 unique clonal forms (also see Fig. 3 and Appendix Tbl. C1). (A) The amount and coordinates of these 60 clonal forms of t(14;18) are mapped to a global genetic plot. The white boxes on the plot indicate the locations of the IgHJ recombination signal sequences (RSSs) that direct V(D)J recombination. (B) A magnified view of each t(14;18) cluster is shown; all clusters were found on the heptamer side of an IgHJ RSS. For details of sequence analysis results on these clonal forms see Appendix Tbl. C1. For details regarding the mapping of the IgHJ RSSs to NT_026437.11, see Appendix Fig. C6.

5.4 Discussion

Droplet-based digital PCR provides a powerful tool for sensitive genetic analysis and has been reported for quantitative detection of point mutations with detection limits of 1 mutant allele in 10^4-10^5 wild type copies.[204,205,224] Here we demonstrated a nested microfluidic dPCR that enables highly sensitive and quantitative detection of rare somatic translocation targets in a vast wild type DNA background. The hemi-nested primer design reduces non-specific PCR amplification; however, we found that significant improvement in sensitivity is mainly conferred by using preamp reactions to increase the amount of target sequence relative to the overall concentration of gDNA used in the dPCR assay, and thus decrease the interference from excessive background. We tested gDNA NTCs (preamp of 3 µg of purely t(14,18)$^-$ gDNA) in dPCR and found that the percentage of false FAM$^+$ beads was strongly dependent on the average concentration of gDNA in droplets. Excessive background (>0.1% false FAM$^+$ beads) was observed when averaged concentrations were greater than 0.1 genomic copies per droplets (~100 pg/µL), due to non-specific amplification of concentrated background gDNA in 2.5 nL droplets. Therefore it is necessary to operate at 0.01-0.1 copies per droplet to achieve highly sensitive detection. This operational limit results in a large dead volume during droplet generation and lowers the effective throughput of the dPCR assay when used to assay target mutations directly. Preamp of the low concentration standards allows us to use diluted gDNA concentration in dPCR, which enable quantitative detection down to concentrations of $1x10^{-7}$ or even lower (Fig. 5.2B and inset) while maintaining the analysis efficiency.

The microfluidic approach described here has digital detection capability for highly quantitative measurement of low-level t(14;18) mutations with single molecule sensitivity and resolution. Conventional qPCR assays developed here and by other researchers also conferred single molecule sensitivity to detect t(14;18) at 10^{-5}-10^{-7} levels, depending on the amount of gDNA screened.[206,212,215,216,225–229] However, these analog measurements remained semi-quantitative, especially at the low concentration range (e.g. $<10^{-5}$ in Fig. 5.2A). Another distinct advantage that the dPCR method offers over analog qPCR assays is that it enables high-throughput, targeted single molecule sequencing and allows various t(14;18) clones to be resolved and quantified individually (Figs 5.4 and 5.5). We demonstrated that the microfluidic nested dPCR method provides single-molecule resolution and enables identification, quantitation, and genomic mapping of unique t(14;18) clonal forms that are unresolvable using the conventional nested qPCR approach (see data for subjects G, Q, H, and HH in Fig 5.3A, Appendix Table C1, and Supplementary Figures 5.4 and 5.5). This technology thus could provide a powerful tool for investigating the clonal evolution of cancer at the single copy level. Clinical studies have identified clonal evolution of t(14;18) in individual patients in response to disease progression.[218] A high-throughput technique with the capability to sequence and quantify multiple t(14;18)$^+$ clones could provide insights into the molecular pathology and clinical implication of t(14;18).[220,221] It could also be used to detect rare cancer stem cells in a large background of normal tissue. In fact, we may have identified t(14;18)$^+$ lymphoma stem cells in this study population, but only continued monitoring in a large prospective study can reveal whether particular t(14;18)$^+$ clones expand and give rise to lymphoma. In addition, in a previous report we have demonstrated that this bead-based dPCR technology can be adapted for multiplexed detection of multiple mutations in single cells, which can provide even deeper insight into disease progression.[71]

Furthermore, we demonstrated that our nested PCR assays for t(14;18) can be used directly on gDNA from whole blood or clot, a biological specimen that is easily collected in population-based studies. With few exceptions, researchers assay for t(14;18) in hematopoietic cell subpopulations that are enriched for B cells. We found significant differences in the t(14;18) qPCR signal provided by donor-matched PBMCs, buffy coat, and clot, with clot gDNA containing the lowest t(14;18) concentrations (Appendix Fig. C1). However, collection strategies in field-based studies of healthy populations often cannot accommodate immediate blood fractionation, and a high sensitivity and throughput t(14;18) assay using clot gDNA of healthy individuals, such as the method described here, would be useful in large prospective cohort studies.

To our knowledge, this is the first time that a highly sensitive t(14;18) assay has been applied to a healthy Chinese population; though our group previously applied a less sensitive assay to PBMC DNA in a smaller Chinese population.[230] This is also the first study to apply microfluidic dPCR to monitor somatic cancer mutations in occupationally exposed human subjects. Through the use of the new microfluidic nested dPCR technology, we detected, sequenced, and quantified 60 t(14;18) clones found in 41 of 93 (~44%) healthy Chinese subjects. Our quantitative genomic mapping of these t(14;18) clones revealed clustering within the MBR region of *BCL2* and within the *IgHJ* locus of chromosome 14, and the clustering we observed is consistent with previous reports. Specifically, we observed clustering within the MBR centered around positions 3520, 3571, and 3629 and mainly involving the J4, J5, and J6 RSSs on the *IgHJ* locus- positions that are essentially identical to those identified in prior reports in Western and North American populations.[213,223,231]

The t(14;18) translocation is thought to be an initiating event in FL, and additional mutations after t(14;18) can be associated with various outcome measures.[213,220] A study that used competitive genomic hybridization (CGH) in biopsies from $t(14;18)^+$ FL cases showed that gain of chromosome X in males and gains involving chromosomes 2, 3q and 5 were among copy number alterations associated with poor outcome.[232] Gene disruptions that are frequently associated with adverse outcome in FL cases include *TNFRSF14* on 1p36 along with *FAS* and *TP53* on 10q and 17p, respectively.[233] A cytogenetic study of $t(14;18)^+$ FL biopsies found that del(6q), +5, +19, and +20 were associated with poorer overall survival, and that del(17p) was associated with poorer event-free survival.[221] While cytogenetics and FISH offer information about mutation concurrence in single cells, these methods are laborious, low-throughput, and do not provide sequence information. Most other modern methods use homogenized samples, and there is no opportunity to achieve large-scale studies of mutation concurrence and synergy during disease progression at the single cell level-where carcinogenesis ultimately occurs.

The dPCR and single molecule sequencing technology established here provides a promising platform for developing new approaches for high-throughput single cells analysis of the concurrence of multiple mutations. Based on this digital microfluidic platform, we recently developed a methodology for high-throughput purification of single cell genomes and multiple-allele sequencing of single cells.[71] Currently, the throughput of our single molecule/cell sequencing procedure is limited by the use of second-round PCR to amplify the bead-bound DNA for the standard Sanger sequencing. However, it is feasible to adapt our bead-based dPCR method to next-generation sequencing technologies for direct, massively parallel sequencing off the post-PCR beads, thus providing unprecedented throughput in single cell genetic analysis. We hope to soon extend this microfluidic single cell analysis technology to an expanded set of genetic markers

of lymphoma and conduct multiple allele sequencing of these regions at the single cell level in lymphoma biopsies. With these further developments, we will add additional dimensions to the mutational landscape developed here so that we can begin to study FL progression at the level of individual cancer stem cells.

5.5 Acknowledgements

We would like to thank Jimmy Duong, Lindy Jiang, Paul Shiu and Joe Thompson for technical assistance.

5.6 Funding

This work was supported by the trans-National Institutes of Health Genes, Environment and Health Initiative, Biological Response Indicators of Environmental Systems Center Grant to MTS and RAM [U54 ES016115-01], and by National Institute of Environmental Health Sciences Superfund Basic Research Program Grant to MTS [P42 ES004705]. JS was supported by the Canary Foundation and ACS Postdoctoral Fellowship Award in Early Detection [116373-PFTED-08-251-01-SIED] from the American Cancer Society. YZ was partially supported by the new faculty start-up funds from the University of Kansas. RN was supported by a National Science Foundation Graduate Research Fellowship. Funding for open access charge: National Institutes of Health [U54 ES016115-01].

Chapter 6: Single cell multiplex gene detection and sequencing using microfluidically-generated agarose emulsions

6.1 Introduction

Genetic assays, such as polymerase chain reaction (PCR), typically report on multiple cells or mixtures of genomic DNA. As a result, they cannot properly characterize the genetic heterogeneity of a cell population or detect the co-occurrence of different mutations within a single cell, which are key to understanding the development, progression, and treatment of cancers.[221,234] In particular, since initial mutagenesis occurs inherently at the single-cell level, the detection and characterization of carcinogenesis will be dramatically facilitated by analytical techniques with single cell resolution.

Cytometric sorting, limiting dilution, and micromanipulation have been previously used to perform single-cell PCR assays in 96-well PCR plates, but these approaches are not ideal for large-scale screening applications.[113] Microfluidic technology offers fundamentally new capabilities for manipulating fluids, molecules, and cells that are very pertinent for developing high-throughput single-cell analysis methods.[102,144,235,236] Microfluidic droplet technology is particularly advantageous for single-cell/molecule analysis by allowing rapid statistical compartmentalization of targets for massively parallel pico- to nanoliter scale assays.[101,107,129] In particular, microfluidicalemulsion PCR (ePCR) enables high-fidelity digital single-molecule counting due to its unique ability to ensure equal population sampling and amplification efficiencies across all reaction compartments.[102,135,161]

To date most single cell genomic analysis have been reported on bacterial samples.[118,237,238] For mammalian cells, droplet-based genetic analyses have predominantly implemented reverse transcriptase PCR for phenotypic profiling.[130,161] A difficulty in single cell PCR is the persistent technical challenge of integrating a robust and scalable DNA extraction method.[237,238] The relative lack of suitable single-cell genomic analysis technologies combined with the significant genetic heterogeneity associated with cancer, underscores the importance of developing new microdroplet methodologies that integrate robust single-cell genome preparation with multiplex PCR.

To address these challenges, we have developed an agarose droplet-based platform that leverages emulsion generator array technology for high-throughput single cell genetic analysis.[102,135] Single cells were microfluidically encapsulated together with primer-functionalized beads in agarose gel droplets for subsequent SDS lysis and proteinase K digestion to release genomic DNA. Using the co-encapsulated primer beads and purified genomes, we demonstrate multi-locus single-cell sequencing of the control gene β-actin and across the chromosomal translocation t(14;18), a mutation associated with 85-90% of follicular lymphoma cases.[221,230] The coupling of our robust and high-throughput single cell DNA purification method with sequencing of multiple gene targets within single cells will enable detailed studies of mutation co-occurrence and synergy during carcinogenesis.

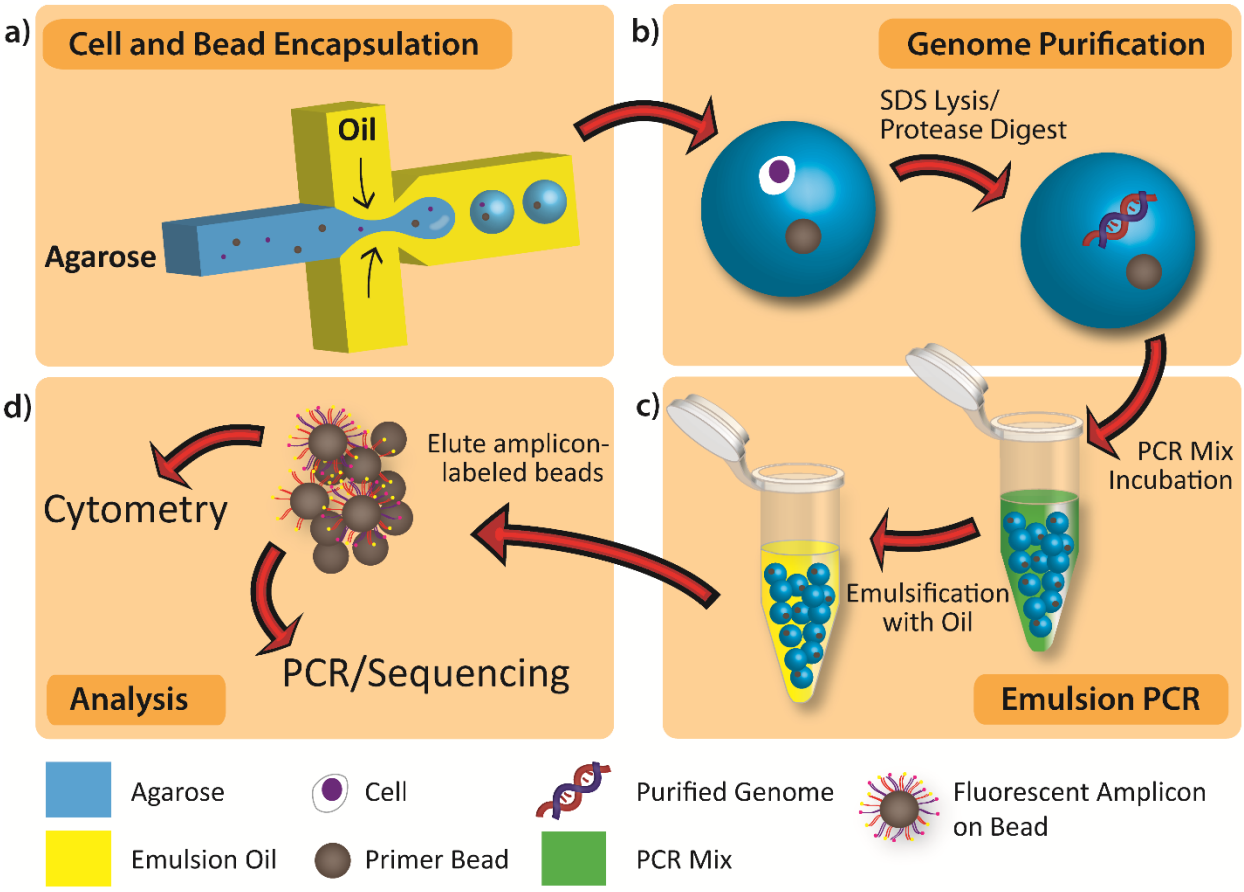

Figure 6.1. Workflow diagram demonstrating the use of agarose emulsion droplets for genetic analysis and multi-locus sequencing of single mammalian cells. (A) Schematic of the 4-layer glass-PDMS microfluidic emulsion generator array used for agarose droplet formation. A 3-valve micropump actuates an agarose-cell-bead suspension from the sample inlet toward cross-channel nozzles where droplet generation occurs. (B) The genomes of single cells are released in the gelled droplets using a standard SDS lysis/proteinase K digestion protocol. (C) The agarose droplets are equilibrated in PCR buffer containing fluorescent forward primers, emulsified with oil by mechanical agitation, and thermally cycled. (D) Following multiplex PCR amplification, primer beads are released by breaking the emulsion and melting the agarose. The fluorescent beads are then rapidly quantified using flow cytometry or further PCR-amplified for sequencing of target genes.

6.2 Results and discussion

The underlying principle of our highly parallel cell digestion and DNA purification method is the microfluidic encapsulation of cells in agarose droplets (Figure 6.1) to maintain single genome fidelity during cell lysis and DNA purification as well as efficient multiplex emulsion PCR target amplification for subsequent analysis. Single lymphoblast cells were encapsulated along with primer-functionalized beads in 1.5% low-melt point agarose using a four-channel microfluidic emulsion generator array (MEGA) (Figure 6.2A).[102] Micropump actuation was optimized to account for the increased viscosity of agarose without modifications of the microfluidic design, demonstrating the versatility of the MEGA platform. Droplet generation at ~40 ^{o}C for 30 min resulted in the encapsulation of approximately 18,000 cells at up to 0.3 cells per droplet (cpd) on average. Figure 6.2B shows the generation of uniform 3-nL agarose droplets containing primer-functionalized beads. The inset highlights an example of cell and bead co-encapsulation in a single droplet.

Agarose droplet encapsulation enables reproducible single-cell DNA extraction and isolation by allowing us to adapt robust DNA purification protocols. An example of this process is depicted in Figure 6.2C, where a bead and a cell were co-encapsulated in one agarose droplet. DNA release was accomplished by overnight incubation of the gel droplets in SDS lysis buffer and proteinase K to lyse the cell and digest DNA-binding histone proteins. The void left by the cell in the agarose is occupied by brightly-fluorescent genomic DNA that exhibits minimal diffusion into the surrounding gel (Figure 6.2D), due to the relatively small pore size of 1.5% agarose (~130 nm).[239]. An incubation temperature of 52^{o}C facilitated enzymatic protein digestion while preserving the integrity of agarose droplets. By staining with propidium iodide, we were able to visualize single high-molecular weight DNA strands protruding from the relatively small agarose droplets (Figure D1D) indicating that the majority of nuclear proteins were removed by the combination of proteinase K and SDS. The agarose droplets were stable for at least one week when stored in ethanol at 4^{o}C as determined by confocal imaging of DNA diffusion radii.

A key benefit of agarose encapsulation is the ability to perform mechanical manipulation of the isolated genomic DNA without mixing the genetic contents of different cells. Agarose droplets equilibrated with PCR mix were re-emulsified by mechanically agitating in dispersing oil to produce uniform nanoliter droplet "reactors" for massively parallel single cell PCR analysis. Excess PCR mix produces microfines (emulsions < 1 μm diameter) that enhance emulsion stability during thermal cycling.[154] The agarose droplets melt during the hot start phase of PCR and remain liquid throughout the amplification process, maximizing reagent and amplicon diffusion rates. We varied the initial heating rate and tested various concentrations of Triton X-100 as well as combinations of Abil em90 and Span 80 detergents in oil. A slow temperature ramp profile (0.1 ^{o}C s^{-1}) resulted in improved short-term stability, while the addition of 4 mg mL^{-1} BSA in PCR mix and 0.8% Triton X-100 in emulsion oil minimized droplet merger over the course of PCR thermal cycling (Figure 6.2E). Fluorescently-labeled amplicons bound to the primer-functionalized beads could be seen inside the agarose droplets following PCR (Figure 6.2F). The 34 μm crosslinked beads were selected due to their ability to amplify targets exceeding 1 kb in amounts of at least 100 amol per bead.[135] Beads in droplets without genomes did not fluoresce, indicating the absence of transfer of genomic targets among agarose droplets.

To demonstrate highly parallel genotyping with single cell resolution, we performed a multiplex PCR assay of cancer cells harboring the t(14;18) translocation at various mutant (RL)-to-wild type (TK6) cell ratios. The Cy5-labeled control gene product, β-actin, enabled quantification of total cell frequency, while the FAM-labeled translocation t(14;18) product, spanning the bcl-2 and IgH genes across their breakpoint regions, determined mutation frequency. A representative flow cytometric profile of beads following multiplex PCR amplification obtained with 50% RL cells at an average cell frequency of 0.3 cpd (Figure 6.3A) demonstrated distinct populations of negative, Cy5-labeled β-actin only positive, and FAM-labeled t(14;18) and Cy5-labeled β-actin double positive beads. Beads containing t(14;18) only were never seen, further indicating the conservation of single-genome integrity during cell lysis or PCR. By maintaining a constant total cell density (0.1 to 0.3 cells per droplet on average) and varying the relative concentrations of mutant RL and wild-type TK6 cells, we generated a standard curve (Figure 6.3B) to confirm that amplification originated from single cells. Linearity ($r = 0.993$) in the 0% to 100% RL cell frequency range tested indicated successful single-cell genetic analysis in the stochastic concentration regime. Importantly, in the subset of samples tested, the ratio of the frequency of total amplicon-positive beads to the observed cell encapsulation frequency indicated high PCR efficiency (113 % ± 24).

Single-cell sequencing of both target gene loci was accomplished by reamplifying the template bound to single beads diluted to the stochastic limit in a standard 96-well plate and separating products from individual wells using gel electrophoresis. Gel analysis further confirmed amplification from single genomes, and frequencies of β-actin single positive to double positive events matched flow cytometry frequency results in the samples tested. Fluorescence-based sorting can be applied to amplicon-labeled beads to sequence only populations of interest and thereby increase efficiency. Size-separated products from single beads were excised from the gel for sequencing. Figure 4 demonstrated recovery of the expected t(14;18) and β-actin sequences (see also Figure D2 and D3). The random nucleotide insertion sequence in t(14;18) matched the unique translocation "fingerprint" determined by sequencing of RL cells in bulk.[230]

The reamplification step enables integration of single cell PCR with standard molecular biology techniques to achieve sequencing of multiple genetic loci in individual cells at a rate required for meaningful population analysis. Using the single bead reamplification and size separation approach, it is possible to sequence multiple target genes from hundreds of single cells in a single experiment and to obtain meaningful statistical analysis of gene sequence variation in a cell population. Furthermore, the number of target loci per cell is limited only by the ability to excise individual bands from a gel, provided the multiplex PCR has been validated. Adaptation of our agarose cell encapsulation and emulsion PCR method to next-generation sequencing technologies has the potential to provide additional gains in throughput for single cell sequencing. Although alternative single cell-resolution genetic analysis approaches, such as fluorescence *in situ* hybridization[240,241] and *in situ* PCR,[242,243] are utilized for investigating cell mutation progression, the throughput offered by these methods is limited, and the lack of amplicon recovery prevents detection of unknown mutations. In the case of follicular lymphoma, identifying the breakpoint sequence along the IgH and bcl-2 genes can help elucidate the mechanisms of erroneous genetic recombination that cause the translocation t(14;18), while the random insertion sequence between the two chromosomes is a unique identifier of distinct mutation events.[230]

Encapsulation enables robust parallel cell lysis and DNA purification of cell types that are difficult to screen using other single-cell PCR methods. The method can be adapted in future applications to encapsulate live single cells for cell culture and subsequent analysis of clonal populations.[244] Although a similar approach has been demonstrated recently for screening and amplifying alginate-encapsulated *E. coli* colonies containing plasmid libraries,[244] our approach enables robust genome purification of mammalian cells, uses 1 % of the reagent volume for emulsion PCR, does not require droplet sorting, and maintains single-cell segregation throughout all downstream analyses by incorporating primer-functionalized beads as amplicon substrates. Furthermore, single-cell sequencing techniques generally involve cell types that are amenable to lysis during PCR and sorting of single cells into 96-well PCR plates.[245,246] However, PCR amplification directly from single cells has been hindered by the lack of a DNA purification step that would remove histones and other nuclear components that inhibit polymerase activity. [245,247] In our approach, the incorporation of a highly parallel single-cell lysis and DNA purification step resulted in near 100% amplification efficiency. Finally, the ability to purify genomic DNA from single cells in a supporting matrix opens up the possibility of single cell epigenetic analysis, such as methylation-specific PCR of gene regulatory sequences following bisulfite conversion.

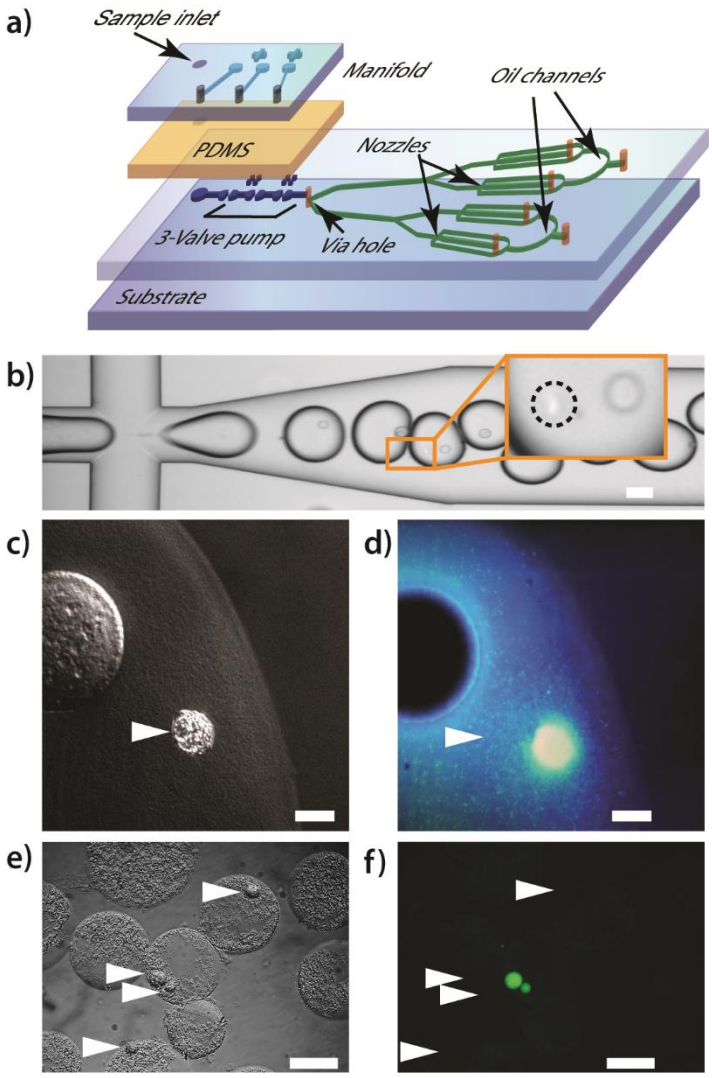

Figure 6.2. Microfluidic agarose encapsulation and genetic analysis of single mammalian cells. (A) Microfluidic emulsion generator array (MEGA) device showing the pneumatic micropump for fluid actuation and the fluidic channels. (B) Agarose emulsion generation showing single cells encapsulated along with primer-labeled beads in uniform 3 nL droplets. Inset highlights a cell (circled) and a bead in one droplet. (C) Differential interference contrast (DIC) image of a cell (arrow) at the edge of an agarose droplet after protease digestion. (D) Projection of confocal micrograph of Figure 2C showing acridine orange stained DNA confined in the agarose after release from the cell (arrow). (E) Following PCR amplification of the chromosomal translocation t(14;18) and β-actin, agarose droplets containing beads (arrows) remain intact and do not merge. (F) Epifluorence micrograph of Figure 2E demonstrates primer-labeled beads (arrows) becoming fluorescent if a $t(14;18)^{+}$ RL cell is present in the same droplet but otherwise remaining dark. Scale bars are 100 μm in B, E, and F and 10 μm in C and D.

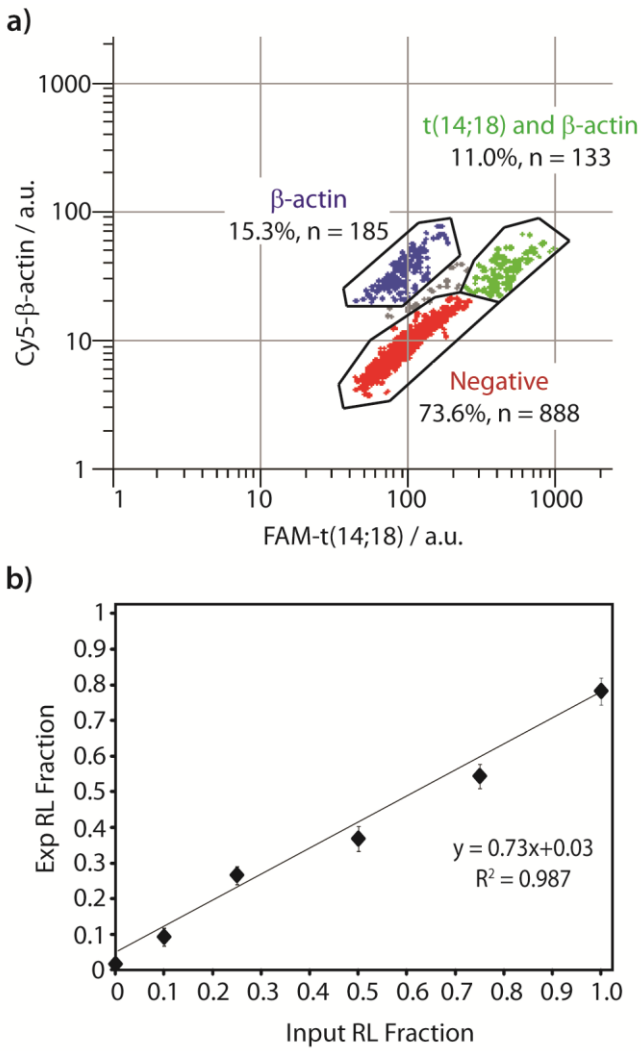

Figure 6.3. High-throughput digital genetic analysis of cancer cells. (A) A representative flow cytometry plot and gated populations of beads from a sample containing 50% RL lymphoblast cells (N=1,206) at a frequency of 0.3 cells per droplet. The observed fraction of total positive events (26.3%) compares favorably with an expected frequency of 25.9% based on the Poisson distribution. (B) Standard curve of $t(14;18)^{+}$ RL cell detection from mixtures of mutant RL and wild-type TK6 cells. Experimental quantification by multiplex emulsion PCR and flow cytometry exhibits a linear response between the 10% and 100% mutant cell frequencies tested.

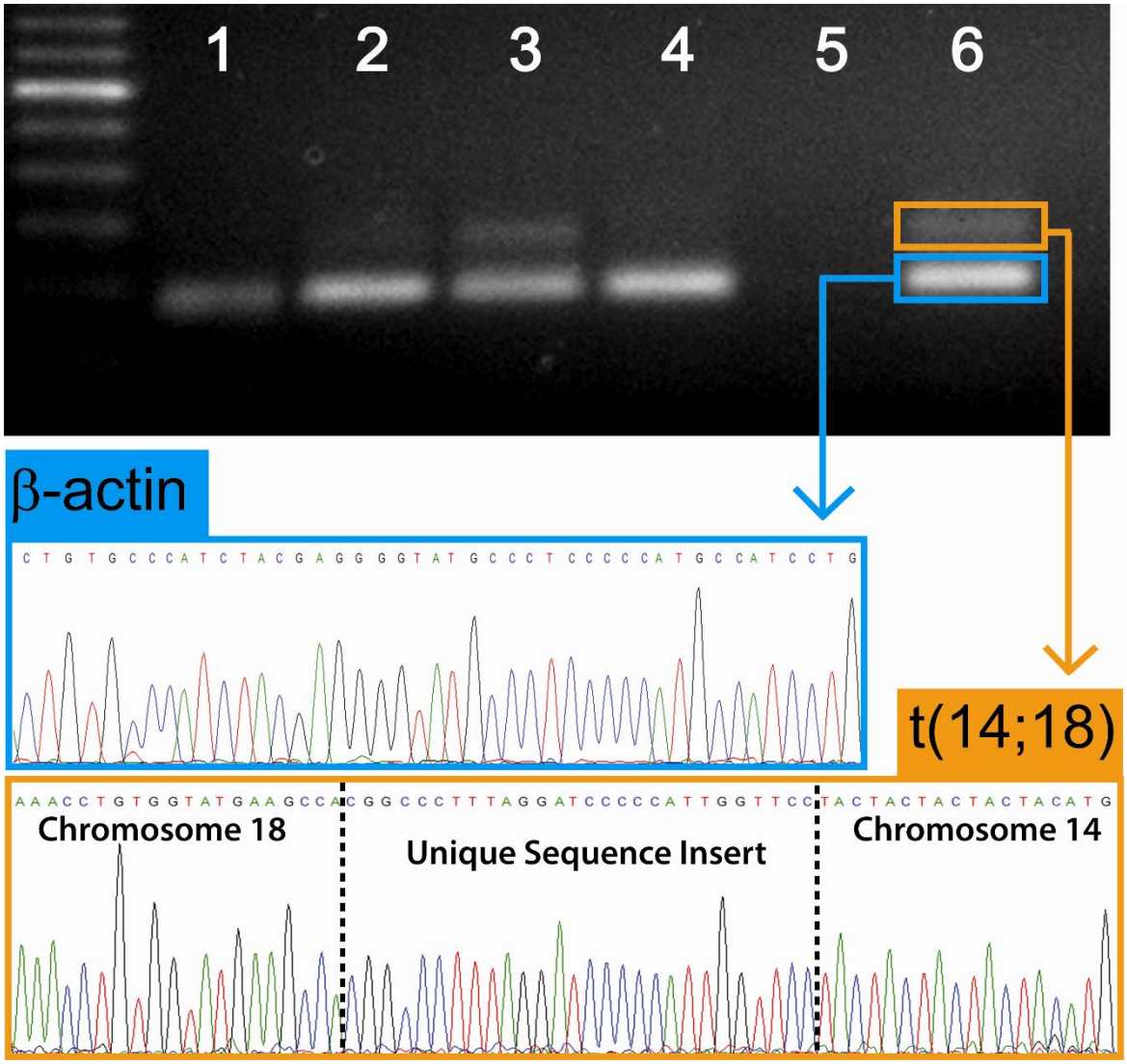

Figure 6.4. Multiplex single-cell sequencing. Sequencing of two loci from DNA products isolated from single cells was accomplished by reamplifying individual amplicon-labeled beads in separate PCR reactions and separating the two products using gel electrophoresis. This representative image of a section of the gel from a 50% RL cell sample shows amplified t(14;18) and β-actin from single beads (lanes 3 and 6), β-actin-only reactions originating from TK6 cells (lanes 1, 2 and 4), reactions from negative beads (lane 5), and a 100 bp DNA ladder. A lack of t(14;18) amplification without β-actin indicates true single cell analysis. Both products were excised and sequenced to obtain sequence data from two genes colocalized in a single cell. The breakpoint locations on chromosomes 14 and 18 as well as the unique insertion sequence confirmed the recovery of the expected RL lymphoblast sequence. By integrating single cell emulsion PCR with a standard sequencing technique, it is possible to sequence multiple genes from hundreds of single cells in the span of 2-3 days, opening up the possibility for population-level analyses of genetic heterogeneity.

6.3 Conclusions

Cancer is an evolving disease driven by genetic instability, which results in a constant clonal divergence of the tumor cell population. Accumulation of mutations in the genes coding for cellular pathways plays an important role in carcinogenesis, metastasis, and therapeutic resistance.[146,248,249] Significant cellular heterogeneity may therefore exist in tumors; this heterogeneity dynamically changes at different stages of disease progression.[241] We have developed a robust agarose microdroplet method for detecting and sequencing multiple genetic targets from single cells in a scalable manner. While mutations in oncogenes such as TP53, CDKN2A, CDKN2B, and blc-6 have been demonstrated to individually correlate with poor prognosis in hematopoetic cancers,[250–254] the ability to sequence multiple targets within single cells in high throughput will facilitate investigation of synergistic effects of mutation co-occurrence and their impact on disease progression and treatment. Furthermore, screening of large cell populations will uncover potential tumor heterogeneity at the single-nucleotide level that is otherwise obscured by the ensemble average. By overcoming the many problems associated with single-cell genetic analysis,[255,256] including non-uniform cell lysis, DNA release, and amplification as well as low throughput, our single-cell agarose encapsulation technology provides the throughput, robustness, and resolution required for probing the stochastic mechanisms of carcinogenesis, progression, and response to chemotherapy.

6.4 Acknowledgements

This work was supported by the trans-NIH Genes, Environment and Health Initiative, Biological Response Indicators of Environmental Systems Center Grant U54 ES016115-01 to MTS and RAM, and by Superfund Basic Research Program NIEHS Grant P42 ES004705 to MTS. RN is supported by an NSF Graduate Research Fellowship, and JS is supported by the Canary Foundation and ACS Early Detection Postdoctoral Fellowship.

Chapter 7: Single-cell forensic short tandem repeat typing within microfluidic droplets

7.1 Abstract

A short tandem repeat (STR) typing method is developed for forensic identification of individual cells. In our strategy, monodisperse 1.5 nL agarose-in-oil droplets are produced with a high frequency using a microfluidic droplet generator. Statistically dilute single cells, along with primer-functionalized microbeads, are randomly compartmentalized in the droplets. Massively parallel single-cell droplet PCR is performed to transfer replicas of desired STR targets from the single-cell genomic DNA onto the coencapsulated microbead. These DNA-conjugated beads are subsequently harvested and reamplified under statistically dilute conditions for conventional capillary electrophoresis STR fragment size analysis. 9-plex STR profiles of single cells from both pure and mixed populations of GM09947 and GM09948 human lymphoid cells shows that all alleles are correctly called and allelic drop-in/drop-out is not observed. The cell mixture study exhibits a good linear relationship between the observed and input cell ratios in the range of 1:1 to 10:1. Additionally, the STR profile of GM09947 cells could be deduced even in the presence of a high-concentration of cell-free contaminating 9948 genomic DNA. Our method will be valuable for the STR analysis of samples containing mixtures of cells/DNA from multiple contributors and for low-concentration samples.

7.2 Introduction

Short tandem repeat (STR) typing is the gold standard for human forensic identification, which is most easily performed on high-quality single contributor genetic samples.[257–259] However, biological evidence samples often present mixtures of contributions (cells/cells or cells/DNA) from multiple individuals at relatively low concentrations.[260,261] These complex biological samples generate mixed genotypes, presenting challenges in interpreting the results, especially when there are more than two contributors.[262,263] Another difficulty arises when the perpetrator cells are much rarer than the victim cells, resulting in preferential amplification of the victim DNA.[260,264] A variety of strategies have been developed to separate different cell populations prior to analysis to reduce the challenges in mixture interpretation, including differential extraction,[265,266] filtration,[267] fluorescence-activated cell sorting[268,269] and microchip-based separation.[270–272] More recently, laser capture microdissection[273–275] and micromanipulation[276–278] have been employed to analyze samples at the single-cell level. However, these methods are limited due to their complexity, low efficiency, low throughput, high risk of sample cross-contamination and/or lack of universality.

State-of-the-art microfluidic technology offers a promising strategy for the rapid generation of monodisperse microdroplets that can be used as miniaturized reactors for high-sensitivity single-cell analysis.[99,279,280] Single cells are compartmentalized within the discrete aqueous droplets surrounded by an immiscible carrier oil, which dramatically reduces the possibility of cross-contamination among different cells. Due to the controllable droplet size and uniformity, the droplet content (e.g., the reagent composition and concentration) can also be precisely tuned to provide the desired microenvironment for individual cell reactions. The ultralow volume (femtoliter to nanoliter) of the droplets means that the nucleic acids and other biomolecules from a single cell are highly concentrated and detectable. Furthermore, the droplet technology allows massively parallel handling of millions of independent reactions with high throughput, thereby enabling the analysis of vast populations of single cells to detect rare events or to probe cellular heterogeneity.[107,124,133,137,139,166,281–285]

Building upon traditional emulsion PCR technology with polydisperse droplets,[95,115,153] we previously developed an efficient single-cell/molecule PCR method using uniform microfluidic nanoliter droplets, and used it to digitally detect pathogenic bacteria, cancer cells and molecular variation in heterogeneous populations with superior sensitivity and throughput.[70,71,102,135] Robust mammalian cell lysis and DNA isolation in a highly parallel fashion was achieved by encapsulating single cells in agarose droplets.[71] The agarose matrix conserved single-genome fidelity during various manipulations without inhibiting subsequent emulsion PCR assays. This mammalian cell genomic DNA isolation method is an enabling technology for STR amplification from single cells, especially in cases where only very small amounts of mixed evidence materials are available.

Here we present a single-cell STR typing method based on droplet microfluidics (Figure 7.1). The technique enables the isolation of genomic DNA from a single cell and multiplex STR amplification within the same nanoliter agarose droplets. STR products are bound on the primer-functionalized microbeads coencapsulated in the droplets which are amplified by a secondary PCR reaction followed by capillary electrophoresis (CE) fragment size analysis. As a proof-of-concept, we validated the technical performance of the method using a 9-plex STR system. The protocols for the microbead-based 9-plex PCR were first optimized both in bulk solution and in microdroplets using DNA standards. Individual cells from pure or mixed cell samples were then typed to evaluate the performance of single-cell STR analysis. In addition, the impact of cell-free DNA on single-cell typing was examined. We conclude that single-cell forensic STR amplification is a valuable new approach for analyzing dilute and mixed cellular populations.

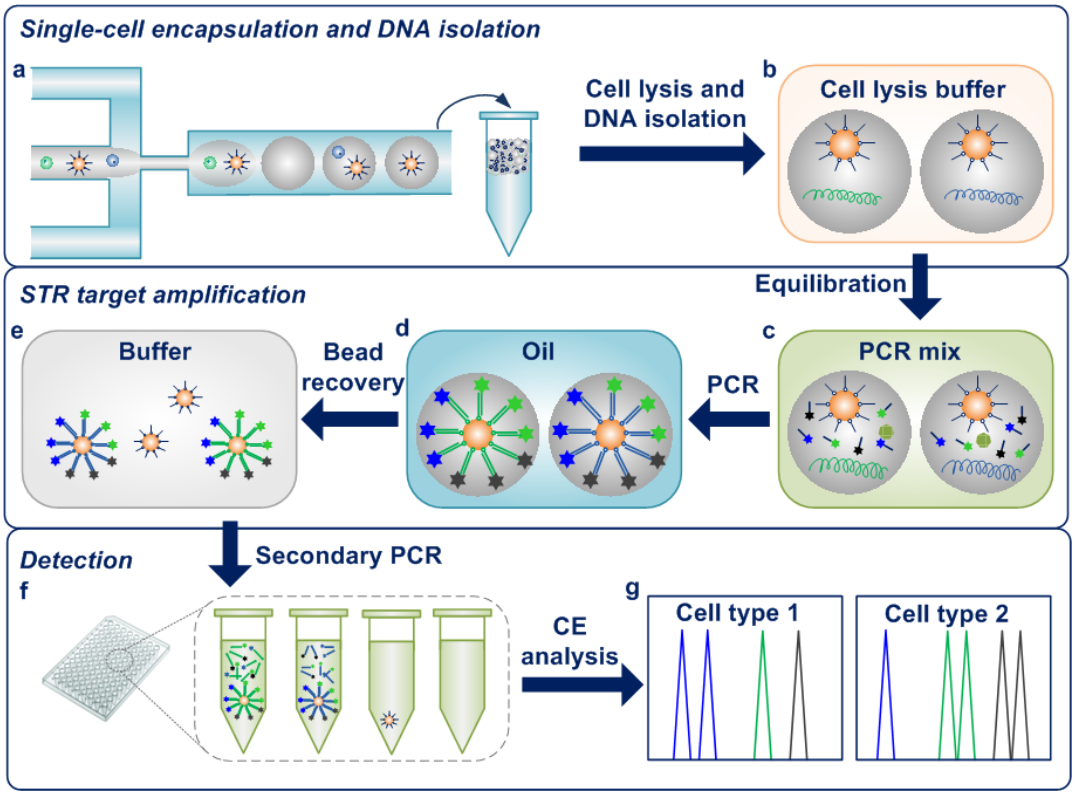

Figure 7.1. Analytical procedure for single-cell forensic STR typing. (A) Statistically dilute individual cells together with primer-functionalized microbeads are encapsulated within agarose microdroplets using a microfluidic droplet generator. (B) The gelled droplets are incubated in cell lysis buffer to release genomic DNA into the gel matrix. (C) The PCR components are diffused into the gel droplets by equilibrating in PCR mix. (D) After the droplets are redispersed in oil, emulsion PCR is performed with a thermal cycler. (E) After the first STR amplification, beads are recovered by melting the agarose. (F) Statistically dilute secondary PCR is conducted starting from single beads in standard PCR plates. (G) The STR products from the positive single bead amplifications are processed using conventional CE system for fragment size analysis. Different types of intact cells in a cellular mixture yield distinct single-cell STR profiles. The total analysis is accomplished in about 22 h, including 3.5 h working time and 18.5 h waiting time for cell lysis (10 h), droplet PCR (3.5 h), secondary PCR (3 h) and CE analysis (2 h).

7.3 Experimental section

Microfluidic Droplet Generator Fabrication. The microfluidic droplet generator was fabricated using standard soft lithography. Briefly, a master mold was made of photoresist SU-8 2075 (MicroChem, Newton, MA) on a 4-inch silicon wafer (Addison Engineering, San Jose, CA). A polydimethylsiloxane (PDMS) replica was produced by pouring degassed PDMS prepolymer mixture (Sylgard 184; Dow Corning, Midland, MI) with a mass ratio of 10:1 (base: curing agent) onto the master, followed by baking at 80 ºC for 2 h. After the PDMS replica and a pre-cleaned glass slide were treated by oxygen plasma, the device was immediately assembled and cured at 80 ºC for 5 min. To increase the surface hydrophobicity, the microchannels were treated with 0.1% (heptadecafluoro-1,1,2,2-tetrahydrodecyl)dimethylchlorosilane (Gelest, Morrisville, PA) in 100% ethanol for 10 min, followed by baking at 100 °C overnight.

Primer-functionalized Bead Preparation. All primers used in this study were designed based on the sequences and fluorescence dye labeling scheme used in Promega PowerPlex® 16 System and purchased from IDT (Coralville, IA) (Table E1). The equimolar concentrations of 5'-amine modified primers with C12 spacers were conjugated on *N*-hydroxysuccinimide (NHS)-activated Sepharose beads (34 μm mean diameter; Amersham Biosciences, Piscataway, NJ) *via* amine-NHS chemistry. The primers conjugated on beads included the reverse primers for Amelogenin, TH01, D13S317, D21S11, and D8S1179 as well as the forward primers for D3S1358, D5S818, vWA, and D7S820. The beads were stored in nuclease-free water at a concentration of 6×10^6 beads/mL at 4 ºC until use.

Cell and DNA Sample Preparation. GM09947 (female) and GM09948 (male) human lymphoid cell lines (Coriell Institute for Medical Research, Camden, NJ) were grown in RPMI 1640 medium (Life Technologies, Grand Island, NY) supplemented with 10% fetal bovine serum (Life Technologies), 2 mM L-glutamine and 100 U/ml penicillin-100 mg/mL streptomycin at 37 ºC in a humidified incubator containing 5% CO_2. Once harvested, the cells were washed for 3 times in Dulbecco's PBS (DPBS; Life Technologies) and incubated at 37 ºC prior to use. Samples were prepared by combining pre-warmed cell suspension (or DNA solution) and bead suspension with molten 3% (w/v) agarose solution using appropriate volumes to achieve desired concentrations. The stock agarose solution (3%) was prepared by dissolving ultra-low-gelling temperature agarose (Type IX; Sigma-Aldrich, St. Louis, MO) in DPBS at 70 ºC for 5 h to remove bubbles and store at room temperature. For experiments involving GM9947A female and GM9948 male standard genomic DNA (Promega, Madison, WI), the DNA samples were diluted to desired concentrations using nuclease-free water. DNA concentration was calculated assuming 3 pg genomic DNA per copy.

Cell Encapsulation and Lysis. Cell/bead-encapsulated microdroplets were generated by infusing the aqueous samples and fluorinated oil (Bio-Rad, Hercules, CA) into the microfluidic droplet generator within a heated air stream (42-45 ºC). The flow rates for the samples and oil were independently controlled by two syringe pumps (PHD 2000 infusion pump; Harvard Apparatus, Holliston, MA). The agarose droplets were collected in 0.5 mL PCR tubes and immediately cooled to 4 ºC. After agarose gelation for at least 1 h, the droplets were isolated from the oil using a cell strainer with 40 μm nylon mesh (BD Biosciences, San Jose, CA), followed by extensively washed with water. Cells in the droplets were lysed by combining equal volume of droplet suspension and 2X cell lysis buffer [1% SDS (Sigma-Aldrich), 200 mM EDTA, 20 mM Tris-HCl and 0.2 mg/mL proteinase K (Roche Applied Science, Indianapolis, IN)] and incubating at 37 ºC overnight.

Afterwards, the droplets were sequentially washed with 2% (w/v) Tween 20 (Sigma-Aldrich) in water once, 100% ethanol once and DPBS containing 0.02% (w/v) Tween 20 for 5 times. Tween 20 was used to prevent the attachment of droplets on the tube wall. The gelled droplets were finally washed with water once and resuspened in water.

Droplet PCR and Bead Recovery. Droplet PCR mix was prepared by mixing 1X *Ampli*Taq® Gold PCR buffer (Life Technologies), 1.5 mM $MgCl_2$ (Life Technologies), 200 µM dNTP (Qiagen, Valencia, CA), 4 µg/µL heat-inactivated BSA (Sigma-Aldrich), 0.01% Tween 80 (Sigma-Aldrich), 0.2 U/µL *Ampli*Taq® Gold DNA polymerase (Life Technologies), primer mixture and 3.6 µL agarose droplets encaging single-cell genomes in each 10 µL PCR reaction. The fluorescently labeled primers were ten times as many as their corresponding reverse-direction primers in the primer mixture (Table E1). The mixtures were incubated in 0.5 mL PCR tubes for 40 min at 4 ºC with occasional agitation to improve the transport of PCR components into agarose matrix structure. Fresh PCR carrier oil was prepared before each run of droplet PCR, containing DC 5225C formulation aid (Dow Chemical, Miland, MI), KF-7312J fluid (Shin-Etsu Silicones, Akron, OH), AR20 silicone oil (Sigma-Aldrich) and Triton X-100 surfactant (Sigma-Aldrich) with a mass ratio of 40:30:30:1. To redisperse the droplets, 150 µL carrier oil was added and mechanically vibrated at a frequency of 13 Hz for 30 s using a TissueLyser mixer (Qiagen). Each tube contained 10 µL PCR mix (including droplets) and 150 µL carrier oil to ensure uniform heating when fitting into the thermoblock of PTC100 thermocycler (MJ Research, Waltham, MA). The thermal cycling condition was composed of initial activation of the *Ampli*Taq® Gold DNA polymerase at 95 ºC for 10 min, followed by 10 cycles of 94 ºC for 1 min, 58 ºC for 1 min, 70 ºC for 1.5 min, 22 cycles of 90 ºC for 1 min, 58 ºC for 1 min, 70 ºC for 1.5 min, and a final extension step for 30 min at 60 ºC. The samples were then cooled to 4 ºC to enable agarose gelation.

Following STR amplification, the gelled droplets were harvested by centrifuging at 250 *g* for 1 min, and sequentially washed with 100% isopropanol once, 100% ethanol once and DPBS containing 0.02% Tween 20 for 5 times to remove the residual oil. The beads carrying STR products were released from the droplets by melting the agarose at 60 ºC for 15 min. The beads were washed with 0.1% SDS once to remove BSA and DPBS for 8 times to remove the DNA fragments unlinked to the beads. Finally, the beads were resuspended in water and stored at 4 ºC.

STR Product Detection. Secondary PCR was performed on the STR-conjugated beads to transfer the STR information into free solution for detection. The DNA-carrying beads were diluted at appropriate concentrations (0.2-20 beads/reaction) in standard 96-well PCR plates or PCR tubes to serve as the DNA templates for reamplification. The secondary PCR was conducted in 12.5 µL reactions using PCR mix containing 1X Gold ST*R buffer (Promega), 0.1 U/µL *AmpliTaq*® Gold DNA polymerase, primer mixture, nuclease-free water and bead solution. The fluorescently labeled primers had the same amounts as their corresponding reverse-direction primers in the primer mixture (Table S1). The PCR protocol involved 10 min hot start at 95 ºC, then 10 cycles of 94 ºC for 30 s, ramp at the rate of 0.5 ºC/s to 58 ºC, hold for 30 s, ramp at the rate of 0.3 ºC/s to 70 ºC, hold for 45 s, followed by 15 cycles of 90 ºC for 30 s, ramp at the rate of 0.5 ºC/s to 58 ºC, hold for 30 s, ramp at the rate of 0.3 ºC/s to 70 ºC, hold for 45 s, and a final extension step at 60 ºC for 30 min. The amplified products in free solutions were processed for fragment size analysis on Applied Biosystems 3730XL DNA Analyzer using Hi-Di formamide (Life Technologies) and GeneScan 500 ROX size standard (Life Technologies). The data were analyzed using Peak Scanner software (Life Technologies).

7.4 Results and discussion

We have developed a highly sensitive and selective microfluidic-droplet-based approach for high-throughput single-cell forensic STR typing. The overall process is illustrated in Figure 7.1. Single cells are initially compartmentalized and lysed to liberate genomic DNA within nanoliter agarose droplets. Massively parallel droplet PCR is then implemented to amplify the STR targets from individual cells and to transfer the STR information onto the coencapsulated primer-functionalized beads. Finally, the STR products bound on individual beads are transferred to free solutions by performing a statistically dilute secondary PCR in standard plates or tubes, followed by conventional CE fragment size analysis.

The PDMS/glass microfluidic droplet generator was constructed to produce monodisperse agarose microdroplets based on a flow-focusing channel geometry. The dispersed (aqueous) phase containing primer-functionalized microbeads, cells/DNA and 3% agarose flowed in the central channel while the continuous (oil) phase flowed in the two side channels, as shown in Figure 7.2A. With optimized channel dimensions (125 μm wide nozzle, 130 μm deep) and flow rates (40 μL/min for aqueous phase and 100 μL/min for oil phase), 1.5 nL agarose droplets could be generated with a high frequency of ~444 Hz in the fluorinated oil. Single cells (or genomic DNA when desired) along with microbeads were stochastically encapsulated into the droplets following Poisson statistics.

Ultra-low-gelling temperature agarose with a gel point about 8-17 ºC and a remelting point of ≤50 ºC was selected to avoid agarose gelation during droplet generation and to provide a convenient medium for template DNA capture and manipulation.[71] The most significant advantage of agarose droplets is their ability to rapidly transform into microgels by simply cooling to below the gelling temperature. Figure 7.2B shows the highly uniform gel droplets suspended in oil. The network structure of the gelled porous matrix enabled the diffusion of reagents (i.e., lytic reagents and PCR components) into interior, while encaging the high-molecular-weight DNA within the droplets.

The incorporation of the cell lysis and DNA isolation step is essential for PCR-based STR analysis as the vast majority of human cellular genomic DNA is tightly packaged in the nucleus. Histones and other DNA-associated nuclear proteins are enzymatically digested to make the DNA more accessible and to remove potential PCR inhibitors. In addition, the microgel enables mechanical manipulation and long-term storage of millions of microdroplets simultaneously while preserving single-genome fidelity. The mechanical properties of the gel microdroplets were adjusted by the concentration of agarose in the feed solutions. We found that 1.5% (w/v) of agarose gel provided sufficient strength without hindering molecular diffusion and compromising PCR performance. During PCR thermal cycling, the agarose was molten and stayed in the liquid state during the whole process. This feature improved the mixing of PCR components and DNA products within the nanoliter reactors. The droplets remained intact after PCR, though a slightly deformation was observed, as demonstrated in Figure 7.2C.

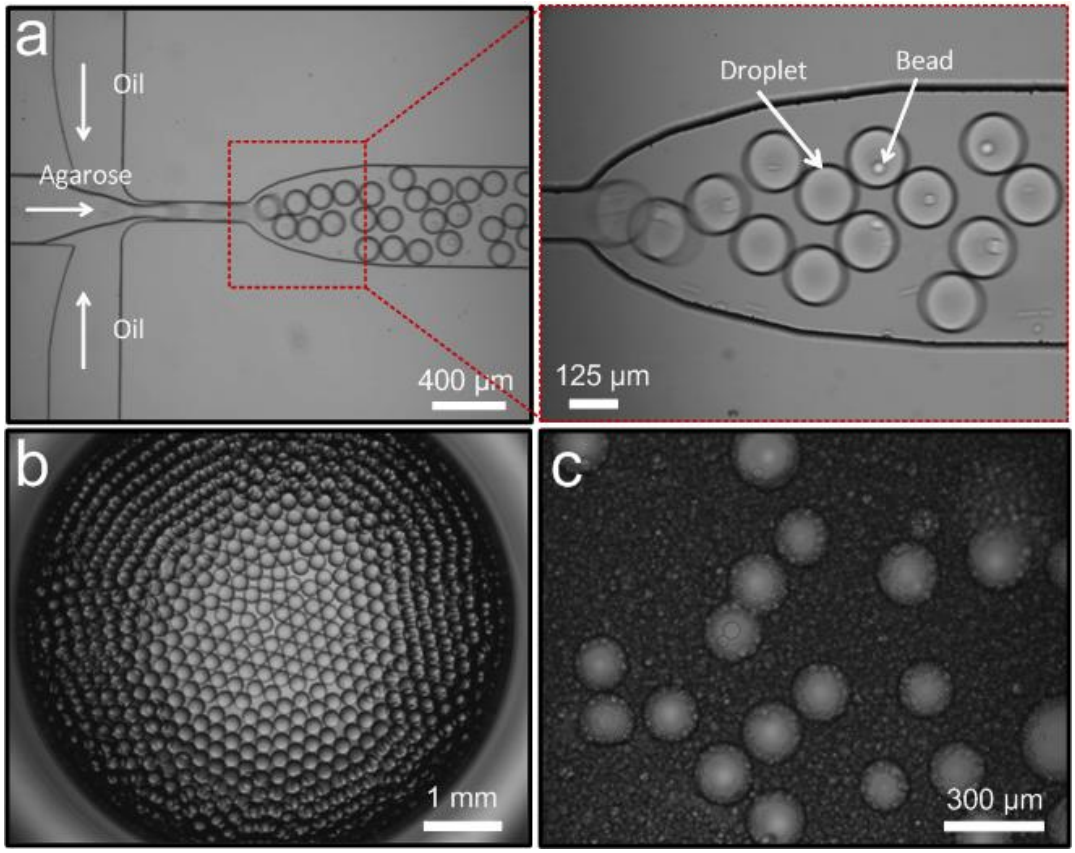

Figure 7.2. Agarose microdroplet generation and manipulation. (A) Microdroplet generation is based on a flow-focusing structure fabricated in a PDMS/glass microfluidic device. Primer-functionalized beads and the desired number of cells (or genomic DNA when desired) are encapsulated within the droplets. Fluorinated oil and 3% agarose solution are infused into the channel using a syringe pump. (B) Uniform gel microdroplets suspended within fluorinated oil in a 96-well plate. (C) Intact droplets after 32 cycles of emulsion PCR in freshly prepared silicon oil mixture.

To explore the utilization of this method for forensic DNA typing, a 9-plex STR system was developed with eight core STR loci (*i.e.* D3S1358, D5S818, D7S820, D8S1179, D13S317, D21S11, vWA, and TH01) from the combined DNA index system (CODIS) and Amelogenin for sex-typing and sample quality evaluation. We first validated the microbead-based solid-phase PCR for 9-plex STR typing with standard 9947A female and 9948 male genomic DNA in bulk solutions. The STR profiles of both types of DNA were in agreement with the established locus information (Table E2), and the peaks are balanced under the optimized PCR condition (Figure E1). Our previous work indicated that up to 100 attomoles of total amplicons were expected to be carried on an individual 34 μm diameter bead.[135] The success of the secondary PCR verified that this amount of STR template was sufficient for high-quality forensic analysis by CE (Figure E2).

Single-molecule emulsion PCR was initially performed with 9947A female genomic DNA based on the optimized amplification protocols (Figure 7.3A). A DNA concentration of 0.2 copies/droplet (corresponding to 1.8 alleles/droplet) was tested, while maintaining bead concentration at 0.9 beads/droplet on average. At this DNA concentration, it is predicted that 83% of the beads will have one or more STR templates and each individual unique heterozygous STR target will appear with a probability of 9.5%. In the secondary PCR, beads were diluted to 0.15 beads/reaction in order to reduce the probability of more than one bead appeared in each well of the PCR plate to 1% (13% of reactions involving only one bead). Note that because this is a true digital amplification, when a template is present there is only one copy leading to uniform peak heights. As expected, in Figure 7.3A incomplete STR profiles were obtained and each DNA-carrying bead exhibited distinct STR genotypes, consistent with random genomic template fragment encapsulation within the microdroplets. The low DNA input of 0.2 copies/droplet resulted in only 1 to 3 peaks detected from an individual bead.

Single-cell STR typing was then demonstrated using pure cell populations of two standard cell lines: GM09947 (female) and GM09948 (male) human lymphoid cells. Each droplet contained on average 0.15 cells and 0.9 microbeads, predicting that 14% of the beads should be bound with STR amplicons (positive). The low cell frequency ensured that no more than one cell was encapsulated in a droplet. 30 samples were tested in the secondary PCR with a bead concentration of 0.9 beads/reaction which predicts $0.14 \times 0.9 = 0.126$ positive beads/reaction. The results in Figure 7.3A and 7.3C show that there were 4 and 2 positive analyses as well as 26 and 28 null results for GM09947 and GM09948 cells, respectively, in close agreement with the value of 12% predicted by the Poisson distribution. In contrast to the genomic DNA encapsulation in Figure 7.3A, full STR profiles were obtained from single GM09947 cells (13 peaks) and single GM09948 cells (15 peaks) with relatively uniform peak intensities. All alleles were correctly called, and no allelic drop-in and drop-out was observed in both cell types. This is expected because when a cell is present the number of STR template copies in the droplet reactor is digitally defined by the genome. The stutter percentages for all allele peaks were below 15%, so the stutter products can be ignored as biological artifact of the samples. Furthermore, all the profiles of the negative samples were clean, confirming the absence of contamination. The 'all or nothing' feature of the single-cell droplet PCR event indicates the conservation of single-cell-genome integrity within the compartmentalized droplets during various manipulations and the successful transfer of STR information from single cells to individual microbeads.

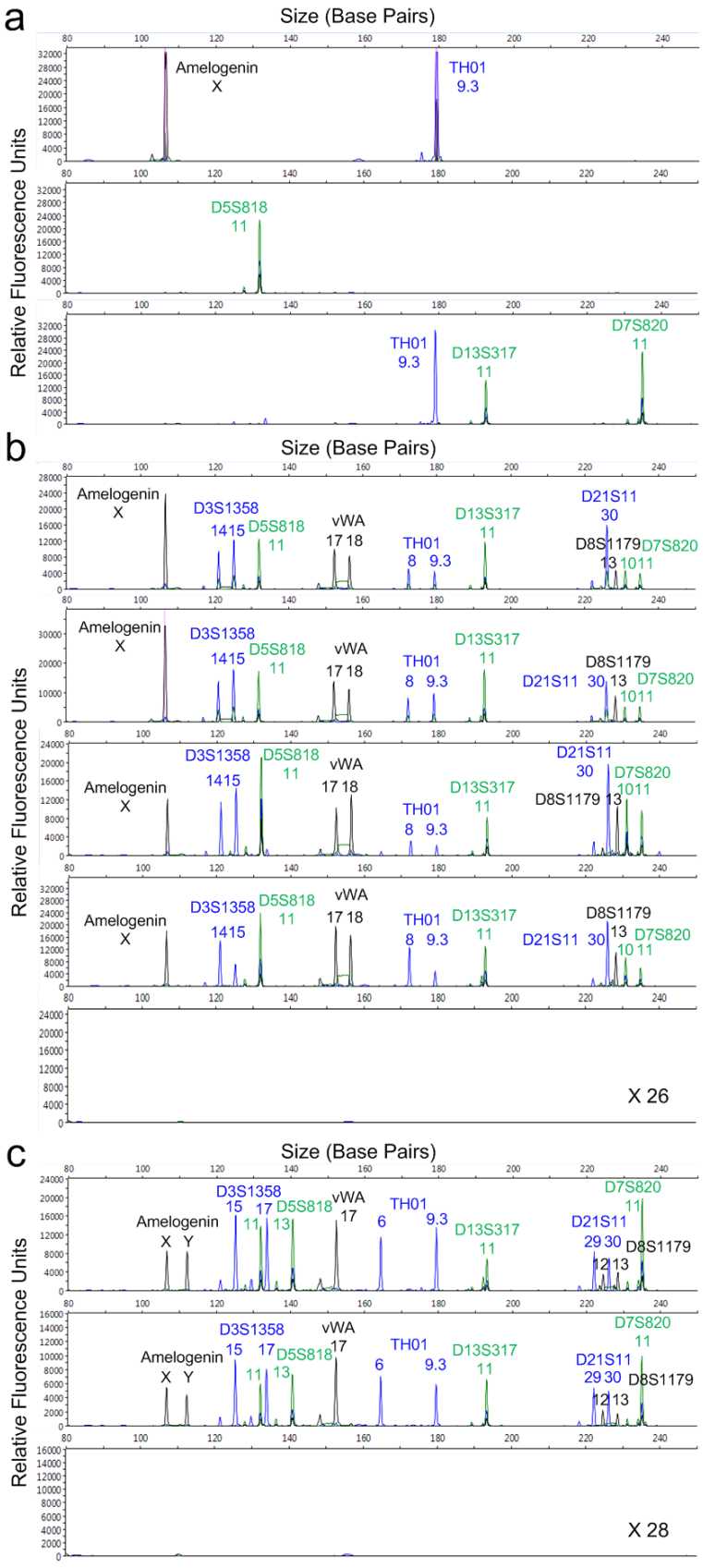
a
Size (Base Pairs)
Relative Fluorescence Units
Amelogenin
X
TH01
9.3
D5S818
11
TH01
9.3
D13S317
11
D7S820
11
b
Size (Base Pairs)
Relative Fluorescence Units
Amelogenin
X
D3S1358
1415
D5S818
11
vWA
17 18
TH01
8 9.3
D13S317
11
D21S11
30
D8S1179
13
D7S820
10 11
X 26
c
Size (Base Pairs)
Relative Fluorescence Units
Amelogenin
X Y
D3S1358
15 17
11 13
D5S818
vWA
17
TH01
6 9.3
D13S317
11
D7S820
11
D21S11
29 30
12 13
D8S1179
X 28

Figure 7.3. (A) Representative STR profiles resulting from microdroplets containing on average 0.2 copies of 9947A female genomic DNA and 0.9 beads per droplet. Under these statistically dilute conditions we calculate that 83% of the beads will have one or more STR templates present in their droplets and each unique heterozygous STR target will appear with a probability of 9.5%. The random appearance of different STR targets in these representative traces is thus expected. (B) and (C) Single-cell STR profiles resulting from microdroplets containing on average 0.15 GM09947 human (female) (B) or GM09948 human (male) (C) lymphoid cells and 0.9 beads per droplet. Under these statistically dilute conditions it is expected that approximately 14% of the beads will be positive for STR products. In total 30 samples were tested in secondary PCR for each experiment using 0.9 beads per reaction (predicting $0.9 \times 0.14 = 0.126$ positive beads per reaction). There were 4 and 2 positive analyses (26 and 28 null results) for GM09947 and GM09948 cells, respectively, which is consistent with the theoretical value of 12% predicted by the Poisson distribution. The lower panel figures show typical null results in the secondary PCR. In all cases, 30 cycles of emulsion PCR were performed followed by 25 cycles of secondary PCR.

To access the selectivity and sensitivity of our single-cell STR typing method, we performed droplet PCR using mixtures of GM09947 (female) and GM09948 (male) human lymphoid cells at various female-to-male cell ratios (1:1, 2:1, 5:1 and 10:1). The total cells were diluted to 0.01 cells/droplet on average to eliminate the chance of cell clumping in the agarose solution, while the bead concentration remained unchanged (0.9 beads/droplet). Since only 1% of the beads should be positive, the number of the secondary PCR reactions was increased to 40-100, and the bead concentration in the secondary PCR step was increased to 20 beads/ reaction resulting in 0.2 positive beads/reaction. In the experiment at the input cell ratio of 1:1 shown in Figure 7.4, 9 positive samples were obtained in 40 reactions, which was consistent with the theoretical prediction of 18%. Among the 9 positive samples, we detected the complete STR profiles from 4 single GM09947 cells and 5 single GM09948 cells. No mixed STR profiles were detected. The quality of the STR profiles was similar to that obtained using pure cell population in terms of the stutter formation (below 15%) as well as incidence of allelic drop-in and drop-out. Nevertheless, the heterozygous peaks for some STR loci such as Amelogenin and TH01 were not fully balanced. This observation is possibly due to the stochastic effects when amplifying low levels of target DNA molecules.

To detect cell mixtures with higher input ratios, more secondary PCR reactions were performed. As an example, 100 PCR reactions were conducted when the female-to-male cell ratio increased to 5:1. There were 19 positive samples which consisted of 16 STR profiles from GM09947 cells and 3 from single GM09948 cells (Figure E3). Similarly, peak height unbalance and allelic drop-out at TH01 loci were observed possibly due to stochastic influences. In the best case, we were able to successfully indentify male cells in the cell mixture when the female cells were 10 times more prevalent than the male cells using 100 PCR assays. Figure E4 summarizes the relationship between the measured female-to-male cell number ratios and the corresponding input ratios. The good linearity ($R^2 = 0.9917$) indicated the high accuracy and reliability of our assay in the range of 1:1 to 10:1 cell ratios.

We then used the GM09947 (female) human lymphoid cells admixed with 9948 male genomic DNA as a model system to investigate the influence of cell-free contaminating DNA on STR typing of the desired single-cell targets. In each droplet, approximately 0.9 microbeads, 1 GM09947 cell and various copy numbers (0.1, 1, 1.5, 2 and 3) of 9948 genomic DNA on average were encapsulated. The bead concentration in the secondary PCR was 0.6 beads/reaction and 70 samples were assayed in each case. Based on the concentrations, it is expected that 63% of the beads should be conjugated with STR amplicons from GM09947 cells. The probability of seeing beads with STR amplicons from 9948 DNA is dependent on the DNA concentration. Except at 0.1 copies/droplet (59%), nearly all beads should have products from 9948 DNA, though the number of STR loci on these beads will be variable due to the stochastic distribution of the various DNA template fragments within the droplets. Mixed genotypes from both GM09947 cells and 9948 genomic DNA (Figure 7.5 and E5-E7) as well as partial genotypes from 9948 genomic DNA were obtained.

By comparing with the known STR profiles of GM09947 cells and 9948 genomic DNA, we found that 6 allele peaks (Amelogenin-X, D3S1358-17, D5S818-13, TH01-6, D21S11-29 and D8S1179-12) were specific for 9948 genomic DNA and distinct from GM09947 cellular DNA profiles. We calculated the percentage of the STR profiles that were composed of all 13 allele peaks from GM09947 cells and had a given number (0, 1, 2, 3, 4, 5 or 6) of 9948-DNA-specifc

peaks, and plotted the percentage as a function of the number of 9948-DNA-specifc peaks in Figure E8. At low background DNA concentration (0.1 copies/droplet), 82% of the profiles had only GM09947 cellular peaks detected and 18% of the profiles had only one additional 9948-DNA-specifc peak. Thus, at this relative concentration the cell-free DNA did not significantly affect the data interpretation. When the input 9948 DNA was increased to 1 copy/droplet, no pure GM09947-cell profiles were obtained, but the percentage of profiles containing one or more 9948-DNA-specific peak was only 30% (Figure 7.5). The background DNA peaks could be easily excluded from the cellular peaks by comparing these STR profiles. As long as the cell-free DNA is not dominant, a peak can be assigned as background DNA if it is not observed in all profiles. The percentages of profiles containing more 9948-DNA-specifc peaks rose with increasing background 9948 DNA loading. At 1.5 copies/droplet, most profiles consisted of four 9948-DNA-specifc peaks plus the GM09947-cell peaks, but still 8% profiles contained only one additional 9948-DNA-specifc peak (Figure E5). At 2 copies/droplet, the highest percentage (32%) of profiles had six 9948-DNA-specifc peaks, and profiles containing two additional 9948-DNA-specifc peaks still could be detected (5.3%) (Figure E6). Even when the DNA concentration was increased to 3 copies/droplet, 5.6 % of the profiles additionally contained four 9948-DNA-specifc peaks. Nevertheless, all six 9948-DNA-specifc peaks appeared in the vast majority (78%) of profiles (Figure E7).

In principle, the cellular STR profile could be deduced from these cell/DNA mixture experiments when sufficient secondary PCR reactions are carried out. Therefore, the droplet microfluidic technique provides a valuable method that statistically dilutes the extracellular DNA fragments together with the target cells, leading to minimal interference with each individual droplet PCR reaction and easy interpretation of STR genotypes. We can conclude from the data that it is feasible to type single cells with contaminating DNA at or below 2 copies of contaminating genomic DNA/target cell. This benefit should also apply to forensic samples contaminated with PCR inhibitors (e.g. environmental elements or natural contaminants). The agarose droplet approach can overcome the effects of PCR inhibitors in two ways. First, the extremely low volume (1.5 nL) of the droplets significantly dilutes the inhibitors (at least cell-impermeable factors) during the random compartmentalization process, decreasing the possibility of encapsulating both cells and contaminants within an single droplet. The droplets solely containing single cells will yield complete STR profiles, whereas DNA amplification will be interfered when contaminating molecules are incorporated in droplets. Second, the cell-containing gelled droplets are extensively washed in multiple steps prior to performing droplet PCR. The washing should remove contaminating molecules that diffuse through the gel. Even inhibitors that are capable of entering into the cells are free to diffuse out during cell lysis and the following washing steps.

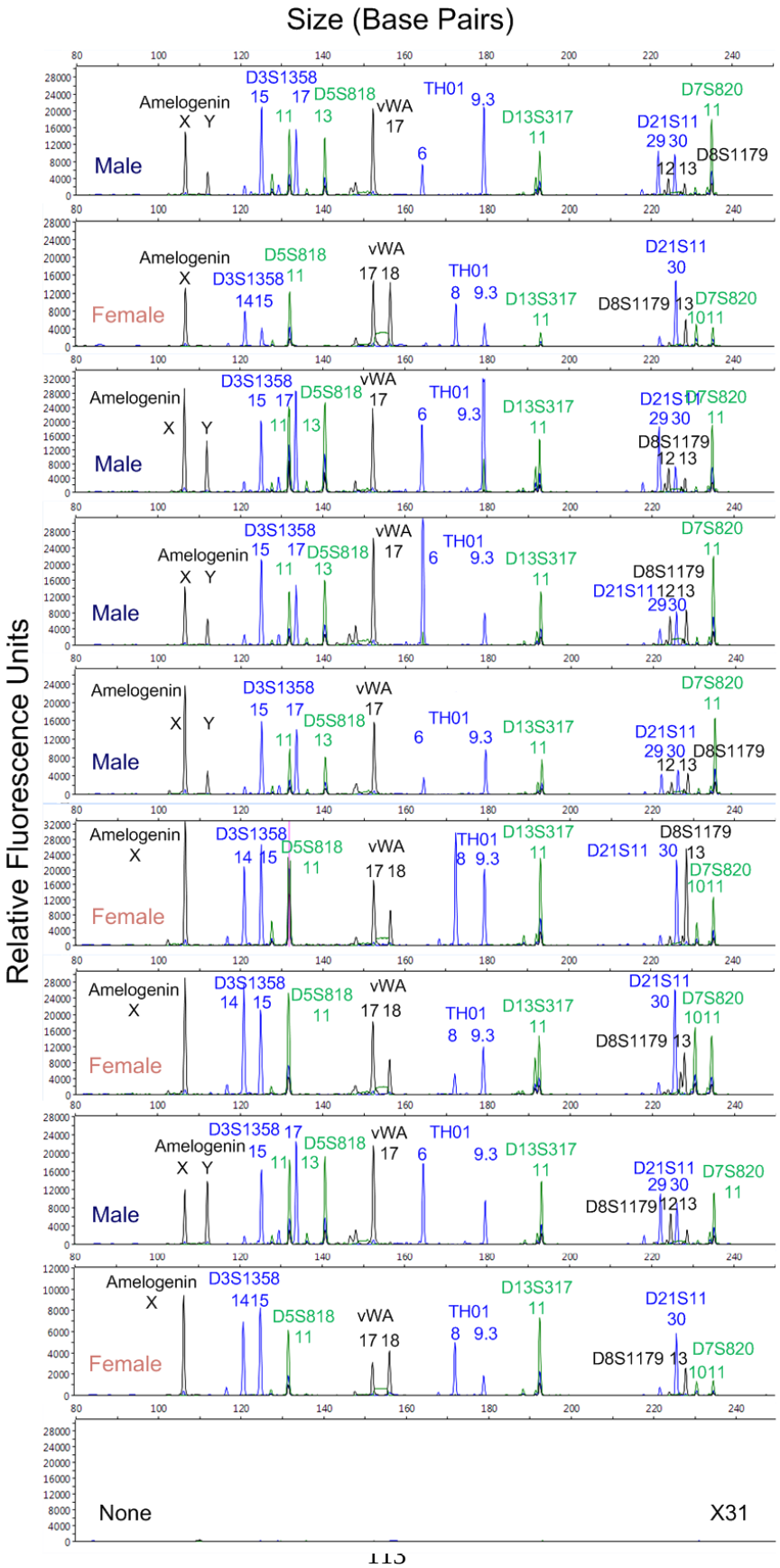
Size (Base Pairs)
Relative Fluorescence Units
Male
Female
None
X31

Figure 7.4. Single-cell STR profiles resulting from microdroplets containing a mixture of 0.005 GM09947 human (female) lymphoid cells and 0.005 GM09948 human (male) lymphoid cells per droplet together with 0.9 beads per droplet on average. Under these statistically dilute conditions it is expected that approximately 1% of the beads will be conjugated with the STR products from either type of cell. In total 40 samples were tested in secondary PCR using 20 beads per reaction (predicting $20 \times 0.01 = 0.2$ positive beads per reaction). The high bead concentration was used to ensure that more positive beads could be analyzed with fewer secondary PCR reactions. There were 9 positive analyses (consistent with the theoretical value of 18% predicted by Poisson distribution), in which 4 STR profiles were from GM09947 cells and 5 were from GM09948 cells. 31 samples yielded null results in the secondary PCR, as exemplified in the bottom panel. In all cases, 30 cycles of emulsion PCR and 25 cycles of secondary PCR were performed.

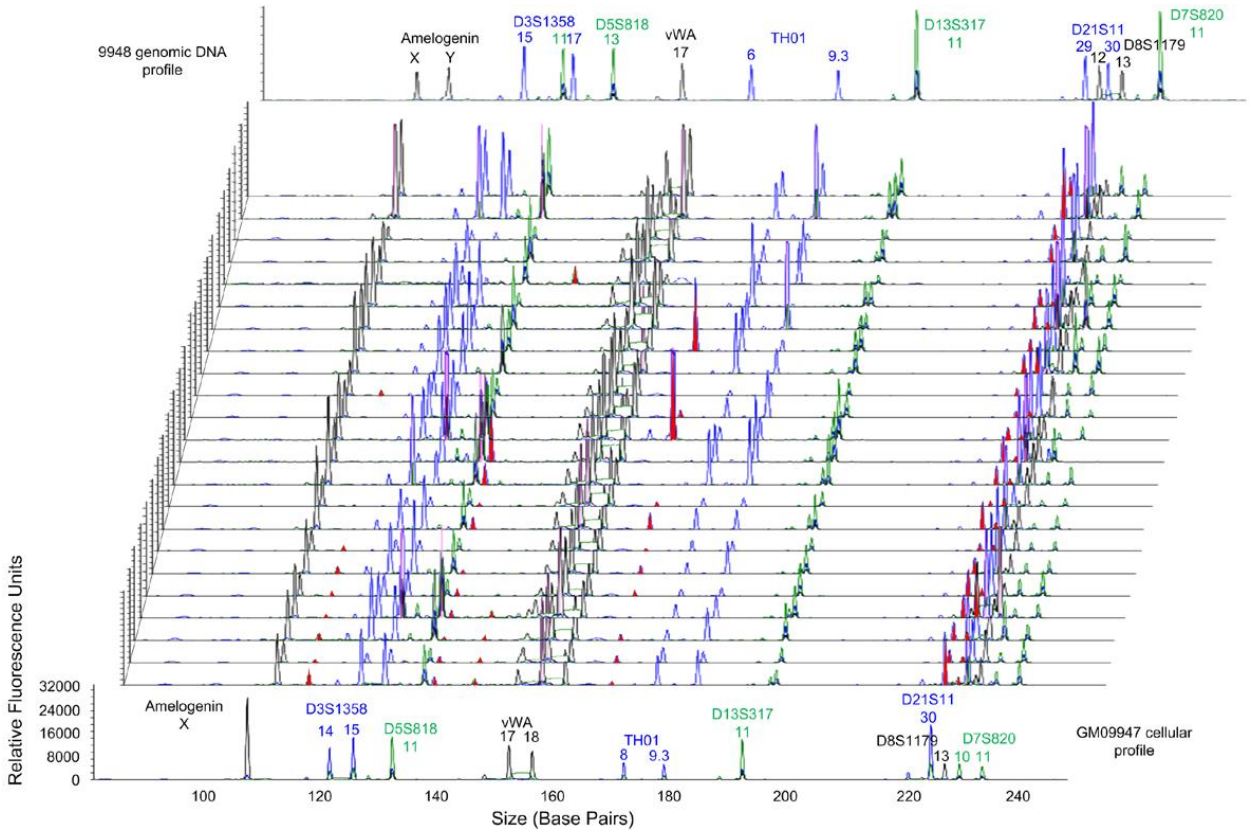

Figure 7.5. Representative STR profiles resulting from microdroplets containing 1 GM09947 human (female) lymphoid cell, 1 copy 9948 genomic DNA and 0.9 beads per droplet on average. Under the statistically dilute conditions it is expected that approximately 63% of the beads will have all GM09947 cellular STR products and 95% of the beads will have at least one of the 9948 DNA-specific STR products. In total 70 samples were tested in secondary PCR using 0.6 beads per reaction (predicting $0.6 \times 0.63 = 0.378$ GM09947-cell-DNA-positive beads per reaction) on average. There were 23 positive analyses, which was consistent with the theoretical value of 31% predicted by the Poisson distribution. In all cases, 30 cycles of emulsion PCR and 25 cycles of secondary PCR were performed. Red filled peaks indicate 9948 DNA-specific peaks which appear randomly.

Our droplet-microfluidics based STR typing technology provides several technological advantages over conventional forensic genetic methods for single-cell analysis. First, it avoids the complex and expensive cell separation instrumentation in other single-cell assays such as laser capture microdissection, fluorescence-activated cell sorting and micromanipulation. All processes can be accomplished in standard laboratory setup, and the microfluidic droplet generators are disposable and affordable. Second, multiple steps, from cell isolation to cell lysis and DNA release for subsequent PCR amplification, are performed in a single droplet reactor for an individual cell, substantially improving the efficiency of sample handling. Another key benefit of microdroplets is that their nanoscale reaction volume significantly increases the concentration of starting materials, thereby improving the single-cell PCR efficiency. Third, compared to other droplet digital PCR assays that typically process extracted DNA samples for one to two genetic targets, our method greatly enhances the level of multiplexing to nine by using the functionalized beads and enables covariance studies in single cells. The relatively large surface area of the beads provides sufficient amplicon-binding spaces for the 9 STR targets without unbalanced amplification for each locus. Moreover, although the overall experimental analysis time (~22 h including 3.5 h working time and 18.5 h waiting time) is not dramatically improved compared to conventional methods using a large number of cells, the complete resolution of the cell mixtures provides a new powerful approach for simplifying complicated mixture interpretation. The throughput for both cell separation and PCR reaction is greatly increased compared to the laser capture microdissection and micromanipulation for analyzing single-cell samples. The power of our method will be further enhanced by expanding the STR multiplex to the full 13 CODIS loci for standard casework analysis. This can be achieved by conjugating 4 more primers on the beads and further optimizing the PCR reactions.

7.5 Conclusions

In summary, we have demonstrated a novel approach for multiplex STR typing at the single-cell level using agarose droplets generated with a simple PDMS/glass microfluidic device. Taking advantage of droplet microfluidics, individual cells were efficiently encapsulated in nanoliter agarose droplets which subsequently served as the reactors for emulsion PCR assays. A large number of single-cell PCR reactions were implemented in a standard PCR tube in a highly parallel manner, substantially increasing the throughput of the analysis - a necessary step to produce statistically valid results when performing single-cell studies. The expected profiles of 9 STR loci were successfully detected from both pure and mixed single-cell samples (GM09947 and GM09948 human lymphoid cells) with high single-genome integrity. Distinct cells could be efficiently discriminated in mixture at a 10:1 background ratio. STR profile interpretation was also effective in the presence of significant background cell-free DNA. Our method has the potential to be immediately used in common forensic laboratories since no sophisticated equipment is involved in our protocol and the final data appears in a familiar conventional STR format. The improvements in sensitivity and selectivity should lead to more accurate and reliable results from samples containing low amounts of cells and/or mixed cells such as samples left on touched surfaces and sexual assault crimes. Future work will extend this method to analyzing real-world mixed and dilute samples to identify multiple suspects from low-abundance materials.

7.6 Acknowledgements

This work was supported by the United States Department of Justice Office of Justice (2009-DN-BX-K180) and by the Mathies Royalty Fund.

Section conclusion

This section presented three applications of droplet PCR for ultra-sensitive detection of single DNA molecules. Chapter 5 highlighted the sensitivity of digital PCR detection combined with the information obtained from subsequent sequencing of amplicons stemming from single molecules. This was applied to single cell analysis in the following chapter with the addition of DNA extraction of single genomes for robust detection of mutations. Finally, Chapter 7 expanded single cell analysis to 9 targets, demonstrating that the highly parallel single cell DNA extraction method results in high quality DNA suitable for multiplexed analysis. Although only STR typing is demonstrated, exchanging the STR primer sets with primers targeting various cancer biomarkers would provide similar levels of multiplexing for highly detailed investigations of mutagenesis, metastasis, and therapy response. The applications presented here demonstrate the power of digital PCR and single cell genetic analysis in probing rare mutations with single nucleotide resolution in high throughput for a single cell-level view of population dynamics. These types of studies are only the beginning of quantitative single cell biology and will undoubtedly unearth novel biomarkers, pathways, and biological phenomena of great academic and clinical value.

Section 3: Multiparameter single cell analysis

Section overview

Up to this point, this thesis has discussed applications of droplets for single cell DNA analysis, where the assay itself occurs within the confines of each droplet. This section adds to that work by introducing a protocol for single cell cultures in droplets in Chapter 8. Isolating single cells provides a platform for monitoring growth rates and correlating that information with other assays, such as RNA expression and splicing presented in Chapter 9. The method facilitates single cell analysis of multiple parameters per cell.

Aside from making cells easier to count, droplet-based culture mimics the concentration of neighboring cells perceived by a given cell. It accomplishes this by reducing the volume of culture medium to that of high-density bulk cultures, which grow and respond to stimuli differently from low-density cultures. Droplets, for better or worse, also retain all cell products and the daughter cells themselves. Maintaining colonies enables study of heritable traits, including genetic noise and memory. The compartmentalization would make it possible to readily analyze secreted proteins or metabolites from single cells by sampling the supernatant or introducing in-droplet assay reagents. On the other hand, droplets accumulate waste byproducts that can be reduced using complex droplet splitting and merging operations that would also reduce the cell number.

Unlike bacterial culture, which has been applied to drug screening and enzyme selection, mammalian single cell culture has had far fewer applications demonstrated in droplets. As the various biological disciplines adopt a single-cell-centric point of view even more, there will be a greater push to design experiments where single cell culture plays a key role. Although the protocol and application described in this section focus on non-adherent cells, modifications, such as those discussed in Chapter 9, should enable all cell types to be cultured in emulsions. Droplets can provide the throughput and ease of single cell culture while maintaining a degree of fidelity compared to bulk culture conditions.

Chapter 8: Protocol for single cell culture in microfluidically generated droplets

8.1 Introduction

This chapter presents a protocol for non-adeherent cell encapsulation in culture medium inside a continuous phase of fluorinated oil and subsequent culture of colonies. The fluorinated oil provides high gas permeability that enable cells to respirate. In this system, droplets are formed by continuous flow of oil and cells through a PDMS microfluidic cross channel droplet generator, though other designs and approaches could be used. The advantage of continuous flow here is the speed of encapsulation combined with ease of sterilization of the device and syringes. PDMS as a material is not critical here since cells pass through the device in a fraction of a second in excess medium and reside for extended times only in biocompatible droplets. Droplet cultures can be maintained in standard incubators, enabling wide adoption of this method by research groups for a wide range of applications.

8.2 Materials and equipment

- Microfluidic droplet generator that produces droplets 3-10 nL in volume. This protocol describes continuous droplet generation using two syringe pumps, though various modifications to droplet generation should still be suitable.
- Two syringe pumps, such as the Harvard Apparatus series pumps
- Two syringes: a small one, such as 500 μL, for cells, and another larger one (>1 mL) for oil
- Teflon or PEEK tubing to connect syringes with droplet generator and for collecting output droplets. Tubing outer diameter should fit the via holes in the microfluidic device
- Sterile polypropylene PCR tubes for droplet collection and tube rack
- Biopsy punch (1-2 mm)
- Resuspended cells for encapsulation
- Culture medium supplemented with 20% Fetal Bovine Serum (FBS) and suitable antibiotics
- 10% w/v Pluronic F68
- Droplet generation oil: must be fluorinated, such as the Droplet Generation Oil sold by Bio-Rad for digital PCR and used in Chapter 9.
- Ethanol
- Pipettes and sterile tips
- Sterile 10 μL gel loading tips for colony collection for analysis and subculturing
- Small plastic Petri dish
- Incubator set to correct cell culture conditions (e.g., 37 ^{o}C, 5% CO_2)
- Microscope for observing droplet generation, confirming droplet size, assessing cell encapsulation frequency, and recovery of droplet colonies

8.3 Protocol for cell encapsulation

1. Prepare microfluidic droplet generator by connecting tubing and flushing several times with ethanol and drying with pressurized air or nitrogen. Flush syringes with ethanol and dry. This step can be performed in the cell culture hood and devices can be left temporarily in UV light for further sterilization.

2. Clean work station, such as the microscope platform, with ethanol.
3. Prepare culture tubes: punch a hole in each tube cap with the biopsy punch to provide air circulation during culture. Place a tube without a punched hole in the rack next to the droplet generator and place outlet tubing into the tube, taking care to let droplets slide down the wall of the tube.
4. Load oil syringe with droplet generation oil, insert into syringe pump, and flush the droplet generator for 10-20 s. Stop the flow and proceed to the next step.
5. Prepare cell encapsulation medium: add Pluronic F68 to cell culture medium to a final concentration of 0.5%. Pluronic F68 provides emulsion stability and at low concentrations helps stabilize cell membranes against shear. Prepare enough for flushing syringe and droplet generator (approximately 500 μL extra but typically 1-2 mL and more is required if large cell dilutions are necessary). Importantly, 20% FBS is needed, compared to the typical 10%, to offset the large surface area-to-volume ratio of droplets compared to regular bulk cell culture. Pre-warm to 37 ^{o}C.
6. Pellet cells (2 min, 1000 rpm) and resuspend with encapsulation medium to a final concentration of < 0.1 cells/droplet. For 10 nL droplets, this corresponds to 10 cells/μL. Dilute cells with encapsulation medium to adjust as needed. Sticky cells may require lower concentrations to avoid cell clumping in the droplet generator and to reduce co-encapsulation. At this point, add any soluble compounds to the medium.
7. Load cell suspension into cell syringe and insert into syringe pump. For some cells and experiments, it may be helpful to pre-warm the syringe to avoid temperature shock.
8. Start oil flow. After it stabilizes (approximately 5-10 s), start cell culture flow. Droplet sizes need to be empirically determined ahead of time for the exact droplet generator design, medium, and experimental requirements. Cell culture flow rates should not exceed ~100 μL/min to avoid shear-induced damage. Some cell types are even more sensitive to shear forces, and suitable flow rates need to be assessed for specific experimental conditions.
9. Encapsulated cells are collected in the PCR tube until sufficient droplets are produced for the particular experiment. For verification, a small number of droplets can be examined microscopically for uniform volume and desired cell encapsulation frequency.
10. Pipette 50-75 μL of droplets into prepared PCR tubes with air vents using a 100 μL pipette with a pipette tip cut to produce an opening ~1 mm wide to avoid shearing droplets.
11. Fluorinated oil evaporates and additional oil is required to avoid drying, which can result in droplet merging. For 3 day culture, 250 μL of oil should be added to each PCR tube by pipetting the oil down the walls. Alternatively, the oil can be preloaded before adding the encapsulated cells.
12. Culture cells in the incubator.

8.4 Recovery of droplet colonies

1. Pipette 300 μL into Petri dish and place on microscope stage
2. Pipette approximately 10 μL of droplets from the PCR tube and transfer to Petri dish
3. Under 100X magnification, find colony and count cells. For some applications, such as those that do not require cell counting, a lower magnification may be easier.
4. Carefully pipette droplet containing the colony into any downstream assay or culture container. For assurance, it may be helpful to transfer the droplet to an empty region of the

Petri dish, re-examine the droplets, and then transfer. This is particularly useful when it is important to avoid co-analysis of multiple colonies.

5. Transferring droplet colonies for subculture only requires adding the droplets and any extra oil directly into prepared microplates with culture medium. Droplets will break open spontaneously. For RT-PCR and other assays requiring lysis, addition of a detergent such as Triton X-100 serves to not only lyse cells but also rapidly break open the droplets.

Chapter 9: Analysis of telomerase expression and splicing in single cell cultures using microfluidic emulsions

This work is in preparation for submission to *Nucleic Acids Research*. Co-authors are Richard Novak, Kristina Hart, and Richard A. Mathies.

9.1 Abstract

Telomerase is a reverse transcriptase that maintains telomeres on the ends of chromosomes, allowing rapidly dividing cells to proliferate while avoiding senescence and apoptosis. Understanding gene expression and splicing at the single cell level could yield insights into the roles of telomerase during normal cell growth as well as cancer development. Here we use droplet-based single cell culture followed by single cell or colony gene expression analysis to investigate the relationship between cell growth and expression of hTR and hTERT genes as well as hTERT splicing. Jurkat and K562 cells are examined under normal cell culture conditions and during exposure to curcumin, a natural compound with anti-carcinogenic and telomerase activity-reducing properties. Individual cells predominantly express single hTERT splice variants, with the α+/β− variant exhibiting significant expression bimodality, and this bimodality is sustained through cell division. Sub-lethal curcumin exposure results in reduced gene expression bimodality of all hTERT splice variants and significant upregulation of alpha splicing. The single cell culture and expression analysis method presented here provides the tools necessary for multiparameter single cell analysis which will be critical for understanding phenotypes of heterogeneous cell populations and for investigating drug activity.

9.2 Introduction

Telomerase is a ribonucleoprotein complex that maintains telomeres at the ends of chromosomes through reverse transcription.[286,287] Telomeres shorten with each cell division, and their maintenance is a key requirement for avoiding apoptosis. In humans, telomerase activity is present primarily during development and in stem cell and immune cell populations.[287,288] Upregulation of telomerase is also observed in approximately 85-90% of all cancers, allowing cancer cells to avoid apoptosis despite uncontrolled cell division.[146,289] The human enzyme consists of an RNA component, hTR, and a protein component, hTERT. hTR acts as a template for reverse transcription, and hTERT provides the catalytic activity as well as various binding sites for other proteins involved in telomere maintenance.[287,290] In cancer cells, hTERT is the limiting factor, as hTERT is expressed from up to tens of mRNA copies per cell on average versus tens of thousands of hTR RNA molecules.[291,292] In addition to regulating telomerase activity via hTERT levels, hTERT mRNA can be subject to alternative splicing that results in catalytically inactive protein.[293] More than 20 alternative splice variants have been discovered, with only the full-length variant exhibiting telomerase activity.[293,294] However, several studies have shown non-enzymatic roles for telomerase, including some of the alternative splice variants.[293] Alpha and beta splice variants are the most frequently observed as well as the best studied, and both have been shown to inhibit telomerase activity.[293,295,296]

While telomerase and the roles of these splice variants have been extensively examined on a population or ensemble level using pools of presumably homogeneous cells, it is unknown how telomerase is expressed at the single cell level. This question is particularly important in the case of tumors, where accumulated mutations can result in highly heterogeneous cell populations.[18,19,297] However, even healthy normal cells have been shown to exhibit high levels of heterogeneity and gene expression bimodality in response to stimuli.[23] Understanding telomerase expression at the single cell level could clarify the role of alternative splice variants during cell division and colony formation. In particular, it is unclear from population-level studies, whether

single cells produce only one or more splice variants, and what role if any alternative splicing plays in response to environmental stimuli. These questions could be important in understanding cancer progression and in understanding the possible role of cell heterogeneity in therapeutic response.

Single cell culture is required to determine cell division rates and analyze telomerase in the daughter cells. Traditional single cell culture in titer plates is laborious and maintains cells at cell concentrations far below that of normal culture conditions, which opens up the possibility of introducing confounding effects due to altered environmental conditions. Microfluidic generators have been used to rapidly produce picoliter to nanoliter droplets with high uniformity for digital PCR, single cell analysis, and other applications requiring high throughput.[70,71,102] Emulsions have also been used for encapsulating and culturing various cell types, though the systems have not demonstrated robust single mammalian cell culture due to the use of droplet volumes too small to accommodate significant cell growth.[106,107] Development of a versatile single cell culture method that takes advantage of the parallelization and small volume scales of microfluidic emulsions would offer a platform for studying multiple parameters of cell physiology and genetics.

In this manuscript we describe and characterize a microfluidic emulsion-based method for culturing thousands of single cells in parallel and apply it to understanding the relationship of telomerase expression and hTERT splicing in the context of normal colony growth and growth with anti-cancer drug exposure. Jurkat and K562 cells in culture medium are encapsulated using a custom microfluidic droplet generator, as shown in Figure 9.1, to form thousands of independent 5.9 nL compartments that are cultured in a standard incubator. The droplet cultures enable growth of cells at rates comparable to that of bulk cultures, while the compartmentalization and ease of manipulation permits the monitoring of colony size and subsequent correlation of cell growth rates with gene expression. We use an optimized RT-PCR assay with single molecule sensitivity followed by high-resolution fragment analysis of amplicons to probe telomerase gene expression levels and hTERT splicing patterns in native cultures. Finally, we investigate the impact of sub-lethal curcumin concentrations in cell culture on cell growth, gene expression, and hTERT splicing to begin to reveal the mechanism of its anti-cancer action.

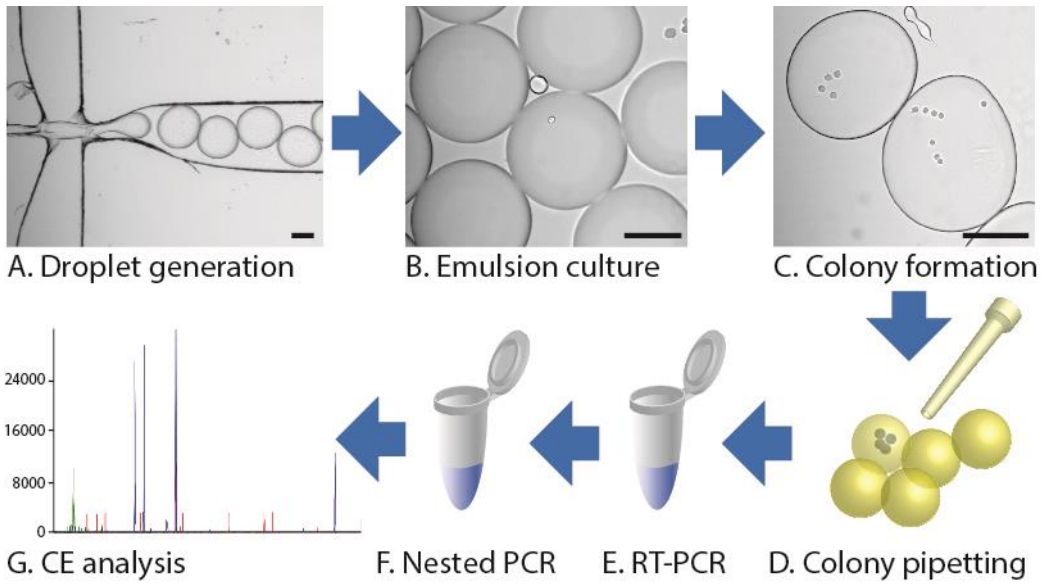

Figure 9.1. Workflow for single cell isolation, culture, and analysis. Single cells are encapsulated in uniform 5.9 nL emulsions of culture medium using a microfluidic droplet generator (A) to form thousands of segregated culture "reactors" (B), where single cells can grow to form colonies (C). Individual encapsulated colonies formed from the founding cells are pipetted (D) into RT-PCR reactions (E) followed by nested PCR reamplification (F) for gene expression analysis of fluorescently labeled amplicons using capillary electrophoresis (CE) fragment analysis (G). Alternatively, colonies can be transferred to cell culture plates for subculture and further analysis. Scale bars are 100 μm.

9.3 Materials and methods

Microfluidic droplet generator fabrication. The droplet generator design (see Figure 9.1A) was created using AutoCAD (Autodesk), and a negative mold was cut into ScotchCal vinyl adhesive film (3M) using a Graphtec Craft Robo Pro CE5000-40 cutting plotter (Graphtec America) as described previously.[298] The 125 μm high channels were transferred into a polystyrene Petri dish, and a polydimethylsiloxane (PDMS; 10:1 base:curing agent) device was cast from the sticker mold by pouring the PDMS mixture over the mold, degassing to remove trapped air bubbles, and curing at 65 °C overnight. Via holes were formed using a 0.75 mm biopsy punch (Ted Pella), and the approximately 5-mm thick device was bonded to a glass microscope slide following O_2 plasma treatment and baked at 70 °C for 5 min to facilitate adhesion. The channels were made hydrophobic by treating with 0.1% (heptadecafluoro-1,1,2,2-tetrahydrodecyl) dimethylchlorosilane (Gelest) in 100% ethanol for 10 min, followed by baking at 100 °C overnight. Devices were reused by flushing with ethanol and distilled water.

Cell encapsulation and culture. Droplets for cell encapsulation and culture were generated using an aqueous phase consisting of 0.5% Pluronic F68 (#P1300, Sigma-Aldrich), RPMI 1640 medium with L-glutamine (#11875-093, Gibco) supplemented with 20% fetal bovine serum (#16000-036, Gibco) and 1X PenStrep (#S108, Axenia Biologix). Cells were diluted to less than 0.1 cells per droplet in order to minimize the chance of co-encapsulation of multiple cells. Droplet Digital PCR fluorinated oil containing surfactant (Bio-Rad) was used as the continuous phase. Both liquid phases were actuated by a PHD 2000 infusion pump (Harvard Apparatus) with Hamilton syringes (gas tight #1001 for oil phase, gas tight #1750 for aqueous phase) at 20 and 30 μL/min flow rates, respectively, to produce 5.9 nL droplets. Syringes, tubing, and chips were cleaned with ethanol and dried with N_2 prior to each droplet generation session. Droplets were collected in 0.5 mL PCR tubes containing 250 μL oil. Encapsulated cells were incubated in a humidified atmosphere at 37 °C and 5% CO_2. Caps were punctured with a 1 mm biopsy punch to allow oxygen and CO_2 flow to the cell colonies. Fluorinated oil allowed for diffusive passage of oxygen and CO_2 in and out of droplets.

Bulk cell culture. Jurkat and K562 cell lines were maintained at 37 °C in a humidified 5% CO_2 atmosphere in RPMI 1640 medium with L-glutamine (#11875-093, Gibco) supplemented with 10% fetal bovine serum (FBS, #16000-036, Gibco) and 1X PenStrep (#S108, Axenia Biologix). Cultures were maintained between 10^5 and 10^6 cells/mL. For bulk culture control experiments, FBS and cell concentrations were adjusted to those of droplet cultures. Cells in log growth phase were used for all experiments.

Curcumin treatment. Curcumin powder (#C1386, Sigma-Aldrich) was dissolved to 10 mM in DMSO and stored at -20 °C in single-use aliquots. Fresh working solutions were prepared by dilution in DMSO and added directly to cell cultures to a final concentration of 0.1% DMSO. Equal concentrations of pure DMSO were used for control cultures. Bulk cultures were maintained in 2 mL total volume in cell culture plates.

Direct RT-PCR from colonies. Droplets were poured into a Petri dish containing a layer of emulsion oil, visualized at 10X magnification using a light microscope, and randomly sampled with a micropipette and MiniFlex gel loading tips (10 μL 0.17 mm inner diameter, #17360, Sorenson Bioscience). The colonies were deposited directly into 25 μL RT-PCR reactions

containing 1X PCR Buffer (Invitrogen), 3 mM $MgCl_2$, 0.2 mM dNTPs, 0.15 mg/mL heat-denatured bovine serum albumin (BSA; #A3803, Sigma-Aldrich), 5 mM DTT (Invitrogen), 1 unit/μL Superase In (Ambion), 10 units/μL SuperScript III (Invitrogen), 0.05 units/μL Platinum Taq (Invitrogen), 0.1% Triton X-100, 1 M betaine, 0.3 μM first round hTERT primers, 0.03 μM first round hTR primers, and 0.03 μM first round GAPDH primers. To accommodate RNA targets with varying amounts of secondary structure, a reverse transcription step of 50 °C for 15 min, 65 °C for 1 min, cold block (-20 °C) incubation for approximately 2 min, followed by additional reverse transcription at 25 °C for 10 min and 50 °C for 10 min was implemented. PCR amplification consisted of an initial heat activation step at 95 °C for 2 min followed by 15 cycles of 95 °C for 15 sec, annealing at 62 °C for 30 sec, and extension at 72 °C for 1 min, with a final 72 °C extension step for 10 min. Primers were modified from the work of Yi et al. [291] and were purchased from Integrated DNA Technologies. See Table F1 for sequence details.

Hemi-nested PCR. Reamplification reactions using hemi-nested primers contained 1X PCR buffer, 3 mM $MgCl_2$, 0.2 mM dNTPs, 0.025 units/μL Platinum Taq (Invitrogen), 1 M betaine, 0.15 μM hemi-nested hTERT primers, 0.15 μM hemi-nested hTR primers, 0.075 μM hemi-nested GAPDH primers, and 1 μL template from RT-PCR. Thermocycling consisted of an initial denaturation step at 95 °C for 2 min followed by 35 cycles of denaturation at 95 °C for 15 sec, annealing at 62 °C for 30 sec, and extension at 72 °C for 1 min, with a final extension step at 72 °C for 10 min.

Fragment sizing. To visualize and quantify fluorescently labeled amplicons, 0.5 mL of sample was added to 10 μL deionized formamide containing 2.5% GeneScan 500 ROX Sizing Standard (Applied Biosystems). Samples were analyzed on an ABI PRISM 3700 by the UC Berkeley DNA Sequencing Facility, and data were visualized and exported using Peak Scanner Software v. 1.0 (Applied Biosystems). Areas of target peaks were extracted using a custom MATLAB (The Mathworks) script and verified visually.

Subculture of colonies. Single colonies at day 2 post-encapsulation were collected by pipetting and placed in round-bottom wells in 96-well plates containing 50 μL RPMI 1640 medium with L-glutamine (#11875-093, Gibco) supplemented with 20% fetal bovine serum (#16000-036, Gibco) and 1X PenStrep (#S108, Axenia Biologix) and maintained at 37 °C in a humidified 5% CO_2 atmosphere. Cultures were increased to 100 μL after 2 days and were supplemented with 50% fresh medium every 3-4 days.

Data analysis. Peak areas for each target were normalized to cell number. Only reactions with GAPDH peaks were considered successful studies of live cells and were used in subsequent analyses. Plots depict means with standard deviation unless indicated otherwise. Hartigan's Dip Test was implemented in MATLAB (The Mathworks) and used to determine statistically significant deviation from unimodality.[299,300] Of the available statistical tests and bimodality indices, this test has been found to most accurately determine multimodality.[301] A two-tailed Student's t-test was used to assess growth rate differences between curcumin-treated and untreated cells. The Mann-Whitney U test (VassarStats) was applied to expression data for curcumin experiments, and threshold probability of $p \leq 0.01$ and fold change >2 or <0.5 were used to determine statistical significance and biological significance, respectively.

9.4 Results

Cell encapsulation and culture in microdroplets. To assess the growth rate of single cells at conditions comparable to standard cell culture, we utilized microfluidic droplet generators (μDG) to encapsulate single lymphocyte cells in segregated reactors. The cross-channel μDG nozzle design with continuous, syringe pump-driven flow of both oil and culture medium produced 3.4, 5.9, and 11.4 nL volume droplets at oil:medium flow rates of 30:20, 20:30, and 12.5:35 μL/min, respectively. Fluorocarbon oil with a biocompatible surfactant facilitated robust emulsions while being highly permeable to O_2 and CO_2. Cells were diluted to statistically dilute concentrations of less than 0.1 cells per droplet on average to minimize co-encapsulation of multiple cells in single droplets. The mean cell concentration was confirmed with microscopy.

The droplet volumes were selected in order to achieve single cell growth rates comparable to that of bulk cultures. Specifically, single cells in 3.4, 5.9, and 11.4 nL droplets correspond to approximately 87,000, 170,000, and 300,000 cells/mL, which spans the lower concentration range when passaging lymphoblasts. Due to the digital nature of encapsulation, the effective cell concentration in droplets with single cells relies solely on droplet volume and further dilution of cells only increases the number of empty droplets. Figure 9.2 compares the growth rate of encapsulated Jurkat cells with bulk cultures started at similar effective cell concentrations. Encapsulated Jurkats parallel the growth trajectory of bulk cell populations at least until day 2 when nutrients are used up in the 3.4 nL droplets, as evidenced by the sharp decline in cell concentration on day 3 for the smallest droplet size. The starting cell concentration has a significant effect on the average growth rate for several days, with higher starting cell concentrations in both bulk and droplet cultures showing shorter doubling times than low starting concentrations. The distribution of colony sizes in Figure F1 indicates that larger droplet volumes resulted in highly variable growth rates for daughter cells. We therefore selected 5.9 nL droplet volumes for subsequent experiments.

Multiplex RT-PCR assay for hTR, hTERT, and GAPDH quantitation. To simultaneously measure targets with a wide range of expression levels in single cells, we developed and optimized a multiplex RT-PCR assay followed by hemi-nested PCR reamplification. A critical requirement was the ability to detect single molecules of the four hTERT α and β mRNA splice variants while detecting hTR RNA despite its strong secondary structure and relatively high transcription level in cancer cells.[290] The RT-PCR reagents chosen enable direct addition of single cells or colonies in order to avoid lengthy RNA extraction steps, template degradation, and an associated decrease in sensitivity. Triton X-100 detergent lyses the cell membranes, while dithiothreitol (DTT) and an RNAse inhibitor stabilize the RNA molecules. GAPDH and hTR primer concentrations were decreased 10-fold versus hTERT primers to avoid overwhelming the reaction with these highly transcribed targets. Finally, the inclusion of 1M betaine as an isostabilizing agent and the implementation of a rapid cooling step during reverse transcription, allowed us to overcome the inhibitory effect of hTR secondary structure formation without affecting other targets. A second, hemi-nested PCR step following the initial reverse transcription and 15 cycles of highly specific PCR allowed for strong amplification of targets with additional specificity and low bias. In Figure 9.3A, the result of a bulk cell experiment with 100 Jurkat cells shows the electropherogram output with fluorescently labeled amplicon peaks where hTR, GAPDH and the four telomerase splice variants are seen.

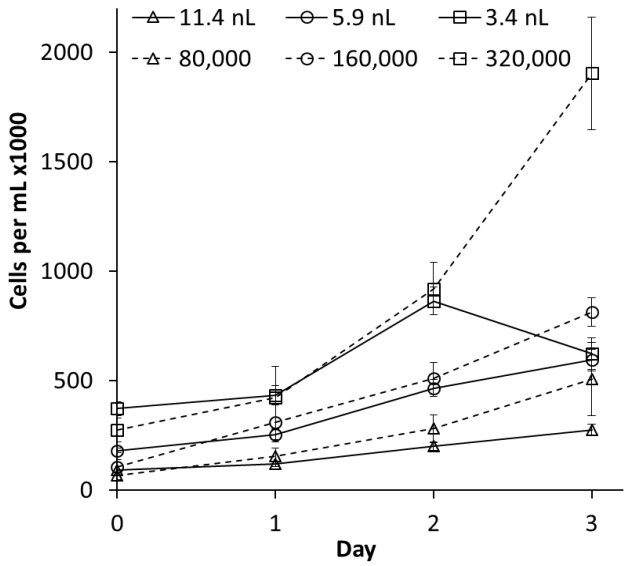

Figure 9.2. Growth rate of Jurkat T cells in 3.4 to 11.4 nL droplets (solid lines) compares favorably with bulk cell cultures at equivalent starting cell concentrations of 80,000 to 32,000 cells per mL (dashed lines). The smallest droplets (squares) do not have adequate nutrients to maintain larger colonies after two days. The large 11.4 nL droplets (triangles) result in extremely slow growth rates. As a result, 5.9 nL droplets (circles) were selected for subsequent experiments. Mean ± standard error shown.

We confirmed assay sensitivity by performing RT-PCR and reamplification on serial dilutions of a 10 Jurkat cells/μL lysate. For each target at each input concentration, the frequency of positive reactions is plotted in Figure 9.3B. For the various splice variants the frequency of positive reactions follows the Poisson distribution, indicating the ability to detect single molecules. Least squares fitting of the frequencies to the λ variable of the Poisson distribution, shown in dashed lines for each target in Figure 9.3B, permitted an estimate of the average number of hTERT splice variant molecules per cell: 1.4 α–/β–, 12.5 α+/β–, 0.16 α–/β+, and 0.19 α+/β+. This agrees with a prior qPCR-derived estimate of 0.44 α+/β+ and 15 total hTERT mRNA copies per cell on average in HL60 promyelocytic leukemia cells, the most similar cell line tested by Yi et al.[291] Absolute GAPDH and hTR copy numbers were difficult to assess due to the significantly lower primer concentrations intentionally used to decrease the reverse transcription efficiency. Nevertheless, even those targets are detected with single molecule sensitivity once the RNA is reverse transcribed. Lastly, we confirmed the lack of significant competition between the assay targets by observing the correlation between expression of hTERT and hTR. The plot of hTR versus hTERT levels in Figure F2 shows minimal correlation (R^2 = 0.0046), indicating low amplification competition as expected from independent primer sets used with homogeneous templates. Furthermore, no bias was observed between the 4 possible hTERT splice variants, presumably due to using a single primer pair to amplify them.

Single colony gene expression and splicing co-occurrence analysis. Jurkat and K562 lymphocyte cells were analyzed at one day intervals using the multiplex RT-PCR assay to investigate the co-occurrence of alternatively spliced hTERT mRNA variants and hTR and to examine changes in these patterns during colony growth. Figure 9.4 shows the results of the analysis for Jurkat (A) and K562 cells (B) on each of the three days of culture ordered by total hTERT expression. On day 0, soon after encapsulation, colonies consisted almost exclusively of single cells, and both cell types exhibit a highly variable expression pattern. Day 0 samples exhibit many cells that express a single splice variant as essentially the only hTERT molecules present. On subsequent days, this trend is overtaken by increased co-occurrence of multiple splice variants, presumably due to the presence of multiple cells in each colony. This finding suggests that single cells are largely expressing one splice variant at a time and that appreciable synchronization of splicing does not exist among daughter cells. In cells and colonies with minimal or no hTERT expression, hTR makes up the majority of measured RNA. While this observation may suggest an anti-correlated relationship, in reality, absolute hTR levels per cell remained relatively stable during colony growth.

Expression of the full-length α+/β+ hTERT splice variant was sporadic at all days of culture, but Jurkat cells showed a general downregulation on day 2 that did not appear in K562 cells. The probability of α–/β– variant expression increases later in cell culture, which would suggest a correlation with decreased growth rate as cells begin to crowd the droplets. Indeed both the α–/β+ and α+/β– variants separately have been shown to be dominant negative inhibitors of telomerase activity, and α+/β– variant overexpression provides increased resistance to apoptosis.[295,296] These findings imply that colonies shift toward a greater probability of expressing alternatively spliced variants, in particular the α–/β– variant, presumably due to the changing microenvironment during culture.

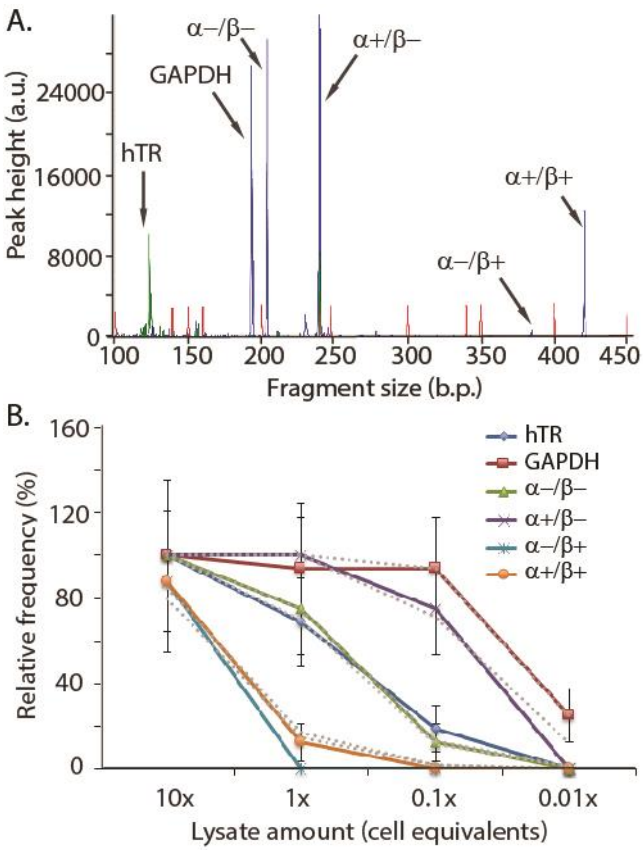

Figure 9.3. (A) Example of electrophoretic fragment analysis of multiplex RT-PCR from approximately 100 Jurkat cells used to simultaneously detect hTR, GAPDH, and 4 potential hTERT splice variants at the α and β splice sites. Primers fluorescently labeled with FITC (blue peaks) and HEX (green peaks) enable accurate product determination and sensitive quantitation. The red peaks are a ROX-labeled size standard. (B) Plot of frequency of positive output reactions versus serial dilutions of Jurkat cell lysate (solid lines) and the least squares Poisson distribution fit (dashed gray lines) for each target; close adherence to the Poisson distribution indicates single molecule detection sensitivity and allows estimation of copy number in each sample. The lysate amount equivalent to a single cell contained on average 1.4 α–/β–, 12.5 α+/β–, 0.16 α–/β+, and 0.19 α+/β+ hTERT copies per cell. Average GAPDH and hTR copy numbers could not be determined from this assay since the respective primer pairs were used at 10-fold lower concentrations compared to the hTERT primer pair in order to avoid amplification bias due to their very high native expression levels.

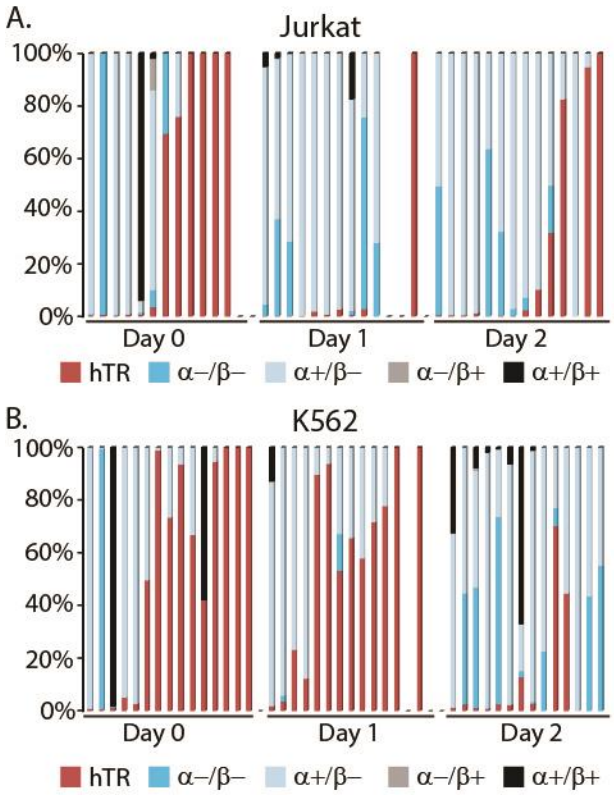

Figure 9.4. Single colony hTR and hTERT splice variant co-expression plots for (A) Jurkat and (B) K562 cells for days 0, 1, and 2. Each column represents results from one cell or colony. For each day, data are ordered by decreasing total hTERT expression levels. On day 0, when nearly all samples consist of single cells, hTERT consists of predominantly a single splice variant. Splice variants co-occur on other days presumably due to multiple cells present per sample, suggesting that a single cell expresses a single hTERT splice variant at any given time.

Bimodality of hTERT expression. hTERT expression is overall more heterogeneous than hTR at the single cell level. This variability persists throughout colony expansion and, unlike hTR, does not trend toward the population average. Figure 9.5A shows that while there is significant heterogeneity in hTR expression in single cells, colonies of both Jurkat and K562 cells converge to a less variable population average with increasing colony size. Furthermore, expression level frequency follows an approximately normal distribution that is statistically not bimodal. In contrast, the α+/β− variant exhibits significant bimodal expression in the K562 cell line (dip = 0.0823, p = 0.0424), best observed in the histogram of Figure 9.5C, which translates into bimodal total hTERT expression (dip = 0.0888, p = 0.0258). The α−/β− splice variant in K562 cells approaches bimodality, though the bimodality is not statistically significant (dip = 0.0906, p = 0.26). In Jurkat cells, both the α−/β− and α+/β− splice variants approach bimodality but do not attain statistical significance (dip = 0.0712, p = 0.472 and dip = 0.0563, p = 0.683, respectively). The α+/β+ full-length variant exhibits a negative correlation with colony size for both cell types, with a markedly more rapid decline for Jurkat cells compared to K562 cells.

Curcumin modulates hTERT expression and splicing. We sought to alter hTERT expression by exposing cells to sub-lethal curcumin concentrations in culture with the goal of observing mRNA expression and splicing modulation without a significant confounding effect caused by high apoptosis rates and other global changes. Curcumin has been shown to impact telomerase enzymatic activity through altered chaperone protein binding as well as expression levels.[302–304] We cultured K562 cells in several curcumin concentrations to determine a sub-lethal dose that would not have a significant growth impact on cells. Figure F3 summarizes the growth of K562 cells in bulk culture (A) and droplet cultures (B). In both droplet and bulk cultures, 10 μM curcumin significantly decreased growth rate, although growth remained positive. Growth rate differences between 1 μM curcumin and controls were not statistically significant on both days of culture (day 1: p = 0.218; day 2: p = 0.307). These results agree with prior assessments of curcumin effects on K562 cells, which found IC_{50} concentrations to be approximately 42 and 54 μM after 48 h exposure.[305,306]

Figure 9.6 presents total hTERT expression levels for control (A) and 1 μM curcumin-treated K562 cultures (B). On day 1, treated cells show nearly-bimodal total hTERT expression patterns similar to the strongly-bimodal controls, though the bimodality is statistically significant only for controls (Control: dip = 0.136, p < 0.0001; Curcumin: dip = 0.0995, p = 0.083). By the second day, however, curcumin treatment results in the disappearance of the low-hTERT population, while the control cells maintain bimodality (Control: dip = 0.111, p = 0.0054; Curcumin: dip = 0.0419, p = 0.993). The decreased bimodality, measured by the decrease in dip value, can be seen in the hTERT histograms.

Non-lethal curcumin exposure also disrupts hTERT splicing patterns. Figure 9.7 presents the expression level of hTR, GAPDH, and the four hTERT splice variants for control and curcumin-treated colonies. While hTR and GAPDH expression changes only subtly in magnitude between day 1 and 2, curcumin has a significant impact on hTERT splicing and expression levels. The two α− splice variants (C and E) are significantly upregulated on day 2 compared to curcumin-treated cells on day 1 and compared to controls on both days. The α+/β− variant (D) is highly expressed for most treated colonies on day 2, thereby decreasing the degree of bimodality compared to treated colonies on day 1 (Day 1: dip = 0.0995, p = 0.0888; Day 2: dip = 0.0463, p =

0.962) and on both days for control cells (Day 1: dip = 0.136 p = 0.0002; Day 2: dip = 0.112, p = 0.0044). Unexpectedly, the α+/β+ full-length hTERT mRNA is also upregulated following curcumin exposure, with treated cultures exhibiting a greater number of colonies expressing the full length product compared to controls.

The strong upregulation of α− splicing is evident from Figure 9.7G, which shows the fold change of mean expression levels of colonies from day 1 to day 2. Curcumin treatment results in a >100-fold statistically-significant increase in expression level signal for the two α− splice variants, whereas β− splicing is not significantly affected. Control cells show only a subtle change in the hTERT variant levels between the two days. GAPDH is downregulated approximately 3-fold for both controls and treated cells, while hTR decreases with a similar magnitude change only in control cells.

Colony subculture. To investigate the persistence of splice variant modulation following curcumin treatment, we subcultured single colonies of 2-9 cells in 96 well culture plates with 50 μL of culture medium lacking curcumin. Ten colonies each were pipetted from curcumin-treated droplet cultures and controls on day 2, and wells were examined using microscopy to confirm the successful transfer of the entire colony and droplet lysis. Figure F4A shows the success or failure of colonies for a given colony size. Both curcumin-treated and control colonies were well-represented and larger initial colony size resulted in more successful subcultures, but curcumin-treated colonies with fewer than 8 cells were much more likely to fail to grow. Twelve days following the initiation of subculture, 5-cell samples were analyzed using the multiplex RT-PCR assay. The results shown in Figure F4B indicate the recovery of hTERT bimodality and splicing from modulation due to the initial curcumin treatment, suggesting that hTERT splicing and expression changes are relatively temporary.

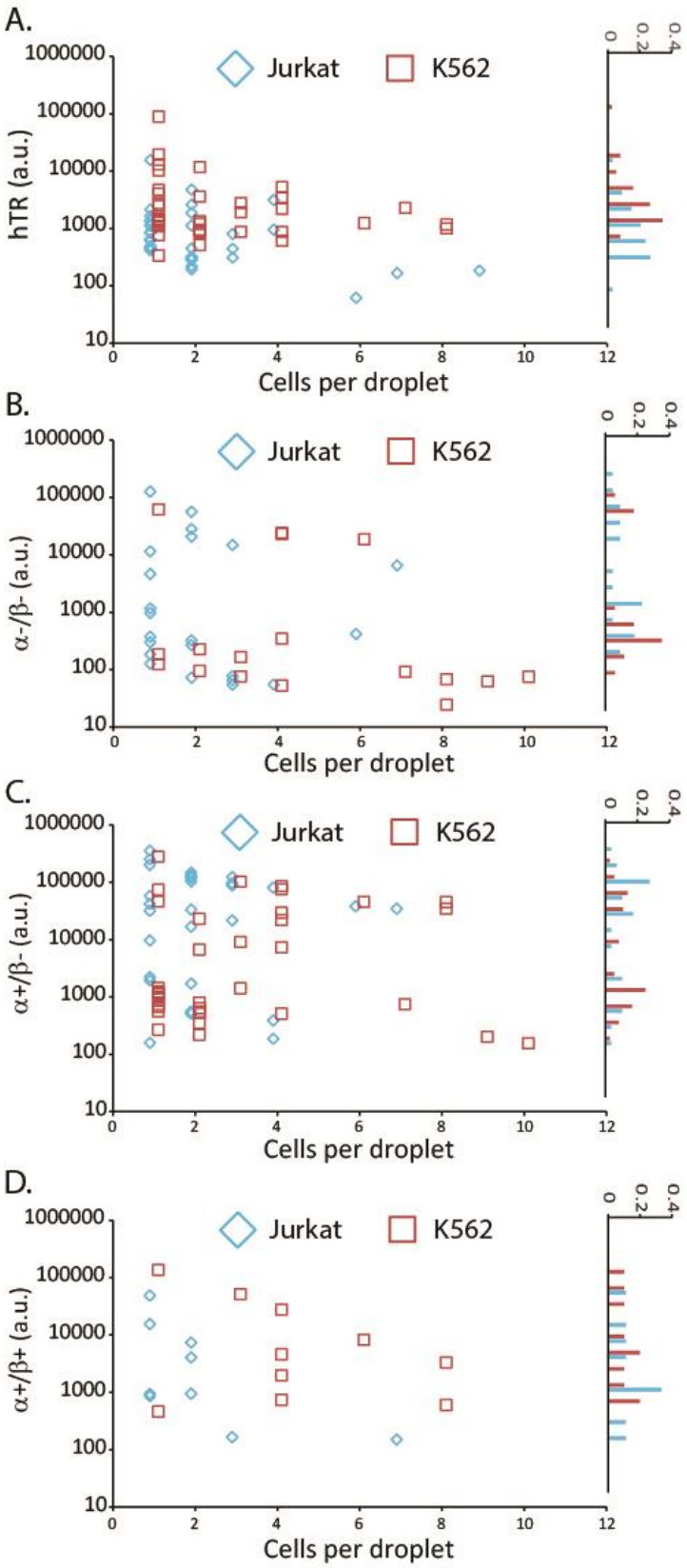
A.
Jurkat
K562
hTR (a.u.)
1000000
100000
10000
1000
100
10
0
2
4
6
8
10
12
Cells per droplet
0
0.2
0.4
B.
Jurkat
K562
α-/β- (a.u.)
Cells per droplet
C.
Jurkat
K562
α+/β- (a.u.)
Cells per droplet
D.
Jurkat
K562
α+/β+ (a.u.)
Cells per droplet

Figure 9.5. (A-D) Scatter plot of cell number per droplet versus gene expression for hTR and 3 hTERT variants (left graph in each panel) with corresponding histograms of expression level frequencies (right graph in each panel) for Jurkat (blue diamonds) and K562 (red squares) cell lines. The α−/β+ variant was not expressed in a significant number of colonies and was omitted. The α−/β− and α+/β− splice variants approach bimodal expression patterns in both cell types, though only the α+/β− splice variant in K562 cells is statistically significant (dip = 0.0823, p = 0.0424) hTR and the α+/β+ variant are not bimodally expressed.

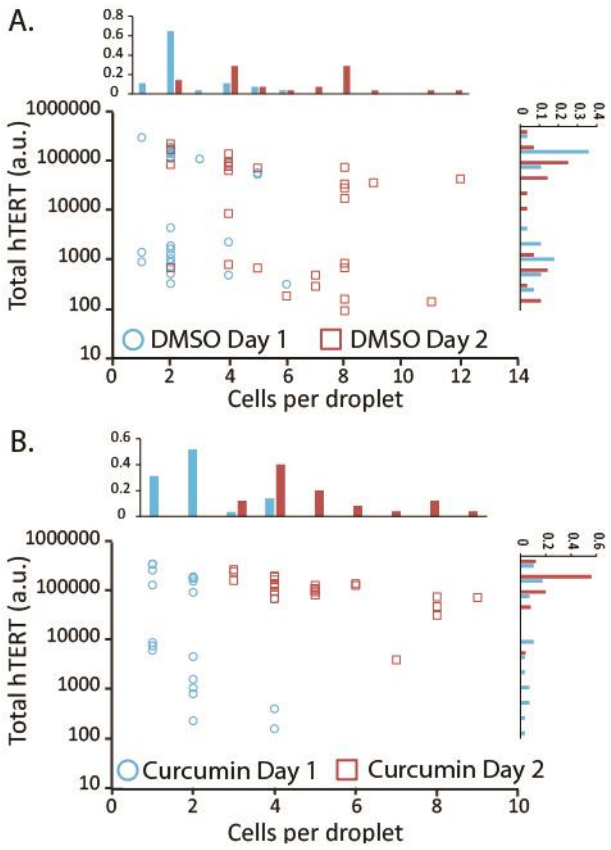

Figure 9.6. (A) Scatter plot of total hTERT expression levels versus cells per droplet for DMSO-treated control K562 cell cultures and associated normalized histograms of cells per droplets (top plot) and expression levels (right plot). Colony size, with peaks at 1, 2, 4, and 8 cells per droplet, indicates relatively synchronized daughter cell division rates. Significant bimodal total hTERT expression can be seen for both day 1 and 2 (Day 1: dip = 0.136, $p < 0.0001$; Day 2: dip = 0.111, $p = 0.0054$). (B) Scatter plot of total hTERT expression levels versus cells per droplet for 1 μM curcumin-treated K562 cell cultures and associated normalized histograms of cells per droplets (top plot) and expression levels (right plot). Curcumin treatment results in smaller colonies, and the frequency distribution is less focused around the expected exponential growth colony sizes. A decrease in hTERT expression bimodality occurs on day 2 (Day 1: dip = 0.0995, $p = 0.083$; Day 2: dip = 0.0419, $p = 0.993$).

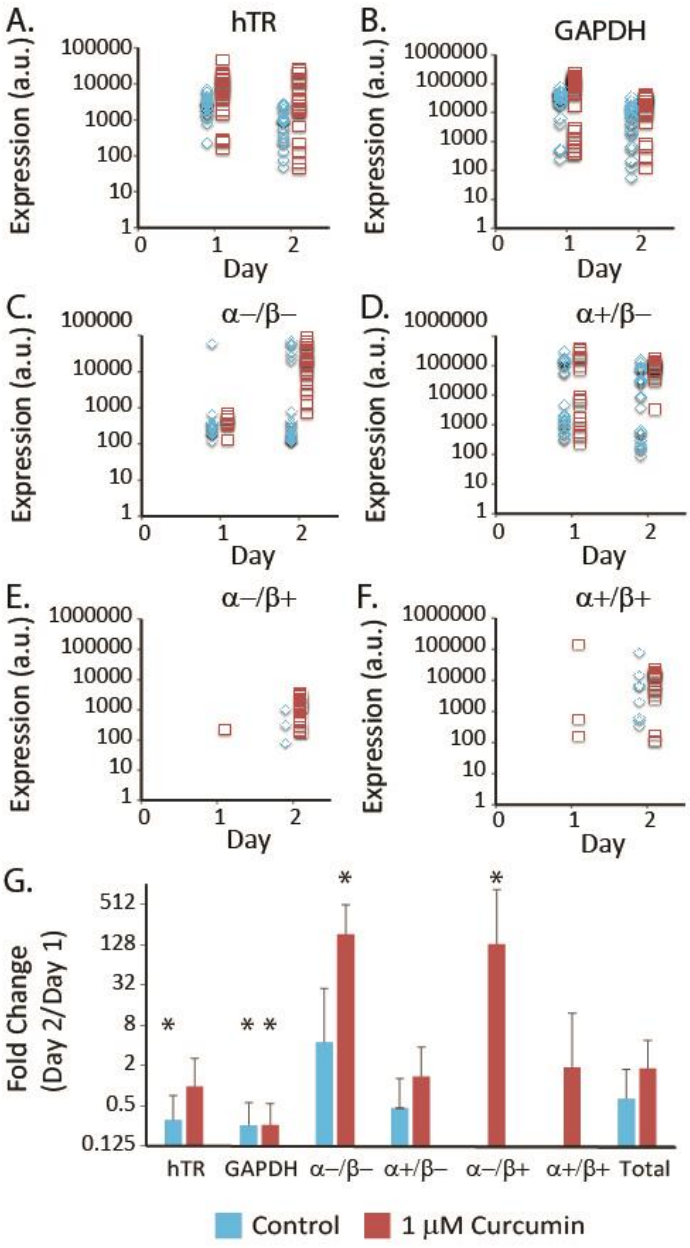

Figure 9.7. (A-F) Scatter plots of expression levels for all gene targets on days 1 and 2 for K562 cell cultures treated with DMSO (blue diamonds) and 1 μM curcumin (red squares). Curcumin treatment results in overall higher expression levels for all targets, but primarily increases expression of both enzymatically-inhibitory α– splice variants, thereby reducing bimodality of total hTERT expression. (G) Graph showing change in mean expression level from day 1 to day 2 for each target. Stars indicate statistically significant ($p < 0.01$) and biologically relevant (fold change > 2 or < 0.5) modulation of RNA levels between day 1 and day 2. The >100 fold increase in expression of α– variants on day 2 suggests a strong impact of curcumin on α– splicing at sub-lethal concentrations.

9.5 Discussion

While single cell analysis has shown great promise in examining pathway dynamics and understanding the role of noise and cell heterogeneity in evolution and disease, most existing methods have not allowed the investigation of multiple biological parameters for the same cell without the incorporation of fluorescent reporters [8,10,19] or have been limited to genes with higher levels of expression.[23] The versatile droplet-based single cell culture method presented here enables monitoring of cell growth, gene expression analysis, dosing with small molecules, and subculturing of single-cell-derived colonies. By encapsulating single cells in nanoliter-scale droplets, it is possible to culture individual cells at concentrations comparable to those of bulk cultures to avoid possible confounding effects of slow growth rates. This is particularly important for cell types that naturally grow at high cell densities. In addition, the rapid droplet generation process uses simple hardware and avoids extensive pipetting and cell sorting. The effective cell concentration experienced by cells is determined by the droplet volume, enabling highly accurate cell densities independent from the number of encapsulated cells. This droplet-based cell culture method can be applied to investigations of paracrine and endocrine signaling. By segregating single cells into independent compartments, complex cell-cell signaling can be eliminated and selectively reintroduced using soluble factors or co-culture of defined cell numbers and types. The approach can be extended to adherent cells by adding solid substrates, such as a bead or hydrogel, for attachment.[71] Thus, culture droplets as described here provide a convenient new tool for generating, culturing, and analyzing single cells for a wide range of applications, including multiparameter single cell analysis.

Culturing single Jurkat and K562 cells in droplets has enabled correlation of cell growth with telomerase gene expression and hTERT splicing. We have shown that the α+/β− splice variant in particular exhibits a high degree of gene expression bimodality independent of colony size, while the α+/β+ variant expression level exhibits a negative relationship with colony size. These results suggest that the full-length hTERT mRNA becomes downregulated as cells approach the droplet culture carrying capacity. In addition, the persistence of the α+/β− splice variant in larger colonies fits with previous studies that have correlated this splice variant with decreased telomerase activity.[293,295,307] The ratio of full-length hTERT to other splice variants may be more biologically relevant than the expression level of a single variant.

The persistence of bimodality in the α+/β− splice variant despite colony growth supports the presence of bursting dynamics of hTERT gene expression, since the occasional expression of a particular hTERT splice variant by relatively few cells would give rise to persistent bimodality among small colonies. As the gene is transcribed on the order of tens of copies per cell, the gene bursting behavior seen in other studies could apply here as well.[8,10] Depending on the frequency of transcription, relatively few cells should contain high levels of an expressed gene. Indeed, we observed single cells predominantly expressing single splice variants, with typically fewer than 25% of single cells containing relatively high levels of a particular splice variant. This low frequency and evidence of predominantly single splice variants per cell suggest that bursting behavior is extended to splice variants, with cells expressing bursts of single splice variants at a given time. This behavior may originate from the physical state of the hTERT DNA in the nucleus. Recent work has shown that chromosome architecture plays a dominant role in hTERT splicing, demonstrating the effect of accessible repetitive DNA in an hTERT minigene on alpha and beta splicing.[308] In addition, there is strong evidence that gene expression burst intervals, including

transcriptional regulation of hTERT, are closely tied to chromosomal architecture and nucleosome assembly and modifications.[309,310] Taken together, these findings point toward single hTERT splice variant bursts in individual cells.

Treating cells with sub-lethal curcumin concentrations enabled us to observe changes in hTERT levels and splicing without the confounding effect of decreased growth rates. Although the resulting 100-1000-fold increase in total hTERT expression signal and decreased expression bimodality was surprising, these findings can be explained by earlier work showing that the α–/β+ and α+/β− variants are inhibitors of telomerase activity,[295,296] and their upregulation may be counteracting the increase in full-length hTERT mRNA during translation. Our data suggest that the α–/β− variant also plays an inhibitory role. Increased active hTERT expression may be counteracted by a similar or greater upregulation of enzymatically-inhibitory alternative splice variants. In addition, studies showing a decrease in both hTERT expression and telomerase activity following curcumin exposure used significantly higher curcumin concentrations that resulted in apoptotic pathway upregulation and decreased cell viability.[303,304] Cui et al. tested 1 μM curcumin, among other concentrations, and found telomerase activity to decrease after 120 h but did not examine hTERT gene expression.[311]

Curcumin exposure also seems to slightly affect colony size by decreasing the number of very large colonies (>8 cells). This effect could be due to modulation of cell cycle; relatively synchronized daughter cell division, with most colonies having 1, 2, 4 or 8 cells, is evident in control cultures, while curcumin cell number frequencies have more intermediate colony sizes suggestive of unsychronized cell division. Indeed, curcumin has been shown to impact cell cycle through G2/M growth arrest in other cell lines.[304]

Upregulation of hTERT may also be a telomerase activity-independent response to stress caused by curcumin exposure. Akiyama et al. demonstrated that K562 cells overexpressing full-length hTERT were less sensitive to apoptosis induced by serum deprivation and double strand DNA breaks.[312] Listerman et al. found that overexpressing the α+/β− variant protected breast cancer cells from cisplatin-induced apoptosis *in vitro*.[295] Our results could indicate a similar protective role for the alpha splice variant as well, though further validation, including an investigation of the effects of curcumin on cell cycle, is needed.

Dosing cells at sub-lethal concentrations and performing single cell analysis of gene expression could enhance our understanding of therapeutic effects of compounds during drug screens. Drug testing has progressed toward screening extremely low concentrations of candidate drugs in Phase 0 trials using microdosing, where pharmaceutical dynamics and kinetics can be estimated from subtherapeutic doses and drug-drug interactions can be predicted safely.[313–315] However, microdosing requires highly sensitive mass spectroscopic approaches that may be difficult to scale to large sample sizes and reach broad adoption. Single cell droplet-based culture offers a new platform for drug screening that takes advantage of cellular heterogeneity. Rather than wait for whole-tissue effects to set in, low drug concentrations could be used to analyze effects on a subpopulation of cells and extrapolated to the bulk for higher concentrations. Furthermore, the effects on a subset of cells can be quite large if assayed at the single cell level, thereby providing a robust way to measure effects masked by the ensemble average. This method would have the advantage of faster turnaround times with the possibility of integrating RNA-seq for large scale, pathway-level analyses of a compound's biological effects. In addition, applying this approach to

tumor therapy as part of a personalized medicine approach could help identify tumor cells that can escape chemotherapy for further subculture and analysis.

Although our current method's bottleneck consists of manually selecting colonies for analysis, this step can be accelerated dramatically using microfluidic or conventional droplet sorting as demonstrated by several groups.[316,317] This would allow screening of thousands of colonies per experiment, limited only by the throughput of genetic analysis. Downstream integration of RNA-seq with single cell culture could dramatically increase the amount of information per cell, which could then be correlated with cell growth and other parameters. A similar single cell genomics approach has been used to understand pathways underlying the heterogeneous response of dendritic cells upon exposure to lipopolysaccharide.[23] Alternatively, both cell culture and analysis could be performed entirely in droplets using splitting and merging of droplets with additional reagents.[134] This approach benefits from high throughput and automation at the cost of greater device complexity.

In summary, the single cell culture method presented here offers a versatile platform for multiparameter analysis of various cell types, including the measurement of low-expression level genes. We show bimodal gene expression of hTERT splicing in single cells and demonstrate effects of sub-lethal curcumin doses on telomerase gene expression and splicing. Our findings suggest a significant role for hTERT alpha splicing in response to curcumin treatment. The combination of single cell culture and multiparameter analysis combined with low concentration drug dosing is a promising approach for understanding effects of drug treatment as part of early stage drug candidate screens and personalized medicine therapies.

9.6 Acknowledgements

The authors gratefully thank Francesca Gazzaniga, Imke Listerman, and Elizabeth Blackburn for invaluable advice and critical feedback, Fenna Sille for assistance with cell culture and providing cell lines, and the UC Berkeley DNA Sequencing Facility for processing fragment analysis samples and technical advice.

Section conclusion

Cells ultimately cannot be analyzed at just one biological level (DNA, RNA, protein, metabolism, etc…), however multiplexed it may be. The real value in single cell analysis is to connect DNA mutations with protein levels, gene expression with growth rate, and other, even more complex multiparameter analyses. Since a second cell cannot be used for this comparison, due to the concept of cellular noise introduced in Chapter 1, it is ultimately necessary to perform simultaneous analysis on single cells for each target parameter and only then combine the results for a population-level view of the process.

Droplets provide a practical platform for these types of studies. It is relatively straightforward to encapsulate cells at biologically-relevant concentrations, cells remain segregated from each other, and the droplets accumulate secreted products for analysis. Droplets provide a simple way to track growth rates, and application-specific large field imaging could increase throughput even further than described in this thesis. The colonies can be analyzed in virtually any downstream assay without complex fluidic manipulation. Although the droplets prevent cell-cell signaling, this component can be reintroduced artificially through addition of specific compounds or cells, facilitating a system for investigating cell-cell signaling and endocrine pathways at the single cell level. Finally, droplet contents can be sampled using mass spectroscopy for rapid metabolomic analysis of single cells. Whatever the application, droplets provide a versatile system for analyzing single cells at a throughput required for meaningful data that can be applied to heterogeneous cell populations. They allow disparate assays to be connected to single cells by providing a physical reactor or container of appropriate size to keep analytes from a single cell at a high detectable concentration. Growing cells in droplets enhances the capacity to investigate multiple biological parameters simultaneously.

Chapter 10: Prospects

10.1 Toward a holistic view of cell heterogeneity

This thesis has focused on applications of microfluidically generated droplets for quantitative and extremely sensitive analysis of single molecules and cells. It describes the evolution from initial droplet generator design optimization and increasing droplet robustness to single DNA molecule analysis, single cell genetic analysis, and lastly, multiparameter assays performed on single cells cultured in droplets. The works presented here highlights practical tools for investigating biological phenomena from the perspective of single cells rather than population averages. However, interactions between single cells are crucial to the understanding of tissue and organ function in healthy and diseased states. Since intrinsic noise results in a ripple effect of gene expression via extrinsic noise in a single cell, it is only natural to assume that this cell-cell variation will be amplified even further when heterogeneous cells interact. Some of it may truly average out, but some cases will result in unpredictable behavior far from the ensemble average. Droplets provide a suitable platform for isolating various stimuli and investigating the effect of a particular signaling molecule or drug, but droplets do not directly facilitate discovery and study of the complex network of interactions evident in tissues and between organs and organ systems. Aside from its undeniable scientific value, accurate comprehension of interaction pathways with the single cell point of view is a crucial step in moving drug development and testing beyond the current standards of animal testing followed by human clinical trials.

Over the last 5 years as a result of large strides in 3D cell culture innovation, there has been a push toward the development of organs-on-a-chip, or microfluidic systems that support the growth of functional miniature human organs.[72,318–320] The principal aim of these systems is the acceleration of drug testing by increasing screening efficacy. In traditional drug development, candidate compound libraries are screened for desired activity in cell lines, with further efficacy and safety studies occurring in animal models and, for the small pool of successful candidates, in a series of 3 human clinical trials. The main problem with this approach is the failure of vast numbers of compounds very late in the development process. In part, this is due to the lack of tissue and organ interactions during cell line testing, and due to animal models not being adequately representative of human disease states and drug side effects. It is also unclear how many candidates fail the screening process in animals but could still prove effective in humans. The proposed solution is to develop microscale human organs that can be linked together into a "human-on-a-chip."[321,322] This setup can then replace animal testing and accelerate drug development by providing a platform where it is possible to screen drugs for safety and efficacy in a human-like clinically-relevant setting. A number of organ systems and some connected organs have been published and significant funding is being allocated to their further development in the United States and European Union.[318,322–324] Despite the advances, less focus has been placed on analytical techniques that can be used to monitor cultures in real time. Analysis of supernatant for various metabolic and secreted protein products is critical for understanding the output of organs that may affect other systems within an individual, and this has been demonstrated for microfluidic cultures.[325] The Ertl group has demonstrated multiparameter real-time monitoring capabilities in simpler on-chip cultures, including electrical impedance and optical monitoring as well as 2D oxygen microenvironment sensing.[326–328] Yet nearly all devices so far have not incorporated robust fluid handling and multiplexing capability that would enable dynamic stimulation and analysis and leverage real-time sensing. Two projects in progress are presented here, which highlight possible paths for future microfluidic device development that would integrate the single cell perspective in the context of tissue and organ function.

10.2 Integrated microfluidic cell culture

To maximize the potential of microfluidic cell culture systems, additional integrated functions, including medium degassing and fluid actuation and routing, are required. These features eliminate bubble formation that is disruptive to cell and tissue layers in the confines of a microchannel, and the pumping provides a low dead volume actuator and fluid routing system for probing the effects of pulsed stimuli and drugs and for device loading and operation. As part of an ongoing collaboration with Peter Ertl's group at the Austrian Institute of Technology and the University of Natural Resources in Vienna, Austria, I incorporated a microdegasser and micropump for long-term microfluidic cell culture and robust operation.

The foundation of the microfluidic cell culture chip is a glass sensing layer composed of gold interdigitated electrodes with 5 and 20 μm pitch and passivated with a 200 nm thick SiN layer as shown in Figure 10.1A. It is fabricated via standard photolithography and gold deposition processes described previously.[326] A 250 μm thick PDMS flow cell, cut with a Graphtec computer controlled cutter, defines the cell culture chamber. Electrical impedance is sensed via a custom digital signal generator and impedance sensing circuit, shown in Figure 10.1B, that can analyze impedance at frequencies from 10 kHz to 100 kHz. The circuit is connected to a National Instruments digital acquisition card (NI USB-8541) and communicates via an I^2C interface. The connection is facilitated via spring-loaded pins in the circuit board and held in place in an aluminum manifold that contains two circuit boards and the microfluidic device. The manifold is maintained at 37 ^oC by continuous perfusion of water from an external heated reservoir. The entire assembly is situated under an upright microscope for time lapse imaging. In initial tests, glass with drilled via holes and glued connectors was used to seal the cell culture chamber. A syringe pump was used to provide continuous perfusion of fresh medium to cells after being passed through an HPLC degasser.

A.

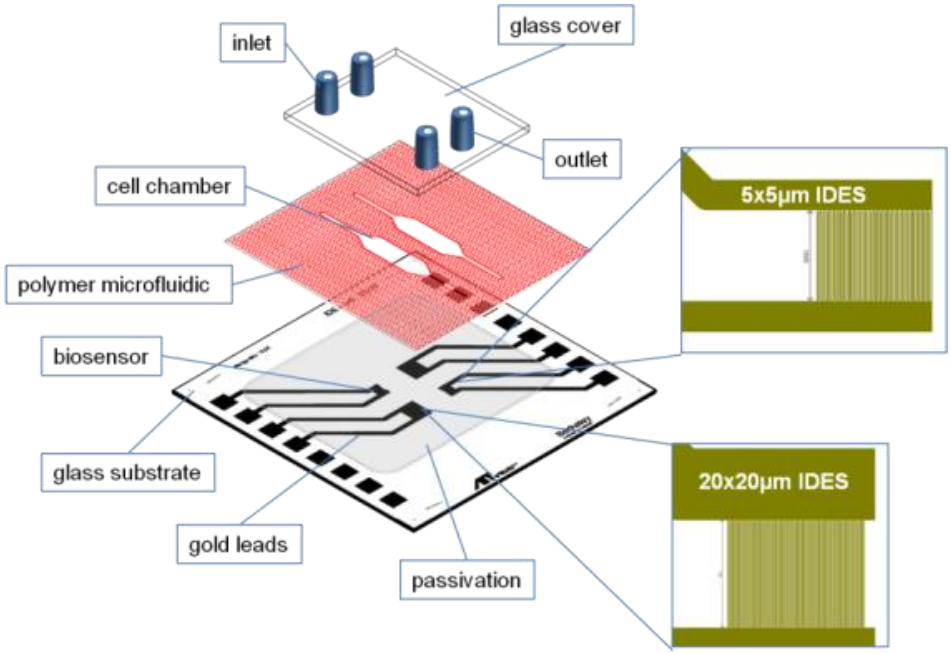

B.

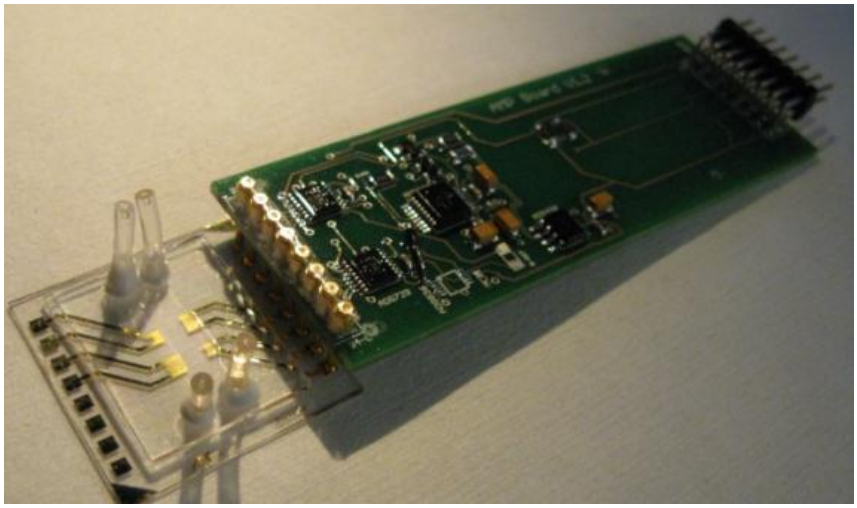

Figure 10.1. (A) Diagram of interdigitated electrodes and basic flow cell fluidics for real-time electrical impedance monitoring of microfluidic cell cultures. Gold electrodes with 5 and 20 µm pitch spacing sense at different channel heights. SiN passivation eliminates DC current and provides a homogenous surface for cell adhesion following coating with fibronectin or gelatin. (B) Microfluidic cell culture with integrated interdigitated electrode sensors shown connected to a custom impedance analyzer circuit. The surrounding aluminum manifold and second circuit board are omitted for clarity. Spring-loaded pins facilitate contact with the chip pads and enable quick chip exchange. The circuit board is connected to a National Instruments digital acquisition card for power and communication.

This simple system was used to maintain a co-culture of human vascular endothelial cells (HUVEC) and basophils as a model of vascular response to allergens. Basophils bind IgE and release histamine in response to antigen recognition. HUVECs are endothelial cells that line blood vessel walls and increase permeability in an allergy response.[329] Figure 10.2 presents the data obtained from this "allergy-on-chip" model system. The impedance measurement trace in Figure 10.2A shows the initial increase in impedance resulting from two serial HUVEC seedings. The cells were allowed to adhere and form a confluent layer over approximately 24 h. Basophils opsonized with IgE were added on top of the layer, best seen in Figure 10.2B, and also allowed to adhere. Due to the thickness of the HUVEC layer relative to the interdigitated electrode pitch, the top basophil layer did not significantly change the impedance sensor readout. However, the addition of antigen to the medium at 33 h resulted in a sudden decrease in impedance due to the release of histamine by the basophils causing increased HUVEC permeability. The data demonstrate the sensitivity provided by electrical impedance measurements that allow detection of subtle cellular properties not visible via microscopy.

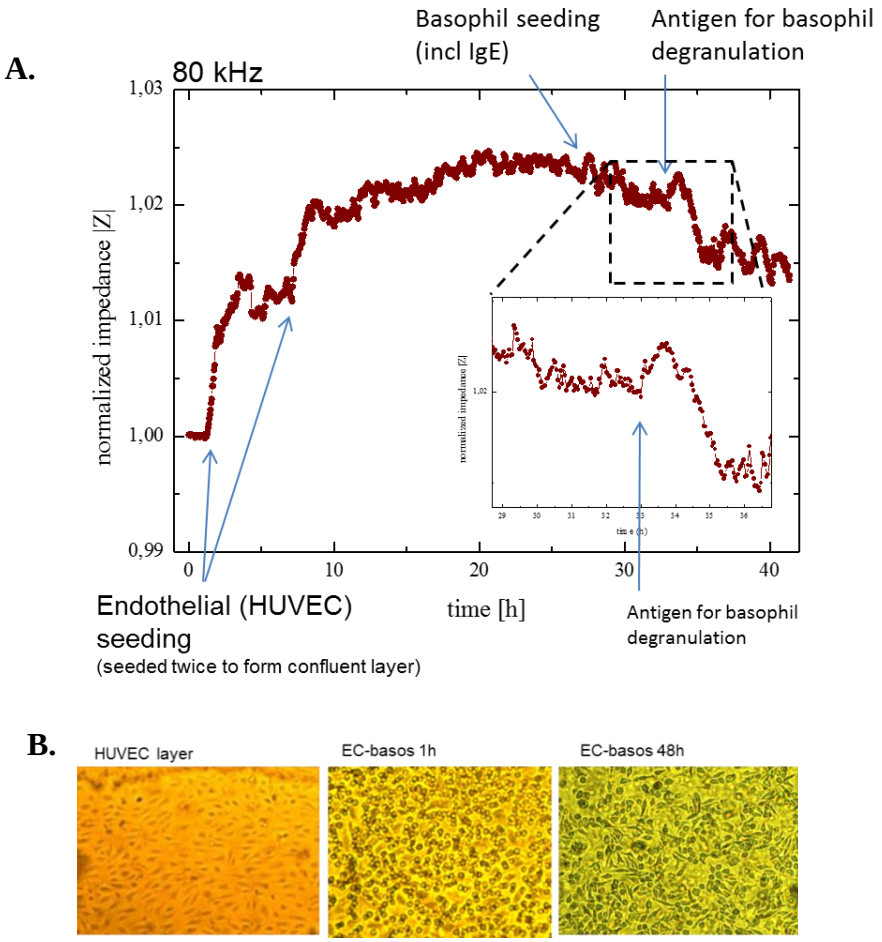

Figure 10.2. HUVEC and basophil co-culture for an allergy-on-chip model system. (A) A confluent layer of HUVECs was formed by two cell seedings, mimicking the artery wall. Basophils opsonized with IgE, while beyond the IDE sensor detection range, resulted in significant impedance shifts by perturbing the confluent endothelial cell layer following degranulation and histamine release. (B) Photographs demonstrate successful co-culture of confluent HUVEC layer with overlaid basophils that is stable for at least 2 days of culture.

This initial syringe pump-based setup limited usability and resulted in noisy electrical impedance data due to solution exchange causing cells to physically shift on the substrate. In addition, the commercial degasser dead volume not only required large culture medium volume but also eliminated the possibility to test short pulses of stimuli due to Taylor dispersion in the long degassing coils. The solution was to integrate pumping and degassing into a single device with the footprint matching that of the existing sensing chip and flow cell. Using rapid prototyping described earlier in this thesis,[298] we fabricated the device shown in Figures 10.3 and 10.4 from cycloolefin copolymer, which offered excellent biocompatibility and optical transparency. Figure 10.3 shows an exploded view of the device layers, highlighting the microfluidic components that provide medium actuation and enable cell loading, pneumatic controls and degassing, and the PDMS flow cell for cell culture. The degasser consists of a sinusoidal channel with a superimposed ladder-like pneumatic structure separated by a thin PDMS membrane. Since PDMS is gas permeable, a constant vacuum provides sufficient degassing to prevent bubble formation inside the device. The glass sensing layer forms the bottom of the cell culture chamber. The assembled device, shown as a diagram in Figure 10.4A and photographed in Figure 10.4B, occupies the space above the flow cell and sensor area, fitting into the existing manifold.

The micropump provides continuous perfusion to cells with minimal dead volume (~10 μL) while reversing the flow enables highly efficient loading of cells via the outlet. The micropump is controlled via a custom pneumatic control box, shown in Figure 10.5A. The control box is designed to be a portable standalone system for long-term use that only requires AC power, a vacuum source, and pressurized air. An Arduino processor and onboard memory controls a bank of three-way solenoid valves, described in greater detail in earlier chapters and published work.[70,102] Tubing connects the control box with the integrated device manifold. Regulated nitrogen and vacuum lines input the control box and are routed to the microfluidic device according to an uploaded program. By selecting actuation pressures and times, a broad range of flow rates (5-35 μL/min) can be achieved with the microfluidic design used here, as presented in Figure 10.5B. Cell cultures were maintained in excess of 7 days without bubble formation or loss of cell viability. The fully integrated approach offers a high degree of dosing precision, as each pump stoke contains a well-defined bolus of fluid, which can be used for metering of drugs or stimuli. In future design iterations, the device can incorporate additional fluidic inputs for automated reagent exchange, staining, and stimulation.

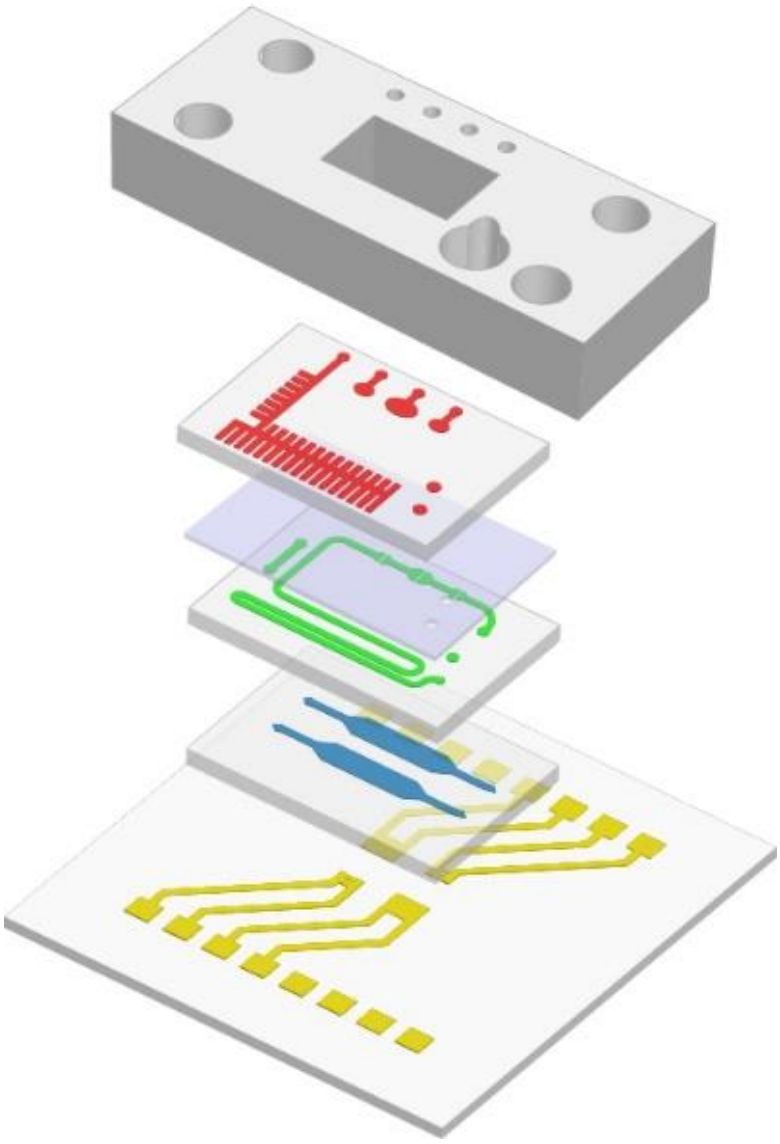

Figure 10.3. Exploded view of five-layer integrated microfluidic cell culture and analysis system showing impedance sensing IDES layer (gold), cell culture chambers (blue), microfluidic channels (green) separated by a thin PDMS sheet from the pneumatic control and degassing layer (red), and an aluminum manifold for ease of assembly and operation (gray).

A.

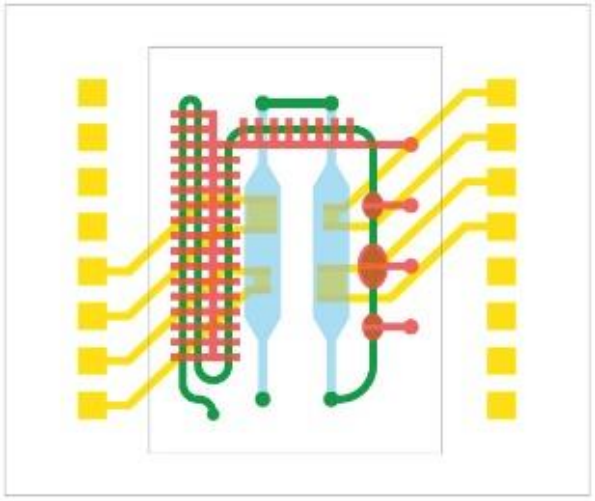

B.

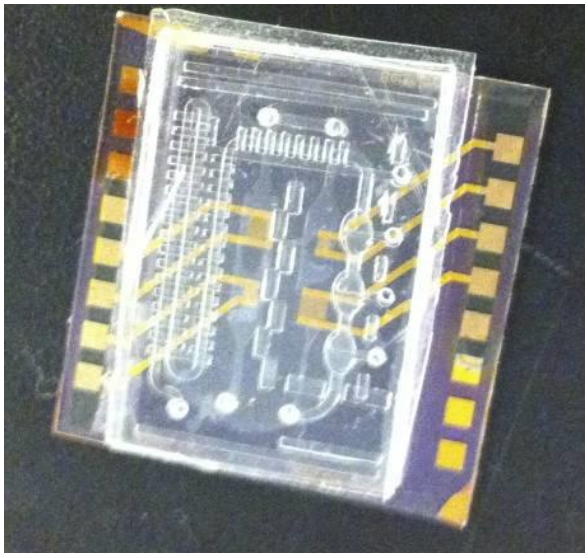

Figure 10.4. Assembled integrated microfluidic cell culture device (A) diagram and (B) photograph, showing the arrangement of microvalves for fluid actuation, an extended degassing region for bubble-free cell culture, and interdigitated electrodes for continuous non-invasive cell monitoring.

A.

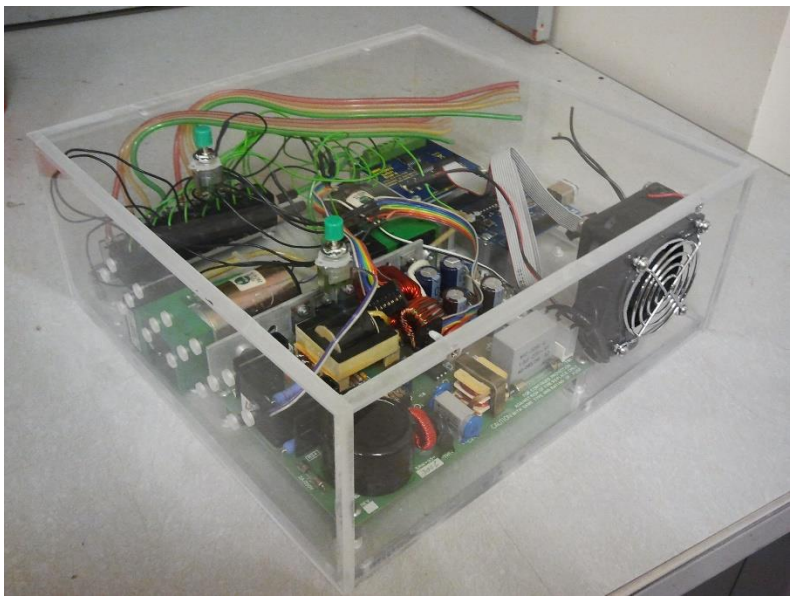

B.

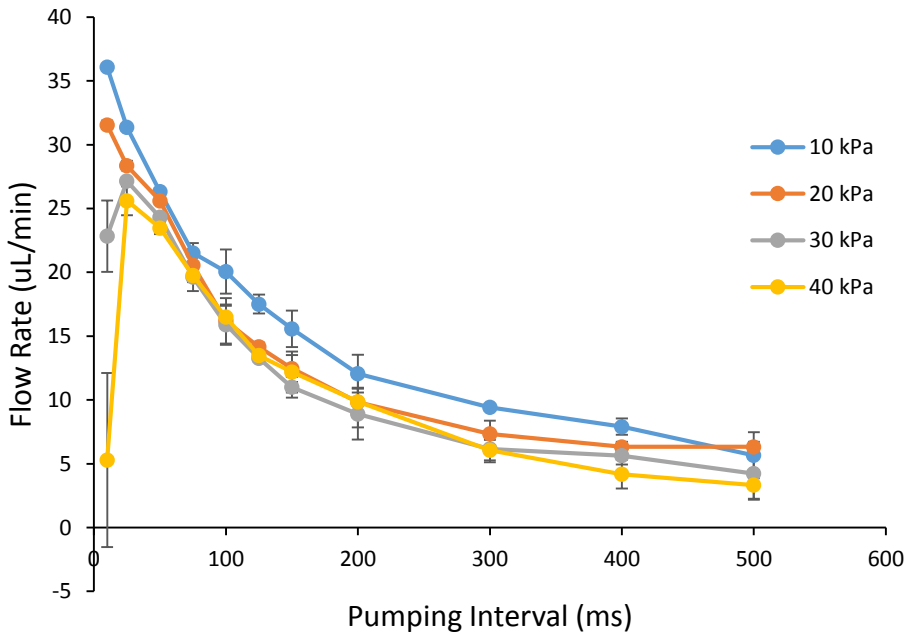

Figure 10.5. (A) Photograph of the standalone pneumatic control box used to control micropumps for cell loading and perfusion. Buttons in the lid select the pump sequence to be run. (B) Plot showing flow rate in μL/min as a function of pumping interval between each pump step at the specified actuation pressures. Vacuum was maintained at -40 kPa throughout.

10.3 Single cell analysis in an organ context

Microfluidic organs-on-chip and related tissue model systems offer an exciting opportunity to investigate single cell behavior. The relatively easy analytical access to these *in vitro* systems combined with real-time multiparameter assay capability provides a unique ability to monitor not only the tissue or organ as a whole but also the individual cells that compose it. Figure 10.6 shows an example of single cell analysis in the context of the allergy model system. In early tests of the basic impedance and optical monitoring platform, we observed basophil degranulation in response to an antigen in the culture medium. The impedance trace in Figure 10.6A shows a sudden increase following antigen exposure, followed by gradual recovery as the medium is exchanged. Although the impedance measurements describe the ensemble average, the micrographs in Figure 10.6B show a more nuanced story: prior to antigen exposure, all cells are stained relatively evenly with methylene blue, but following antigen exposure, there is a dramatic range of degranulation response among the cell population. This example alone demonstrates the need for incorporating high sensitivity, single cell resolution measurements in organ-on-chip systems. Such data will help clarify drug response, particularly when applied to genetically heterogeneous tumors. Rare tumor cells, such as cancer stem cells, may evade therapy and avoid detection when viewed at a population level, but a single cell resolution assay could improve drug efficacy and foster the development of personalized medicine approaches.

The concept of microdosing[314] is especially appropriate for organ-on-chip systems with single cell analysis capability. Although microdosing currently requires ultrasensitive mass spectroscopy for detecting subtle changes in drug availability and metabolite levels in human trials, single cell assays in organ-on-chip systems could provide a similar, if not greater, level of detail without expensive and specialized equipment. For example, a real-time single cell assay could identify the frequency of cells undergoing apoptosis. As with digital PCR, counting of individual cells provides greater accuracy and precision compared to bulk analog assays, enabling assays to discriminate between small changes. Using this approach, drug candidates could be screened for safety much more rapidly than current assays allow by observing any upticks in apoptotic cells in real time. As another example, basophils collected from a patient could be quantitatively screened *in vitro* for a range of allergens, as the assays require minimal numbers of cells and could provide a degree of antigen response with far greater accuracy than current skin prick tests. Although these tests are relatively basic, the concept of viewing tissue and organ behavior not as a population but as the additive response of individual heterogeneous cells that compose them will prove immensely informative. Future organ-on-chip designs will incorporate multiparameter analysis in real-time, along with current end-point immunostaining and other assays, for high-resolution single cell-level data for drug screening and clinical applications.

A.

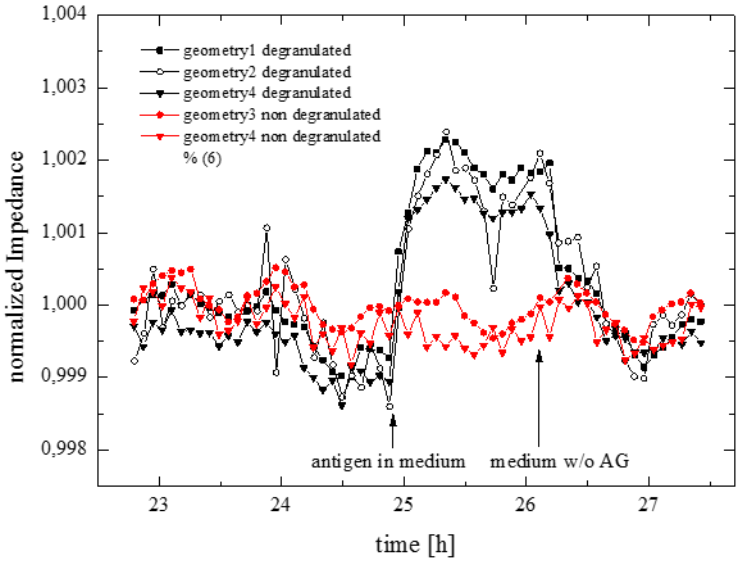

B.

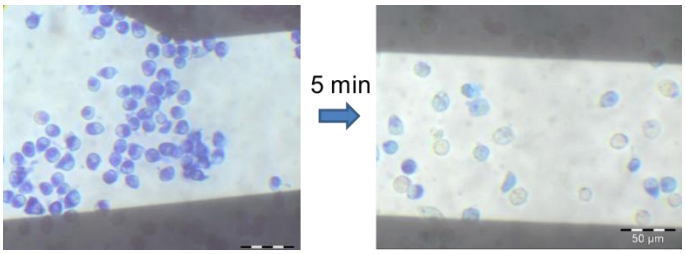

Figure 10.6. Basophil degranulation in a microfluidic device. (A) Electrical impedance measurements for an antigen-treated chamber (black) and a control (red) for several electrode geometries. Antigen addition results in increased impedance in the treated chamber only, while flushing with fresh medium results in basophil recovery over approximately 1 h. (B) Photographs of basophils stained with methylene blue show granulated cells (left) and substantial degranulation (right) following antigen addition.

10.4 Time-resolved immunoassay of microculture medium

Analyzing secreted metabolites and proteins is an attractive means of monitoring organs-on-chip and other cultures with very small cell numbers, enabling assessment of inflammation and metabolic status.[325,330] It can provide the information needed to connect single cell-level phenotypes with population-level behavior. The addition of highly multiplexed real-time measurement of the secretome would add to our understanding of organ model systems.

The scale of microfluidic systems combined with constant perfusion of fresh medium are a double edged sword. On the one hand, organs-on-chip provide the capability to perform dynamic studies of cellular response. For example, pulsed doses can be delivered and removed with very high time resolution and with predictable changes in local concentration due to diffusion. On the other hand, microfluidic systems simply do not produce amounts of secreted protein or metabolites sufficient for traditional bulk scale assays. Collecting large volumes of culture medium can overcome the lack of analyte, but this then prevents dynamic studies of cell behavior that is necessary to observe in real-time or near real-time. This technological barrier must be overcome to enable sensitive analysis of organ-on-chip secretomes.

As part of the Marshal Plan Scholarship, I worked in the Ertl group to devise a way to measure secreted interleukin 6 (IL-6) inflammatory cytokine from stimulated fibroblasts with very high time resolution. Figure 10.7 presents the microfluidic processor for multiplexed, time-resolved immunoassays. The device allows 6 samples to be serially monitored by a single sensor functionalized with anti-IL-6 capture antibodies.

The microfluidic device was fabricated using the optimized nickel mold fabrication and hot embossing protocol described in Chapter 4, with the final device embossed into 1 mm-thick polycarbonate sheets. A 250 μm-thick PDMS membrane sandwiched between the fluidic and pneumatic layers provides valving and pumping capability. Bus valves, best seen in Figure 10.7A, allow liquid to pass through the main fluidic channel even when valves to other inputs are closed. As in the integrated micropump-actuated cell culture system, a custom pneumatic control box shown in Figure 10.7C controls on-chip pumping and reagent selection through microvalve regulation. The compact form factor enables the microfluidic device to be set up in various SPR systems and easily resituated.

Figure 10.8 presents the experimental setup for initial time-resolved immunoassay characterization. The sensor consists of a sheet of glass with a 45 nm evaporated gold layer that is functionalized with a biotinylated thiol self-assembled monolayer, followed by streptavidin and, later, biotinylated anti-IL-6 capture antibodies. The glass is coupled to a prism in a standard Kretchmann configuration. A 633 nm laser beam is used for illumination. The beam is passed through a 1 kHz beam chopper and detected by the SPR CCD detector using a lock-in amplifier to remove extraneous signals, including ambient light. The SPR setup is mounted on a computer-controlled dual stepper motor gantry that enables accurate angular positioning. Fluidic coupling is achieved by a Teflon and glass flow cell, approximately 9 mm by 15 mm and 100 μm high. The microfluidic device programmatically selects sample inputs and reagents and pumps them via the integrated micropump through the flow cell.

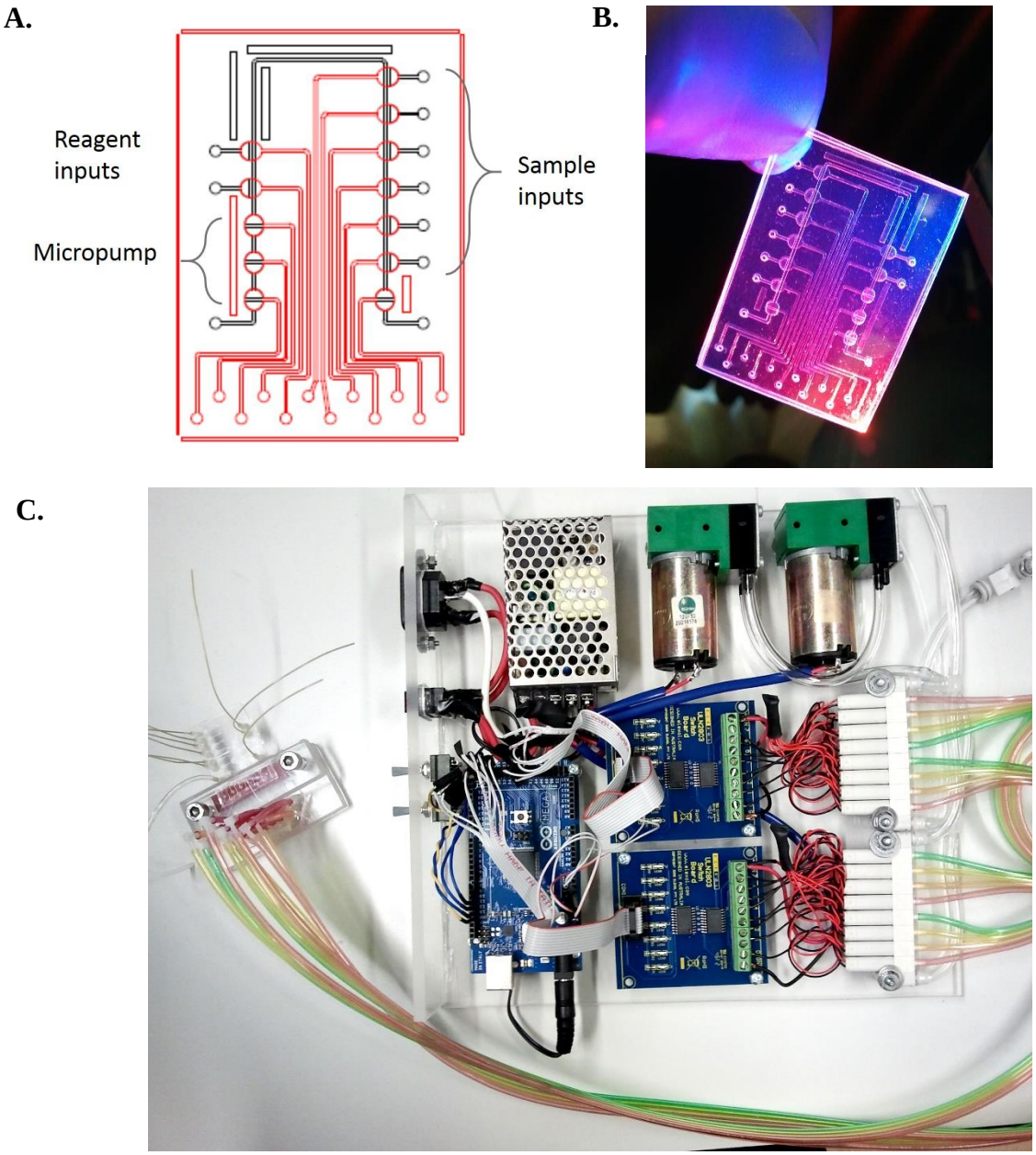

Figure 10.7. Microfluidic processor for time-resolved immunoassays. (A) Diagram of microfluidic design for routing 6 samples to a sensor and providing supporting reagents for washing between samples, labeling with fluorescent secondary antibody, and regenerating sensor surface. The pneumatic lines (red) control PDMS membrane valves along the fluidic line (black), enabling fully automated immunoassays through programmable valving and integrated pumping. (B) Photograph of assembled device fabricated from polycarbonate using the rapid prototyping method described in Chapter 4. (C) Custom pneumatic control box for portable microfluidic control of pumping and fluid routing connected to the microfluidic device in a manifold on the left. An Arduino processor enables complex programs to be uploaded and run by toggling control buttons.

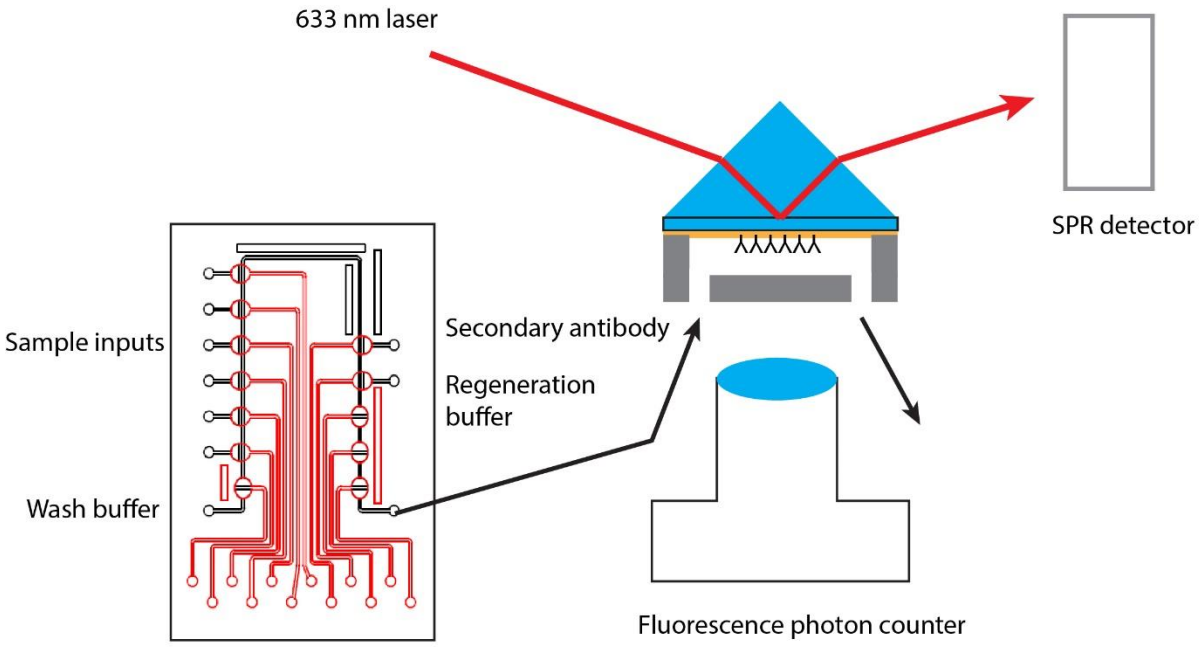

Figure 10.8. Diagram of time-resolved immunoassay experimental layout. The microfluidic processor on the left controls reagent selection and provides fluid actuation through an integrated micropump. Inputs are sampled serially for a capacity of 6 independent samples using this device. All fluid is pumped through the SPR sensor flow cell via PEEK tubing. The sensor consists of a glass prism coupled to a gold-coated glass plate functionalized with anti-IL-6 capture antibodies. A 633 nm laser passing through the prism and into the SPR detector is used to detect refractive index changes due to protein capture. In parallel, the laser beam provides excitation for Alexa 647-labeled secondary antibodies whose fluorescence is sensed by the photon counter.

The microfluidic system automatically conducted cyclic immunoassays, including sensor flushing, sampling of analytes, further washing, labeling with Alexa 647-labeled anti-IL-6 secondary antibody in a sandwich assay format, washing off excess secondary label, followed by sensor regeneration with glycine buffer pH 1.5. Figure 10.9A presents fluorescence and SPR measurements over time as a 100 ng/mL IL-6 sample is repeatedly assayed via different inputs. Not only do repeat fluorescence measurements exhibit high reproducibility, but the trace indicates successful sensor regeneration without loss of sensor specificity or sensitivity. Indeed, we were able to regenerate the sensor more than 50 times with no discernible deterioration. The SPR signal, however, could not detect IL-6 binding below 100 ng/mL even after secondary antibody labeling. As a result, we opted to utilize the fluorescence readout for greater sensitivity. The SPR flow cell fluidic resistance proved to be a significant obstacle to robust micropumping in the current chip design. We incorporated an inline peristaltic pump to replace the onboard micropump for the remainder of the experiments, though this could be solved by integrating SPR and fluorescence measurements with the chip. Figure 10.9B shows three overlapping fluorescence traces over time during fully automated standard curve generation. The highly reproducible fluid handling enabled generation of the standard curve in Figure 10.9C with a limit of detection between 10 and 100 pg/mL, comparing favorably to the 10 pg/mL limit of detection for the antibody set used. Note that full analysis of 6 samples, complete with sensor regeneration, required less than 90 min.

A.

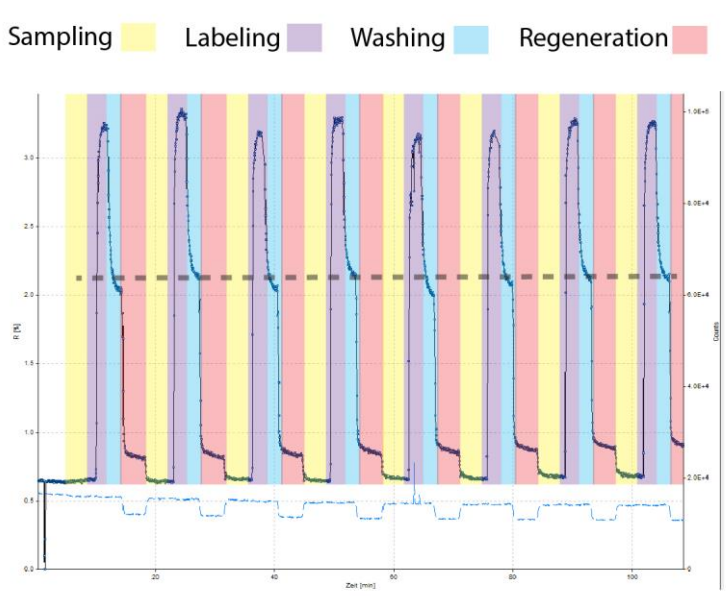
Sampling
Labeling
Washing
Regeneration

B.

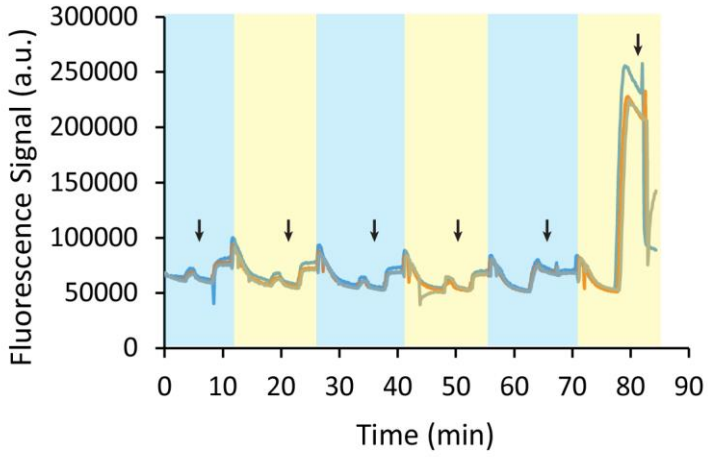
Fluorescence Signal (a.u.)
300000
250000
200000
150000
100000
50000
0
0
10
20
30
40
50
60
70
80
90
Time (min)

C.

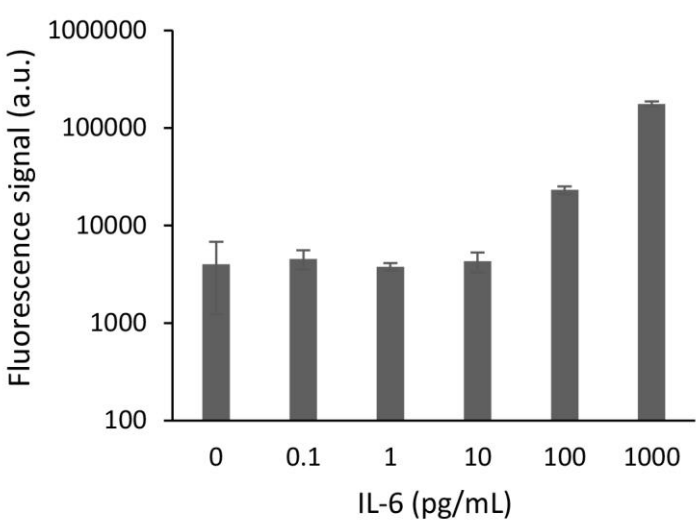
Fluorescence signal (a.u.)
1000000
100000
10000
1000
100
0
0.1
1
10
100
1000
IL-6 (pg/mL)

Figure 10.9. Automated microfluidic IL-6 immunoassay results. (A) Time trace of SPR (dotted light blue line) and fluorescence (solid dark blue line) signals during a fully automated repeated analysis of a 100 ng/mL IL-6 sample in buffer. Color shading highlights specific assay states. The dashed gray line is a visual guide showing the approximate assay readout for each sample, demonstrating high reproducibility across 8 samples. The SPR signal changes significantly only during sensor regeneration. (B) Time trace of fluorescence signal during three repeats of a negative control and five increasing 10-fold IL-6 dilutions, with each sample distinguished by a change in shading. Arrows indicate fluorescence measurement points taken after washing off excess labeling antibody. Excellent run-to-run reproducibility can be observed. (C) Standard curve of IL-6 detection based on fluorescence obtained using the fully automated setup. Limit of detection lies between 10 and 100 pg/mL.

10.5 Integrated organ-on-chip analytical platform

Given the several pitfalls observed during the development of the time-resolved immunoassay system, a second generation platform that not only overcomes the technical barriers but adds greater multiplexing capability and portability is presented in Figure 10.10. The proposed design integrates earlier microfluidic cell culture designs with multiparameter analysis of both the organ cultures as well as secreted products. The underlying design is based on the microfluidic layout used for time-resolved immunoassay development. A single micropump at the outlet actuates all fluidic components, including cell culture perfusion. Six culture chambers can be maintained and assayed in parallel. Upstream of each chamber, additional microvalves could be added to provide high time resolution dosing capability. Each chamber is addressed serially, and a defined volume of medium is pumped across the sensor, thus replacing medium in the cell chambers. Adequate medium exchange is possible due to rapid fluid actuation stemming from a fully integrated all-microfluidic system. Capture antibodies for several proteins are patterned in the sensing region to not only provide greater multiplexing capability but also concentrate the analytes for greater sensitivity. Multiplexed capture antibodies also provide a convenient internal control. Following analyte capture, secondary antibodies labeled with a single fluorophore are flowed into the chamber, providing a label for epifluorescence imaging and subsequent image analysis and target quantitation. Epifluorescence imaging is preferable to SPR analysis as it is readily multiplexed and can be built in a compact and portable form factor for bench-top analysis.

This integrated organ-on-chip analytical platform provides the capabilities and scalability needed for basic investigations into the role of cell heterogeneity in tissue and organ behavior as well as for more rapid and effective drug screening. The platform allows additional expansion of analytical modes, such as through the addition of mass spectroscopy to the outlet for metabolite monitoring or the addition of digital RT-PCR for measurement of secreted RNA. Single cell analysis can be further enhanced by the addition of sophisticated microscopy techniques, such as Raman microscopy and end-point single cell transcriptome analysis *in situ*,[30,38] since most organ-on-chip devices are conveniently planar.[318] Alternatively, single cell genetic analysis can be performed in droplets as described in earlier chapters if cells are released from the culture chambers. The application of massively multiplexed multiparameter assays to single cells and organ-level interactions will undoubtedly provide a wealth of data for understanding fundamental cellular biology mechanisms, provide novel targets for therapy, more effectively screen drug libraries, and better guide clinical decisions.

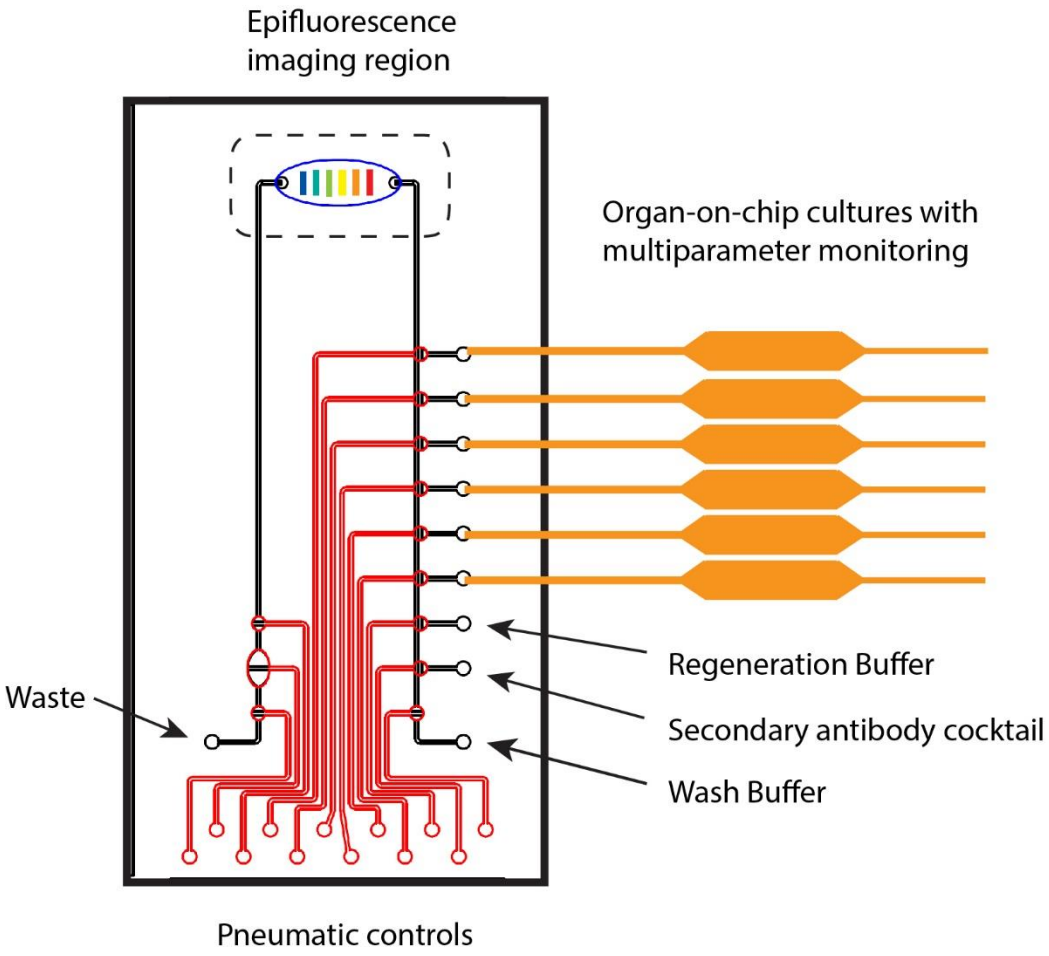

Figure 10.10. Proposed second generation time-resolved immunoassay multiplexed for 6 organs-on-a-chip and 6 protein targets. The microfluidic device shares many attributes of the initial design, but this system implements immunofluorescence imaging in an integrated sensing region with patterned capture antibodies against 6, and probably more, protein targets represented here by the multicolored bars. Patterning capture antibodies will also increase sensitivity by concentrating the signal to a smaller area. The low fluidic resistance system facilitates robust pumping and fast reagent exchange for low assay times. Organs-on-chip are connected directly to the sample input ports, and rapid serial sampling of medium provides culture perfusion. Each organ-on-chip culture is also monitored in real time as demonstrated previously.

10.6 Conclusions

How do single cells contribute to the concerted behavior of a tissue, organ, or individual? What is going on in our bodies and those of other organisms when observed from the perspective of a single cell? We now know that single cells, even clonal cells in cell lines, exhibit exceptional levels of heterogeneity, a fact that is only recently becoming appreciated as having significant biological impact in healthy and diseased states. We are at the start of a shift away from population-level thinking about biology and toward a deep appreciation for the role of the single cell. That this shift is happening now is not surprising. The technology required for single cell analysis is just now reaching a point of maturity where it can graduate from the engineer's workshop and into everyday use by the biologist.

The enabling technology for single cell analysis is undoubtedly the microfluidic "chip." The scale of manipulation, reagent volume, and scalability offered by microfluidic systems is truly the foundation of single cell analysis. This thesis describes the development of microfluidic emulsions and associated hardware. Droplets provide a practical means of effectively interrogating vast numbers of cells through the use of fluidic compartments. I have demonstrated their application for high sensitivity single DNA molecule detection and sequencing, for single cell genetic analysis in the context of early cancer biomarkers and forensic identification, and for growing colonies from single cells for investigating the role of gene expression noise and bimodality during cell growth. Later developments include the application of rapid prototyping for producing integrated platforms for organ-on-chip culture and multiparameter analysis that can begin to answer questions about the role of single cell variation in population-level behavior.

It should be evident that the final data points are built upon many innovations, from initial hardware development to conceiving of practical fabrication methods to the assays themselves. While this is a normal course of events in all fields, greater contact among scientists and clinicians will only accelerate and improve the design process. The traditional boundaries of academic departments need to be semi-permeable, because a tool maker must draw upon the knowledge and wisdom of the tool user for a good partnership. Microfluidics is one field where this is slowly happening. Engineers are talking to biologists and doctors to identify the biggest challenges and device appropriate and practical solutions. More of this kind of collaboration is needed, and more of it is sure to come as we embark on the journey to observe the world from the point of view of the single cell.

References

(1) Pratt, E. D.; Huang, C.; Hawkins, B. G.; Gleghorn, J. P.; Kirby, B. J. *Chem. Eng. Sci.* **2011**, *66*, 1508–1522.
(2) Nagrath, S.; Sequist, L. V.; Maheswaran, S.; Bell, D. W.; Irimia, D.; Ulkus, L.; Smith, M. R.; Kwak, E. L.; Digumarthy, S.; Muzikansky, A.; Ryan, P.; Balis, U. J.; Tompkins, R. G.; Haber, D. A.; Toner, M. *Nature* **2007**, *450*, 1235–1239.
(3) Riethdorf, S.; Fritsche, H.; Müller, V.; Rau, T.; Schindlbeck, C.; Rack, B.; Janni, W.; Coith, C.; Beck, K.; Jänicke, F.; Jackson, S.; Gornet, T.; Cristofanilli, M.; Pantel, K. *Clin. Cancer Res.* **2007**, *13*, 920–928.
(4) Alix-Panabières, C.; Pantel, K. *Clin. Chem.* **2013**, *59*, 110–118.
(5) Bidard, F.-C.; Mathiot, C.; Delaloge, S.; Brain, E.; Giachetti, S.; Cremoux, P. de; Marty, M.; Pierga, J.-Y. *Ann. Oncol.* **2010**, *21*, 729–733.
(6) Maheswaran, S.; Sequist, L. V.; Nagrath, S.; Ulkus, L.; Brannigan, B.; Collura, C. V.; Inserra, E.; Diederichs, S.; Iafrate, A. J.; Bell, D. W.; Digumarthy, S.; Muzikansky, A.; Irimia, D.; Settleman, J.; Tompkins, R. G.; Lynch, T. J.; Toner, M.; Haber, D. A. *N. Engl. J. Med.* **2008**, *359*, 366–377.
(7) Heitzer, E.; Auer, M.; Gasch, C.; Pichler, M.; Ulz, P.; Hoffmann, E. M.; Lax, S.; Waldispuehl-Geigl, J.; Mauermann, O.; Lackner, C.; Höfler, G.; Eisner, F.; Sill, H.; Samonigg, H.; Pantel, K.; Riethdorf, S.; Bauernhofer, T.; Geigl, J. B.; Speicher, M. R. *Cancer Res.* **2013**, *73*, 2965–2975.
(8) Elowitz, M. B.; Levine, A. J.; Siggia, E. D.; Swain, P. S. *Science* **2002**, *297*, 1183–1186.
(9) Swain, P. S.; Elowitz, M. B.; Siggia, E. D. *Proc. Natl. Acad. Sci.* **2002**, *99*, 12795–12800.
(10) Longo, D.; Hasty, J. *Mol. Syst. Biol.* **2006**, *2*.
(11) Newman, J. R. S.; Ghaemmaghami, S.; Ihmels, J.; Breslow, D. K.; Noble, M.; DeRisi, J. L.; Weissman, J. S. *Nature* **2006**, *441*, 840–846.
(12) Eldar, A.; Elowitz, M. B. *Nature* **2010**, *467*, 167–173.
(13) Buganim, Y.; Faddah, D. A.; Cheng, A. W.; Itskovich, E.; Markoulaki, S.; Ganz, K.; Klemm, S. L.; van Oudenaarden, A.; Jaenisch, R. *Cell* **2012**, *150*, 1209–1222.
(14) Suda, T.; Suda, J.; Ogawa, M. *Proc. Natl. Acad. Sci.* **1983**, *80*, 6689–6693.
(15) Chang, H. H.; Hemberg, M.; Barahona, M.; Ingber, D. E.; Huang, S. *Nature* **2008**, *453*, 544–547.
(16) Beaumont, H. J. E.; Gallie, J.; Kost, C.; Ferguson, G. C.; Rainey, P. B. *Nature* **2009**, *462*, 90–93.
(17) Eldar, A.; Chary, V. K.; Xenopoulos, P.; Fontes, M. E.; Losón, O. C.; Dworkin, J.; Piggot, P. J.; Elowitz, M. B. *Nature* **2009**, *460*, 510–514.
(18) Marusyk, A.; Polyak, K. *Biochim. Biophys. Acta* **2010**, *1805*, 105.
(19) Dalerba, P.; Kalisky, T.; Sahoo, D.; Rajendran, P. S.; Rothenberg, M. E.; Leyrat, A. A.; Sim, S.; Okamoto, J.; Johnston, D. M.; Qian, D.; Zabala, M.; Bueno, J.; Neff, N. F.; Wang, J.; Shelton, A. A.; Visser, B.; Hisamori, S.; Shimono, Y.; van de Wetering, M.; Clevers, H.; Clarke, M. F.; Quake, S. R. *Nat. Biotechnol.* **2011**, *29*, 1120–1127.
(20) Maley, C. C.; Galipeau, P. C.; Finley, J. C.; Wongsurawat, V. J.; Li, X.; Sanchez, C. A.; Paulson, T. G.; Blount, P. L.; Risques, R.-A.; Rabinovitch, P. S.; Reid, B. J. *Nat. Genet.* **2006**, *38*, 468–473.
(21) Bedard, P. L.; Hansen, A. R.; Ratain, M. J.; Siu, L. L. *Nature* **2013**, *501*, 355–364.
(22) Beckman, R. A.; Schemmann, G. S.; Yeang, C.-H. *Proc. Natl. Acad. Sci.* **2012**, *109*, 14586–14591.
(23) Shalek, A. K.; Satija, R.; Adiconis, X.; Gertner, R. S.; Gaublomme, J. T.; Raychowdhury, R.; Schwartz, S.; Yosef, N.; Malboeuf, C.; Lu, D.; Trombetta, J. J.; Gennert, D.; Gnirke, A.; Goren, A.; Hacohen, N.; Levin, J. Z.; Park, H.; Regev, A. *Nature* **2013**, *498*, 236–240.
(24) McConnell, M. J.; Lindberg, M. R.; Brennand, K. J.; Piper, J. C.; Voet, T.; Cowing-Zitron, C.; Shumilina, S.; Lasken, R. S.; Vermeesch, J. R.; Hall, I. M.; Gage, F. H. *Science* **2013**, *342*, 632–637.
(25) Schubert, W.; Bonnekoh, B.; Pommer, A. J.; Philipsen, L.; Böckelmann, R.; Malykh, Y.; Gollnick, H.; Friedenberger, M.; Bode, M.; Dress, A. W. M. *Nat. Biotechnol.* **2006**, *24*, 1270–1278.
(26) Shimomura, O.; Johnson, F. H.; Saiga, Y. *J. Cell. Comp. Physiol.* **1962**, *59*, 223–239.

(27) Chalfie, M.; Tu, Y.; Euskirchen, G.; Ward, W. W.; Prasher, D. C. *Science* **1994**, *263*, 802–805.
(28) Tsien, R. Y. *Annu. Rev. Biochem.* **1998**, *67*, 509–544.
(29) Lieber, C. A.; Majumder, S. K.; Ellis, D. L.; Billheimer, D. D.; Mahadevan-Jansen, A. *Lasers Surg. Med.* **2008**, *40*, 461–467.
(30) Freudiger, C. W.; Min, W.; Saar, B. G.; Lu, S.; Holtom, G. R.; He, C.; Tsai, J. C.; Kang, J. X.; Xie, X. S. *Science* **2008**, *322*, 1857–1861.
(31) Tjio, J. H.; Levan, A. *Hereditas* **1956**, *42*, 1–6.
(32) *Can. Med. Assoc. J.* **1961**, *84*, 1142.
(33) Trask, B. J. *Trends Genet.* **1991**, *7*, 149–154.
(34) Pellegrini-Giampietro, D. E.; Bennett, M. V.; Zukin, R. S. *Proc. Natl. Acad. Sci.* **1991**, *88*, 4157–4161.
(35) Imataka, G.; Arisaka, O. *Cell Biochem. Biophys.* **2012**, *62*, 13–17.
(36) Mergenthaler-Gatfield, S.; Holzgreve, W.; Hahn, S. *Methods Mol. Biol. Clifton NJ* **2008**, *444*, 3–26.
(37) Nuovo, G. J.; MacConnell, P. B.; Simsir, A.; Valea, F.; French, D. L. *Cancer Res.* **1995**, *55*, 267–275.
(38) Larsson, C.; Grundberg, I.; Söderberg, O.; Nilsson, M. *Nat. Methods* **2010**, *7*, 395–397.
(39) Low, J.; Huang, S.; Blosser, W.; Dowless, M.; Burch, J.; Neubauer, B.; Stancato, L. *Mol Cancer Ther* **2008**, *7*, 2455–2463.
(40) Liu, A. Y.; Roudier, M. P.; True, L. D. *Am. J. Pathol.* **2004**, *165*, 1543–1556.
(41) Krutzik, P. O.; Crane, J. M.; Clutter, M. R.; Nolan, G. P. *Nat. Chem. Biol.* **2008**, *4*, 132–142.
(42) Irish, J. M.; Hovland, R.; Krutzik, P. O.; Perez, O. D.; Bruserud, Ø.; Gjertsen, B. T.; Nolan, G. P. *Cell* **2004**, *118*, 217–228.
(43) Baerlocher, G. M.; Vulto, I.; de Jong, G.; Lansdorp, P. M. *Nat. Protoc.* **2006**, *1*, 2365–2376.
(44) Robertson, K. L.; Thach, D. C. *Anal. Biochem.* **2009**, *390*, 109–114.
(45) Yu, H.; Ernst, L.; Wagner, M.; Waggoner, A. *Nucleic Acids Res.* **1992**, *20*, 83–88.
(46) Bendall, S. C.; Nolan, G. P.; Roederer, M.; Chattopadhyay, P. K. *Trends Immunol.* **2012**, *33*, 323–332.
(47) Bendall, S. C.; Nolan, G. P. *Nat. Biotechnol.* **2012**, *30*, 639–647.
(48) Bendall, S. C.; Simonds, E. F.; Qiu, P.; Amir, E. D.; Krutzik, P. O.; Finck, R.; Bruggner, R. V.; Melamed, R.; Trejo, A.; Ornatsky, O. I.; Balderas, R. S.; Plevritis, S. K.; Sachs, K.; Pe'er, D.; Tanner, S. D.; Nolan, G. P. *Science* **2011**, *332*, 687–696.
(49) Coronella, J. A.; Telleman, P.; Truong, T. D.; Ylera, F.; Junghans, R. P. *Nucleic Acids Res.* **2000**, *28*, e85–e85.
(50) Meijer, P.-J.; Andersen, P. S.; Haahr Hansen, M.; Steinaa, L.; Jensen, A.; Lantto, J.; Oleksiewicz, M. B.; Tengbjerg, K.; Poulsen, T. R.; Coljee, V. W.; Bregenholt, S.; Haurum, J. S.; Nielsen, L. S. *J. Mol. Biol.* **2006**, *358*, 764–772.
(51) Islam, S.; Kjällquist, U.; Moliner, A.; Zajac, P.; Fan, J.-B.; Lönnerberg, P.; Linnarsson, S. *Nat. Protoc.* **2012**, *7*, 813–828.
(52) Ramsköld, D.; Luo, S.; Wang, Y.-C.; Li, R.; Deng, Q.; Faridani, O. R.; Daniels, G. A.; Khrebtukova, I.; Loring, J. F.; Laurent, L. C.; Schroth, G. P.; Sandberg, R. *Nat. Biotechnol.* **2012**, *30*, 777–782.
(53) Dominguez, M. H.; Chattopadhyay, P. K.; Ma, S.; Lamoreaux, L.; McDavid, A.; Finak, G.; Gottardo, R.; Koup, R. A.; Roederer, M. *J. Immunol. Methods* **2013**, *391*, 133–145.
(54) Chattopadhyay, P. K.; Roederer, M. *Methods* **2012**, *57*, 251–258.
(55) Squires, T. M.; Quake, S. R. *Rev. Mod. Phys.* **2005**, *77*, 977.
(56) Whitesides, G. M. *Nature* **2006**, *442*, 368–373.
(57) Toepke, M. W.; Beebe, D. J. *Lab. Chip* **2006**, *6*, 1484–1486.

(58) Shim, J.; Ranasinghe, R. T.; Smith, C. A.; Ibrahim, S. M.; Hollfelder, F.; Huck, W. T. S.; Klenerman, D.; Abell, C. *ACS Nano* **2013**, *7*, 5955–5964.
(59) Tsai, S. C.; Tsai, C. S. *IEEE Trans. Ultrason. Ferroelectr. Freq. Control* **2013**, *60*, 1746–1755.
(60) Unger, M. A.; Chou, H. P.; Thorsen, T.; Scherer, A.; Quake, S. R. *Science* **2000**, *288*, 113–116.
(61) Grover, W. H.; Skelley, A. M.; Liu, C. N.; Lagally, E. T.; Mathies, R. A. *Sens. Actuators B Chem.* **2003**, *89*, 315–323.
(62) Thorsen, T.; Maerkl, S. J.; Quake, S. R. *Science* **2002**, *298*, 580–584.
(63) Heyries, K. A.; Tropini, C.; VanInsberghe, M.; Doolin, C.; Petriv, O. I.; Singhal, A.; Leung, K.; Hughesman, C. B.; Hansen, C. L. *Nat. Methods* **2011**, *8*, 649–651.
(64) Jensen, E. C.; Bhat, B. P.; Mathies, R. A. *Lab. Chip* **2010**, *10*, 685–691.
(65) Grover, W. H.; Ivester, R. H. C.; Jensen, E. C.; Mathies, R. A. *Lab. Chip* **2006**, *6*, 623–631.
(66) Jensen, E. C.; Grover, W. H.; Mathies, R. A. *J. Microelectromechanical Syst.* **2007**, *16*, 1378–1385.
(67) Kim, J.; Kang, M.; Jensen, E. C.; Mathies, R. A. *Anal. Chem.* **2012**, *84*, 2067–2071.
(68) Jensen, E. C.; Zeng, Y.; Kim, J.; Mathies, R. A. *J. Assoc. Lab. Autom.* **2010**, *15*, 455–463.
(69) Kim, J.; Jensen, E. C.; Megens, M.; Boser, B.; Mathies, R. A. *Lab. Chip* **2011**, *11*, 3106–3112.
(70) Shuga, J.; Zeng, Y.; Novak, R.; Lan, Q.; Tang, X.; Rothman, N.; Vermeulen, R.; Li, L.; Hubbard, A.; Zhang, L.; Mathies, R. A.; Smith, M. T. *Nucleic Acids Res.* **2013**, *41*, e159–e159.
(71) Novak, R.; Zeng, Y.; Shuga, J.; Venugopalan, G.; Fletcher, D. A.; Smith, M. T.; Mathies, R. A. *Angew Chem Int Ed Engl* **2011**, *50*, 390–5.
(72) Domansky, K.; Inman, W.; Serdy, J.; Dash, A.; Lim, M. H. M.; Griffith, L. G. *Lab. Chip* **2010**, *10*, 51–58.
(73) Schiffenbauer, Y. S.; Kalma, Y.; Trubniykov, E.; Gal-Garber, O.; Weisz, L.; Halamish, A.; Sister, M.; Berke, G. *Lab. Chip* **2009**, *9*, 2965–2972.
(74) Deutsch, M.; Deutsch, A.; Shirihai, O.; Hurevich, I.; Afrimzon, E.; Shafran, Y.; Zurgil, N. *Lab. Chip* **2006**, *6*, 995–1000.
(75) Sims, C. E.; Allbritton, N. L. *Lab. Chip* **2007**, *7*, 423–440.
(76) Di Carlo, D.; Wu, L. Y.; Lee, L. P. *Lab. Chip* **2006**, *6*, 1445–9.
(77) Di Carlo, D.; Aghdam, N.; Lee, L. P. *Anal. Chem.* **2006**, *78*, 4925–4930.
(78) Chung, K.; Rivet, C. A.; Kemp, M. L.; Lu, H. *Anal. Chem.* **2011**, *83*, 7044–7052.
(79) Kobel, S.; Valero, A.; Latt, J.; Renaud, P.; Lutolf, M. *Lab. Chip* **2010**, *10*, 857–863.
(80) Frimat, J.-P.; Becker, M.; Chiang, Y.-Y.; Marggraf, U.; Janasek, D.; Hengstler, J. G.; Franzke, J.; West, J. *Lab. Chip* **2011**, *11*, 231–237.
(81) DeKosky, B. J.; Ippolito, G. C.; Deschner, R. P.; Lavinder, J. J.; Wine, Y.; Rawlings, B. M.; Varadarajan, N.; Giesecke, C.; Dörner, T.; Andrews, S. F.; Wilson, P. C.; Hunicke-Smith, S. P.; Willson, C. G.; Ellington, A. D.; Georgiou, G. *Nat. Biotechnol.* **2013**, *31*, 166–169.
(82) Love, J. C.; Ronan, J. L.; Grotenbreg, G. M.; van der Veen, A. G.; Ploegh, H. L. *Nat. Biotechnol.* **2006**, *24*, 703–707.
(83) Han, Q.; Bradshaw, E. M.; Nilsson, B.; Hafler, D. A.; Love, J. C. *Lab. Chip* **2010**, *10*, 1391–1400.
(84) Gong, Y.; Ogunniyi, A. O.; Love, J. C. *Lab. Chip* **2010**, *10*, 2334–2337.
(85) Lecault, V.; VanInsberghe, M.; Sekulovic, S.; Knapp, D. J. H. F.; Wohrer, S.; Bowden, W.; Viel, F.; McLaughlin, T.; Jarandehei, A.; Miller, M.; Falconnet, D.; White, A. K.; Kent, D. G.; Copley, M. R.; Taghipour, F.; Eaves, C. J.; Humphries, R. K.; Piret, J. M.; Hansen, C. L. *Nat. Methods* **2011**, *8*, 581–586.
(86) Taylor, R. J.; Falconnet, D.; Niemistö, A.; Ramsey, S. A.; Prinz, S.; Shmulevich, I.; Galitski, T.; Hansen, C. L. *Proc. Natl. Acad. Sci.* **2009**, *106*, 3758–3763.
(87) White, A. K.; VanInsberghe, M.; Petriv, O. I.; Hamidi, M.; Sikorski, D.; Marra, M. A.; Piret, J.; Aparicio, S.; Hansen, C. L. *Proc. Natl. Acad. Sci.* **2011**, *108*, 13999–14004.

(88) Leung, K.; Zahn, H.; Leaver, T.; Konwar, K. M.; Hanson, N. W.; Pagé, A. P.; Lo, C.-C.; Chain, P. S.; Hallam, S. J.; Hansen, C. L. *Proc. Natl. Acad. Sci.* **2012**, *109*, 7665–7670.
(89) Thorsen, T.; Roberts, R. W.; Arnold, F. H.; Quake, S. R. *Phys. Rev. Lett.* **2001**, *86*, 4163–4166.
(90) Umbanhowar, P. B.; Prasad, V.; Weitz, D. A. *Langmuir* **2000**, *16*, 347–351.
(91) Chen, C.-H.; Shah, R. K.; Abate, A. R.; Weitz, D. A. *Langmuir* **2009**, *25*, 4320–4323.
(92) Shum, H. C.; Abate, A. R.; Lee, D.; Studart, A. R.; Wang, B.; Chen, C.-H.; Thiele, J.; Shah, R. K.; Krummel, A.; Weitz, D. A. *Macromol. Rapid Commun.* **2010**, *31*, 108–118.
(93) Utada, A. S.; Lorenceau, E.; Link, D. R.; Kaplan, P. D.; Stone, H. A.; Weitz, D. A. *Science* **2005**, *308*, 537–541.
(94) Holtze, C.; Rowat, A. C.; Agresti, J. J.; Hutchison, J. B.; Angile, F. E.; Schmitz, C. H. J.; Koster, S.; Duan, H.; Humphry, K. J.; Scanga, R. A.; Johnson, J. S.; Pisignano, D.; Weitz, D. A. *Lab. Chip* **2008**, *8*, 1632–1639.
(95) Diehl, F.; Li, M.; He, Y.; Kinzler, K. W.; Vogelstein, B.; Dressman, D. *Nat Meth* **2006**, *3*, 551–559.
(96) Guo, M. T.; Rotem, A.; Heyman, J. A.; Weitz, D. A. *Lab. Chip* **2012**, *12*, 2146.
(97) Schmitz, C. H. J.; Rowat, A. C.; Koster, S.; Weitz, D. A. *Lab. Chip* **2009**, *9*, 44–49.
(98) Link, D. R.; Anna, S. L.; Weitz, D. A.; Stone, H. A. *Phys. Rev. Lett.* **2004**, *92*, 054503.
(99) Song, H.; Chen, D. L.; Ismagilov, R. F. *Angew Chem Int Ed Engl* **2006**, *45*, 7336–56.
(100) Schneider, T.; Yen, G. S.; Thompson, A. M.; Burnham, D. R.; Chiu, D. T. *Anal. Chem.* **2013**, *85*, 10417–10423.
(101) Schaerli, Y.; Hollfelder, F. *Mol. Biosyst.* **2009**, *5*, 1392.
(102) Zeng, Y.; Novak, R.; Shuga, J.; Smith, M. T.; Mathies, R. A. *Anal Chem* **2010**, *82*, 3183–90.
(103) Baroud, C. N.; Gallaire, F.; Dangla, R. *Lab. Chip* **2010**, *10*, 2032–2045.
(104) Christopher, G. F.; Anna, S. L. *J. Phys. Appl. Phys.* **2007**, *40*, R319.
(105) Lee, W.; Walker, L. M.; Anna, S. L. *Phys. Fluids 1994-Present* **2009**, *21*, 032103.
(106) Köster, S.; Angilè, F. E.; Duan, H.; Agresti, J. J.; Wintner, A.; Schmitz, C.; Rowat, A. C.; Merten, C. A.; Pisignano, D.; Griffiths, A. D.; Weitz, D. A. *Lab. Chip* **2008**, *8*, 1110.
(107) Clausell-Tormos, J.; Lieber, D.; Baret, J.-C.; El-Harrak, A.; Miller, O. J.; Frenz, L.; Blouwolff, J.; Humphry, K. J.; Köster, S.; Duan, H.; Holtze, C.; Weitz, D. A.; Griffiths, A. D.; Merten, C. A. *Chem. Biol.* **2008**, *15*, 427–437.
(108) Chiu, D. T.; Lorenz, R. M.; Jeffries, G. D. M. *Anal. Chem.* **2009**, *81*, 5111–5118.
(109) Baret, J.-C.; Kleinschmidt, F.; El Harrak, A.; Griffiths, A. D. *Langmuir* **2009**, *25*, 6088–6093.
(110) Poisson, S. D. *Recherches sur la probabilité des jugements en matière criminelle et en matière civile: précédées des règles générales du calcul des probabilités*; Bachelier, 1837.
(111) Bortkiewicz, L. von. *Das Gesetz der kleinen Zahlen*; B.G. Teubner, 1898.
(112) Sykes, P. J.; Neoh, S. H.; Brisco, M. J.; Hughes, E.; Condon, J.; Morley, A. A. *BioTechniques* **1992**, *13*, 444–449.
(113) Vogelstein, B.; Kinzler, K. W. *Proc. Natl. Acad. Sci.* **1999**, *96*, 9236–9241.
(114) Williams, R.; Peisajovich, S. G.; Miller, O. J.; Magdassi, S.; Tawfik, D. S.; Griffiths, A. D. *Nat. Methods* **2006**, *3*, 545–550.
(115) Nakano, M.; Komatsu, J.; Matsuura, S.; Takashima, K.; Katsura, S.; Mizuno, A. *J. Biotechnol.* **2003**, *102*, 117–124.
(116) Chen, W. W.; Balaj, L.; Liau, L. M.; Samuels, M. L.; Kotsopoulos, S. K.; Maguire, C. A.; LoGuidice, L.; Soto, H.; Garrett, M.; Zhu, L. D.; Sivaraman, S.; Chen, C.; Wong, E. T.; Carter, B. S.; Hochberg, F. H.; Breakefield, X. O.; Skog, J. *Mol. Ther. — Nucleic Acids* **2013**, *2*, e109.
(117) Men, Y.; Fu, Y.; Chen, Z.; Sims, P. A.; Greenleaf, W. J.; Huang, Y. *Anal. Chem.* **2012**, *84*, 4262–4266.
(118) Ottesen, E. A.; Hong, J. W.; Quake, S. R.; Leadbetter, J. R. *Science* **2006**, *314*, 1464–1467.

(119) Tsui, N. B. Y.; Kadir, R. A.; Chan, K. C. A.; Chi, C.; Mellars, G.; Tuddenham, E. G.; Leung, T. Y.; Lau, T. K.; Chiu, R. W. K.; Lo, Y. M. D. *Blood* **2011**, *117*, 3684–3691.
(120) Bhat, S.; Herrmann, J.; Armishaw, P.; Corbisier, P.; Emslie, K. R. *Anal. Bioanal. Chem.* **2009**, *394*, 457–467.
(121) Yung, T. K. F.; Chan, K. C. A.; Mok, T. S. K.; Tong, J.; To, K.-F.; Lo, Y. M. D. *Clin. Cancer Res.* **2009**, *15*, 2076–2084.
(122) Brenan, C.; Morrison, T. *Drug Discov. Today Technol.* **2005**, *2*, 247–253.
(123) Shen, F.; Du, W.; Davydova, E. K.; Karymov, M. A.; Pandey, J.; Ismagilov, R. F. *Anal. Chem.* **2010**, *82*, 4606–4612.
(124) Shi, X.; Lin, L.-I.; Chen, S.; Chao, S.; Zhang, W.; Meldrum, D. R. *Lab. Chip* **2011**, *11*, 2276–2281.
(125) Du, W.; Li, L.; Nichols, K. P.; Ismagilov, R. F. *Lab. Chip* **2009**, *9*, 2286–2292.
(126) Shen, F.; Du, W.; Kreutz, J. E.; Fok, A.; Ismagilov, R. F. *Lab. Chip* **2010**, *10*, 2666–2672.
(127) Kreutz, J. E.; Munson, T.; Huynh, T.; Shen, F.; Du, W.; Ismagilov, R. F. *Anal. Chem.* **2011**, *83*, 8158–8168.
(128) Abate, A. R.; Hung, T.; Sperling, R. A.; Mary, P.; Rotem, A.; Agresti, J. J.; Weiner, M. A.; Weitz, D. A. *Lab. Chip* **2013**, *13*, 4864–4869.
(129) Huebner, A.; Sharma, S.; Srisa-Art, M.; Hollfelder, F.; Edel, J. B.; deMello, A. J. *Lab. Chip* **2008**, *8*, 1244–1254.
(130) Kiss, M. M.; Ortoleva-Donnelly, L.; Beer, N. R.; Warner, J.; Bailey, C. G.; Colston, B. W.; Rothberg, J. M.; Link, D. R.; Leamon, J. H. *Anal. Chem.* **2008**, *80*, 8975–8981.
(131) Zhong, Q.; Bhattacharya, S.; Kotsopoulos, S.; Olson, J.; Taly, V.; Griffiths, A. D.; Link, D. R.; Larson, J. W. *Lab. Chip* **2011**, *11*, 2167–2174.
(132) Zhang, W. Y.; Zhang, W.; Liu, Z.; Li, C.; Zhu, Z.; Yang, C. J. *Anal. Chem.* **2012**, *84*, 350–355.
(133) Zhang, H.; Jenkins, G.; Zou, Y.; Zhu, Z.; Yang, C. J. *Anal Chem* **2012**, *84*, 3599–606.
(134) Eastburn, D. J.; Sciambi, A.; Abate, A. R. *Anal. Chem.* **2013**, *85*, 8016–8021.
(135) Kumaresan, P.; Yang, C. J.; Cronier, S. A.; Blazej, R. G.; Mathies, R. A. *Anal. Chem.* **2008**, *80*, 3522–3529.
(136) Geng, T.; Novak, R.; Mathies, R. A. *Anal. Chem.* **2013**.
(137) Huebner, A.; Srisa-Art, M.; Holt, D.; Abell, C.; Hollfelder, F.; deMello, A. J.; Edel, J. B. *Chem. Commun. Camb. Engl.* **2007**, 1218–1220.
(138) Hufnagel, H.; Huebner, A.; Gulch, C.; Guse, K.; Abell, C.; Hollfelder, F. *Lab. Chip* **2009**, *9*, 1576–1582.
(139) Juul, S.; Ho, Y. P.; Koch, J.; Andersen, F. F.; Stougaard, M.; Leong, K. W.; Knudsen, B. R. *ACS Nano* **2011**, *5*, 8305–10.
(140) Juul, S.; Nielsen, C. J. F.; Labouriau, R.; Roy, A.; Tesauro, C.; Jensen, P. W.; Harmsen, C.; Kristoffersen, E. L.; Chiu, Y.-L.; Frøhlich, R.; Fiorani, P.; Cox-Singh, J.; Tordrup, D.; Koch, J.; Bienvenu, A.-L.; Desideri, A.; Picot, S.; Petersen, E.; Leong, K. W.; Ho, Y.-P.; Stougaard, M.; Knudsen, B. R. *ACS Nano* **2012**, *6*, 10676–10683.
(141) Miller, O. J.; Harrak, A. E.; Mangeat, T.; Baret, J.-C.; Frenz, L.; Debs, B. E.; Mayot, E.; Samuels, M. L.; Rooney, E. K.; Dieu, P.; Galvan, M.; Link, D. R.; Griffiths, A. D. *Proc. Natl. Acad. Sci.* **2012**, *109*, 378–383.
(142) Debs, B. E.; Utharala, R.; Balyasnikova, I. V.; Griffiths, A. D.; Merten, C. A. *Proc. Natl. Acad. Sci.* **2012**, *109*, 11570–11575.
(143) Cai, L.; Friedman, N.; Xie, X. S. *Nature* **2006**, *440*, 358–362.
(144) Toriello, N. M.; Douglas, E. S.; Thaitrong, N.; Hsiao, S. C.; Francis, M. B.; Bertozzi, C. R.; Mathies, R. A. *Proc. Natl. Acad. Sci. U. S. A.* **2008**, *105*, 20173–20178.

(145) King, K. R.; Wang, S.; Irimia, D.; Jayaraman, A.; Toner, M.; Yarmush, M. L. *Lab. Chip* **2007**, *7*, 77–85.
(146) Hanahan, D.; Weinberg, R. A. *Cell* **2000**, *100*, 57–70.
(147) Klein, C. A.; Blankenstein, T. J. F.; Schmidt-Kittler, O.; Petronio, M.; Polzer, B.; Stoecklein, N. H.; Riethmüller, G. *Lancet* **2002**, *360*, 683–689.
(148) Fuhrmann, C.; Schmidt-Kittler, O.; Stoecklein, N. H.; Petat-Dutter, K.; Vay, C.; Bockler, K.; Reinhardt, R.; Ragg, T.; Klein, C. A. *Nucleic Acids Res.* **2008**, *36*, e39.
(149) Batchelor, E.; Loewer, A.; Lahav, G. *Nat. Rev. Cancer* **2009**, *9*, 371–377.
(150) Li, X.; Ling, V.; Li, P. C. H. *Anal. Chem.* **2008**, *80*, 4095–4102.
(151) Pantel, K.; Brakenhoff, R. H.; Brandt, B. *Nat. Rev. Cancer* **2008**, *8*, 329–340.
(152) Marcus, J. S.; Anderson, W. F.; Quake, S. R. *Anal. Chem.* **2006**, *78*, 3084–3089.
(153) Dressman, D.; Yan, H.; Traverso, G.; Kinzler, K. W.; Vogelstein, B. *Proc. Natl. Acad. Sci. U. S. A.* **2003**, *100*, 8817–8822.
(154) Margulies, M.; Egholm, M.; Altman, W. E.; Attiya, S.; Bader, J. S.; Bemben, L. A.; Berka, J.; Braverman, M. S.; Chen, Y.-J.; Chen, Z.; Dewell, S. B.; Du, L.; Fierro, J. M.; Gomes, X. V.; Godwin, B. C.; He, W.; Helgesen, S.; Ho, C. H.; Irzyk, G. P.; Jando, S. C.; Alenquer, M. L. I.; Jarvie, T. P.; Jirage, K. B.; Kim, J.-B.; Knight, J. R.; Lanza, J. R.; Leamon, J. H.; Lefkowitz, S. M.; Lei, M.; Li, J.; Lohman, K. L.; Lu, H.; Makhijani, V. B.; McDade, K. E.; McKenna, M. P.; Myers, E. W.; Nickerson, E.; Nobile, J. R.; Plant, R.; Puc, B. P.; Ronan, M. T.; Roth, G. T.; Sarkis, G. J.; Simons, J. F.; Simpson, J. W.; Srinivasan, M.; Tartaro, K. R.; Tomasz, A.; Vogt, K. A.; Volkmer, G. A.; Wang, S. H.; Wang, Y.; Weiner, M. P.; Yu, P.; Begley, R. F.; Rothberg, J. M. *Nature* **2005**, *437*, 376–380.
(155) Diehl, F.; Li, M.; Dressman, D.; He, Y.; Shen, D.; Szabo, S.; Diaz, L. A., Jr; Goodman, S. N.; David, K. A.; Juhl, H.; Kinzler, K. W.; Vogelstein, B. *Proc. Natl. Acad. Sci. U. S. A.* **2005**, *102*, 16368–16373.
(156) Li, M.; Diehl, F.; Dressman, D.; Vogelstein, B.; Kinzler, K. W. *Nat. Methods* **2006**, *3*, 95–97.
(157) Diehl, F.; Schmidt, K.; Choti, M. A.; Romans, K.; Goodman, S.; Li, M.; Thornton, K.; Agrawal, N.; Sokoll, L.; Szabo, S. A.; Kinzler, K. W.; Vogelstein, B.; Diaz Jr, L. A. *Nat. Med.* **2008**, *14*, 985–990.
(158) Li, M.; Chen, W.-D.; Papadopoulos, N.; Goodman, S. N.; Bjerregaard, N. C.; Laurberg, S.; Levin, B.; Juhl, H.; Arber, N.; Moinova, H.; Durkee, K.; Schmidt, K.; He, Y.; Diehl, F.; Velculescu, V. E.; Zhou, S.; Diaz, L. A., Jr; Kinzler, K. W.; Markowitz, S. D.; Vogelstein, B. *Nat. Biotechnol.* **2009**, *27*, 858–863.
(159) Teh, S.-Y.; Lin, R.; Hung, L.-H.; Lee, A. P. *Lab. Chip* **2008**, *8*, 198–220.
(160) Beer, N. R.; Hindson, B. J.; Wheeler, E. K.; Hall, S. B.; Rose, K. A.; Kennedy, I. M.; Colston, B. W. *Anal. Chem.* **2007**, *79*, 8471–8475.
(161) Beer, N. R.; Wheeler, E. K.; Lee-Houghton, L.; Watkins, N.; Nasarabadi, S.; Hebert, N.; Leung, P.; Arnold, D. W.; Bailey, C. G.; Colston, B. W. *Anal. Chem.* **2008**, *80*, 1854–1858.
(162) Mazutis, L.; Araghi, A. F.; Miller, O. J.; Baret, J.-C.; Frenz, L.; Janoshazi, A.; Taly, V.; Miller, B. J.; Hutchison, J. B.; Link, D.; Griffiths, A. D.; Ryckelynck, M. *Anal. Chem.* **2009**, *81*, 4813–4821.
(163) Roubos, J. A.; Krabben, P.; Luiten, R. G. M.; Verbruggen, H. B.; Heijnen, J. J. *Biotechnol. Prog.* **2008**, *17*, 336–347.
(164) Yu, S.-H.; Buchholz, R.; Kim, S.-K. *Biotechnol. Tech.* **1999**, *13*, 609–614.
(165) Mazutis, L.; Baret, J.-C.; Griffiths, A. D. *Lab. Chip* **2009**, *9*, 2665–2672.
(166) Brouzes, E.; Medkova, M.; Savenelli, N.; Marran, D.; Twardowski, M.; Hutchison, J. B.; Rothberg, J. M.; Link, D. R.; Perrimon, N.; Samuels, M. L. *Proc. Natl. Acad. Sci.* **2009**, *106*, 14195–14200.
(167) Markoulatos, P.; Siafakas, N.; Moncany, M. *J. Clin. Lab. Anal.* **2002**, *16*, 47–51.
(168) Mead, P. S.; Slutsker, L.; Dietz, V.; McCaig, L. F.; Bresee, J. S.; Shapiro, C.; Griffin, P. M.; Tauxe, R. V. *Emerg. Infect. Dis.* **1999**, *5*, 607–625.
(169) Nugen, S. R.; Baeumner, A. J. *Anal. Bioanal. Chem.* **2008**, *391*, 451–454.

(170) Batt, C. A. *Science* **2007**, *316*, 1579–1580.
(171) Beyor, N.; Yi, L.; Seo, T. S.; Mathies, R. A. *Anal. Chem.* **2009**, *81*, 3523–3528.
(172) Zhong, J. F.; Chen, Y.; Marcus, J. S.; Scherer, A.; Quake, S. R.; Taylor, C. R.; Weiner, L. P. *Lab. Chip* **2008**, *8*, 68–74.
(173) Lagally, E. T.; Scherer, J. R.; Blazej, R. G.; Toriello, N. M.; Diep, B. A.; Ramchandani, M.; Sensabaugh, G. F.; Riley, L. W.; Mathies, R. A. *Anal. Chem.* **2004**, *76*, 3162–3170.
(174) Liu, R. H.; Yang, J.; Lenigk, R.; Bonanno, J.; Grodzinski, P. *Anal. Chem.* **2004**, *76*, 1824–1831.
(175) Cady, N. C.; Stelick, S.; Kunnavakkam, M. V.; Batt, C. A. *Sens. Actuators B Chem.* **2005**, *107*, 332–341.
(176) Thaitrong, N.; Toriello, N. M.; Del Bueno, N.; Mathies, R. A. *Anal. Chem.* **2009**, *81*, 1371–1377.
(177) Fiorini, G. S.; Chiu, D. T. *BioTechniques* **2005**, *38*, 429–446.
(178) Becker, H.; Locascio, L. E. *Talanta* **2002**, *56*, 267–287.
(179) Chin, C. D.; Linder, V.; Sia, S. K. *Lab. Chip* **2012**, *12*, 2118.
(180) Leech, P. W. *J. Micromechanics Microengineering* **2009**, *19*, 055008.
(181) Illa, X.; Ordeig, O.; Snakenborg, D.; Romano-Rodriguez, A.; Compton, R. G.; Kutter, J. P. *Lab. Chip* **2010**, *10*, 1254–1261.
(182) Gubala, V.; Le, N. C. H.; Gandhiraman, R. P.; Coyle, C.; Daniels, S.; Williams, D. E. *Colloids Surf. B Biointerfaces* **2010**, *81*, 544–548.
(183) Jena, R. K.; Yue, C. Y.; Lam, Y. C.; Tang, P. S.; Gupta, A. *Sens. Actuators B Chem.* **2012**, *163*, 233–241.
(184) Hupert, M. L.; Guy, W. J.; Llopis, S. D.; Shadpour, H.; Rani, S.; Nikitopoulos, D. E.; Soper, S. A. *Microfluid. Nanofluidics* **2007**, *3*, 1–11.
(185) Wang, Y.; Balowski, J.; Phillips, C.; Phillips, R.; Sims, C. E.; Allbritton, N. L. *Lab. Chip* **2011**, *11*, 3089–3097.
(186) Goral, V. N.; Hsieh, Y.-C.; Petzold, O. N.; Faris, R. A.; Yuen, P. K. *J. Micromechanics Microengineering* **2011**, *21*, 017002.
(187) Koerner, T.; Brown, L.; Xie, R.; Oleschuk, R. D. *Sens. Actuators B Chem.* **2005**, *107*, 632–639.
(188) Svoboda, M.; Schrott, W.; Slouka, Z.; Přibyl, M.; Šnita, D. *Microelectron. Eng.* **2010**, *87*, 1527–1530.
(189) Miserere, S.; Mottet, G.; Taniga, V.; Descroix, S.; Viovy, J.-L.; Malaquin, L. *Lab. Chip* **2012**, *12*, 1849.
(190) Metwally, K.; Robert, L.; Queste, S.; Gauthier-Manuel, B.; Khan-Malek, C. *Microsyst. Technol.* **2012**, *18*, 199–207.
(191) Edwards, T. L.; Harper, J. C.; Polsky, R.; Lopez, D. M.; Wheeler, D. R.; Allen, A. C.; Brozik, S. M. *Biomicrofluidics* **2011**, *5*, 044115–044115–14.
(192) Bartholomeusz, D. A.; Boutte, R. W.; Andrade, J. D. *J. Microelectromechanical Syst.* **2005**, *14*, 1364 – 1374.
(193) Sundberg, S. O.; Wittwer, C. T.; Gao, C.; Gale, B. K. *Anal. Chem.* **2010**, *82*, 1546–1550.
(194) Fiorini, G. S.; Jeffries, G. D. M.; Lim, D. S. W.; Kuyper, C. L.; Chiu, D. T. *Lab. Chip* **2003**, *3*, 158–163.
(195) Kim, J.; deMello, A. J.; Chang, S.-I.; Hong, J.; O'Hare, D. *Lab. Chip* **2011**, *11*, 4108–4112.
(196) Mair, D. A.; Rolandi, M.; Snauko, M.; Noroski, R.; Svec, F.; Frechet, J. M. J. *Anal. Chem.* **2007**, *79*, 5097–5102.
(197) Meer, A. D. van der; Vermeul, K.; Poot, A. A.; Feijen, J.; Vermes, I. *Am. J. Physiol. - Heart Circ. Physiol.* **2010**, *298*, H719–H725.
(198) Lu, H.; Koo, L. Y.; Wang, W. M.; Lauffenburger, D. A.; Griffith, L. G.; Jensen, K. F. *Anal. Chem.* **2004**, *76*, 5257–5264.

(199) Mair, D. A.; Geiger, E.; Pisano, A. P.; Fr?chet, J. M. J.; Svec, F. *Lab. Chip* **2006**, *6*, 1346.
(200) Carter, H.; Chen, S.; Isik, L.; Tyekucheva, S.; Velculescu, V. E.; Kinzler, K. W.; Vogelstein, B.; Karchin, R. *Cancer Res.* **2009**, *69*, 6660–6667.
(201) Chiu, B. C.-H.; Dave, B. J.; Blair, A.; Gapstur, S. M.; Zahm, S. H.; Weisenburger, D. D. *Blood* **2006**, *108*, 1363–1369.
(202) Béné, M. C.; Kaeda, J. S. *Haematologica* **2009**, *94*, 1135–1150.
(203) Shuga, J.; Zeng, Y.; Novak, R.; Mathies, R. A.; Hainaut, P.; Smith, M. T. *Environ. Mol. Mutagen.* **2010**, *51*, 851–870.
(204) Hindson, B. J.; Ness, K. D.; Masquelier, D. A.; Belgrader, P.; Heredia, N. J.; Makarewicz, A. J.; Bright, I. J.; Lucero, M. Y.; Hiddessen, A. L.; Legler, T. C.; Kitano, T. K.; Hodel, M. R.; Petersen, J. F.; Wyatt, P. W.; Steenblock, E. R.; Shah, P. H.; Bousse, L. J.; Troup, C. B.; Mellen, J. C.; Wittmann, D. K.; Erndt, N. G.; Cauley, T. H.; Koehler, R. T.; So, A. P.; Dube, S.; Rose, K. A.; Montesclaros, L.; Wang, S.; Stumbo, D. P.; Hodges, S. P.; Romine, S.; Milanovich, F. P.; White, H. E.; Regan, J. F.; Karlin-Neumann, G. A.; Hindson, C. M.; Saxonov, S.; Colston, B. W. *Anal. Chem.* **2011**, *83*, 8604–8610.
(205) Pekin, D.; Skhiri, Y.; Baret, J.-C.; Le Corre, D.; Mazutis, L.; Salem, C. B.; Millot, F.; El Harrak, A.; Hutchison, J. B.; Larson, J. W.; Link, D. R.; Laurent-Puig, P.; Griffiths, A. D.; Taly, V. *Lab. Chip* **2011**, *11*, 2156–2166.
(206) Schüler, F.; Dölken, L.; Hirt, C.; Kiefer, T.; Berg, T.; Fusch, G.; Weitmann, K.; Hoffmann, W.; Fusch, C.; Janz, S.; Rabkin, C. S.; Dölken, G. *Int. J. Cancer* **2009**, *124*, 958–963.
(207) Aster, J. C.; Longtine, J. A. *Am. J. Pathol.* **2002**, *160*, 759–763.
(208) Weiss, L. M.; Warnke, R. A.; Sklar, J.; Cleary, M. L. *N. Engl. J. Med.* **1987**, *317*, 1185–1189.
(209) Bakhshi, A.; Jensen, J. P.; Goldman, P.; Wright, J. J.; McBride, O. W.; Epstein, A. L.; Korsmeyer, S. J. *Cell* **1985**, *41*, 899–906.
(210) Cleary, M. L.; Sklar, J. *Proc. Natl. Acad. Sci.* **1985**, *82*, 7439–7443.
(211) Korsmeyer, S. J. *Cancer Res.* **1999**, *59*, 1693s–1700s.
(212) Rabkin, C. S.; Hirt, C.; Janz, S.; Dölken, G. *JNCI Monogr.* **2008**, *2008*, 48–51.
(213) Biagi, J. J.; Seymour, J. F. *Blood* **2002**, *99*, 4265–4275.
(214) Bretherick, K. L.; Bu, R.; Gascoyne, R. D.; Connors, J. M.; Spinelli, J. J.; Brooks-Wilson, A. R. *Blood* **2010**, *116*, 6146–6147.
(215) Agopian, J.; Navarro, J.-M.; Gac, A.-C.; Lecluse, Y.; Briand, M.; Grenot, P.; Gauduchon, P.; Ruminy, P.; Lebailly, P.; Nadel, B.; Roulland, S. *J. Exp. Med.* **2009**, *206*, 1473–1483.
(216) Roulland, S.; Navarro, J.-M.; Grenot, P.; Milili, M.; Agopian, J.; Montpellier, B.; Gauduchon, P.; Lebailly, P.; Schiff, C.; Nadel, B. *J. Exp. Med.* **2006**, *203*, 2425–2431.
(217) Fuscoe, J. C.; Setzer, R. W.; Collard, D. D.; Moore, M. M. *Carcinogenesis* **1996**, *17*, 1013–1020.
(218) Paltiel, O.; Zelenetz, A.; Sverdlin, I.; Gordon, L.; Ben-Yehuda, D. *Ann. Oncol. Off. J. Eur. Soc. Med. Oncol. ESMO* **2000**, *11 Suppl 1*, 75–80.
(219) Tsujimoto, Y.; Gorham, J.; Cossman, J.; Jaffe, E.; Croce, C. M. *Science* **1985**, *229*, 1390–1393.
(220) Bende, R. J.; Smit, L. A.; van Noesel, C. J. M. *Leukemia* **2006**, *21*, 18–29.
(221) D' Amore, F.; Chan, E.; Iqbal, J.; Geng, H.; Young, K.; Xiao, L.; Hess, M. M.; Sanger, W. G.; Smith, L.; Wiuf, C.; Hagberg, O.; Fu, K.; Chan, W. C.; Dave, B. J. *Clin. Cancer Res.* **2008**, *14*, 7180–7187.
(222) Schlissel, M. S.; Kaffer, C. R.; Curry, J. D. *Genes Dev.* **2006**, *20*, 1539–1544.
(223) Raghavan, S. C.; Swanson, P. C.; Wu, X.; Hsieh, C.-L.; Lieber, M. R. *Nature* **2004**, *428*, 88–93.
(224) Taniguchi, K.; Uchida, J.; Nishino, K.; Kumagai, T.; Okuyama, T.; Okami, J.; Higashiyama, M.; Kodama, K.; Imamura, F.; Kato, K. *Clin. Cancer Res.* **2011**, *17*, 7808–7815.
(225) Crescenzi, M.; Seto, M.; Herzig, G. P.; Weiss, P. D.; Griffith, R. C.; Korsmeyer, S. J. *Proc. Natl. Acad. Sci.* **1988**, *85*, 4869–4873.

(226) Dölken, G.; Dölken, L.; Hirt, C.; Fusch, C.; Rabkin, C. S.; Schüler, F. *JNCI Monogr.* **2008**, *2008*, 44–47.
(227) Gribben, J. G.; Freedman, A.; Woo, S. D.; Blake, K.; Shu, R. S.; Freeman, G.; Longtine, J. A.; Pinkus, G. S.; Nadler, L. M. *Blood* **1991**, *78*, 3275–3280.
(228) Liu, Y.; Hernandez, A. M.; Shibata, D.; Cortopassi, G. A. *Proc. Natl. Acad. Sci.* **1994**, *91*, 8910–8914.
(229) Rauzy, O.; Galoin, S.; Chale, J. J.; Adoue, D.; Albarede, J. L.; Delsol, G.; Saati, T. al. *Mol. Pathol.* **1998**, *51*, 333–338.
(230) McHale, C. M.; Lan, Q.; Corso, C.; Li, G.; Zhang, L.; Vermeulen, R.; Curry, J. D.; Shen, M.; Turakulov, R.; Higuchi, R.; Germer, S.; Yin, S.; Rothman, N.; Smith, M. T. *JNCI Monogr.* **2008**, *2008*, 74–77.
(231) Wyatt, R. T.; Rudders, R. A.; Zelenetz, A.; Delellis, R. A.; Krontiris, T. G. *J. Exp. Med.* **1992**, *175*, 1575–1588.
(232) Eide, M. B.; Liestøl, K.; Lingjærde, O. C.; Hystad, M. E.; Kresse, S. H.; Meza-Zepeda, L.; Myklebost, O.; Trøen, G.; Aamot, H. V.; Holte, H.; Smeland, E. B.; Delabie, J. *Blood* **2010**, *116*, 1489–1497.
(233) Wrench, D.; Montoto, S.; Fitzgibbon, J. *Curr. Opin. Hematol. July 2010* **2010**, *17*, 333–340.
(234) Riethdorf, S.; Wikman, H.; Pantel, K. *Int. J. Cancer J. Int. Cancer* **2008**, *123*, 1991–2006.
(235) Andersson, H.; Berg, A. van den. *Curr. Opin. Biotechnol.* **2004**, *15*, 44–49.
(236) El-Ali, J.; Sorger, P. K.; Jensen, K. F. *Nature* **2006**, *442*, 403–411.
(237) Chao, T.-C.; Ros, A. *J. R. Soc. Interface* **2008**, *5*, S139–S150.
(238) Zare, R. N.; Kim, S. *Annu. Rev. Biomed. Eng.* **2010**, *12*, 187–201.
(239) Xiong, J.-Y.; Narayanan, J.; Liu, X.-Y.; Chong, T. K.; Chen, S. B.; Chung, T.-S. *J. Phys. Chem. B* **2005**, *109*, 5638–5643.
(240) Hicks, J.; Muthuswamy, L.; Krasnitz, A.; Navin, N.; Riggs, M.; Grubor, V.; Esposito, D.; Alexander, J.; Troge, J.; Wigler, M.; Maner, S.; Lundin, P.; Zetterberg, A. *Cold Spring Harb. Symp. Quant. Biol.* **2005**, *70*, 51–63.
(241) Navin, N.; Krasnitz, A.; Rodgers, L.; Cook, K.; Meth, J.; Kendall, J.; Riggs, M.; Eberling, Y.; Troge, J.; Grubor, V.; Levy, D.; Lundin, P.; Månér, S.; Zetterberg, A.; Hicks, J.; Wigler, M. *Genome Res.* **2010**, *20*, 68 –80.
(242) Leppänen, P. M.; Koponen, J.; Turunen, M. P.; Pakkanen, T.; Ylä-Herttuala, S. *J. Gene Med.* **2001**, *3*, 173–178.
(243) Mulrooney, P. M.; Michalak, T. I. *J. Virol.* **2003**, *77*, 970–979.
(244) Walser, M.; Pellaux, R.; Meyer, A.; Bechtold, M.; Vanderschuren, H.; Reinhardt, R.; Magyar, J.; Panke, S.; Held, M. *Nucl Acids Res* **2009**, *37*, e57.
(245) Zhang, L.; Cui, X.; Schmitt, K.; Hubert, R.; Navidi, W.; Arnheim, N. *Proc. Natl. Acad. Sci. U. S. A.* **1992**, *89*, 5847–5851.
(246) *Current Protocols in Molecular Biology*; Ausubel, F. M.; Brent, R.; Kingston, R. E.; Moore, D. D.; Seidman, J. G.; Smith, J. A.; Struhl, K., Eds.; John Wiley & Sons, Inc.: Hoboken, NJ, USA, 2001.
(247) Goldenberger, D.; Perschil, I.; Ritzler, M.; Altwegg, M. *Genome Res.* **1995**, *4*, 368 –370.
(248) Vermeulen, L.; Todaro, M.; de Sousa Mello, F.; Sprick, M. R.; Kemper, K.; Perez Alea, M.; Richel, D. J.; Stassi, G.; Medema, J. P. *Proc. Natl. Acad. Sci.* **2008**, *105*, 13427–13432.
(249) Navin, N. E.; Hicks, J. *Mol. Oncol.* **2010**, *4*, 267–283.
(250) Robles, A. I.; Harris, C. C. *Cold Spring Harb. Perspect. Biol.* **2010**, *2*.
(251) Vitolo, U.; Botto, B.; Capello, D.; Vivenza, D.; Zagonel, V.; Gloghini, A.; Novero, D.; Parvis, G.; Calvi, R.; Ariatti, C.; Milan, I.; Bertini, M.; Boccomini, C.; Freilone, R.; Pregno, P.; Orsucci, L.; Palestro, G.; Saglio, G.; Carbone, A.; Gallo, E.; Gaidano, G. *Leuk. Off. J. Leuk. Soc. Am. Leuk. Res. Fund UK* **2002**, *16*, 268–275.

(252) Young, K. H.; Leroy, K.; Moller, M. B.; Colleoni, G. W. B.; Sanchez-Beato, M.; Kerbauy, F. R.; Haioun, C.; Eickhoff, J. C.; Young, A. H.; Gaulard, P.; Piris, M. A.; Oberley, T. D.; Rehrauer, W. M.; Kahl, B. S.; Malter, J. S.; Campo, E.; Delabie, J.; Gascoyne, R. D.; Rosenwald, A.; Rimsza, L.; Huang, J.; Braziel, R. M.; Jaffe, E. S.; Wilson, W. H.; Staudt, L. M.; Vose, J. M.; Chan, W. C.; Weisenburger, D. D.; Greiner, T. C. *Blood* **2008**, *112*, 3088–3098.
(253) Lossos, I. S.; Levy, R. *Semin. Cancer Biol.* **2003**, *13*, 191–202.
(254) O'Shea, D.; O'Riain, C.; Taylor, C.; Waters, R.; Carlotti, E.; MacDougall, F.; Gribben, J.; Rosenwald, A.; Ott, G.; Rimsza, L. M.; Smeland, E. B.; Johnson, N.; Campo, E.; Greiner, T. C.; Chan, W. C.; Gascoyne, R. D.; Wright, G.; Staudt, L. M.; Lister, T. A.; Fitzgibbon, J. *Blood* **2008**, *112*, 3126–3129.
(255) Brown, R. B.; Audet, J. *J. R. Soc. Interface* **2008**, *5*, 131–138.
(256) Huang, H.; Bu, Y.; Zhou, G.-H. *World J. Gastroenterol. WJG* **2006**, *12*, 3814–3820.
(257) Hammond, H. A.; Jin, L.; Zhong, Y.; Caskey, C. T.; Chakraborty, R. *Am J Hum Genet* **1994**, *55*, 175–89.
(258) Butler, J. M. *J Forensic Sci* **2006**, *51*, 253–65.
(259) Horsman-Hall, K. M.; Orihuela, Y.; Karczynski, S. L.; Davis, A. L.; Ban, J. D.; Greenspoon, S. A. *Forensic Sci Int Genet* **2009**, *3*, 242–50.
(260) Van Oorschot, R. A.; Ballantyne, K. N.; Mitchell, R. J. *Investig Genet* **2010**, *1*, 14.
(261) Torres, Y.; Flores, I.; Prieto, V.; Lopez-Soto, M.; Farfan, M. J.; Carracedo, A.; Sanz, P. *Forensic Sci Int* **2003**, *134*, 180–6.
(262) Ladd, C.; Lee, H. C.; Yang, N.; Bieber, F. R. *Croat Med J* **2001**, *42*, 244–6.
(263) Budowle, B.; Onorato, A. J.; Callaghan, T. F.; Della Manna, A.; Gross, A. M.; Guerrieri, R. A.; Luttman, J. C.; McClure, D. L. *J Forensic Sci* **2009**, *54*, 810–21.
(264) Clayton, T. M.; Whitaker, J. P.; Sparkes, R.; Gill, P. *Forensic Sci Int* **1998**, *91*, 55–70.
(265) Gill, P.; Jeffreys, A. J.; Werrett, D. J. *Nature* **1985**, *318*, 577–9.
(266) Yoshida, K.; Sekiguchi, K.; Mizuno, N.; Kasai, K.; Sakai, I.; Sato, H.; Seta, S. *Forensic Sci Int* **1995**, *72*, 25–33.
(267) Chen, J.; Kobilinsky, L.; Wolosin, D.; Shaler, R.; Baum, H. *J Forensic Sci* **1998**, *43*, 114–8.
(268) Schoell, W. M.; Klintschar, M.; Mirhashemi, R.; Pertl, B. *Obstet Gynecol* **1999**, *94*, 623–7.
(269) Di Nunno, N.; Melato, M.; Vimercati, A.; Di Nunno, C.; Costantinides, F.; Vecchiotti, C.; Frezzini, C.; Cina, S.; Vimercati, F. *Am J Forensic Med Pathol* **2003**, *24*, 254–70.
(270) Horsman, K. M.; Barker, S. L.; Ferrance, J. P.; Forrest, K. A.; Koen, K. A.; Landers, J. P. *Anal Chem* **2005**, *77*, 742–9.
(271) Bienvenue, J. M.; Duncalf, N.; Marchiarullo, D.; Ferrance, J. P.; Landers, J. P. *J Forensic Sci* **2006**, *51*, 266–73.
(272) Norris, J. V.; Evander, M.; Horsman-Hall, K. M.; Nilsson, J.; Laurell, T.; Landers, J. P. *Anal Chem* **2009**, *81*, 6089–95.
(273) Di Martino, D.; Giuffre, G.; Staiti, N.; Simone, A.; Todaro, P.; Saravo, L. *Forensic Sci Int* **2004**, *146 Suppl*, S155–7.
(274) Sanders, C. T.; Sanchez, N.; Ballantyne, J.; Peterson, D. A. *J Forensic Sci* **2006**, *51*, 748–57.
(275) Li, C. X.; Han, J. P.; Ren, W. Y.; Ji, A. Q.; Xu, X. L.; Hu, L. *PLoS One* **2011**, *6*, e22316.
(276) Findlay, I.; Taylor, A.; Quirke, P.; Frazier, R.; Urquhart, A. *Nature* **1997**, *389*, 555–6.
(277) Bruck, S.; Evers, H.; Heidorn, F.; Muller, U.; Kilper, R.; Verhoff, M. A. *J Forensic Sci* **2011**, *56*, 176–80.
(278) Pereira, J.; Neves, R.; Forat, S.; Huckenbeck, W.; Olek, K. *Forensic Sci Int Genet* **2012**, *6*, 228–35.
(279) Theberge, A. B.; Courtois, F.; Schaerli, Y.; Fischlechner, M.; Abell, C.; Hollfelder, F.; Huck, W. T. *Angew Chem Int Ed Engl* **2010**, *49*, 5846–68.

(280) Joensson, H. N.; Andersson Svahn, H. *Angew Chem Int Ed Engl* **2012**, *51*, 12176–92.
(281) He, M.; Edgar, J. S.; Jeffries, G. D.; Lorenz, R. M.; Shelby, J. P.; Chiu, D. T. *Anal Chem* **2005**, *77*, 1539–44.
(282) Baret, J. C.; Beck, Y.; Billas-Massobrio, I.; Moras, D.; Griffiths, A. D. *Chem Biol* **2010**, *17*, 528–36.
(283) Gu, S. Q.; Zhang, Y. X.; Zhu, Y.; Du, W. B.; Yao, B.; Fang, Q. *Anal Chem* **2011**, *83*, 7570–6.
(284) Rane, T. D.; Zec, H. C.; Puleo, C.; Lee, A. P.; Wang, T. H. *Lab Chip* **2012**, *12*, 3341–7.
(285) Zhu, Z.; Zhang, W.; Leng, X.; Zhang, M.; Guan, Z.; Lu, J.; Yang, C. J. *Lab Chip* **2012**, *12*, 3907–13.
(286) Blackburn, E. H. *Nature* **1991**, *350*, 569–573.
(287) Blackburn, E. H. *Nature* **2000**, *408*, 53–56.
(288) Morrison, S. *Immunity* **1996**, *5*, 207–216.
(289) Shay, J. W.; Zou, Y.; Hiyama, E.; Wright, W. E. *Hum. Mol. Genet.* **2001**, *10*, 677–685.
(290) Chen, J.-L.; Blasco, M. A.; Greider, C. W. *Cell* **2000**, *100*, 503–514.
(291) Yi, X.; Shay, J. W.; Wright, W. E. *Nucleic Acids Res.* **2001**, *29*, 4818–4825.
(292) Ulaner, G. A.; Hu, J. F.; Vu, T. H.; Giudice, L. C.; Hoffman, A. R. *Cancer Res.* **1998**, *58*, 4168–4172.
(293) Bollmann, F. M. *Biochimie* **2013**, *95*, 1965–1970.
(294) Hrdličková, R.; Nehyba, J.; Bose, H. R. *Mol. Cell. Biol.* **2012**, *32*, 4283–4296.
(295) Listerman, I.; Sun, J.; Gazzaniga, F. S.; Lukas, J. L.; Blackburn, E. H. *Cancer Res.* **2013**, *73*, 2817–2828.
(296) Colgin, L. M.; Wilkinson, C.; Englezou, A.; Kilian, A.; Robinson, M. O.; Redder, R. R. *Neoplasia N. Y. N* **2000**, *2*, 426–432.
(297) Marjanovic, N. D.; Weinberg, R. A.; Chaffer, C. L. *Clin. Chem.* **2013**, *59*, 168–179.
(298) Novak, R.; Ranu, N.; Mathies, R. A. *Lab. Chip* **2013**, *13*, 1468–1471.
(299) Hartigan, P. M. *J. R. Stat. Soc. Ser. C Appl. Stat.* **1985**, *34*, 320–325.
(300) Hartigan, J. A.; Hartigan, P. M. *Ann. Stat.* **1985**, *13*, 70–84.
(301) Freeman, J. B.; Dale, R. *Behav. Res. Methods* **2013**, *45*, 83–97.
(302) Lee, J. H.; Chung, I. K. *Cancer Lett.* **2010**, *290*, 76–86.
(303) Ramachandran, C.; Fonseca, H. B.; Jhabvala, P.; Escalon, E. A.; Melnick, S. J. *Cancer Lett.* **2002**, *184*, 1–6.
(304) Khaw, A. K.; Hande, M. P.; Kalthur, G.; Hande, M. P. *J. Cell. Biochem.* **2013**, *114*, 1257–1270.
(305) Lu, J.-J.; Cai, Y.-J.; Ding, J. *Mol. Cell. Biochem.* **2012**, *360*, 253–260.
(306) Anuchapreeda, S.; Thanarattanakorn, P.; Sittipreechacharn, S.; Chanarat, P.; Limtrakul, P. *Acta Pharmacol. Sin.* **2006**, *27*, 360–366.
(307) Lincz, L. F.; Mudge, L.-M.; Scorgie, F. E.; Sakoff, J. A.; Hamilton, C. S.; Seldon, M. *Neoplasia N. Y. N* **2008**, *10*, 1131–1137.
(308) Wong, M. S.; Chen, L.; Foster, C.; Kainthla, R.; Shay, J. W.; Wright, W. E. *Cell Rep.* **2013**, *3*, 1028–1035.
(309) Brown, C. R.; Mao, C.; Falkovskaia, E.; Jurica, M. S.; Boeger, H. *PLoS Biol.* **2013**, *11*, e1001621.
(310) Wang, S.; Hu, C.; Zhu, J. *Mol. Biol. Cell* **2010**, *21*, 821–832.
(311) Cui, S.-X.; Qu, X.-J.; Xie, Y.-Y.; Zhou, L.; Nakata, M.; Makuuchi, M.; Tang, W. *Int. J. Mol. Med.* **2006**, *18*, 227–231.
(312) Akiyama, M.; Yamada, O.; Kanda, N.; Akita, S.; Kawano, T.; Ohno, T.; Mizoguchi, H.; Eto, Y.; Anderson, K. C.; Yamada, H. *Cancer Lett.* **2002**, *178*, 187–197.
(313) Lappin, G.; Garner, R. C. *Nat. Rev. Drug Discov.* **2003**, *2*, 233–240.
(314) Lappin, G.; Noveck, R.; Burt, T. *Expert Opin. Drug Metab. Toxicol.* **2013**, *9*, 817–834.
(315) Croft, M. M.; Keely, B.; Morris, I.; Tann, L.; Lappin, G. *Clin. Pharmacokinet.* **2012**, *51*, 237–246.

(316) Baret, J.-C.; Miller, O. J.; Taly, V.; Ryckelynck, M.; El-Harrak, A.; Frenz, L.; Rick, C.; Samuels, M. L.; Hutchison, J. B.; Agresti, J. J.; Link, D. R.; Weitz, D. A.; Griffiths, A. D. *Lab. Chip* **2009**, *9*, 1850–1858.
(317) Lim, S. W.; Abate, A. R. *Lab. Chip* **2013**, *13*, 4563–4572.
(318) Huh, D.; Matthews, B. D.; Mammoto, A.; Montoya-Zavala, M.; Hsin, H. Y.; Ingber, D. E. *Science* **2010**, *328*, 1662–1668.
(319) Schimek, K.; Busek, M.; Brincker, S.; Groth, B.; Hoffmann, S.; Lauster, R.; Lindner, G.; Lorenz, A.; Menzel, U.; Sonntag, F.; Walles, H.; Marx, U.; Horland, R. *Lab. Chip* **2013**, *13*, 3588–3598.
(320) Sonntag, F.; Schilling, N.; Mader, K.; Gruchow, M.; Klotzbach, U.; Lindner, G.; Horland, R.; Wagner, I.; Lauster, R.; Howitz, S.; Hoffmann, S.; Marx, U. *J. Biotechnol.* **2010**, *148*, 70–75.
(321) Chan, C. Y.; Huang, P.-H.; Guo, F.; Ding, X.; Kapur, V.; Mai, J. D.; Yuen, P. K.; Huang, T. J. *Lab. Chip* **2013**, *13*, 4697.
(322) Huh, D.; Hamilton, G. A.; Ingber, D. E. *Trends Cell Biol.* **2011**, *21*, 745–754.
(323) Ghaemmaghami, A. M.; Hancock, M. J.; Harrington, H.; Kaji, H.; Khademhosseini, A. *Drug Discov. Today* **2012**, *17*, 173–181.
(324) Moraes, C.; Mehta, G.; Lesher-Perez, S. C.; Takayama, S. *Ann. Biomed. Eng.* **2012**, *40*, 1211–1227.
(325) Shintu, L.; Baudoin, R.; Navratil, V.; Prot, J.-M.; Pontoizeau, C.; Defernez, M.; Blaise, B. J.; Domange, C.; Péry, A. R.; Toulhoat, P.; Legallais, C.; Brochot, C.; Leclerc, E.; Dumas, M.-E. *Anal. Chem.* **2012**, *84*, 1840–1848.
(326) Charwat, V.; Purtscher, M.; Tedde, S. F.; Hayden, O.; Ertl, P. *Lab. Chip* **2013**, *13*, 785–797.
(327) Gottschamel, J.; Richter, L.; Mak, A.; Jungreuthmayer, C.; Birnbaumer, G.; Milnera, M.; Brückl, H.; Ertl, P. *Anal. Chem.* **2009**, *81*, 8503–8512.
(328) Ungerböck, B.; Charwat, V.; Ertl, P.; Mayr, T. *Lab. Chip* **2013**, *13*, 1593–1601.
(329) Ehringer, W. D.; Edwards, M. J.; Miller, F. N. *J. Cell. Physiol.* **1996**, *167*, 562–569.
(330) Satoh, W.; Takahashi, S.; Sassa, F.; Fukuda, J.; Suzuki, H. *Lab. Chip* **2009**, *9*, 35–37.
(331) Zhang, L.; Tang, X.; Rothman, N.; Vermeulen, R.; Ji, Z.; Shen, M.; Qiu, C.; Guo, W.; Liu, S.; Reiss, B.; Freeman, L. B.; Ge, Y.; Hubbard, A. E.; Hua, M.; Blair, A.; Galvan, N.; Ruan, X.; Alter, B. P.; Xin, K. X.; Li, S.; Moore, L. E.; Kim, S.; Xie, Y.; Hayes, R. B.; Azuma, M.; Hauptmann, M.; Xiong, J.; Stewart, P.; Li, L.; Rappaport, S. M.; Huang, H.; Fraumeni, J. F.; Smith, M. T.; Lan, Q. *Cancer Epidemiol. Biomarkers Prev.* **2010**, *19*, 80–88.

Appendices

A. Supplemental information for Chapter 2
B. Supplemental information for Chapter 3
C. Supplemental information for Chapter 5
D. Supplemental information for Chapter 6
E. Supplemental information for Chapter 7
F. Supplemental information for Chapter 9

Appendix A: Supplemental information for Chapter 2

A.1 Supplementary materials and methods

MEGA Fabrication and Preparation. MEGA devices are constructed from three 100-mm-diameter glass wafers and a thin PDMS membrane, as shown schematically in Figure 2 in the main text. The valve structure was first photolithographically transferred to the top side of a Borofloat wafer (500 μm thick, Schott, Duryea, PA) and etched to a depth of 100 μm in 49% HF. Backside alignment lithography (KS Aligner; Süss MicroTec, Santa Clara, CA) was used to fabricate the 100 μm microchannel features onto the bottom of the same wafer in register with those on the top side. Fluidic and interlayer access holes were diamond drilled before thermally bonding the wafer to a 1.1-mm-thick Borofloat wafer at 650°C for 6 h. Pneumatic channels and microvalve displacement chambers were etched 100 μm deep on a second 1.1-mm-thick wafer, after which PCR reagent and pneumatic access holes were drilled. The bonded chip having two 4-channel MEGAs and the pneumatic manifold wafer were diced into pieces of proper sizes. Three 1/16-inch barbed pneumatic ports were epoxy glued onto the top side of a pneumatic manifold chip.

Prior to operation, the bonded all-glass channels were coated with a 0.1% solution of octadecyltrichlorosilane (OTS, purity > 90%, Sigma-Aldrich) in dry toluene for 10 min. A 254-μm-thick PDMS membrane (Bisco, Schaumberg, IL) with a PCR reagent access hole was sandwiched between a bonded chip and a pneumatic manifold piece immediately after 2 min UV-ozone-activation of the interacting surfaces. The MEGA stack was then assembled with a custom plexiglass manifold, to which PEEK tubings (Upchurch, Oak Harbor, WA) for oil infusion and PTFE tubings (Cole Parmer, Vernon Hills, IL) for routing droplets from the device into PCR tubes were connected (Figure 2D). O-rings (McMaster-Carr, Cleveland, OH) and custom silicone ferrules were used to provide fluidic sealing between the manifold and the chip. To eliminate carryover between experiments, the fluid lines and channels were cleaned with a 10% (v/v) solution of household bleach at 80°C, followed by rinsing with deionized water and isopropanol prior to each run. Heated bleach solution deteriorates the quality of the organic coating on the channel surface. To restore surface hydrophobicity, the glass channels were rinsed with piranha solution at 120°C and recoated with OTS after several experiments.

Cell Preparation. All cell culture and preparation were performed in a Class II biosafety cabinet (Labconco, Kansas City, MO) to avoid contamination. Two types of cells were used here: *E. coli* K12 MG1655 (American type Culture Collection, ATCC #700926) and nontoxigenic *E. coli* O157 NCTC 12900 (ATCC 700728). Cell were grown separately in a 2 mL tube containing Tryptic Soy Broth medium (TSB, Hardy Diagnostics K131) placed in a shaking incubator overnight at 37°C. *E. coli* K12 cells were transfected with a 3.9-kb pCR 2.1-TOPO vector (Invitrogen, Carlsbad, CA) to confer ampicillin resistance. *E. coli* K12 was grown with 1 μg/mL ampicillin added to the media, while *E. coli* O157 was untreated and frequently tested for contamination by PCR. Following growth, cells were washed three times in phosphate buffered saline (PBS pH 7.4, Ambion, Austin, TX). Final cell density was determined by using a hemacytometer (Hausser Scientific, Horsham, PA).

Bead Preparation. All reagents were handled in a UV-treated laminar flow hood (UVP, Upland, CA). The oligonucleotides used in this study (Table A1) were ordered from IDT (Coralville, IA). Reverse primers were labeled with 6-FAM or Cy5 dye on the 5-prime end. 5' amine modified forward primers were linked to agarose beads (34 μm mean diameter, Amersham Biosciences, Piscataway, NJ) through amine-NHS conjugation chemistry. An additional twenty one ‘T’ bases

were inserted between the 5' amine and the priming site of the forward primer to minimize steric hindrance during on-bead amplification. Agarose beads (~0.1 g) were washed 3 times with cold 0.1 M HCl, cold H_2O once, and cold 0.1 M PBS (pH 7.5) twice to completely remove propanol that the beads were stored in. Amine labeled forward primer for pUC18 target was mixed with the beads in ~0.3 mL 0.1 M PBS (pH 7.5) with a ratio of ~1.5 μmol oligos per gram beads and incubated overnight with stirring at room temperature. For the experiments on *E. coli* cells, 0.1 g beads were reacted with equimolar amine labeled forward primers at ~0.3 μmol oligos per gram beads following the same procedure. After reaction, beads were washed 3 times with 0.1 M PBS to remove any unbound oligos and stored in pure water at 3 ºC until needed. Final bead concentration was determined by counting with a hemacytometer.

PCR Reagent Preparation. For pUC18 experiments using the 32-channel MEGA, 480 μL of reaction mix was prepared with 1X *Ampli* Taq Gold® buffer with 1.5 mM $MgCl_2$ (Applied Biosystems), 0.2 mM dNTPs (Invitrogen), 1 μg/μL heat inactivated molecular biology grade BSA (Sigma, St. Louis, MO), 0.4 ng/μL lambda DNA (New England Biolabs, Boston, MA), 0.01% Tween-80 (Sigma), 0.4 μM reverse and 0.04 μM forward primers, ~ 40 forward primer labelled beads/μL (i.e. 0.1 beads/2.5 nL droplet), 0.4 U/μL *Ampli* Taq Gold® Polymerase (Applied Biosystems), and ~400 template DNA/μL (i.e. 1 copy/2.5 nL droplet). For *E. coli* experiments with an average cell concentration ≤ 1 cell per droplet (cpd), the PCR mix contains 1X *Ampli* Taq Gold® buffer with 1.5 mM $MgCl_2$, 0.2 mM dNTPs, 0.5 μg/μL heat inactivated BSA, 0.01% Tween-80, 0.4 μM reverse and 0.04 μM forward primers for each cell target, 0.1 beads/2.5 nL droplet, 0.2 U/μL *Ampli* Taq Gold® Polymerase, and various amount of cells. At the average cell concentrations of 10 and 100 cpd, the PCR mix was optimized to have 3 mM $MgCl_2$, 2 μM reverse and 0.2 μM forward primers for *E. coli* K12, with other ingredients kept the same. PCR mix (100–1500 μL) was prepared for each sample depending on the MEGA device used and the time for droplet generation. To minimize DNA/polymerase adsorption on glass and PDMS surface, the MEGA device was primed with a coating solution consisting of 1X *Ampli* Taq Gold® buffer with 1.5 mM $MgCl_2$, 0.5 μg/μL heat deactivated BSA, and 0.01% Tween-80.

Droplet Generation. Carrier oil and the microfine solution were prepared following a modified protocol to enhance the thermal stability of large microdroplets.[154] Carrier oil is a mix of 39.8 % (w/w) DC 5225C Formulation Aid (Dow Chemical Co., Midland, MI), 30% (w/w) DC 749 Fluid (Dow Chemical Co.), 30% (w/w) AR20 Silicone Oil (Sigma-Aldrich), and 0.2% (w/w) Triton X-100 surfactant (Sigma-Aldrich). The microfine solution, which confers additional stability to droplet PCR, was prepared by emulsifying a mix of carrier oil and coating solution (20 μL each) in 0.6 mL PCR tubes with a TissueLyser mixer (Qiagen) at 25 Hz for 5 min. Carrier oil from gastight syringes (Hamilton Company, Reno, NV) was infused into a MEGA using a syringe pump (PHD 2000, Harvard Apparatus, Holliston, MA). PCR reagent, along with beads, was injected into the channels by the on-chip 3-valve diaphragm pump. A homemade pneumatic control system composed of multiple solenoid valves (Humphrey Products, Kalamazoo, MI) was used to actuate the micro-pump. The three valves form input, displacement and output of a diaphragm pump and are cycled in a four-step fashion under the control of a LABVIEW graphical interface (National Instruments): open input and close output, open displacement, close input and open output, close displacement.[135] One droplet is generated every pumping cycle. The oil infusion and pumping settings for generating 2.5 nL droplets are summarized in Table A2.

The MEGA device was prerun with the coating solution for ~30 min, after which the coating solution was replaced with PCR mix and the droplet production was initiated. The sample reservoir was constantly replenished with PCR mix to sustain the droplet generation. Droplets were collected into individual 0.6 mL PCR tubes containing microfine solution, which were then thermocycled as follows: for pUC18, 10 min at 95°C–hotstart initiation, 40× (30 s at 95°C, 90 s at 55°C, 60 s at 72°C) – amplification, 7 min at 72°C–final extension; for *E. coli*, 10 min at 95°C, 6× (30s at 94°C, 90s at 65°C, 60s at 72°C), 8× (30s at 94°C, 90s at 63°C, 60s at 72°C), 10× (30s at 94°C, 90s at 60°C, 60s at 72°C), 13× (30s at 94°C, 90s at 55°C, 60s at 72°C), and 7 min at 72°C.

Bead Recovery and Flow Cytometry Quantitation. The emulsion in PCR tubes was vacuumed to pass a 15 μm mesh filter (Qasina, Edgewood, NY) in a 13 mm-diameter plastic filter holder (Pall Life Sciences, Ann Arbor, MI). The droplets were broken and the beads were retained by the filter. After rinsing with isopropanol, 100% ethanol and 1× Dulbeccos PBS (DPBS, GIBCO) (~15 mL each), the beads were recovered using a 5 mL syringe and stored in 1× DPBS for flow cytometry analysis. The bead suspension in PBS was analyzed by using a multicolor flow cytometer (FC-500, Beckman-Coulter, Fullerton, CA). FAM labelled DNA product on the bead surface was quantified against standard beads with different known amounts of fluorophores (Bangs Laboratories Inc, Fishers, IN). The flow cytometry data were analyzed by using WinMDI (Scripps, La Jolla, CA) and QuickCal (Bangs Laboratories Inc, Fishers, IN).

Table A1. Primer sequences for gene targets

Gene target	T_m (°C)	Sequence	Size (bp)
pUC18			
forward primer	60.5	5′-TGCGGCATCAGAGCAGATTGTACT-3′	624
reverse primer	58.7	5′-FAM-ACCGTATTACCGCCTTTGAGTGAG-3′	
***E. coli* K12 #128 Island**			
forward primer	60.2	5′-TTCGATTACACGGAGTGCTGGGAA-3′	262
reverse primer	60.3	5′-FAM-CGTTGATTTGCCGTTCCATGTCGT-3′	
***E. coli* O157 #43 Island**			
forward primer	59.5	5′-GGGCAGGAAGAGAGTGACAGG -3′	192
reverse primer	59.1	5′-Cy5-CGGCCTTACCCGTGAACAGTA-3′	

Table A2. Operation conditions for the generation of 2.5 nL droplets using MEGA devices.

MEGA device	**Syringe**	**Total flow rate of oil phase**	**Pneumatic setting (pressure/vacuum)**	**Actuation time for each pumping step**
4-channel	2 × 2.5 mL	8 μL/min	+30 kPa /-85 kPa	40 ms/40 ms/22 ms/18 ms
32-channel	1 × 10 mL	56 μL/min	+40 kPa /-85 kPa	45 ms/45 ms/45 ms/45 ms
96-channel	1 × 10 mL	190 μL/min	+32 kPa /-85 kPa	50 ms/48 ms/24 ms/20 ms

Appendix B: Supplemental information for Chapter 3

B.1 Supplementary materials and methods

Fabrication of nickel molds. A Graphtec Craft Robo Pro CE5000-40 Cutting Plotter (Graphtec America, Inc.) was used to plot CAD designs directly from a .dwg or .dxf file with a programmed step size of 10 μm. An 80 μm thick vinyl adhesive film (3M Scotchcal 220, Gerber Scientific Products, Inc.) was used as the positive electroplating mask. Following plotting, features to be plated up were removed manually using fine-tipped forceps. The plotted design was overlaid with laboratory tape prior to removal from the backing substrate. Feature heights greater than 80 μm were formed by layering one or more vinyl adhesive films over the first prior to cutting. Optimal electroplating uniformity was achieved by the addition of 500 μm wide perimeter boundary features within 500 μm of the designs.

Stainless steel sheets (0.030" thick 304 grade steel with a "mirror-like" finish; #9785K51, McMaster-Carr, Inc.) were machined into circular 90 mm diameter wafers and washed with isopropanol and distilled water. Following a nickel strike of the wafer at 235 $A\text{-}m^{-2}$ for 2 min at 50-55 ^{o}C in a continually-stirred Wood's Nickel Strike Solution (240 $g\text{-}L^{-1}$ $NiCl_2 \bullet 6\ H_2O$, 25% v/v HCl) with an electrolytic nickel anode, the sticker mask was transferred to the steel wafer and the transfer tape or film was removed. The exposed features were electroplated to the desired height in a continually-stirred commercial bright nickel plating solution (#42027, Alfa Aesar, Inc.) at 55 ^{o}C. Multi-level features were fabricated by uncovering regions with the tallest features, and later removing the sticker mask from lower height features. For a repeatable and uniform plating rate, the sticker mask-coated wafer and the nickel anode were held in place in a custom acrylic manifold. A laboratory power supply (GPS-3030DD, Instek, Inc.) was used in current control mode to regulate the plating current density. Any remaining adhesive following sticker removal was dissolved with a 1:1 mixture of acetone and toluene. Care should be taken with handling and disposal of nickel salt solutions as nickel contact can cause allergic reactions in some people and ingestion or inhalation has been associated with increased cancer risk.

Hot embossing plastic microfluidic devices. Zeonor 1060R and 1420R cyclo-olefin copolymer (COC) sheets (1 mm thick) were obtained directly from Zeon Chemical, Inc. Extruded 250 μm thick THV500 samples were kindly provided by Dyneon, Inc. Hot embossing was performed in a hot embossing insert built in-house (see Fig. S1) attached to an H6231Z 10 Ton Hydraulic Press (Grizzly Industrial, Inc.). A sheet of polymer was sandwiched between the nickel mold and a sheet of glass and placed between the heated platens. Best results were obtained at pressures of 5-15 MPa for 0.5-2 min and >10 ^{o}C above the polymer's glass transition temperature (T_g). Devices were cooled under pressure and de-embossed 10 ^{o}C below T_g.

Heated platen insert design details. The insert consists of two 4.5" diameter 3/8" thick aluminum platens, each with a 300W concentric ring heating element (A203/120, Omega, Inc.). Teflon sheets (1/4" thick, 4.5" diameter) and a Teflon washer (1" diameter) were used for thermal insulation. The insert components were attached together using headless screws. The temperature of each platen was independently maintained using two T-type thermocouples (5TC-GG-T-24-36, Omega, Inc.) and two PID controllers (CN7823, Omega, Inc.) connected to the heating elements *via* solid state relays (SSRL240DC25, Omega, Inc.).

Device assembly. Via holes in COC devices were drilled using a 1/32" milling bit operated at low speed (approximately 100-200 rpm) to minimize surface roughness. Via holes in THV500 devices were made using a 1 mm biopsy punch. Following drilling of via holes, devices were cleaned with

distilled water and isopropyl alcohol and dried with nitrogen prior to bonding. Rapid bonding of the embossed COC sheets was accomplished using a solvent-assisted lamination approach modified from the work of Miserere *et al.*[189] We identified o-xylene as an optimal solvent for bonding COC devices due to the absence of hazing or cracking, compared to cyclohexane[196] and hexadecane,[189] and low toxicity and carcinogenicity. Specifically, pipetting 1:1 o-xylene:isopropyl alcohol to cover the featureless polymer sheet and incubating for 30 s (Zeonor 1420R) or 10 s (Zeonor 1060R) resulted in a thin low-Tg layer that could be laminated to the embossed sheet at temperatures that would not distort the channels. The sheets were quickly dried with nitrogen prior to bonding at or slightly below the polymers' T_g in a Peach 3500 Photo Pouch Laminator (PEACH 3500, Oregon Laminations, Inc.) at the slowest speed setting. THV500 devices were washed briefly with acetone and dried prior to laminator bonding. Devices with integrated PDMS membrane valves were bonded using a UV/O_3 cleaner (Jelight Company, Inc.) by activating each COC surface as well as both sides of the 250 μm PDMS membrane (B&J Rubber Products, Inc.) for 2.5 min. If necessary, a permanent bond was achieved by heating the assembled device for >10 min at 70 ^{o}C or more.

Droplet generator operation. Droplets were generated using the droplet generator fabricated from THV500, with Droplet Generator Oil (#186-3005, Bio-Rad, Inc.) as the continuous phase. The aqueous phase consisted of standard PCR mix with 1.5 mg/mL BSA (A7906, Sigma-Aldrich) and 5% w/v Pluronic F68 for stabilizing droplets during PCR. Droplets were generated at flow rates of 83 μL/min (oil phase) and 30 μL/min (PCR mix).

Imaging and characterization. Bright field and fluorescence microscopy images were taken with a Retiga EXi CCD camera (Q Imaging, Inc.) mounted on a Nikon SMZ1500 dissecting microscope fitted with a 515 nm long pass filter (OG515LP, Nikon, Inc.) and custom built illumination module containing a 470 nm Luxeon Star LED (LXML-PB01-0030, Quadica Developments, Inc.) and FITC excitation filter (FM475-35, Thorlabs, Inc.). Scanning Electron Microscopy (SEM) was performed on a Hitachi S-2460N. Nickel molds were imaged directly while polymer devices were sputtered with approximately 15 Å of gold using a Polaron SEM Coating System. Height and lipping characterization of nickel molds was performed using a Dektak 3030 Surface Profiler. Values are expressed as means with 95% confidence intervals unless stated otherwise.

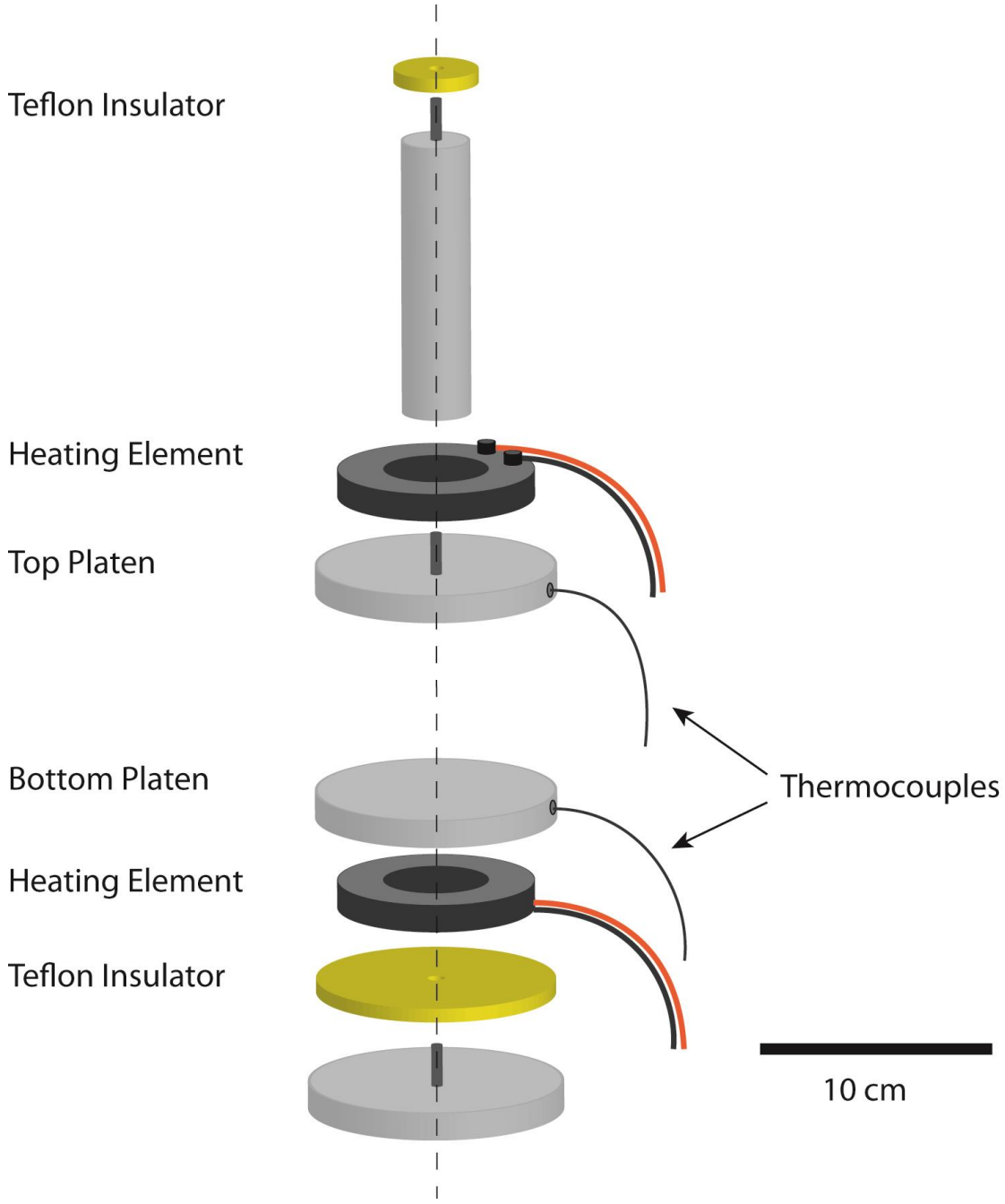

Figure B1. Exploded rendering of the insert designed to convert a hydraulic press into an inexpensive hot embossing machine for easy access to hot embossing of thermoplastic microfluidic devices. Platens machined from 3/8" aluminum stock, thermally insulating 1/4" Teflon sheets, and a 1" wide aluminum force transduction rod were fastened together and to the press with headless screws. Two concentric heating elements are independently regulated by two PID controllers (not shown) that receive feedback from the thermocouples inserted into the platens.

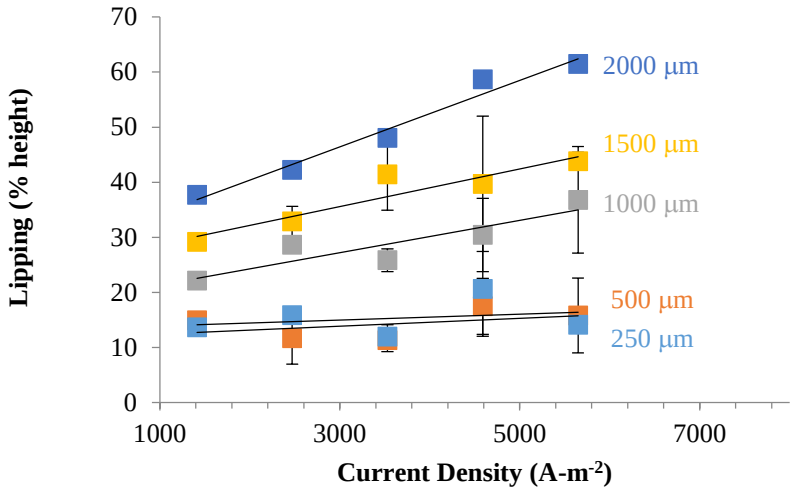

Figure B2. Lipping of feature edges expressed as a percentage of feature height increases both as a function of average current density and distance of the boundary feature from the studied feature. To generate these data, 1.5 mm wide boundaries were placed at the specified distances from 1.5 mm wide features and electroplated at various current densities. Error bars show standard deviation of the mean.

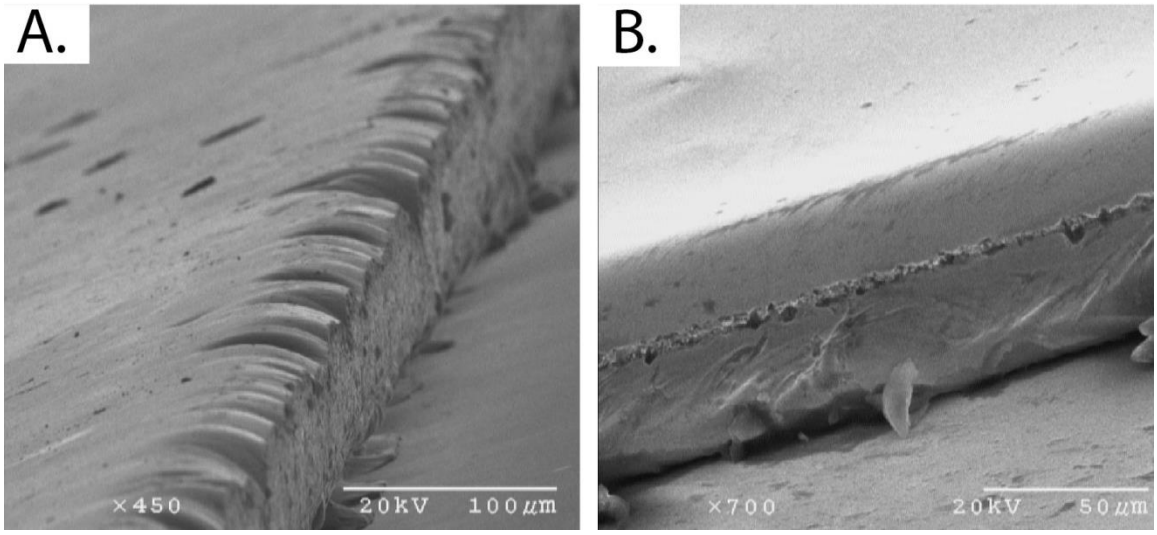

Figure B3. Details of nickel molds illustrating the incorporation of electroplating boundaries. SEM images of electroplated features show pronounced lipping and uneven edges in an unbounded feature (A) and smooth and uniform edges with decreased lipping in a feature adjacent to a boundary (B).

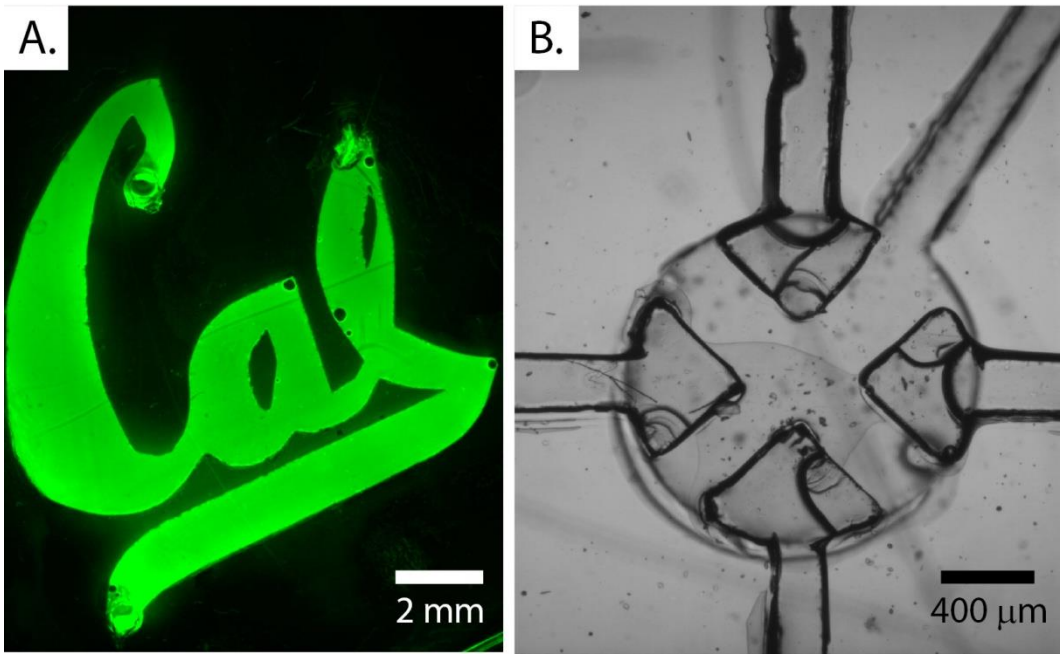

Figure B4. Images of sticker mold-fabricated and assembled functional devices. (A) Extremely wide low aspect ratio channels filled with calcein to demonstrate the uniform 50 μm channel height after bonding. (B) The rapid prototyping method can be used to produce functional components, such as a four-way pneumatic valve made with an integrated PDMS membrane.

Appendix C: Supplemental information for Chapter 5

C.1 Supplementary materials and methods

Study Subjects. The study population and exposure assessment have been previously described in detail.[331] This study was approved by the Institutional Review Boards at the U.S. National Cancer Institute and the Guangdong Poisoning Control Center. Participation was voluntary and written informed consent was obtained. A formaldehyde-exposed worker population was enrolled from two factories, one that produced a formaldehyde-melamine resin, and one that used formaldehyde-melamine resin to manufacture plastic utensils. A control population was selected from three workplaces in the same geographic region as the factories with formaldehyde exposure, and this control population consisted of workers with similar demographic and socioeconomic characteristics and who were primarily engaged in manufacturing. All exposed workers met two inclusion criteria: (1) they had formaldehyde exposure levels of ~1-2 ppm on most days during the initial screening; and (2) they held the same job for at least the previous three months in the same factory. Exclusion criteria for both exposed and control populations were history of cancer, chemotherapy and radiotherapy, as well as previous occupations with notable exposure to benzene, butadiene, styrene, and/or ionizing radiation. We enrolled 43 study subjects exposed to relatively high levels of formaldehyde (mostly between 0.6 and 2.5 ppm), and we enrolled 51 controls who were frequency matched by age (+/- 5 years) and gender to the exposed workers. For more detail regarding the demographic characteristics of the study subjects, please see Appendix Tbl. C2. Data on t(14;18) were not available for one of the 43 formaldehyde-exposed workers. In addition to the 93 study subjects that were tested for t(14;18), one of the authors carries low levels of t(14;18) and this individual provided peripheral blood for comparison of relative signal in clot, buffy coat, and PBMCs (Appendix Fig. C1).

Exposure Assessment. Formaldehyde exposure was monitored with UMEx 100 diffusion samplers, and the limit of detection was 0.012 ppm. These samplers were worn by workers in the exposed workplaces for a full shift (>240 min) on ~3 working days over a 3-wk period. Biological samples were collected toward the end of this period. Each formaldehyde-exposed subject had a minimum of two diffusion samplers collected. The average formaldehyde exposure level was calculated by taking the arithmetic mean of each subject's measurements. A subgroup of workers in the unexposed workplaces was monitored for formaldehyde exposure on a single day. For more detail regarding the exposure characteristics of the study subjects, please see Appendix Tbl. C2.

Biological Sampling. In June and July 2006, we obtained biological samples from the 94 study subjects at their workplaces after informed consent was obtained. Biological samples were collected after the formaldehyde-exposed workers had been monitored at least twice for personal formaldehyde exposure in their workplace. Peripheral blood samples were collected from each study subject and delivered to the processing laboratories within 4 hours of collection. Peripheral blood from each study subject was drawn into different vacutainer tubes by specially trained nurses, and was then allowed to clot before shipment to Bioreliance, Inc. under contract to the National Cancer Institute. Bioreliance then extracted clot gDNA, recoded the samples, and sent the samples to the University of California at Berkeley laboratory for analysis. Thus, all laboratory analyses carried out after completion of the field phase of the study were done blinded to exposure status.

Cell Culture. Cell lines of t(14;18)$^{-}$ TK6 (CRL 8015) and t(14;18)$^{+}$ RL (CRL 2261) (ATCC, Manassas, VA) lymphoblasts were maintained in RPMI 1640 medium (Gibco, Carlsbad, CA)

supplemented with 10% FBS (Omega Scientific, Tarzana, CA) at a cell density of ($2x10^5$ - $2x10^6$)/mL and incubated at 37°C in a 5% CO_2 atmosphere.

Cell and gDNA Purification. For purification of clot gDNA we used Clotspin® baskets and the Gentra® Puregene® blood kit according to the manufacturer's recommendations (Qiagen, Valencia, CA). Buffy coat was prepared by spinning whole blood at 200x g for 10 min at room temperature and then removing the concentrated leukocyte band plus a small portion of the plasma and concentrated red blood cells. We then isolated DNA from buffy coat using the FlexiGene DNA kit and the manufacturer's instructions (Qiagen). PBMCs were purified from whole blood using density gradient centrifugation through Ficoll-Paque™ PLUS according to the manufacturer's recommendations (GE Healthcare, Piscataway, NJ). To purify gDNA from cell lines and PBMCs we used a standard cell lysis with RNA and protein digests followed by a phenol-chloroform DNA extraction (solvents from Sigma-Aldrich, St. Louis, MO). Briefly, cells ($5x10^6$/mL) were lysed in a 10 mM Tris-HCl buffer (pH=8.0) with 100 mM EDTA and 0.5% SDS and then treated first with RNAse (20 mg/L, from Roche) at 37 °C for 1 hour and then with Proteinase K (100 mg/L, from Qiagen) at 56 °C for 3-24 hours. Phenol-chloroform extraction was then performed in Phase Lock Gel™ tubes (Eppendorf) using an initial wash with phenol/chlorofrom/isoamyl alcohol (25/24/1, v/v/v, [PCI]), followed by a second Proteinase K treatment (50 mg/L, 2-4 hours at 56 °C), followed by three more washes in PCI, and finally followed by a single wash with chloroform/isoamyl alcohol (24/1, v/v). DNA was then precipitated by adding ammonium acetate to 500 mM and isopropyl alcohol to ~43% (v/v). DNA was spooled onto a pipette tip and washed thrice in 70% ethanol before air drying. DNA was then resuspended in Tris-EDTA buffer (10 mM Tris-HCl, 5 mM EDTA, pH=8.0) and the concentration was measured by UV absorption (A_{260}) and adjusted to 200ng/µL. The quality of gDNA was assessed and copy number was normalized using quantitative PCR for β-actin. The β-actin PCR mix contained 1X *Ampli* Taq Gold® buffer with 5 mM $MgCl_2$, 0.2 mM dNTPs (dUTP was used at 0.4 mM instead of dTTP), 0.01 U μL^{-1} uracil DNA glycosylase (UDG, Roche), 2.5% DMSO, 1 µM ROX reference dye, 0.3 µM each of the oligonucleotides (F-ActB, R-ActB, ActB probe, please see Supplementary Tbl. 3 for sequences), 0.035 U μL^{-1} *Ampli* Taq Gold® Polymerase and 1 µg gDNA per 50 µL reaction. Thermal cycling in an ABI 7300 cycler consisted of a UDG reaction (50 °C for 2 min), followed by a 10 min hot start at 95 °C, and 40 cycles of 95 °C for 15 s, 60 °C for 30 s, and 72 °C for 30 s.

MEGA Device fabrication and assembly. The 4-channel MEGA devices were constructed from 100-mm diameter glass wafers and a thin poly(dimethylsiloxane) (PDMS) membrane, as detailed previously (26). Briefly, the valve seat structure was first microfabricated on the top side of a Borofloat® glass wafer. Using backside alignment lithography, the microchannels were patterned onto the bottom of the same wafer in register with the pump structure. Fluidic and interlayer access holes were drilled and the wafer was thermally bonded to a clean substrate to enclose the microfluidic network. The on-chip pump assembly was completed by sandwiching a 200 µm PDMS membrane between the chip and a pneumatic manifold plate with microfabricated valve displacement chambers. The glass channels were rendered hydrophobic by coating with a 0.1% solution of octadecyltrichlorosilane (OTS, Sigma-Aldrich) in dry toluene for 10 min.

Bead functionalization. All reagents were handled in a UV-treated laminar flow hood (UVP, Upland, CA). All oligonucleotides used in this study (Appendix Tbl. C3) were obtained from IDT (Coralville, IA). For emulsion dPCR, the Nv3 primer was labeled with 6-FAM on the 5' end. We added a C_{12} spacer and a 5' amine modification to JH Exo and then covalently linked the primer to

6% cross-linked NHS-activated Sepharose beads (34 μm mean diameter, #17-0716-01, GE Healthcare) at ~0.5 μmol g^{-1} through amine-NHS conjugation chemistry (26). After overnight incubation, primer beads were washed and re-suspended in water at final bead concentrations of 4000-8000 beads μL^{-1}.

Droplet generation. The fresh carrier oil was prepared daily and contains 39.8% (w/w) DC 5225C Formulation Aid (Dow Chemical Co., Midland, MI), 30% (w/w) DC 749 Fluid (Dow Chemical Co.), 30% (w/w) AR20 Silicone Oil (Sigma-Aldrich), and 0.2% (w/w) Triton X-100 surfactant (Sigma-Aldrich). Following the completion of this work, we have discovered that recent batches of 749 Fluid exhibit decreased emulsion stability. We find that omitting Tween 80 from the PCR cocktail is sufficient to restore stability during thermal cycling. The MEGA device was assembled with a custom aluminum manifold which provides fluidic connection for oil infusion and droplet collection. Carrier oil was continuously injected into the MEGA device from two gastight syringes (Hamilton Company, Reno, NV) using a syringe pump (PHD 2000, Harvard Apparatus, Holliston, MA). Emulsion dPCR mix containing t(14;18) amplicon and primer beads was injected into the microchannels for droplet generation by the on-chip 3-valve diaphragm pump, which was pneumatically actuated by a solenoid valve controller system built in house. The pumping was conducted in a four-step fashion under the control of a LABVIEW graphical interface (National Instruments, Austin, TX).[135]

Pumping parameters were optimized to produce uniform ~2.5 nL PCR reaction droplets (actuation times: valves 1 and 2 open, 42 ms; valve 1 close, 42 ms; valve 3 open, 20 ms; valves 2 and 3 close, 18 ms; total oil flow rate: 14 μL min^{-1}; pneumatic line pressure/vacuum: +35/-85 kPa). The sample reservoir was constantly replenished with PCR mix to sustain the droplet generation. PCR droplets were collected in 0.5 mL PCR tubes (Eppendorf) filled with microfine emulsion.

Hemi-Nested PCR. All oligonucleotides used in this study were obtained from IDT (please see Supplementary Tbl. 3 for sequences), and unless otherwise noted, PCR reagents were from Life Technologies (Carlsbad, CA). The preamp reaction mix contained 1X *Ampli* Taq Gold® buffer with 5 mM $MgCl_2$, 0.2 mM dNTPs (dUTP was used at 0.4 mM instead of dTTP), 0.01 U μL^{-1} UDG (Roche), 2.5% DMSO, 0.3 μM each of the oligonucleotides (JH Exo and RT0001), 0.035 U μL^{-1} *Ampli* Taq Gold® Polymerase and three μg gDNA per 50 μL reaction. Thermal cycling in an ABI GeneAmp® 9700 cycler consisted of a UDG reaction (50 ºC for 2 min), followed by a 10 min hot start at 95 ºC, and 20 cycles of 95 ºC for 15 s, 60 ºC for 30 s, and 72 ºC for 30 s.

The hemi-nested reaction mix contained 1X *Ampli* Taq Gold® buffer with 5 mM $MgCl_2$, 0.2 mM dNTPs (dUTP was used at 0.4mM instead of dTTP), 2.5% DMSO, 1 μM ROX reference dye, 0.3 μM each of the oligonucleotide sequences (JH Exo, Nv3, and BCL2MBRTM2), 0.035 U μL^{-1} *Ampli* Taq Gold® Polymerase and 1 μL of the preamp reaction product per 50 μL nested reaction. Thermal cycling in an ABI 7300 cycler consisted of a 10 min hot start at 95 ºC, and 33 cycles of 95 ºC for 15 s, 60 ºC for 30 s, and 72 ºC for 30 s. Quantitative standards were made by diluting RL gDNA in TK6 gDNA and were used to establish a linear relationship between C_t and the logarithm of t(14;18) concentration (please see Fig. 5.1 and Appendix Fig. C2). Each assay plate included three quantitative standards (10^2, 10^1, and 3 copies in 3 μg) as well as a negative DNA standard (3 μg of purely negative TK6 DNA) to ensure robust and specific detection at the level of 1 copy/μg. Positive reactions were loaded on a 1.5% agarose gel and electrophoresed to separate amplicons of different size that were then excised, purified using a QIAquick Gel

Extraction Kit (QIAGEN), and sequenced on an ABI 3730 at the UC Berkeley Core Sequencing Facility.

Digital PCR. The dPCR mix contained 1x *Ampli* Taq Gold® buffer with 3 mM $MgCl_2$, 0.2 mM dNTPs, 0.4 µg/µL heat-inactivated BSA, 0.01% Tween 80, 0.3 µM FAM-Nv3, 0.03 µM JH Exo, 0.125 U μL^{-1} *Ampli* Taq Gold® Polymerase, ~85 beads functionalized with JH Exo per µL (target ~0.2 beads per 2.5-nL droplet), and 0.5-0.05 µL of preamp product per 50 µL dPCR reaction volume (titrated to achieve 0.01-0.2 copies per 2.5-nL droplet). For preamp reactions with low t(14;18) frequencies, 0.5 µL of the preamp reaction yielded droplets that were sufficiently dilute to quantify t(14;18) (i.e., not saturated). However, for some of the higher t(14;18) concentration reactions, 0.5 µL of the preamp reaction yielded droplets that were 100% $t(14;18)^+$. These high t(14;18) concentration samples were diluted 10-fold in water and reanalyzed (i.e. 0.05 µL of product from the preamp reaction was used per 50 µL dPCR reaction volume for these high concentration samples). Thermal cycling was carried out in a PTC200 thermocycler (MJ Research, Waltham, MA) and involved a 10 min hot start at 95 °C, and 33 cycles of 95 °C for 30 s, 60 °C for 60 s, 72 °C for 90 s, and a final 72 °C extension for 5 min. The reactions were then cooled to 4 °C until bead recovery (typically overnight).

Techniques to prevent PCR contamination. In addition to using UDG in preamplification, we also used dedicated work spaces for pre- and post-PCR work. All components of PCR mixes were prepared in a sterile laminar-flow hood; and the sterile hood and the pipettes used to set up PCR reactions underwent routine UV sterilization between experiments. In addition, all samples that were positive based on cleavage of the probe sequence in qPCR, or based on concentration of FAM^+ beads in dPCR, were then confirmed by sequencing the clonal form of t(14;18). In the rare event that the t(14;18) sequence from the CRL 2261 positive control cell line (3615-CGGCCCTTTAGGATCCC-87330523 [BCL2-N-IgHJ]) was identified, the "positive" result of that particular assay was disqualified. Negative controls (from preamp of CRL 8015 gDNA) were included on every nested qPCR assay 96-well plate, and a negative control sample was also included in every run through the droplet generator, and in all cases these negative control reactions tested negative for t(14;18).

Bead recovery and flow cytometry quantitation. The dPCR reaction tube was vacuumed to pass through a 15 µm mesh filter (Qosina, Edgewood, NY) held in a 13 mm-diameter plastic filter holder (Pall Life Sciences, Ann Arbor, MI). The droplets were broken and the beads were retained by the filter. After rinsing with isopropanol, ethanol and 1× Dulbecco's PBS (DPBS, GIBCO) (~15 mL each), the beads were recovered using a 5 mL syringe and stored in DPBS for flow cytometry analysis. The bead suspension in DPBS was analyzed by using a multicolor flow cytometer (FC-500, Beckman-Coulter, Fullerton, CA). The flow cytometry data were analyzed by using WinMDI (Scripps, La Jolla, CA) and WinList 6.0 (Verity Software, Topsham, ME).

Single-molecule sequencing. Single molecule sequencing was accomplished by re-amplifying amplicon-bound beads from dPCR in 50 µL t(14;18) qPCR reactions in 96 well PCR plates. PCR mix contained 1X *Ampli* Taq Gold® buffer with 5 mM $MgCl_2$, 0.2 mM dNTPs (dUTP was used at 0.4 mM instead of dTTP), 2.5% DMSO, 1 µM ROX reference dye, 0.3 µM each of the nucleotide sequences (JH Exo, Nv3, and BCL2MBRTM2), and 0.035 U μL^{-1} *Ampli* Taq Gold® Polymerase. Beads were counted using a hemocytometer and added at ~1 bead per 50 µL reaction. Thermal cycling in an ABI 7300 cycler consisted of a 10 min hot start at 95 °C, and 20 cycles of 95 °C for 15 s, 60 °C for 30 s, and 72 °C for 30 s. The bead-bound amplicon was very stable and could be

re-amplified even after six months of storage at 4 ^{o}C. Reaction products were loaded on a 1.5% agarose gel and electrophoresed to separate various amplicons that were then excised, purified using a QIAquick Gel Extraction Kit (QIAGEN), and sequenced on an ABI 3730 at the UC Berkeley Core Sequencing Facility.

Sequence Analysis. Sequencing reads were aligned to the reference assembly of the human genome using NCBI's nucleotide basic local alignment search tool (BLASTn at www.ncbi.nlm.nih.gov/blast/). The chromosome 14 breakpoint was defined as the terminus of the best alignment with NT_026437.11 and the chromosome 18 breakpoint was defined as the terminus of the best alignment with NM_000633.2. The "N sequence" insert was identified as the *de novo* sequence found between the two breakpoints in a particular translocation clone (see Fig. C4 for a graphical representation of the sequence analysis). Typically, a single sequencing read of amplicon generated with the Nv3 primer provided sufficient length and quality to fully define the particular clonal form(s) of t(14;18) in a given PCR reaction. However, in some cases, the chromosome 18 breakpoint fell too close to the Nv3 primer location, and it was then necessary to generate a paired read using the JH Exo primer. These paired reads were then aligned to each other to generate a full amplicon-length consensus read that spanned completely from Nv3 to JH Exo. This consensus read was then aligned to the human genome using BLASTn to define the breakpoints on chromosomes 14 and 18 as well as the N sequence insert.

To assess the effect of sequencing errors, we used a tracking sequence on the BCL2 side of the translocation, which is less variable than the IgHJ side of the translocation. The tracking sequence (AGAGCCCTCCTGCCCT) extends from position 3498 to position 3513 on NM_000633.2, and it was chosen because it appears in the vast majority of sequencing reads due to both its proximity to the Nv3 sequencing primer and its distance from most of the BCL2 breakpoints. The single exception is that of clone 1 from Subject S; this clonal form (3507-N-87331509 [BCL2-N-IgHJ]) had a BCL2 breakpoint at 3507 and therefore did not contain the complete tracking sequence. Overall, we observed that 67% of all sequencing reads from bead based amplifications contained no errors in this tracking sequences; while 33% of reads contained at least one error. The most common type of sequencing error were insertions (50% of all observed errors), while substitutions accounted for 30% of all errors and multiple errors accounted for the remaining 20% of misread sequences. However, these types of sequencing errors did not impact the results presented here since each clonal form of t(14;18) was sequenced multiple times, allowing a definitive consensus sequence to be assembled, despite the presence of sequencing errors.

Finally, to map the locations of the V(D)J recombination signal sequences (RSSs) to the chromosome 14 contig (NT_026437.11), we mapped all allowable RSS nonamers and heptamers to the contig and then found nonamer-heptamer pairs that were separated by appropriately sized spacer sequences (please see Fig. 5.5 and Fig. C6).

Statistical Analysis. Quantitative analysis and linear regression of t(14;18) concentrations for subjects and for specific clonal forms were performed in Excel (Microsoft, Redmond, WA). Data is presented as average +/- standard deviation for replicate measurements, except where otherwise indicated. We quantified the amount of a t(14;18) clonal form using the overall t(14;18) concentration from hemi-nested PCR weighted by the relative amount of a clonal form as determined by dPCR.

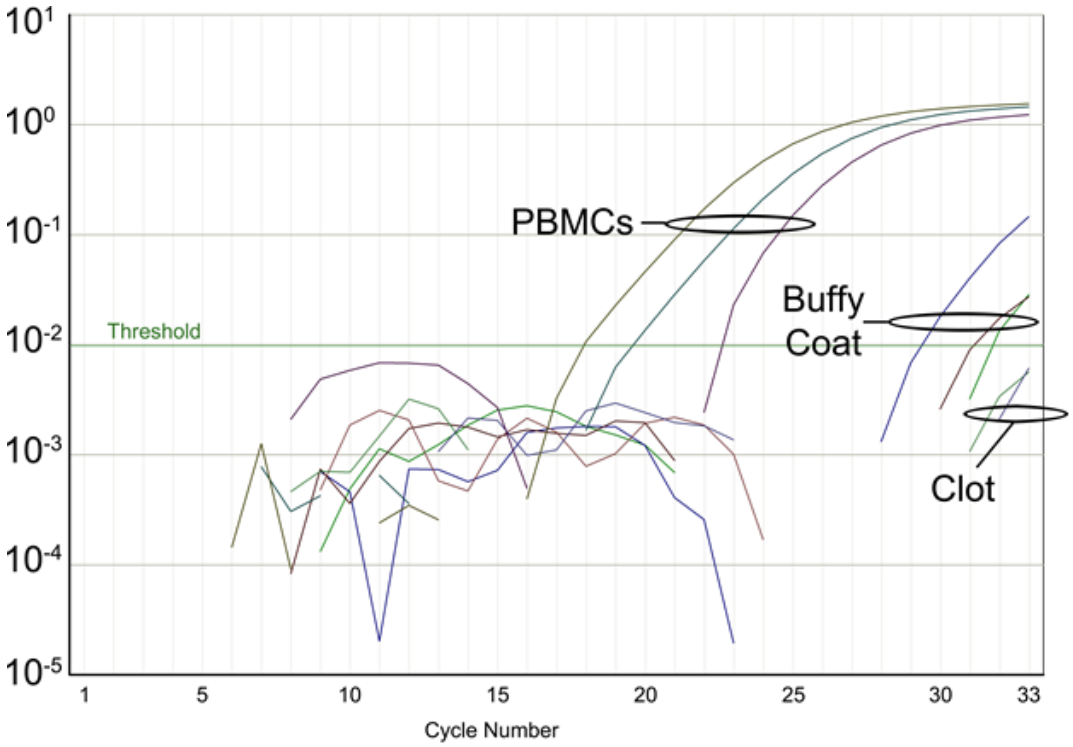

gDNA source	Total Assays	Positive Assays	t(14;18 conc.) (copies/μg)	std dev
PBMCs	10	10	90.378	112.614
Buffy Coat	8	5	0.062	0.074
Clot	8	0	negative	negative

Figure C1. Comparison of t(14;18) concentration in the matched gDNA from various blood fractions. Peripheral blood was collected from a single t(14;18)+ subject and was split for processing in three different manners prior to isolation of gDNA: (1) whole blood was allowed to clot, (2) whole blood was centrifuged to obtain buffy coat (BC), and (3) whole blood was centrifuged in Ficoll-Paque™ to obtain peripheral blood mononuclear cells (PBMCs). These various blood fractions were then assayed for t(14;18) concentration using qPCR. The amplification curves (delta RN vs. cycle number) are shown for a typical experiment where each blood faction was assayed in triplicate. The PBMC and BC gDNAs undergo sufficient amplification to cross threshold in this trial, but no assays of clot gDNA cross threshold (though 2/3 clot gDNA reactions show some indication of amplification very late in the PCR). The overall results from several different experiments are then summarized in the table below the amplification curves. The t(14;18) concentration in the PBMC gDNA of this subject was ~1000-fold higher than the signal found in the BC gDNA. Furthermore, the t(14;18) concentration in BC was substantially higher than that measured in clot gDNA, with t(14;18) detectable in 5/8 BC assay reactions vs. 0/8 assay reactions on clot gDNA.

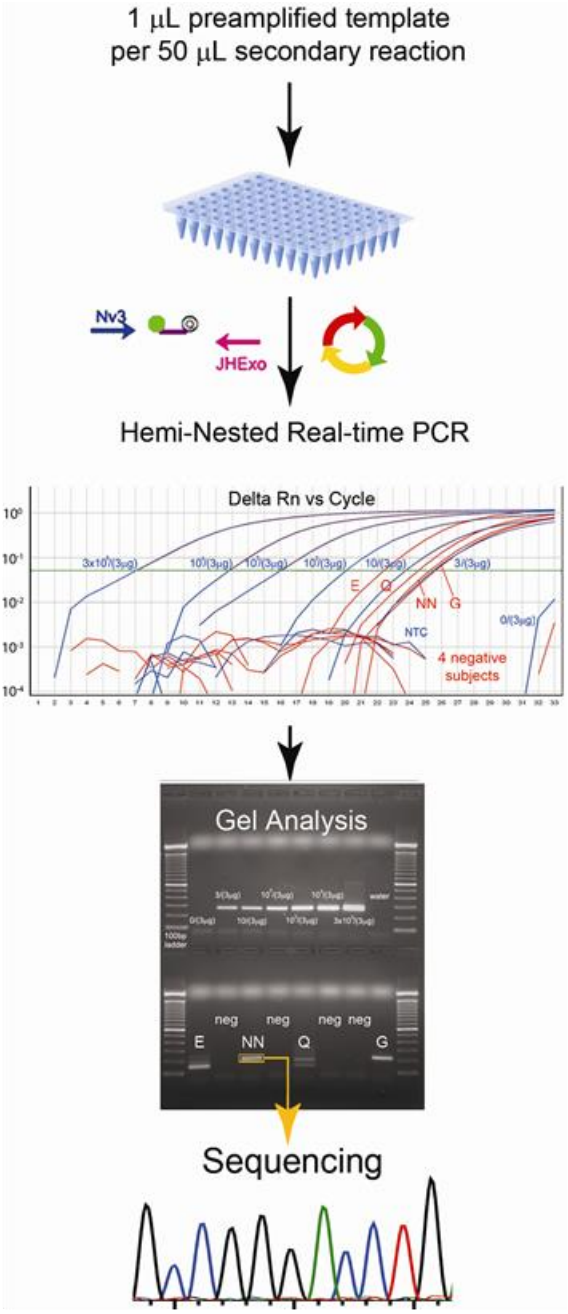

Figure C2. Standard hemi-nested qPCR. Bulk analysis of template is conducted in 50 µL PCR reactions and a BCL2-specific probe is used to provide a real-time signal for positive reactions. During typical screening, only positive reactions are subjected to gel analysis and sequencing. However, in this illustration of the assay, the results for four positive subjects are shown along with the results for four negative subjects. Following gel separation, amplicon from these reactions is used in sequencing reactions to fully define the clonal form(s) of t(14;18) in a sample.

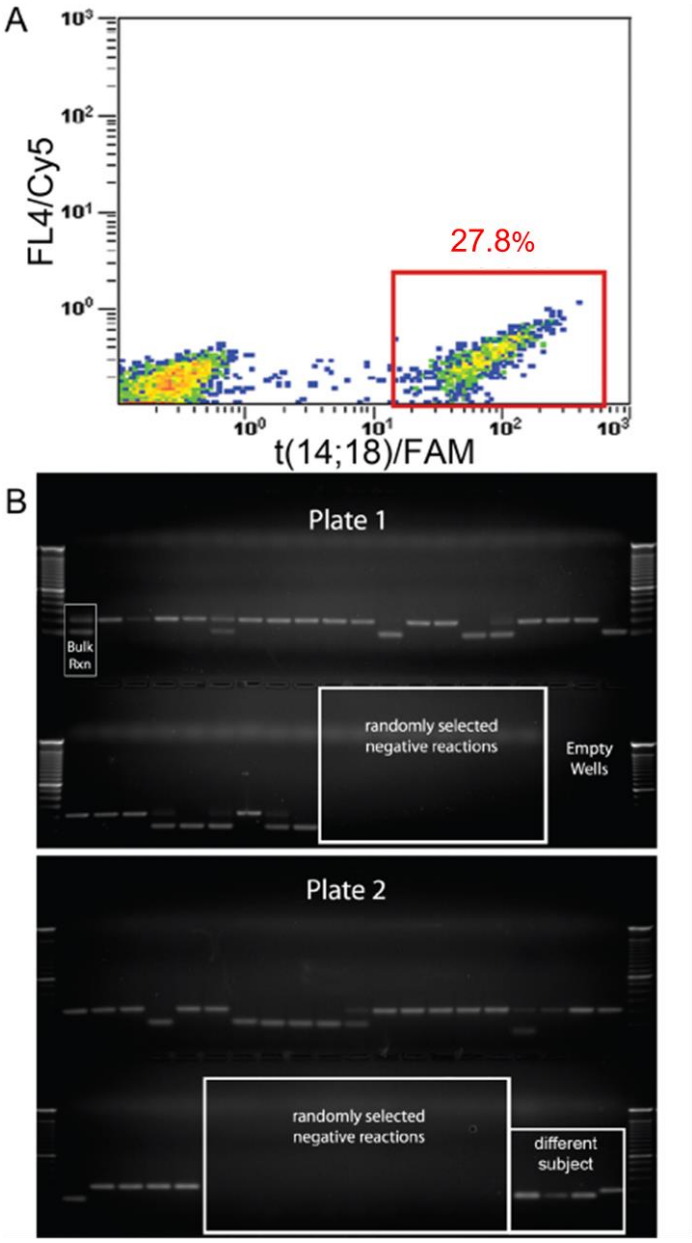

Figure C3. Full Gels for Two 96-well plates of dPCR Beads from Subject "D". (A) Flow cytometry plot showing that the beads from dPCR on this subject are ~28% FAM+. (B) When the beads were plated at ~1 bead per reaction and analyzed by digital real-time PCR, 53 of the 192 wells on two 96-well plates (~27.6% of wells) gave a positive signal from the BCL2-specific probe. When these 53 positive reactions were run on a gel and the clonal forms were counted, it was determined that the ratio of the small form ("clone 1") to the large form ("clone 2") was 18:37 in these 53 wells. Two of these 53 bead-templated reactions yielded both clonal forms, indicating either that two positive beads were loaded in a single well on the 96-well plate, or that two copies of t(14;18) were co-encapsulated within a single nL-scale reaction droplet.

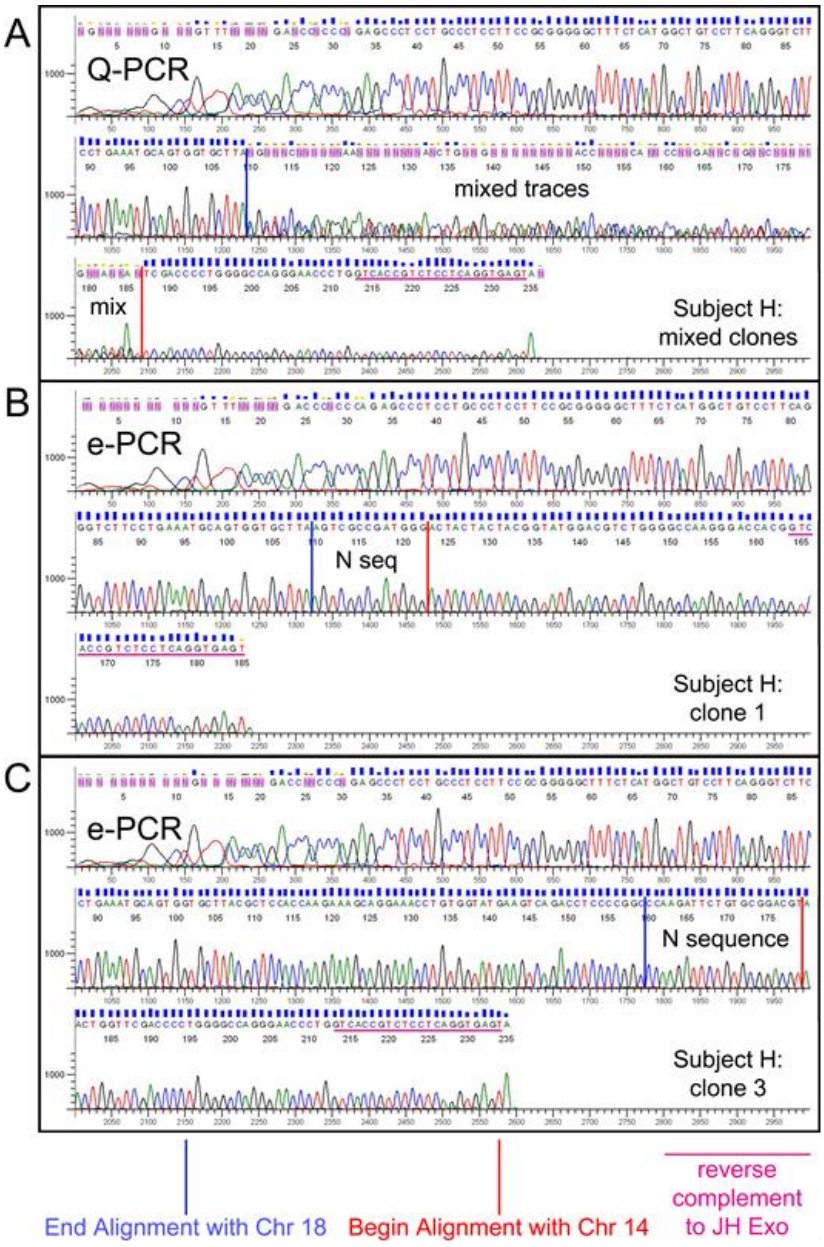

Figure C4. Resolving Clones of Similar Size in Subject H using dPCR. It was difficult to resolve two of the three clonal forms of t(14;18) that were present in Subject H using standard qPCR and gel analysis. However, microfluidic dPCR was capable of resolving these similarly sized clones. The key features from sequence analysis are indicated on the electropherograms, including: (1) the end of alignment with Chromosome 18; (2) the N sequence (or mixed trace portion); (3) the beginning of alignment with Chromosome 14; and (4) the reverse complement to JH Exo (end of amplicon). (A) A mixed trace primed with Nv3 following standard qPCR and gel analysis. (B) The smaller of the clonal forms (Subject H clone 1, 215 bp) is resolved following dPCR. (C) The larger of the clonal from (Subject H clone 3, 266 bp) is resolved following dPCR.

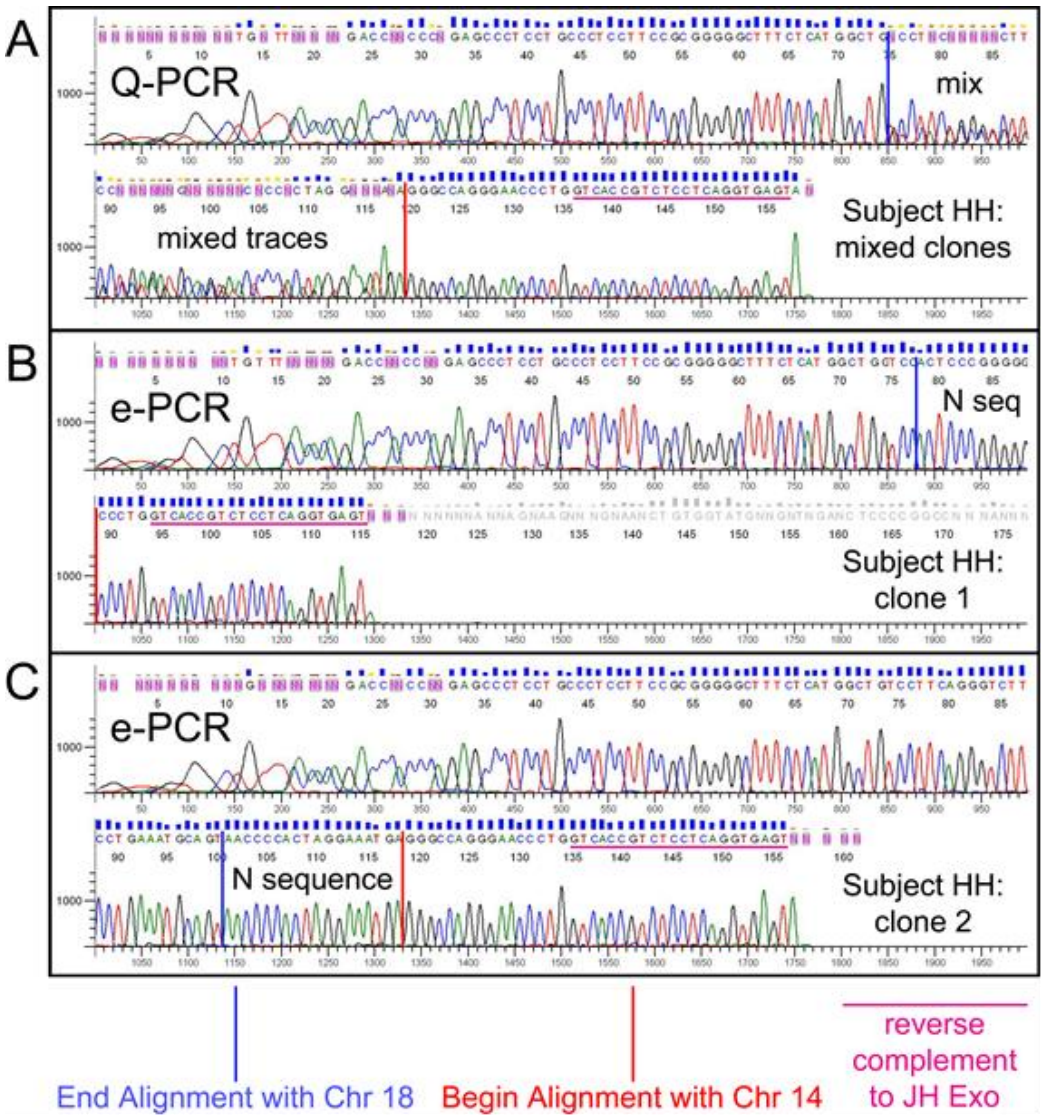

Figure C5. Resolving Clones of Similar Size in Subject HH using dPCR. It was difficult to resolve the two clonal forms of t(14;18) that were present in Subject HH using standard qPCR and gel analysis. However, microfluidic dPCR was capable of resolving these similarly sized clones. The key features from sequence analysis are indicated on the electropherograms, including: (1) the end of alignment with Chromosome 18; (2) the N sequence (or mixed trace portion); (3) the beginning of alignment with Chromosome 14; and (4) the reverse complement to JH Exo (end of amplicon). (A) A mixed trace primed with Nv3 following standard qPCR and gel analysis. (B) The smaller of the clonal forms (Subject HH clone 1, 145 bp) is resolved following dPCR. (C) The larger of the clonal froms (Subject HH clone 2, 187 bp) is resolved following dPCR.

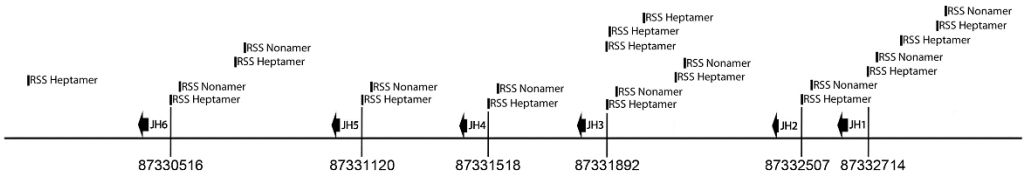

Recombination Signal Sequences on IgHJ region of NT_026437.11

```
Query  1         CACAATGGCAGAATGTCCATCCTCACCCCACAAAAACC  38          J6
                 ||||||||||||||||||||||||||||||||||||||      hep-22-non
Sbjct  87330516  CACAATGGCAGAATGTCCATCCTCACCCCACAAAAACC  87330553

Query  1         CAGACGGCTGCTAAGTCACCCCCAGGAGTCCAAAAACC  38  JPsi3
                 ||||||||||||||||||||||||||||||||||||||      hep-22-non
Sbjct  87330721  CAGACGGCTGCTAAGTCACCCCCAGGAGTCCAAAAACC  87330758

Query  1         CACATTGTGACAACAATGCCAGGACCCCAGGCAAGAACT  39          J5
                 ||||||||||||||||||||||||||||||||||||||      hep-23-non
Sbjct  87331120  CACATTGTGACAACAATGCCAGGACCCCAGGCAAGAACT  87331158

Query  1         CACATTGTGGGAGGCCCCATTAAGGGGTGCACAAAAACC  39          J4
                 ||||||||||||||||||||||||||||||||||||||      hep-23-non
Sbjct  87331518  CACATTGTGGGAGGCCCCATTAAGGGGTGCACAAAAACC  87331556

Query  1         CACAGGGACACAGTCCCTGTTCCTGCCCAGACACAAACC  39          J3
                 ||||||||||||||||||||||||||||||||||||||      hep-23-non
Sbjct  87331892  CACAGGGACACAGTCCCTGTTCCTGCCCAGACACAAACC  87331930

Query  1         CACACTAAAGCGCAGGCCTGGTCCCCGGCACATGAACA  38  JPsi2
                 ||||||||||||||||||||||||||||||||||||      hep-22-non
Sbjct  87332108  CACACTAAAGCGCAGGCCTGGTCCCCGGCACATGAACA  87332145

Query  1         CACAGCCTCTGCCCTCCTGCTTCTCCCATACAAAAACA  38          J2
                 ||||||||||||||||||||||||||||||||||||      hep-22-non
Sbjct  87332507  CACAGCCTCTGCCCTCCTGCTTCTCCCATACAAAAACA  87332544

Query  1         CACGGTGAGTCAGCCCTGAGCCAGGGGCTACAGAAACC  38          J1
                 ||||||||||||||||||||||||||||||||||||      hep-22-non
Sbjct  87332714  CACGGTGAGTCAGCCCTGAGCCAGGGGCTACAGAAACC  87332751

Query  1         GCCAGTGCTCTCCCTTCCGCTGTTAGCCCCAAAACA  36    JPsi1
                 ||||||||||||||||||||||||||||||||||          hep-20-non
Sbjct  87332933  GCCAGTGCTCTCCCTTCCGCTGTTAGCCCCAAAACA  87332968
```

Allowable Heptamers (RSS involvement, if any): CACAGTG, CACGGTG (J1), CACAGCC (J2), CACAGGG (J3), CACATTG (J4,J5), CACAATG (J6), GCCAGTG (JPsi1), CACAGTC, CACACTA (JPsi2), CACACAG, CAGACGG (JPsi3)

Allowable Nonamers (RSS involvement, if any): ACAAAAACC (J6,J4), GCAAGAACT (J5), ACACAAACC (J3), ACAAAAACA (J2), ACAGAAACC (J1), CAAAGAACC, CCCAAAACA (JPsi1), ACATGAACA (JPsi2), ACAAGAACC, CCAAAAACC (JPsi3)

Figure C6. Mapping Recombination Signal Sequences (RSSs) on Chromosome 14 contig NT_026437.11. Map of all RSS heptamers and nonamers on the IgHJ region of Chromosome 14. Appropriately spaced nonamer-heptamer pairs were confirmed as RSSs and mapped to NT_026437.11. If an RSS location corresponded with Chromosome 14 breakpoints observed in this study then the RSS was displayed on Figure C5.

Table C1. Further Details of t(14;18) Clonal Forms. Breakpoint coordinates are given for all the t(14;18) clones defined in these study subjects. The values in the table refer to position on NT_026437.11 (Chromosome 14 breakpoints) and position on NM_000633.2 (Chromosome 18 breakpoints). The unique "N sequence" insert of these clones is also provided (the N sequence is not shown on Figure 5.5). The two clonal forms that were discovered only through dPCR are highlighted (G clone 3 and Q clone 3). It should also be noted that the clonal forms for subjects H and HH could not be resolved without the use of emulsion dPCR. Alternative Chromosome 14 alignments, if found, are also given.

Subject ID	Chr 18 break point	N sequence	Chr 14 break point	Alternate Chr 14 Align(s)	JH RSS proximal to Chr 14 break
S	3507	CTTGCCTTNGATTTGAGG	87331509		**J4**
D clone 2	3514	TCG	87330486		**J6**
P	3516	GTCTCCACAGCGGGCT	87331513		**J4**
G	3518	GCCGCCACAAGCCTAAAATCGACAACAACCGAAGGGTA	87330515		**J6**
E clone 2	3519	TTGGAGGTGGGTCTACGGT	87330495		**J6**
U	3519	CCCCCATG	87330511		**J6**
H clone 2	3520	none	87330486		**J6**
OO	3521	CCCCGGACGGATTAA	87331510		**J4**
W	3521	C	87331115		**J5**
Y	3521	CTACATCGACGTCGGT	87330511		**J6**
Q clone 3	3521	CCACTCCCTCC	87331112		**J5**
J clone 2	3522	CACT	87331117		**J5**
C	3522	CAGTCCC	87331510		**J4**
T clone 2	3526	ACTCACCCCCAC	87331511		**J4**
JJ clone 2	3530	ATACGGT	87330495		**J6**
HH	3543	ACTCCCGGGGG	87331089	87331490 & 87332682	**J5/J4/J1**
O clone 3	3543	NACACCTATTATAA	87331102	87331503	**J5/J4**
I	3554	TAAACCAGTCCCTTCCCAGG	87330506		**J6**
O	3556	CCAAT	87331517		**J4**
B	3560	CCTCCTACCTCCCAAT	87331118		**J5**
DD	3561	CAACGCCTTAGCG	87331509		**J4**
G clone 2	3563	GCGAACCCGCACTCTGGGACCGCTTTTTCAT	87330510		**J6**
MM	3567	CGCTAATCTGAAC	87330508		**J6**
HH clone 2	3567	AACCCCACTAGGAAATGA	87331100	87331501	**J5/J4**
N	3569	GGT	87330495		**J6**
AA	3570	TCGCCCCACTGAGT	87331517		**J4**
A	3571	GCAATA	87331104		**J5**
S clone 2	3571	TCTCCCTCAAGAC	87331507		**J4**
D	3572	CAGGGCAGTGGCTGGTACTG	87330514		**J6**
F	3573	CTTTCCCCCGTAAAGGGGTAACA	87330510		**J6**
K	3574	CCCCCTGGGG	87330511		**J6**
Q	3574	TATTACCC	87331112		**J5**
KK	3575	ATAGCCTCGACAGGGATCG	87331515		**J4**
H	3575	AGTCGCCGATGGG	87330509		**J6**
R clone 3	3575	AGCCCGGGCCCTCCCTGT	87330511		**J6**
M	3575	AGGCTTGGGAGTAA	87331510		**J4**
EE	3575	GGACACATCTTTAAT	87330507		**J6**
CC	3576	ATCGCAGCG	87331511		**J4**
BB	3576	TGTATT	87331116		**J5**
E	3576	none	87332502		**J2**
O clone 2	3577	TTAGGGGA	87331099	87331500	**J5/J4**
BB clone 2	3577	GTAGTTTGTAGTACCAGCTGCTATGG	87330511		**J6**
GG	3577	AAGGGATG	87331513		**J4**
JJ	3584	CCTGATCGAGGAACCACCCGCCCCCCCGAGATCG… …CCTACAGGTGGGATTAGNATAGCAACCAAT	87330510		**J6**
X	3584	GGCG	87332704		**J1**
J	3596	GGATCT	87331512		**J4**
G clone 3	3596	GGTCGGCGGA	87331889		**J3**
L	3600	GATAAAC	87330517		**J6**
LL	3621	ATATCATACGGT	87330495		**J6**
II	3621	GG	87330509		**J6**
Z	3622	GGGC	87331509		**J4**
FF	3623	TTTCATCCCTACGGT	87330495		**J6**
NN	3625	C	87330502		**J6**
R clone 2	3626	AAGGCTACCNGGATTTGNGGT	87330511		**J6**
V clone 2	3627	TCTCCGGGTATAGCAGCAGG	87331114		**J5**
H clone 3	3627	CCAAGATTCTGTGCGGACGT	87331117		**J5**
R	3630	GTTGGTT	87331512		**J4**
T	3631	none	87331506		**J4**
V	3635	CCGTCGAAACATGC	87331510		**J4**
Q clone 2	3665	ACCAGCCCTTACTGC	87331510		**J4**

Table C2. Demographic and exposure characteristics of study subjects from Guangdong, China. Modified and reprinted, with permission from (L. Zhang, X. Tang, N. Rothman et al., Cancer Epidemiol Biomarkers Prev 19 (1), 80 (2010)).

Formaldehyde exposure	Study subjects (n)	Formaldehyde air level (ppm)*	Age (y)	Gender		Current smoking		Current alcohol drinking		Recent respiratory infections		Body mass index
				Male	Female	Yes	No	Yes	No	Yes	No	
Controls	51	0.026 (0.0085, 0.026)†	30 ± 7‡	44 (86)§	7 (14)	23 (45)	28 (55)	21 (41)	30 (59)	15 (29)	36 (71)	22.16 ± 3.18
Exposed	43	1.28 (0.63, 2.51)†	31 ± 6‡	37 (86)	6 (14)	18 (42)	25 (58)	11 (26)	32 (74)	17 (40)	26 (60)	21.46 ± 2.54

*Assigned values in controls are based on the 8-h time-weighted average level in their respective control factories using measurements of a subgroup of workers. Assigned values in exposed workers are an 8-h time-weighted average based on arithmetic mean of individual exposure measurements.

†Median exposure (10th, 90th percentile). A value of the limit of detection divided by square root of 2 was assigned to individuals for nondetectable formaldehyde exposure.

‡Mean ± SD.

§Subject number (%).

Table C3. Oligonucleotides used as primers and probes in this study. The sequence, modifications, and uses of the various oligonucleotides in this study.

oligo name	uses	5' mod	3' mod	Sequence (5'-3')
RT0001	preamplification reaction	none	none	TGG CGA ATG ACC AGC AGA TT
Nv3	hemi-nested Q-PCR hemi-nested ePCR (fluorescently label t(14;18) amplicon on-bead) sequencing reactions	none FAM none	none none none	CTA TGG TGG TTT GAC CTT TAG AGA GTT
BCL2MBRTM2	Q-PCR probe sequence	FAM	TAMRA	TTT CAA CAC AGA CCC ACC CAG AGC CCT CCT G
JH Exo	preamplification reaction paired-end sequencing reactions (used with Nv3 to define short amplicons) on-bead PCR (covalently bound to agarose beads)	none none amine + C12	none none none	ACT CAC CTG AGG AGA CGG TGA C
F-ActB	quality control reactions on gDNA	none	none	TAC GTT GCT ATC CAG GCT GTG C
R-ActB	quality control reactions on gDNA	none	none	GCC ATC TCT TGC TCG AAG TCC A
ActB probe	Q-PCR probe sequence	JOE	Iowa Black	TAT CCC TGT ACG CCT CTG GCC GTA CCA CT

Appendix D: Supplemental information for Chapter 6

D.1 Supplementary materials and methods

Device fabrication and assembly. The 4-channel MEGA devices were constructed from 100-mm diameter glass wafers and a thin poly(dimethylsiloxane) (PDMS) membrane, as detailed previously [102]. Briefly, the valve seat structure was first microfabricated on the top side of a Borofloat glass wafer. Using backside alignment lithography, the microchannels were patterned onto the bottom of the same wafer in register with the pump structure. Fluidic and interlayer access holes were drilled and the wafer was thermally bonded to a clean substrate to enclose the microfluidic network. The on-chip pump assembly was completed by sandwiching a 200 μm PDMS membrane between the chip and a pneumatic manifold plate with microfabricated valve displacement chambers (Figure 2A). The glass channels were rendered hydrophobic by coating with a 0.1% solution of octadecyltrichlorosilane (OTS, Sigma-Aldrich) in dry toluene for 10 min.

Bead functionalization. All reagents were handled in a UV-treated laminar flow hood (UVP, Upland, CA). The oligonucleotides used in this study (Table S-1) were obtained from IDT (Coralville, IA). Forward primers were labeled with 6-FAM or Cy5 dye on the 5' end. Equimolar 5' amine modified reverse primers with a C12 spacer were linked to 6% cross-linked NHS-activated Sepharose beads (34 μm mean diameter, #17-0716-01, GE Healthcare, Piscataway, NJ) at ~0.5 μmol g^{-1} through amine-NHS conjugation chemistry.[102,135] After overnight incubation, primer beads were washed and re-suspended in water at final bead concentrations of 4000-6000 beads μL^{-1}.

Cell culture and preparation. Cell lines of $t(14;18)^-$ TK6 (CRL 8015) and $t(14;18)^+$ RL (CRL 2261) (ATCC, Manassas, VA) lymphoblasts were maintained in RPMI 1640 media supplemented with 10% FBS at a cell density between 2 x 10^5 and 2 x 10^6 and incubated at 37 ºC in a 5% CO_2 atmosphere. Cell preparation was performed in a Class II biosafety cabinet (Labconco, Kansas City, MO) to avoid contamination. Final cell density was determined by using a hemacytometer (Hausser Scientific, Horsham, PA). Cells were combined with primer-functionalized beads in PBS and incubated at 40 ºC prior to the addition of agarose for a final concentration of 400 beads μL^{-1}, and 80-120 cells μL^{-1} in 1.5% agarose.

Agarose droplet generation. The fresh carrier oil was prepared daily, which contains 39.8% (w/w) DC 5225C Formulation Aid (Dow Chemical Co., Midland, MI), 30% (w/w) DC 749 Fluid (Dow Chemical Co.), 30% (w/w) AR20 Silicone Oil (Sigma-Aldrich), and 0.2% (w/w) Triton X-100 surfactant (Sigma-Aldrich). The MEGA device was assembled with a custom aluminum manifold which provides fluidic connection for oil infusion and droplet collection. Carrier oil was continuously injected into the MEGA device from two gastight syringes (Hamilton Company, Reno, NV) using a syringe pump (PHD 2000, Harvard Apparatus, Holliston, MA). Molten agarose solution containing cells and beads was injected into the microchannels for droplet generation by the on-chip 3-valve diaphragm pump, which was pneumatically actuated by a solenoid valve system built in house. The pumping was conducted in a four-step fashion under the control of a LABVIEW graphical interface (National Instruments).[135]

The whole MEGA assembly was continually heated using a heated air stream (42-45ºC) to avoid agarose gelling in the device. Pumping parameters were optimized to produce uniform ~3 nL 1.5% agarose droplets (actuation times: valves 1 and 2 open, 42 ms; valve 1 close, 42 ms; valve

3 open, 20 ms; valves 2 and 3 close, 18 ms; total oil flow rate: 14 μL min^{-1}; pneumatic line pressure/vacuum: +35/-85 kPa). The sample reservoir was constantly replenished with agarose suspension to sustain the droplet generation. Agarose droplets were collected and immediately gelled in 0.5 mL PCR tubes placed in freezer trays (Eppendorf).

Genome purification. Agarose droplets were extracted from carrier oil by washing with isopropanol, 100% ethanol, and PBS (10 mL each) and resuspended in 1 mL PBS. To lyse cells, 1 mL 2X SDS lysis buffer (1% SDS, 200 mM EDTA, 20 mM Tris-HCl) and 100 mg/mL proteinase K (Roche Applied Science, Indianapolis, IN) were added, and samples were incubated overnight at 52 °C. Droplets were washed with 2% (w/v) Tween 20 (Baker Chemical, Phillipsburg, NJ) as Tween 20 has been shown to reduce the PCR-inhibitory effect of SDS.[247] A 100% ethanol wash to inactivate any remaining proteinase K was followed by 5 washes of 0.02% (w/v) Tween 20 (10 mL each). Agarose droplets were washed with 10 mL H_2O and supernatant was removed. Samples not immediately used were stored at 4°C in 100% ethanol and washed with H_2O just prior to emulsion PCR.

Emulsion PCR. The PCR mix contained 1X *Ampli* Taq Gold® buffer with 1.5 mM $MgCl_2$, 0.2 mM dNTPs, 4 μg/μL heat-inactivated BSA, 0.01% Tween 80, 0.45 μM forward and 0.045 μM reverse primers for each target gene, 0.25 U μL^{-1} *Ampli* Taq Gold® Polymerase, and 12.5 μL agarose droplets containing purified single cell genomes in each 50 μL PCR reaction. Agarose droplets were equilibrated in PCR mix in standard 0.5 mL PCR tubes for 30 min at 4°C with occasional agitation. To re-emulsify the agarose droplets, 160 μL carrier oil were added and mechanically agitated. Carrier oil was identical to the oil used for initial agarose droplet formation but contained 0.8% (w/w) Triton X-100 surfactant for increased stability. Emulsions were generated by mechanical agitation. Thermal cycling, carried out in a PTC200 thermocycler (MJ Research, Waltham, MA), involved ramping to 95 °C (0.1°C/s) in order to melt agarose droplets without merging, followed by 10 min hot start at 95 °C, and 33 cycles of 95 °C for 30 s, 60 °C for 60 s, 72 °C for 90 s, and a final 72 °C extension for 5 min. The reactions were cooled to 4 °C.

Bead recovery and flow cytometry quantitation. The emulsion in PCR tubes was centrifuged (2,000 rpm; 1 min) to pellet agarose droplets and supernatant was removed. After rinsing with 100% isopropanol, 100% ethanol and 1× Dulbecco's PBS (DPBS, GIBCO) (600 μL each), the beads were recovered by heating the samples (65 °C, 10 min) to melt the agarose. This treatment was found to not significantly affect the amplicon loading of beads. Samples were washed with 0.1% SDS to help remove BSA, transferred to flow cytometry tubes, and washed in 1X DPBS. The bead suspension in PBS was analyzed by using a multicolor flow cytometer (FC500, Beckman-Coulter, Fullerton, CA). The flow cytometry data were analyzed by using WinMDI (Scripps, La Jolla, CA) and WinList 6.0 (Verity Software, Topsham, ME).

Multiplex single-cell sequencing. Single cell sequencing was accomplished by re-amplifying amplicon-bound beads from emulsion PCR in a TaqMan qPCR reaction in 50 μL reactions in standard 96 well PCR plates. Beads were counted using a hemocytometer and diluted to approximately 1 bead per reaction. PCR mix contained 1X *Ampli* Taq Gold® buffer with 5 mM $MgCl_2$, 0.2 mM dNTPs, 0.025% DMSO, 1 μM ROX reference dye, 0.15 μM forward and 0.15 μM reverse primers and 0.15 μM TaqMan probe for each target gene, 0.035 U μL^{-1} *Ampli* Taq Gold® Polymerase. Thermal cycling in an ABI7300 cycler consisted of a 10 min hot start at 95 °C,

and 20 cycles of 95 ^{o}C for 15 s, 60 ^{o}C for 30 s, and 72 ^{o}C for 30 s. The amplicon on beads could be re-amplified after six months of storage at 4 ^{o}C. Reactions were loaded on a 1.5% agarose gel and electrophoresed to separate the two amplicons that were then excised, purified using a QIAquick Gel Extraction Kit (QIAGEN, Valencia, CA), and sequenced on an ABI3730 at the UC Berkeley Core Sequencing Facility.

Fluorescence imaging. Spinning disk confocal microscopy was performed with 491 and 561 nm excitation lasers through a 63x 1.4 NA oil immersion objective (Carl Zeiss, Inc., Thornwood, NY) and a Chroma 42953 and 41674 filter sets. Images were captured using a Cascade II charge-coupled device (Photometrics, Tuscon, AZ). Samples were stained with (50 μg mL^{-1}) acridine orange or (500 μg mL^{-1}) propidium iodide. Epifluorescence imaging of amplicon-labeled beads was performed using a 10x 0.25 NA Nikon Plan objective and an F HQ filter cube set (Nikon Instruments, Inc., Melville, NY). Images were contrast-adjusted and cropped if needed for optimal viewing.

Table D1. Primer sequences for gene targets

Gene target	T_m (°C)	Sequence	Size (bp)
β-actin			
Forward	60.5	5′- Cy5 -TACGTTGCTATCCAGGCTGTGC-3′	200
Reverse	58.7	5′- CTGTAGCCGCGCTCGGT-3′	
Probe	73.9	5′- JOE - TATCCCTGTACGCCTCTGGCCGTACCACT - Iowa Black FQ -3′	
t(14;18)			
Forward [230]	60.2	5′- TGGCGAATGACCAGCAGATT-3′	296
Reverse [230]	60.3	5′- FAM -ACTCACCTGAGGAGACGGTGAC-3′	
Probe	74.6	5′- FAM - TTTCAACACAGACCCACCCAGAGCCCTCCTG - TAMRA -3′	

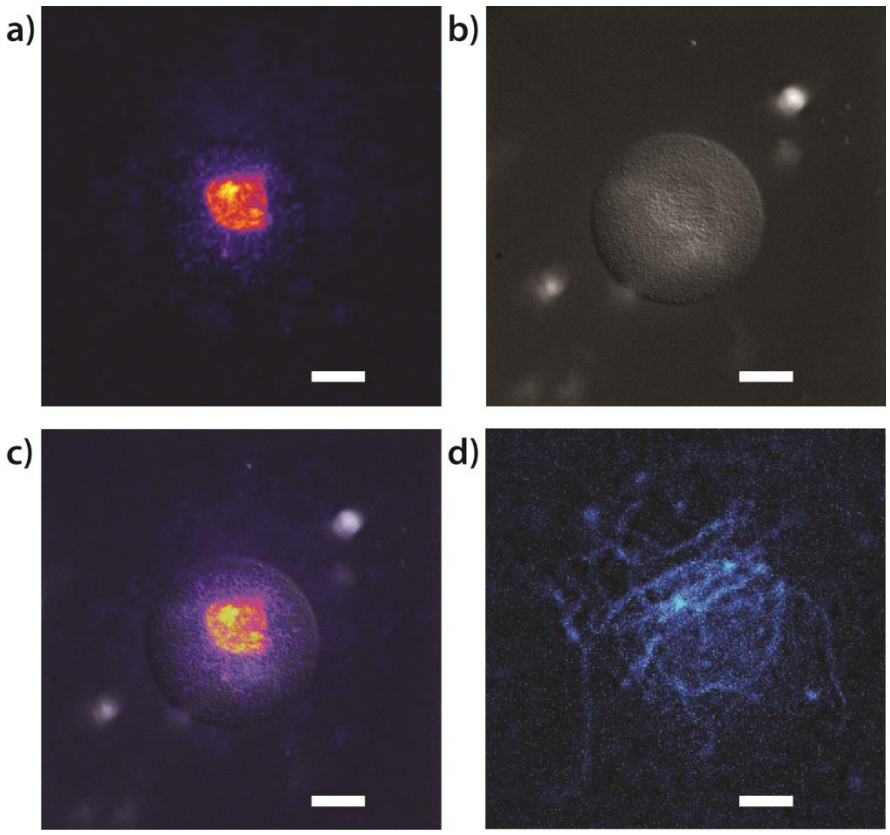

Figure D1. A) Confocal micrograph maximum-intensity projection of a single TK6 cell encapsulated in a 1.25% agarose droplet generated by mechanical agitation, treated overnight with SDS lysis buffer and proteinase K, and stained with propidium iodide to demonstrate that released genomic DNA was able to partially diffuse the short distance through the agarose in these small droplets. For PCR amplification where DNA diffusion is undesirable, large agarose droplets were generated using a microfluidic system. B) DIC image of the same droplet. C) Overlay of A and B. D) Close-up view of a single confocal slice showing single DNA strands on the surface of the agarose droplet. Scale bars are 10 μm in A-C and 5 μm in D.

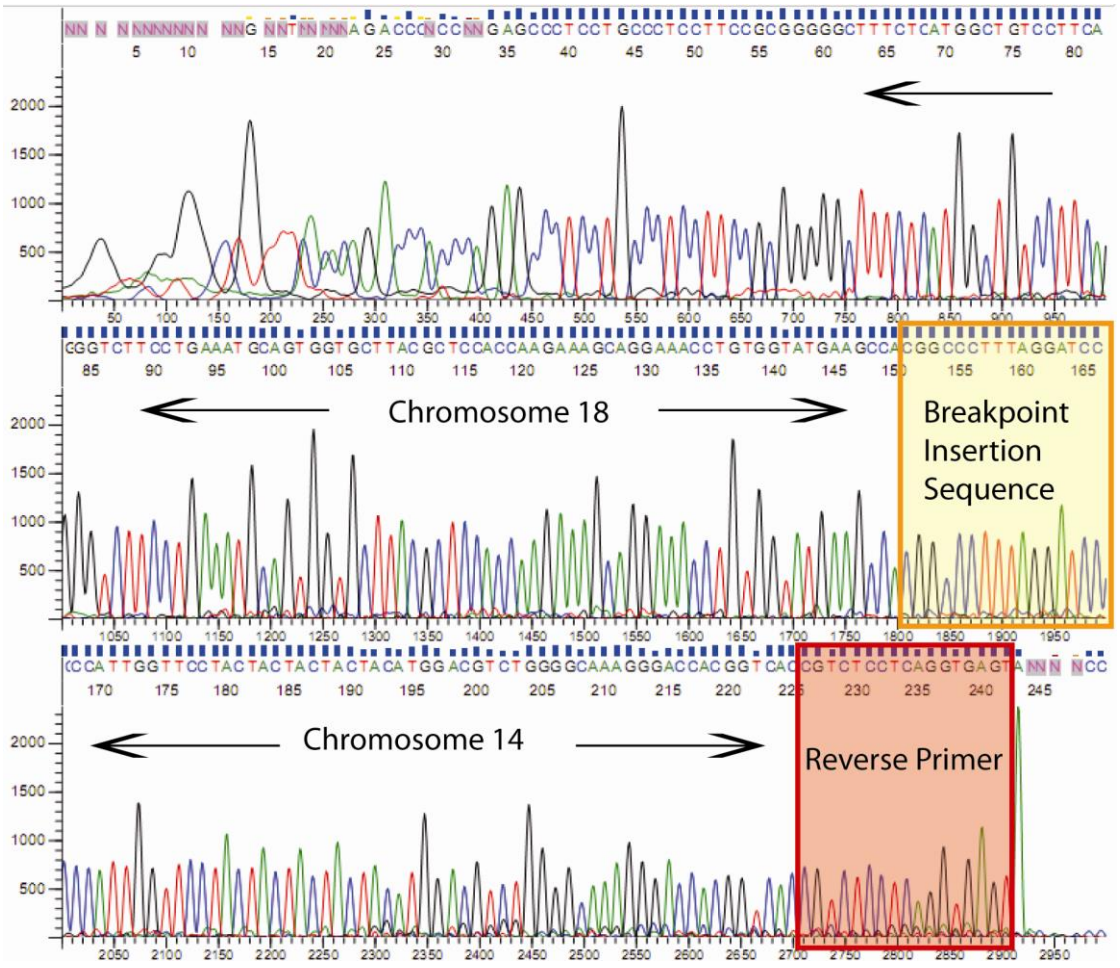

Figure D2. A representative electropherogram of the t(14;18) translocation sequence from the ABI3730 sequencer obtained by re-amplification of bead-bound template from a single cell showing the joining of chromosomes 14 and 18 with a unique inserted sequence as well as the reverse primer site. Two genes from 4 RL cells were sequenced to demonstrate proof of principle.

Figure D3. A representative electropherogram of the β-actin sequence from the ABI3730 sequencer obtained by re-amplification of bead-bound template from a single cell.

Appendix E: Supplemental information for Chapter 7

Table E1. Primer information for multiplex PCR

Primer		Sequence and Dye Labeling	Emulsion PCR (µM)	Secondary PCR (µM)
Amelogenin	F	**[TAMRA]-**CCCTGGGCTCTGTAAAGAA	0.18	0.18
	R	ATCAGAGCTTAAACTGGGAAGCTG	0.018	0.18
vWA	F	GCCCTAGTGGATGATAAGAATAATCAGTATGTG	0.022	0.22
	R	**[TAMRA]-**GGACAGATGATAAATACATAGGATGGATGG	0.22	0.22
D8S1179	F	**[TAMRA]-**ATTGCAACTTATATGTATTTTTGTATTTCATG	0.64	0.64
	R	ACCAAATTGTGTTCATGAGTATAGTTTC	0.064	0.64
TH01	F	**[FAM]-**GTGATTCCCATTGGCCTGTTC	0.21	0.21
	R	ATTCCTGTGGGCTGAAAAGCTC	0.021	0.21
D3S1358	F	ACTGCAGTCCAATCTGGGT	0.018	0.18
	R	**[FAM]-**ATGAAATCAACAGAGGCTTGC	0.18	0.18
D21S11	F	ATATGTGAGTCAATTCCCCAAG	0.056	0.56
	R	**[FAM]-**TGTATTAGTCAATGTTCTCCAGAGAC	0.56	0.56
D5S818	F	GGTGATTTTCCTCTTTGGTATCC	0.02	0.2
	R	**[JOE]-**AGCCACAGTTTACAACATTTGTATCT	0.2	0.2
D7S820	F	**[JOE]-**ATGTTGGTCAGGCTGACTATG	0.45	0.45
	R	GATTCCACATTTATCCTCATTGAC	0.045	0.45
D13S317	F	**[JOE]-**ATTACAGAAGTCTGGGATGTGGAGGA	0.1	0.1
	R	GGCAGCCCAAAAAGACAGA	0.01	0.1

Abbreviations: F: Forward; R: Reverse.

Table E2. Locus-specific information for 9947A female and 9948 male genomic DNA

STR Locus	9947A female DNA		9948 male DNA	
	Repeat number	Amplicon size (bp)	Repeat number	Amplicon size (bp)
Amelogenin	X, X	106	X, Y	106, 112
vWA	17, 18	151, 155	17,17	151
D8S1179	13, 13	227	12, 13	223, 227
TH01	8, 9.3	172, 179	6, 9.3	164, 179
D3S1358	14, 15	123, 135	15, 17	127, 135
D21S11	30, 30	227	29, 30	223, 227
D5S818	11, 11	135	11, 13	135, 143
D7S820	10, 11	231, 235	11, 11	235
D13S317	11, 11	181	11, 11	181

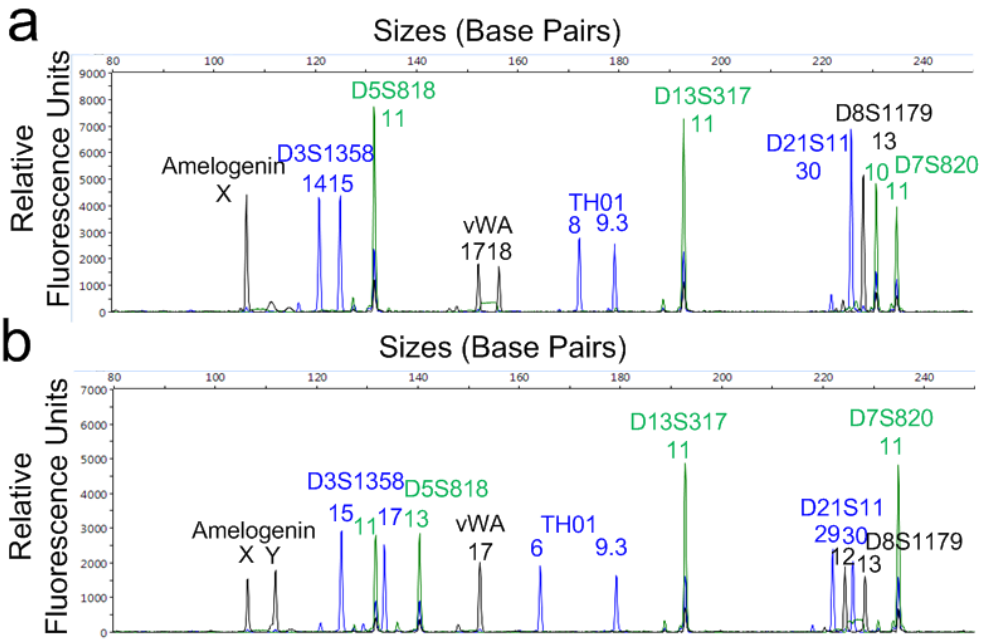

Figure E1. Representative 9-plex STR profiles resulting from PCR amplification of (A) 9947A female genomic DNA and (B) 9948 male genomic DNA at high concentrations in bulk solutions containing multiplex-primer-functionalized microbeads. The PCR was performed with 32 cycles from 40 pg/μL (~13 copies/μL) of the genomic DNA. The PCR products in free solution were processed by a conventional CE system for fragment sizing analysis. These traces illustrate the success in balancing the solid-phase 9-plex PCR involving microbeads.

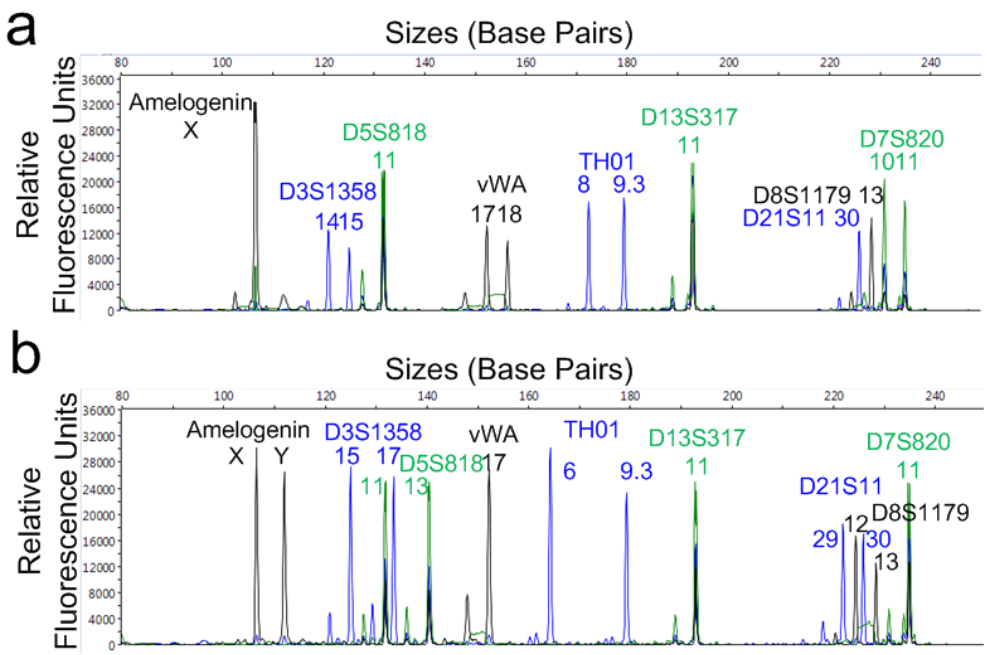

Figure E2. Representative 9-plex STR profiles resulting from secondary PCR amplification of single beads carrying STR products of (A) 9947A female genomic DNA and (B) 9948 male genomic DNA. The amplicon-bound beads were prepared by performing 32 cycles of PCR seeded with isolated DNA in bulk solution. The PCR starting from single beads was performed in standard PCR plates with 30 cycles. These traces illustrate the success in balancing the 9-plex PCR starting from a single-beads carrying STR products.

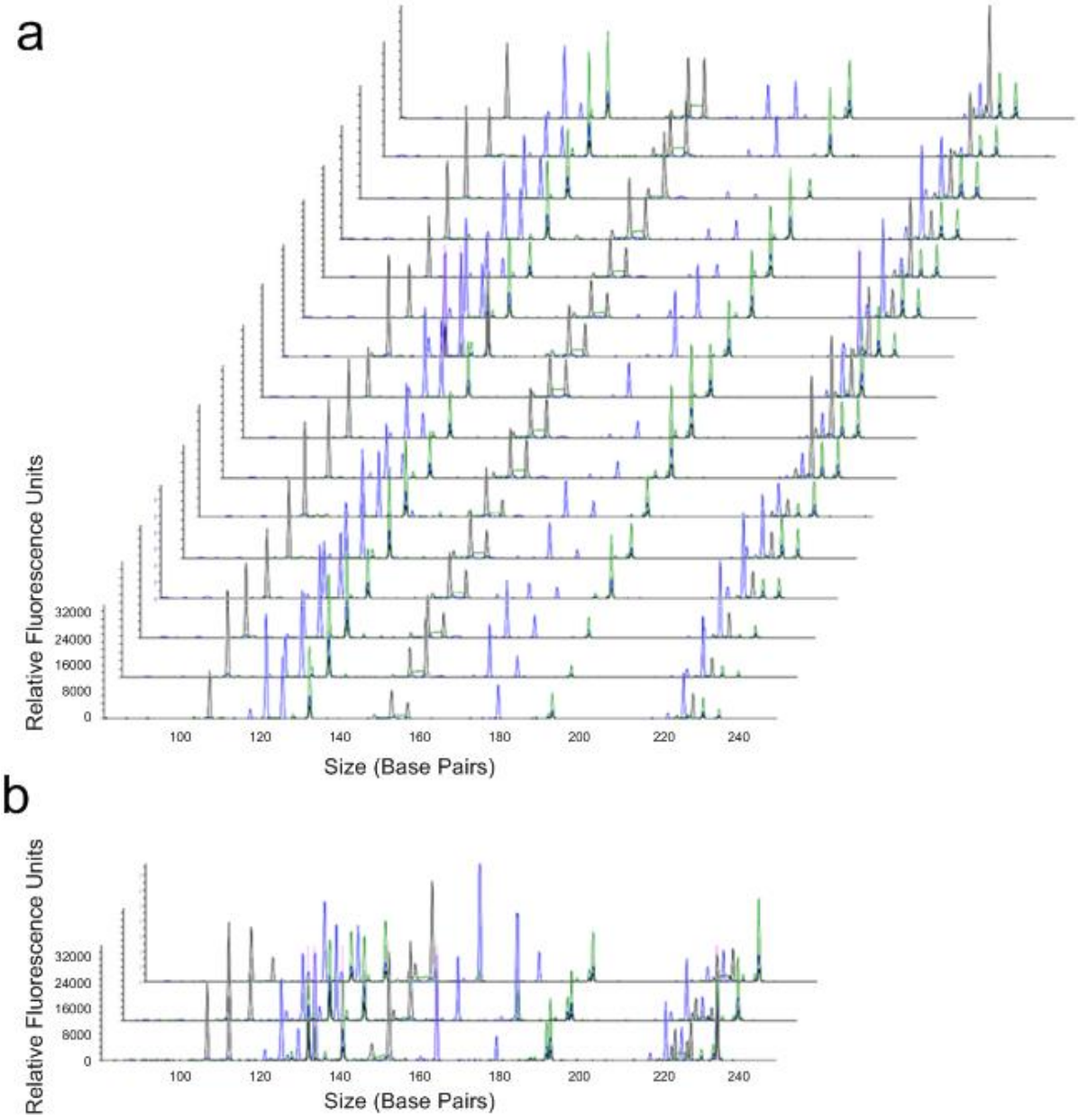

Figure E3. Single-cell STR profiles resulting from microdroplets containing on average 0.01 GM09947 human (female) and GM09948 human (male) lymphoid cells with a ratio of 5:1 as well as 0.9 beads per droplet. Under the statistically dilute conditions it is expected that approximately 1% beads will have all STR products from either type of cells. In total 100 samples were tested in secondary PCR using 20 beads per reaction (predicting $20 \times 0.01 = 0.2$ positive beads per reaction) on average. There were 19 positive analyses (consistent with the theoretical value of 18% predicted by Poisson distribution), in which 16 STR profiles were from GM09947 cells (A) and 3 were from GM09948 cells (B). 81 samples yielded null results in the secondary PCR. In all cases, 30 cycles of emulsion PCR and 25 cycles of secondary PCR were performed.

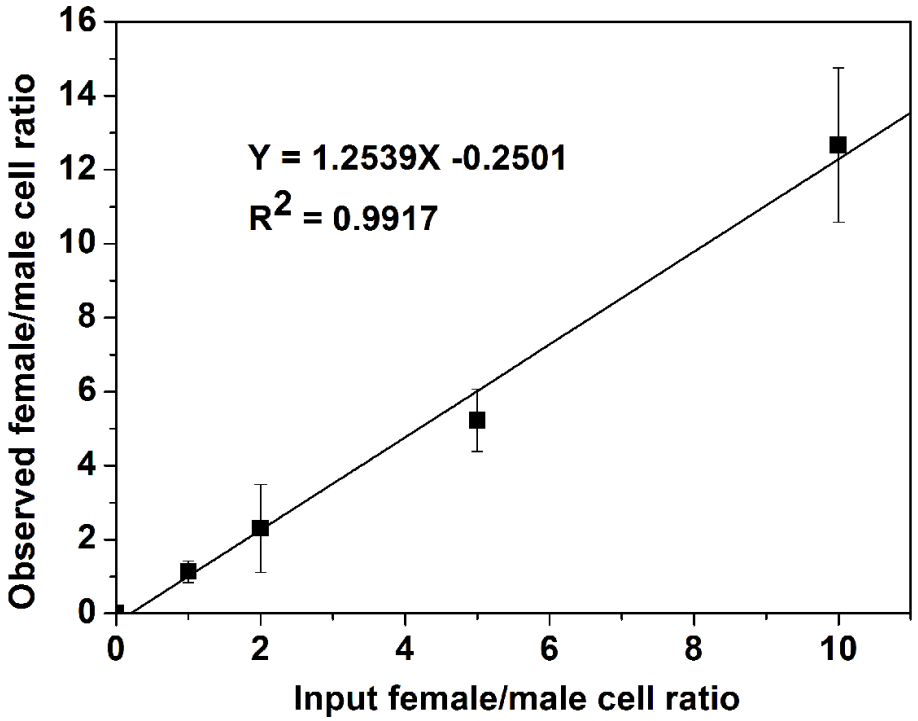

Figure E4. Single-cell STR typing of the GM09947 human (female) and GM09948 human (male) lymphoid cell mixtures. Plot of experimental cell number ratio vs. input cell number ratio exhibits a linear relationship. Cells were encapsulated in microdroplets with various GM09947: GM09948 cell ratios (1:1, 2:1, 5:1 and 10:1) at the frequency of 0.01 total cells (together with 0.9 beads) per droplet on average. Under these statistically dilute conditions it is expected that approximately 1% of the beads will have STR products from either type of cell. In total 40, 70 or 100 samples were tested based on 20 beads per reaction (predicting 20 × 0.01 = 0.2 positive beads per reaction) on average. In all cases, 30 cycles of emulsion PCR and 25 cycles of secondary PCR were performed. Each data point was generated by 3 independent assays.

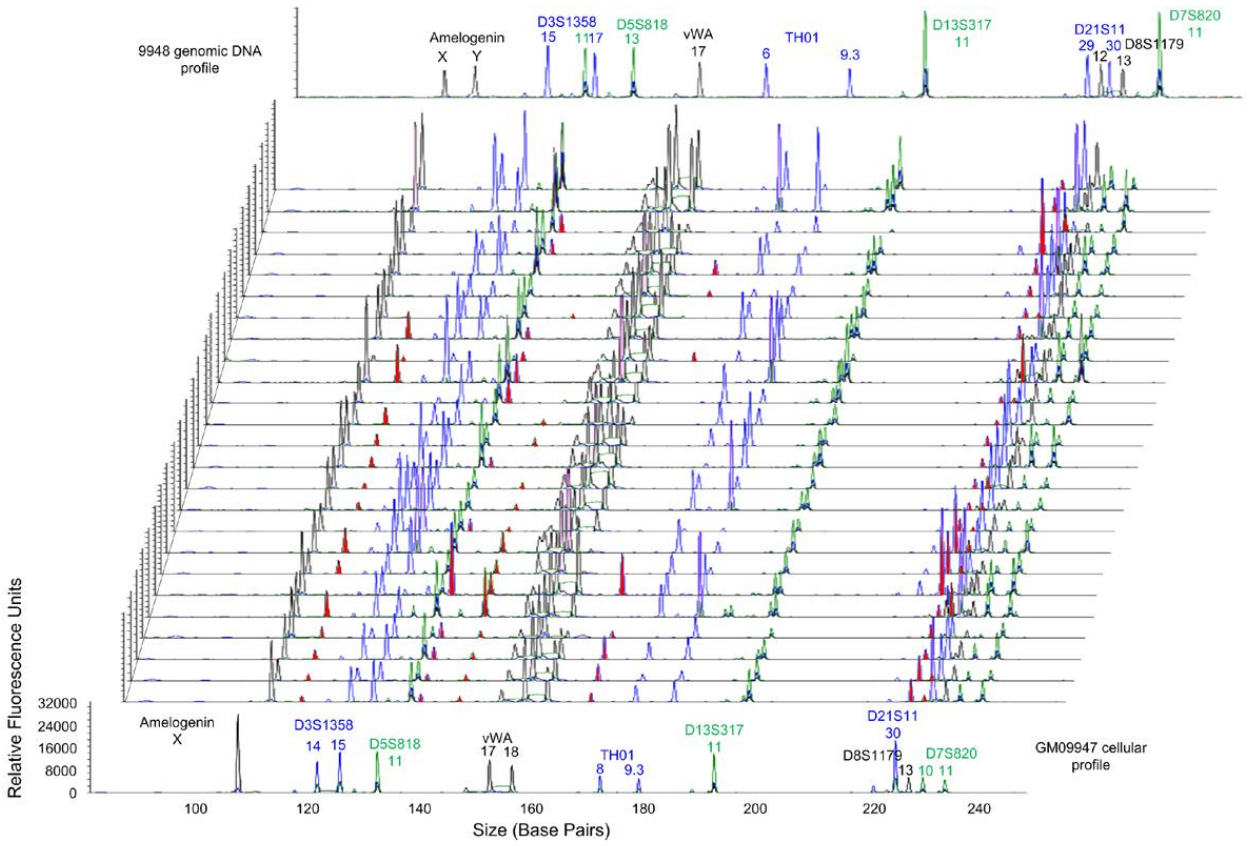

Figure E5. Representative STR profiles resulting from microdroplets containing 1 GM09947 human (female) lymphoid cell, 1.5 copies 9948 genomic DNA and 0.9 beads per droplet on average. Under the statistically dilute conditions it is expected that approximately 63% of the beads will have all GM09947 cellular STR products and 98.89% of the beads will have at least one of the 9948 DNA-specific STR products. In total 70 samples were tested in secondary PCR using 0.6 beads per reaction (predicting $0.6 \times 0.63 = 0.378$ GM09947-cell-DNA-positive beads per reaction) on average. There were 25 positive analyses, which was consistent with the theoretical value of 31% predicted by the Poisson distribution. In all cases, 30 cycles of emulsion PCR and 25 cycles of secondary PCR were performed. Red filled peaks indicate 9948 DNA-specific peaks which appear randomly.

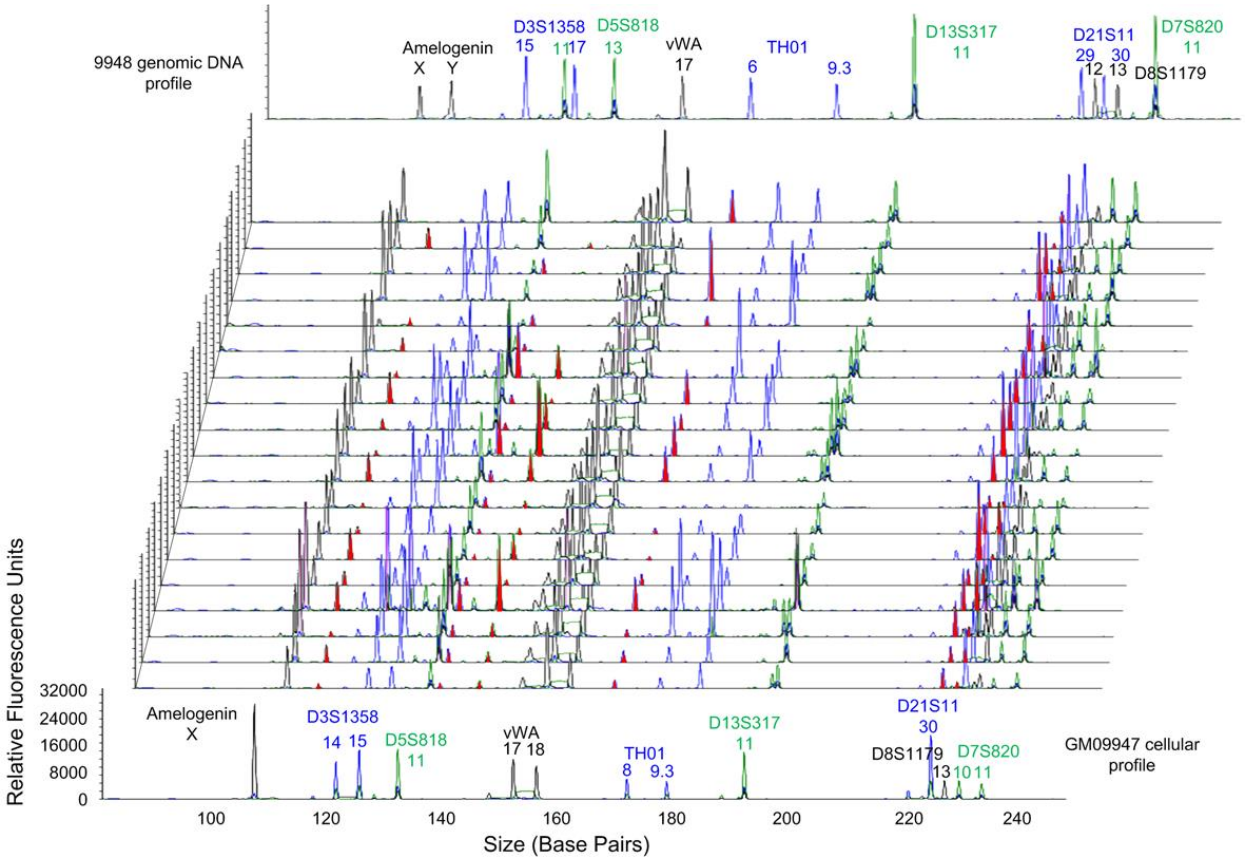

Figure E6. Representative STR profiles resulting from microdroplets containing 1 GM09947 human (female) lymphoid cell, 2 copies 9948 genomic DNA and 0.9 beads per droplet on average. Under the statistically dilute conditions it is expected that approximately 63% of the beads will have all GM09947 cellular STR products and 99.75% of the beads will have at least one of the 9948 DNA-specific STR products. In total 70 samples were tested in secondary PCR using 0.6 beads per reaction (predicting $0.6 \times 0.63 = 0.378$ GM09947-cell-DNA-positive beads per reaction) on average. There were 19 positive analyses, which was consistent with the theoretical value of 31% predicted by the Poisson distribution. In all cases, 30 cycles of emulsion PCR and 25 cycles of secondary PCR were performed. Red filled peaks indicate 9948 DNA-specific peaks which appear randomly.

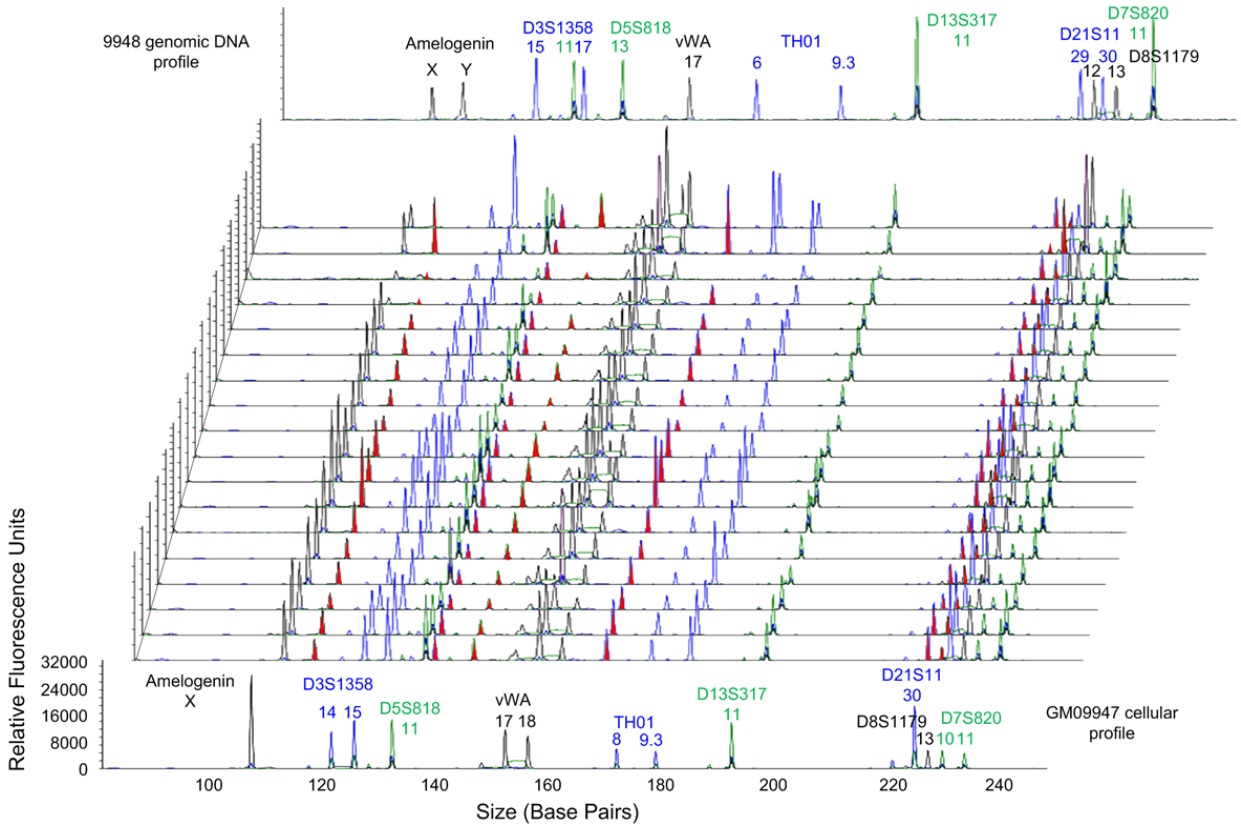

Figure E7. Representative STR profiles resulting from microdroplets containing 1 GM09947 human (female) lymphoid cell, 3 copies 9948 genomic DNA and 0.9 beads per droplet on average. Under the statistically dilute conditions it is expected that approximately 63% of the beads will have all GM09947 cellular STR products and 99.99% of the beads will have at least one of the 9948 DNA-specific STR products. In total 70 samples were tested in secondary PCR using 0.6 beads per reaction (predicting 0.6 × 0.63 = 0.378 GM09947-cell-DNA-positive beads per reaction) on average. There were 18 positive analyses, which was consistent with the theoretical value of 31% predicted by the Poisson distribution. In all cases, 30 cycles of emulsion PCR and 25 cycles of secondary PCR were performed. Red filled peaks indicate 9948 DNA-specific peaks which appear randomly.

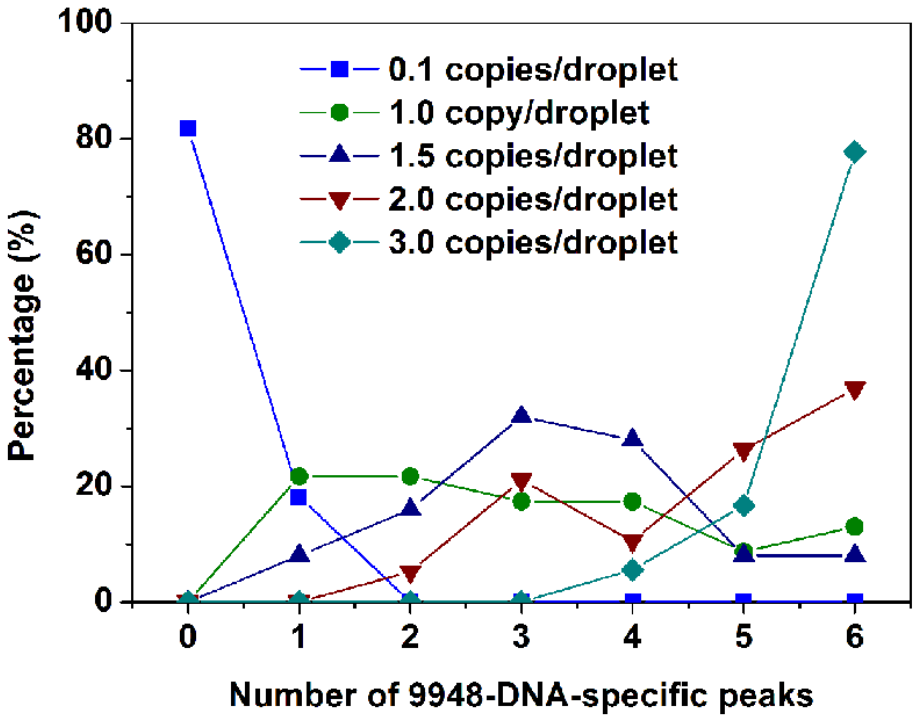

Figure E8. Single-cell STR typing in presence of cell-free contaminating DNA. The percentage of profiles containing all GM09947 cellular peaks and a certain number (0, 1, 2, 3, 4, 5 or 6) of 9948-DNA-specific peaks in profiles containing all GM09947 cellular peaks (any profile containing all peaks from a GM09947 cell) is plotted vs. the number of 9948-DNA-specific peaks as a function cell-free DNA concentration. 9948 genomic DNA was encapsulated in microdroplets together with GM09947 human (female) lymphoid cells at the frequency of 0.1, 1, 1.5, 2 and 3 copies DNA, 1 cell and 0.9 beads per droplet on average. Under the statistically dilute conditions it is expected that approximately 63% beads will have all STR products from GM09947 cells, and 26%, 95%, 98.89%, 99.75% and 99.99% beads will have at least one of the 9948 DNA-specific STR products, respectively. In total 70 samples were tested in secondary PCR using 0.6 beads per reaction on average. In all cases, 30 cycles of emulsion PCR and 25 cycles of secondary PCR were performed.

Appendix F: Supplemental information for Chapter 9

Table F1. Primers used for RT-PCR and hemi-nested PCR reamplification. Melt points are shown for both RNA and DNA targets for the relevant RT-PCR primers (RNA T_m/DNA T_m), and all temperatures were calculated for the experimental conditions using Oligo Analyzer 3.1 (Integrated DNA Technologies).

RT Primers	**T_m (°C)**	**Sequence (5'➔3')**
FAM Rev-hTERT RT-PCR*	64.5/67	/56-FAM/CGCAAACAGCTTGTTCTCCATGTC
For-hTERT*	63.5	GCCTGAGCTGTACTTTGTCAA
Rev-GAPDH	50.8/56.7	CAAAGTTGTCATGGATGACC
Cy5 For-GAPDH RT-PCR	61.3	/5Cy5/AGTCCACTGGCGTCTTCAC
HEX Rev-hTR	48.6/59.6	/5HEX/TAGAATGAACGGTGGAAGGC
For-hTR RT-PCR	65.5	TTGCGGAGGGTGGGCCT

Hemi Nested Primers	**T_m (°C)**	**Sequence (5'➔3')**
FAM Rev-hTERT Nested*	66.7	/56-FAM/AGGCTGCAGAGCAGCGTGGAGAGG
For-hTERT*	62.6	GCCTGAGCTGTACTTTGTCAA
Rev-GAPDH	58.0	CAAAGTTGTCATGGATGACC
FAM For-GAPDH Nested	62.7	/56-FAM/CCATGGAGAAGGCTGGGG
HEX Rev-hTR	61.9	/5HEX/TAGAATGAACGGTGGAAGGC
HEX For hTR Nested	60.5	/5HEX/CATTTTTTGTCTAACCCTAACTGAG

*Adapted from Yi, et al., 2001.[291]

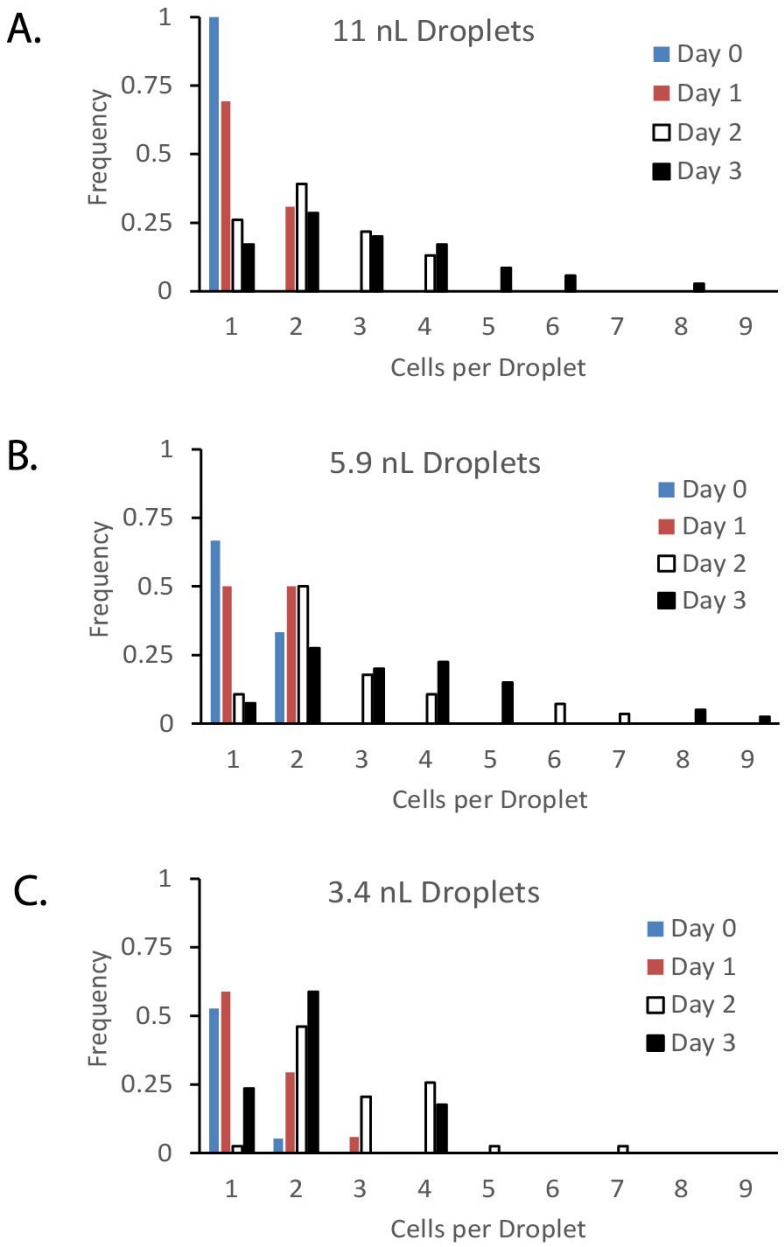

Figure F1. Histograms of colony size for days 0-3 in 11 nL, 5.9 nL, and 3.4 nL droplets. The smallest droplet volume results in rapid consumption of nutrients and cells show poor growth from day 2. The two larger droplet volumes provide sufficient nutrients to support cell growth. The histogram in Figure F1A shows a skewed normal distribution of colony size instead of the expected peaks at 1, 2, 4, and 8 cells, seen in Figure F1B and C, indicating slow and heterogenous growth rates not representative of bulk cultures.

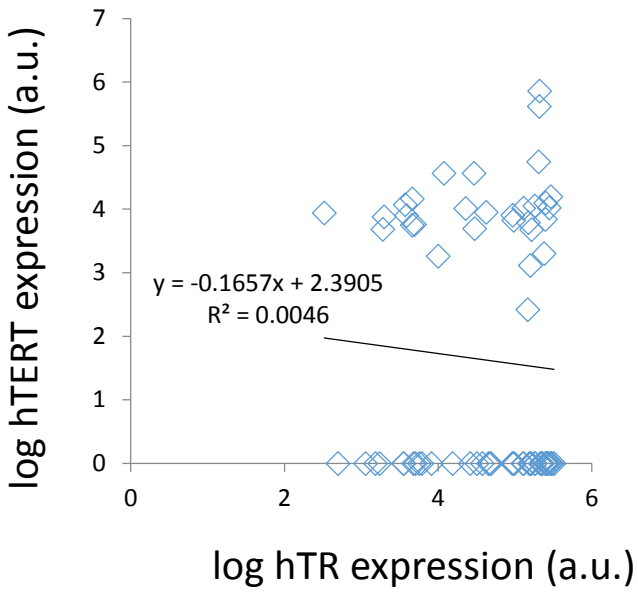

Figure F2. Plot of $\log_{10}$-transformed hTR and hTERT expression levels obtained from serial dilutions of Jurkat cell lysate. Each point represents a separate RT-PCR reaction. The lack of correlation indicates minimal amplification competition between the targets.

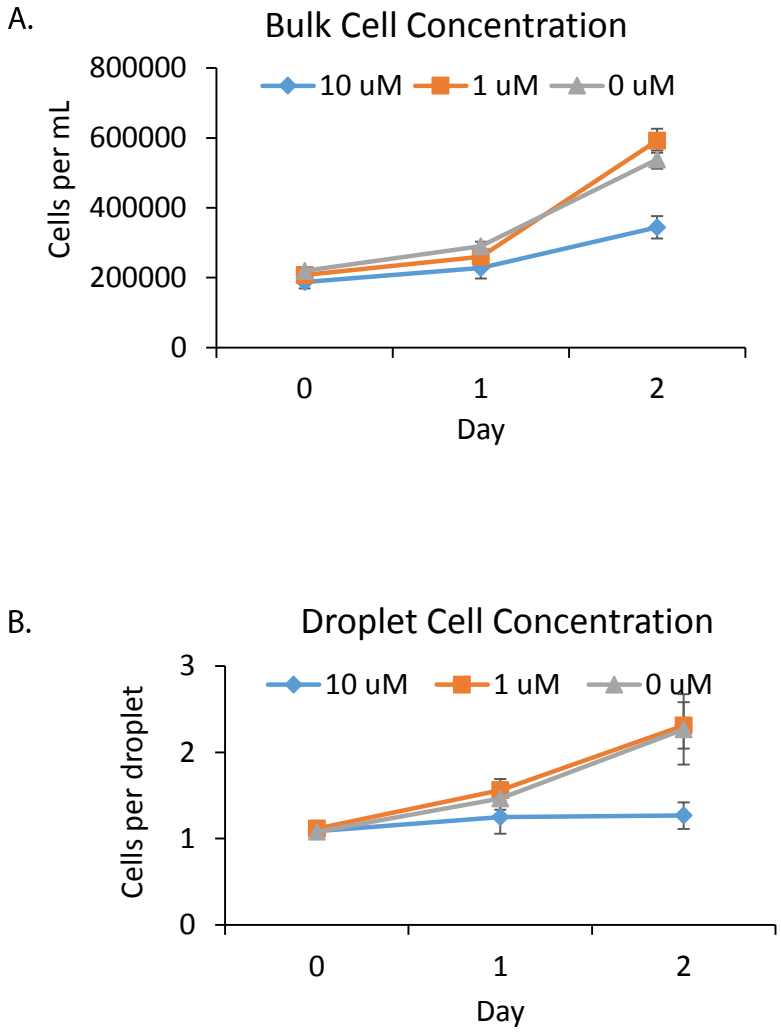

Figure F3. Comparison of growth rates among two curcumin concentrations and a DMSO control reveals a significant growth impact of 10 μM curcumin on cell growth and no significant effect between 0 μM and 1 μM curcumin. The results demonstrate that cellular drug response in droplets parallels that of traditional bulk cultures.

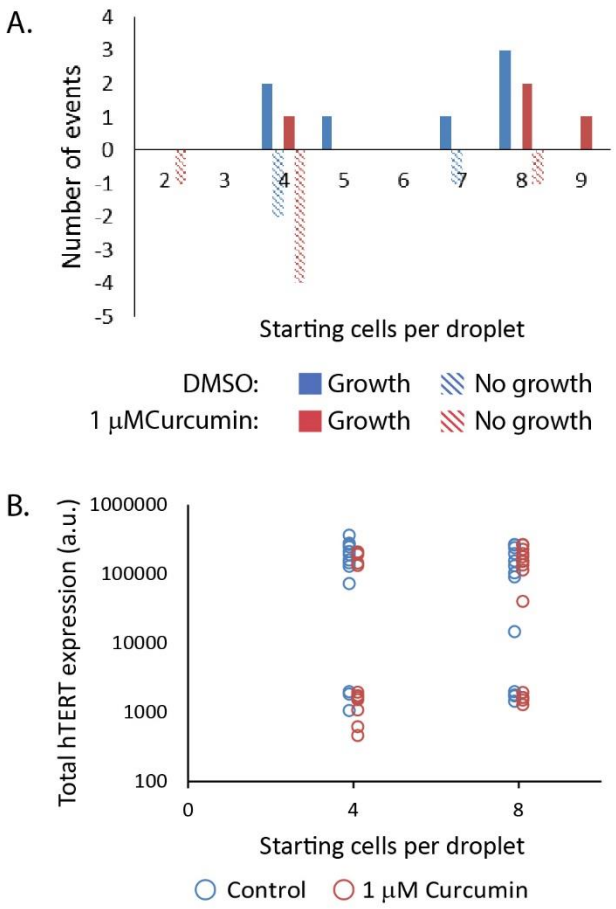

Figure F4. Subculture of droplet colonies for downstream analysis. (A) Frequency plot of survival of K562 colonies following subculture into wells containing 50 μL medium, with successful and failed subcultures represented by positive and negative values, respectively. Faster growing colonies (7-9 cells per droplet) have a greater probability of survival in subculture than slower growing colonies (2-5 cells per droplet). (B) Expression data with each point representing ~5-cell samples for 4-cell and 8-cell colonies each taken from control or curcumin-treated cells shows a reversion of total hTERT expression to the original bimodal pattern after two weeks of culture in curcumin-free medium.